This is to certify that the
dissertation entitled

Exploratory Synthesis of Complex Intermetallic Tetrelides and Antimonides Using Liquid Aluminum as a Solvent

presented by

Xiuni Wu

has been accepted towards fulfillment
of the requirements for the

Ph. D. degree in Chemistry

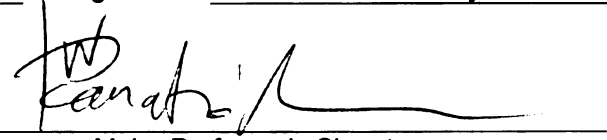

Major Professor's Signature

5/10/2006

Date

EXPLORATORY SYNTHESIS OF COMPLEX INTERMETALLIC TETRELIDES AND ANTIMONIDES USING LIQUID ALUMINUM AS A SOLVENT

By

Xiuni Wu

A DISSERTATION

Submitted to
Michigan State University
in partial fulfillment of the requirements
for the degree of

DOCTOR OF PHILOSOPHY

Department of Chemistry

2006

ABSTRACT

EXPLORATORY SYNTHESIS OF COMPLEX INTERMETALLIC TETRELIDES AND ANTIMONIDES USING LIQUID ALUMINUM AS A SOLVENT

By

Xiuni Wu

The metal flux method has been recently suggested as a preparative tool to synthesize intermetallic compounds. Our group initiated the investigations on the quaternary systems RE/TM/Al/Tr (RE = rare earth metal, TM = transition metal, Tr = tetrelide) using Al as a flux. In this dissertation we employed the Al flux to study the systems RE/Au/Al/Ge, TM/Al/Tr, RE/Ni/Al and RE/Al/Sb aiming at discovering new materials with interesting physical properties.

We extended the studies involving first row transition metals to the third row transition metals such as Au. Our exploratory investigations led to the discovery of two quaternary families $REAuAl_4Ge_2$ and $REAuAl_4(Au_xGe_{1-x})_2$, the structures of which are related and both can be represented as alternating stacking of RE layers and $AuAl_4Ge_2$ (or $AuAl_4(Au_xGe_{1-x})_2$) slabs along the *c*-axis.

By studying the ternary systems TM/Al/Tr (TM = V, Co) in liquid aluminum, we obtained new ternary compounds $V_2Al_5Ge_5$, $Co_{19}Al_{45}Si_{10-x}$ (x = 0.13) and $Co_5Al_{14}Si_2$. The structure of $V_2Al_5Ge_5$ features pentagonal columns composed of Al and Ge atoms with the V atoms forming a long-short alternating chain residing in the center of the column. Both $Co_{19}Al_{45}Si_{10-x}$ (x = 0.13) and $Co_5Al_{14}Si_2$ show exceptionally complex structures and large unit cells. $Co_5Al_{14}Si_2$ shows interesting thermal oxidation resistance up to 1000°C which is due to the formation of an Al_2O_3 layer on the surface of the crystals.

Th

due to th

transition

properties

were studi

compound

the Fe at

susceptibi

Du

phases Yb

thermodyn

with the A

oxidation s

The ternary compounds $Yb_3Ni_5Al_{19}$ and $Yb_{1.1}Ni_3Al_{8.9}$, are particularly interesting due to their unusual physical properties such as mixed valence and metamagnetic transition. The thermal expansion properties of $Yb_3Ni_5Al_{19}$ as well as the magnetic properties with substitutions of Ni by the other transition metals (e.g. Mn, Fe and Cu) were studied. During the study of substituting Ni by Fe, we discovered a new quaternary compound $YbNi_{2-x}Fe_xAl_8$. Both magnetic properties and Mössbauer spectra show that the Fe atoms do not carry a magnetic moment. Temperature dependent magnetic susceptibility indicates that the Yb atoms are in intermediate oxidation state.

During the investigations of the system Yb/Al/Sb, we isolated two new Zintl phases Yb_3AlSb_3 and $Yb_9Al_3Sb_9$ from molten Al, among which Yb_3AlSb_3 is the more thermodynamically stable form. These two compounds exhibit related structure types with the $AlSb_4$ tetrahedral unit as the common feature, and the Yb ions are in divalent oxidation state.

Fir

Professor

the past fi

lot from hi

I w

McCusker,

discussions

Mohanti an

for me.

I wa

has been a

informal an

me many ex

It w

from my p

encouraged

provided mu

been very fo

and valuable

Fina

acknowledg

ACKNOWLEDGMENTS

First of all, I would like to express my deep and sincere gratitude to my advisor, Professor Mercouri G. Kanatzidis, for his guidance, encouragement and support during the past five years. Professor Kanatzidis is a very knowledgeable chemist and I learned a lot from him. He has helped me strive to be a successful scientist.

I would also like to acknowledge my committee members, Professors James McCusker, Thomas Pinnavaia and James Geiger for their valuable suggestions and discussions. Dr. Reza Loloee helped me with magnetic experiments; Professor S. D. Mohanti and his students Daniel Bilc and Zsolt Rak did electronic structure calculations for me.

I want to thank all the Kanatzidis group members for their help and friendship. It has been a real pleasure working with so many wonderful and talented colleagues in an informal and friendly environment. Special thanks go to Dr. Susan Latturner, who taught me many experimental techniques in my first year at MSU.

It would not have been possible for me to succeed without the love and support from my parents, my sister and brother-in-law. They have always supported and encouraged me to pursue my goals. I would also like to thank my parents-in-law who provided much needed help to take care of my daughter during the past two years. I have been very fortunate to have my husband Yiqian with me. His love, his confidence in me and valuable advice have always been there during the toughest years of my Ph.D. study.

Finally the financial support from Department of Energy is gratefully acknowledged.

TABLE OF CONTENTS

LIST OF TABLES

LIST OF FIGURES

RE

TM

CCD

SEM

EDS

XRD

SQUID

BM

LIST OF ABBREVIATIONS

RE	Rare Earth
TM	Transition Metal
CCD	Charge Couple Device
SEM	Scanning Electron Microscope
EDS	Energy Dispersive Spectroscopy
XRD	X-ray Diffraction
SQUID	Superconducting Quantum Interference Device
BM	Bohr Magneton

1-1. Int

the imp

applicat

commur

packagir

S

determin

Intermeta

aroused

strength a

high temp

candidates

intermetal

resistance.

Chinese a

restorative

intermetal

Russia.[4] S

crystal str

studied.

CHAPTER ONE

Introduction

1-1. Introduction to Intermetallics

Solid state chemistry has been growing rapidly since 1950s as scientists realized the importance of solid state materials in advanced technology in a higher level. The applications of these materials span a wide range of fields from microelectronics, communication, information, energy conversion and storage, construction, electronic packaging to domestic and advanced ceramics. [1]

Solid state chemistry is focused on the design, synthesis and structural determination of new materials and characterization of their physical properties. Intermetallics are one of the oldest class of materials in solid state chemistry and have aroused great interest in materials science and technology due to their mechanical strength and high temperature performance. For example, the oxidation resistance and high temperature strength of iron and nickel aluminides make these materials attractive candidates in industries including steel, chemicals and petroleum.[2] Back to B.C. 1600, intermetallics already got extensive use due to their remarkable hardness and wearing resistance. The bronze mirrors (e.g. composition $Cu_{31}Sn_8$) were used by the ancient Chinese and Romans; the amalgam (Cu_4Hg_3, Ag_2Hg_3) found applications as dental restorative materials in ancient Germany and China.[3] Intensive scientific work on intermetallics emerged in 1900s, initiated by Tammann in Germany and Kurnakov in Russia.[4] Since then a wide variety of intermetallic compounds were discovered; their crystal structure and properties including mechanical and magnetic properties were studied. In 1950s, more activities aroused investigating intermetallics as high

tempera

its exc

thermal

Conside

material

industri

tremend

Ordnanc

back to t

memory

applicati

CuZnAl

large fam

which is

crystal str

intermetal

Ov

understand

example i

Lu, Tm,

supercond

intermetali

discovered

temperature structural materials. One of the most extensively studied examples is $MoSi_2$: its excellent oxidation resistance, high melting point, relatively low density, and high thermal conductivity found itself an attractive material in advanced engine applications.[5] Considerable success had also been achieved on some transition metal aluminides. These materials, such as TiAl, are of intense interest to the gas turbine and aircraft engine industries, where their high temperature properties and low density offer prospects for tremendous weight savings.[6] In 1961, Nitinol, which stands for Nickel Titanium Naval Ordnance Laboratory, discovered that some Ni-Ti alloys after being strained, could revert back to their original shape at a certain temperature. These materials are called "shape memory alloys", and they have been applied to different fields such as aeronautical applications and surgical tools. The most effective and widely used alloys are NiTi, CuZnAl and CuAlNi.[7] Another equally important discovery during this period was a large family of superconducting binary phases with A15 structure type,[8] such as V_3Si, which is a superconductor with critical temperature as high as 17 K.[9] Since then, the crystal structures, electronic structures and superconducting properties of these binary intermetallics were extensively studied.[10]

Over the past twenty years, there have been considerable advances into the understanding of the structure and behavior of intermetallic compounds. A more recent example is exhibited by the superconducting quaternary intermetallic $LnNi_2B_2C$ (Ln = Lu, Tm, Er, Ho, Y) with critical temperature T_c up to 16.6 K.[11] The discovery of superconducting $LnNi_2B_2C$ has motivated intensive experimental work on these complex intermetallic systems. In 2001, MgB_2, a simple binary intermetallic compound discovered half an century ago,[12] was found to be a superconductor, with a surprising

high cr

intermet

some kr

of exten

fermion

highly c

intermet

1-2. Cry

A

that conta

constituti

crystal va

form alloy

solutions.

They do n

on a main

popular st

solutions,

constitutio

valence ele

that many

which the

high critical temperature — 39 K.[13] This discovery stimulated a great interest in intermetallics, not only the development of new materials, but also the reinvestigation of some known compounds. Rare earth-containing intermetallics have become the subject of extensive study due to their special behaviors such as the valence fluctuations, heavy fermion and Kondo-lattice behavior, which originate from the interaction between the highly correlated f electrons and delocalized conduction electrons.[14] Such phenomena of intermetallics will be discussed in detail in the following context.

1-2. Crystal Structure and Basic Properties of Intermetallics

According to the definition from Schulze, intermetallics are a branch of alloys that contain two or more metals resulting in crystal structures different from those of the constitutional elements.[15] Under certain conditions, one metal diffuses into another via crystal vacancies made available by defects, mechanical stress or grain boundaries to form alloys. Alloys may be homogeneous solid solutions or intermetallics. In solid solutions, the atoms of one metal are distributed randomly among the atoms of the other. They do not have specific chemical formula, and the best way to describe them is based on a main metal with a certain percentage of other metals added in. For example, a popular stainless steel, has the composition Fe-18%Cr-8%Ni. Different from solid solutions, intermetallics have definite crystal structures and specific formula. While constitutional metals are different in atomic size or electronegativity or the number of valence electrons, intermetallic compounds tend to form instead of solid solutions. Given that many intermetallics are formed due to the size effect or are electron compounds (in which the crystal structure types are related to particular valence electron concentrations),

they do

surround

ionic bo

contribut

In

crystal st

can be o

resistanc

surface p

makes pr

intermeta

1-3. Mani

Th

group ele

°C, Fe 15

the solid r

to overco

welder ar

intermetal

In

called co

characteri

they do not follow the valency rule. In intermetallics, atoms are preferentially surrounded by different kinds of atoms; not only metallic bonding, covalent and even ionic bonding can also be found. It is the strong bonding between different atoms that contributes to the excellent mechanical properties of intermetallic materials.

Intermetallics are comprised of a huge variety of compounds that differ greatly in crystal structure, bonding, and properties. However there are some basic properties that can be observed more or less in intermetallics: high melting point, high hardness, wear resistance and good oxidation resistance. That is why many have found applications as surface protecting materials. On the other hand, intermetallics are brittle materials, which makes processing difficult and it is one of the main challenges for the application of intermetallics in metallurgy.

1-3. Manipulation of Metal Flux to Synthesize Intermetallics

The melting points of most transition metals, rare earth metals and some main group elements are typically over 1000 °C. For example, the melting point of Ni is 1455 °C, Fe 1538 °C, Nd 1024 °C, Si 1414 °C. In order to achieve enough diffusion between the solid metals, synthesis of intermetallics usually requires high temperature techniques to overcome the energy barrier. Conventionally, high-power equipment such as arc-welder and radio-frequency reduction furnace has been used for the synthesis of intermetallic compounds.

In the past two decades, a new method to synthesize intermetallics, which is called combustion synthesis, has attracted considerable attention due to its unique characteristics.[16] In this process, the metal powders are mixed and pressed in the form of

cylindr

the co

high t

throug

interm

limitati

binary

avoid a

occurs

formed.

determi

single c

boundar

S

single cry

properties

Bridgman

However,

and the te

such circ

intermetal

cylindrical pellets. The pellets are ignited through an electrical coil or a laser beam. If the combinations of thermochemical and thermophysical properties are appropriate, a high temperature reaction front is initiated (1500-3500 °C) which then propagates through the reactants.[17] However, the reactions may not be completed with various intermediate phases; meanwhile the products formed are generally porous.[18]

For the high temperature techniques discussed above, there are two important limitations. Firstly, thermodynamically stable phases, which are usually simple known binary compounds, tend to form from these reactions. These phases are too stable to avoid and they hinder the formation of kinetically stable phases. Secondly, the reaction occurs too fast to allow single crystals to grow, so polycrystalline products are often formed. Obviously, the polycrystalline form of the materials limits their structural determinations. In addition, polycrystalline samples do not have the other chief merits of single crystals, including uniformity of composition, anisotropy, and the absence of boundaries between individual grains.

Sometimes extended annealing at high temperatures facilitates the growth of single crystals. However even then the crystals may not be large enough for desired properties measurements. Some other methods, such as floating-Zone, Czochralski and Bridgman growth methods are often employed to obtain single crystals of intermetallics. However, these techniques are suitable only when the material is congruently melting; and the temperature needed to melt the sample may also be inconveniently high. Under such circumstances other techniques are necessary to grow single crystals of intermetallics.

at relat

tempera

choosin

the mel

reaction

people f

crystals

2800 °C

crystals

intensive

from seve

Fo

the candi

temperatu

other con

should no

formation

chemical

periodic ta

be excelle

fluxes hav

Molten metal flux synthesis is such a technique that single crystals can be grown at relatively low temperatures. An excess amount of a metal is used as a high temperature solvent in which the crystals grow freely in a non-constrained fashion. By choosing an appropriate metal, we can run the reaction at a temperature much lower than the melting point of the constitutional metals. As is well known, low temperature reactions are likely to produce new kinetically stable compounds. Half a century ago, people found that this metal flux method was particularly useful to synthesize single crystals of borides and carbides due to their extremely high melting points (e.g. TiB_2 2800 °C, $TaC_{0.98}$ 3983 °C).[19] Rowcliffe and Warren were able to grow 2mm single crystals of $TaC_{0.96}$ by combining Ta and C in iron solution[20]; SiC, one of the most intensively studied crystals with potential applications in many fields, has been prepared from several metal solutions such as Si/Fe, Si/Ag and Si/Ni.[21]

For a metal to be suitable as a flux, several key conditions have to be met. First, the candidate metal should melt at reasonably low temperature; obviously high temperatures are not convenient with respect to the instrument required. Second, the other constituents have to be considerably soluble in this metal solvent; and the solvent should not react with the solute to form stable binary phases, which might prevent the formation of the desired product. Finally the excess metal can be easily removed by chemical or physical methods. Based on the criteria mentioned above, inspection of the periodic table reveals that the group III elements (Al, Ga, In), Sn, Pb, Bi and Zn appear to be excellent candidates for the high temperature solvents. Indeed, Al, Ga, In, Sn and Zn fluxes have been actively studied by several research groups including the Kanatzidis

group.

and a

1-4. F

they

proper

alumir

the co

candid

point (6

point ar

range o

immedia

elements

can easil

crucible o

above 660

which atta

distinct fr

not only t

but also fr

Ba) to inte

group, the Kauzlarich group, the Chan group, the Jeitschko group and the Pöttgen group, and a great progress has been made to synthesize new intermetallic compounds.[22,23,24,25]

1-4. Rationale for Al Flux Synthesis

Aluminides may be one of the most common groups of intermetallic compounds; they are considered as emerging materials due to their high specific mechanical properties.[26] An alternative way to synthesize intermetallic aluminides is utilizing aluminum as a metal flux, since aluminum tends to serve as a reactive solvent. Based on the conditions for metal flux discussed above, aluminum appears to be an attractive candidate for high temperature solvent. First, aluminum has reasonably low melting point (660 °C) and very high boiling point (2792 °C). The difference between its boiling point and melting point is almost 2000 °C, so Al can stay in its liquid form over a wide range of temperatures. Second, inspection of the Al-containing alloy phase diagram immediately reveals that many transition metals such as Cu, Fe and Ni, and main group elements such as Si, Ge and Sb are considerably soluble in liquid aluminum. Third, we can easily find appropriate containers for aluminum flux reactions, such as alumina crucible or graphite tube. Fourth, excess aluminum can be removed either via spin-off above 660 °C or etching away by simply reacting it with a base solution (e.g. NaOH) which attacks the desired product at a much slower rate. Finally, what makes aluminum distinct from the other metal flux candidates is its reducing ability which has been seen not only from the well-known thermite reaction in which Fe_2O_3 is reduced to Fe by Al, but also from reducing more complicated oxides such as perovskites $MTiO_3$ (M = Ca, Sr, Ba) to intermetallic compounds including $M_3Au_{6+x}Al_{26}Ti$.[27]

A

ternary i

utilize a

as LaB_6

properti

of the w

solvent.

optimum

point of

A

systems

environm

discovere

example,

composit

crystal str

Ce, Pr, Sm

Nd, Sm, G

$GdRe_2Al_2$

structure;

as another

in these s

Aluminum has been known as an effective solvent for the synthesis of binary and ternary intermetallics for a few decades. Back to 1970s, some Japanese groups started to utilize aluminum flux to synthesize single crystals of binary boron-rich compounds, such as LaB_6,[28] VB_2,[29] Cr_3B_4[30] and TiB_2[31]. Single crystal X-ray diffraction, transport properties and oxidation resistance were studied on these compounds. Interestingly, most of the work focused on the early transition metals and Al was serving as a non-reactive solvent. A few ternary examples were also reported, such as WAlB[32] and $YbAlB_4$.[33] The optimum temperature for these reactions is about 1500 °C, much lower than the melting point of boron which is 2300 °C.

About one decade ago, Jeitschko and his coworkers started to examine the systems RE/TM/Al (RE = rare earth metal, TM = transition metal) in liquid aluminum environment and had made a great success.[34] Series of new ternary families were discovered, which suggests a rich chemistry provided by liquid Al in these systems. For example, the family $RETM_2Al_{10}$ (TM = Mn, Fe, Ru, Os and Re) has a homogeneous composition, while different reaction conditions led to the discovery of four different crystal structure types. $REMn_2Al_{10}$ (RE = Y, La-Nd, Sm, Gd-Dy) and $RERe_2Al_{10}$ (RE = Ce, Pr, Sm) crystallize in tetragonal $CaCr_2Al_{10}$ structure type;[35] $RETM_2Al_{10}$ (RE = Y, La-Nd, Sm, Gd-Lu and TM = Fe, Ru, Os) have the orthorhombic $YbFe_2Al_{10}$ structure type;[36] $GdRe_2Al_{10}$ and $TbRe_2Al_{10}$, crystallize with a stacking variant of the $YbFe_2Al_{10}$ type structure;[37] $RERe_2Al_{10}$ (RE = Ho-Lu) form in a new structure type and may be considered as another variant of $YbFe_2Al_{10}$.[35a] It is noteworthy that Al tends to be a reactive solvent in these systems and almost all the compounds are Al-rich.

RE TM

and hav

line of

intermet

These sy

soluble i

and Al-C

never be

compoun

the cryst

incorpora

properties

chemical

[42] Thus t

corrosion

earth-cont

mixed va

which are

level with

It

along with

$Sm_2Ni(Ni,$

Recently our group initiated exploratory studies on the systems RE/Al/Tr and RE/TM/Al/Tr (RE = rare earth metal, TM = first row late transition metal, Tr = Si, Ge), and have achieved a great success in this field.[38] Although Si and Ge are on the border line of metals and nonmetals, silicides and germanides are usually regarded as intermetallics because of their similar characteristics and generally metallic properties. These systems are of particular interest for several reasons. First, both Si and Ge are soluble in liquid Al, and they do not form stable binary compounds according to Al-Si and Al-Ge alloy phase diagram. Second, the quaternary system RE/TM/Al/Tr, which has never been investigated before, imposes challenges to the aluminum flux. If quaternary compounds do form, they would be of fundamental interest in solid state chemistry from the crystal structures as well as physical properties point of view. Third, the incorporation of a tetrelide especially Si into the system, may contribute to the refractory properties of the material. Silicides are well known for their high hardness, high chemical stability and oxidation resistance[39,40] with $MoSi_2$ as the most famous example.[41, 42] Thus they can be used in technological applications such as high temperature wear and corrosion resistant coatings and thermoelectric energy conversion.[43,44,45] Finally, the rare earth-containing intermetallics display various interesting physical properties such as mixed valency,[46] Kondo lattice behavior,[47] spin fluctuations[48] and heavy fermion[49], which are strongly correlated to the electronic structure and position of the 4f electron level with respect to the Fermi energy.

It was observed that Al can serve as a reactive solvent. It can dissolve Si (or Ge) along with other metals to produce new quaternary intermerallic compounds such as $Sm_2Ni(Ni_xSi_{1-x})Al_4Si_6$ (x = 0.18-0.27),[38] $YNiAl_4Ge_2$,[38] $RE_4Fe_{2+x}Al_{7-x}Si_8$ (Re = Ce, Pr,

Nd, Sm

(RE = C

unfamil

design t

and rela

the flux

T

and sec

metals.

aluminu

explorat

resulted

series,[38]

hexagona

structure.

Ge instea

exhibiting

stable bin

systems

between S

example,

Ge) can b

metal to t

Nd, Sm),[50] $RE_8Ru_{12}Al_{49}Si_9(Al_xSi_{12-x})$ (RE = Pr, Nd, Sm, Gd, Tb, Er),[38] and $RE_2MAl_6Si_4$ (RE = Gd, Tb, Dy; M = Au, Pt).[51] Compounds with such complicated formulas are very unfamiliar to solid state chemists and obviously it is almost impossible to predict or design these compounds. However their single crystal form can be obtained from Al flux and relatively easily characterized. In this sense, exploratory synthesis employing Al as the flux is a great way to discover novel intermetallic materials.

The achievements of exploratory synthesis in liquid aluminum including the first and second row transition metals stimulated us to investigate the third row transition metals. Gold is of particular interest not only because it is very reactive in liquid aluminum, but gold-aluminum alloys have found applications in electronic devices.[52] The exploratory synthesis comprising of a rare earth metal, gold and silicon in Al flux resulted in a number of new phases such as the $Th_2(Au_xSi_{1-x})[AuAl_2]_nSi_2$ homologous series,[38] $REAu_4Al_8Si$,[53] $RE_2AuAl_6Si_4$[44] and $REAu_3Al_7$.[54] These compounds feature hexagonal antifluorite-type slabs which can be regarded as fragments of the bulk $AuAl_2$ structure. In the present work, the study of the Au system in liquid Al was extended to Ge instead of Si. Ge is similar as Si in many aspects: they belong to the same group exhibiting similar electronic structure; both are soluble in liquid Al and do not form stable binary phases with Al. Bradley Sieve, a former group member, had studied the systems RE/TM/Al/Si(Ge) systematically, and he indeed found parallel chemistry between Si and Ge with both systems tending to form quaternary compounds. For example, $RE_{2-x}TMAl_4Tr_2(Al_{1-y}Tr_y)(Al_{1-z}Tr_z)_2$ (RE = Sm, Dy, Er; TM = Ni, Co; Tr = Si, Ge) can be formed with both Si and Ge,[55] when the reaction ratio between the rare earth metal to transition metal is smaller than 1. The RE-rich family $RE_2Ni(Ni_xSi_{1-x})Al_4Si_6$

(RE =

Sm_2Co

such as

Nd, Sm

By stu

informat

studies r

metals ir

the syste

and Yb)

crystal

dissertat

S

intermeta

systems

of materi

of these t

thermoele

In spite

informati

hand, sinc

large num

region of

(RE = Pr, Nd, Sm, Gd, Dy, Tb) was found as well as their isostructral Ge analogue $Sm_2Co(Co_xAl_{1-x})Al_4Ge_{6-y}$.[55] When the transition metal was changed to the earlier ones such as Mn and Fe, the results led to the discovery of $RE_4TM_{2+x}Al_{7-x}Si_8$ (RE = Ce, Pr, Nd, Sm; TM = Mn, Fe),[50] while isostructural Ge-analogues have not been found so far. By studying the system RE/Au/Al/Ge systematically, we expect to obtain more information on the reaction pattern of Al with tetrelides (Si, Ge); on the other hand, these studies may help us to compare the chemistry between first row and third row transition metals in these systems. Chapter 2 presents two new quaternary families discovered in the system RE/Au/Al/Ge: $REAuAl_4Ge_2$ (RE = Ce, Pr, Nd, Sm, Eu, Gd, Tb, Dy, Er, Tm and Yb) and $REAuAl_4(Au_xGe_{1-x})_2$ (x = 0.4) (RE = Ce and Eu). The synthesis, single crystal X-ray diffraction and magnetic measurements will be described in this dissertation.

So far most of the work described here has focused on rare earth-containing intermetallics because of the interesting physical phenomena described previously. The systems TM-Al-Si(Ge) (TM = transition metal) are also of great importance in the field of material science and metallurgy. Extensive research has been done on the applications of these ternary materials as high temperature structural materials,[56] protective coatings,[57] thermoelectric power conversion,[58] and soft magnetic thin films and magnetic sheets.[59] In spite of the broad applications of these materials, there is significant lack of information on the crystal structure and phase equilibrium of these phases. On the other hand, since the discovery of an icosahedral phase in a rapidly quenched Al-Mn alloy,[60] a large number of quasicrystalline approximants have been found to occur in the Al-rich region of the Al-TM and related ternary systems. α-$Al_{50}Mn_{12}Si_7$ is a well-known

prototyp

$Mn_{14}Al$

unique p

in half

investig

knowled

techniqu

structure

which c

using m

five pha

of this s

ternary s

structure

C

electroni

interestir

and nega

electron

than thos

difficult t

metal. O

prototype of an approximant crystalline phase presenting Mackay-type clusters.[61] $Mn_{14}Al_{56+x}Ge_{3-x}$ (x = 0 - 0.6) was recently reported by Wu and Seo, which shows a unique partially destroyed Mackay icosahedra that retain the icosahedral symmetry only in half of the individual polyhedra.[62] In this work Chapter 3 presents the results of investigations on the ternary system V/Al/Ge using Al as the flux. To the best of our knowledge, past explorations of this system using high temperature direct combination techniques only yielded pseudo-binary phases $V_3Al_{(1-x)}Ge_x$ which belong to the A15 structure type.[63] We obtained a new ternary phase $V_2Al_5Ge_5$ from liquid aluminum which crystallizes in a new structure type. Chapter 4 explores the system Co/Al/Si by using molten Al as a flux. German has made a tentative study on this system, and found five phases though only two of them were structurally characterized.[64] In our own study of this system in liquid Al, we found two complex phases in the Al-rich corner of this ternary system — $Co_{19}Al_{45}Si_{10-x}$ (x = 0.13) and $Co_5Al_{14}Si_2$. In Chapter 4, the crystal structures and physicochemical properties of these two phases are described.

Chapters 5 and 6 include studies on the Yb-containing intermetallics. Due to the electronic transition between Yb^{2+} and Yb^{3+} ions, Yb-containing compounds can exhibit interesting behaviors such as mixed valence,[65] Kondo-lattice behavior,[66] heavy fermion[67] and negative thermal expansion.[68] Although Yb ($4f^{13}$-$4f^{14}$) can be regarded as hole-electron analogue of Ce ($4f^{1}$-$4f^{0}$), the studies of Ce compounds are far more extensive than those of Yb compounds. One of the main reasons might be that it is relatively more difficult to synthesize Yb-containing intermetallics due to the high vapor pressure of Yb metal. Our studies in the system Yb/Ni/Al in liquid Al not only led to the discovery of

ternary

modify

V elem

alkaline

or a gr

family,

discove

$A_2Zn_{4.5}S$

the 14-

$Eu_{14}Mn$

The sir

measure

the Yb

phases:

stoichio

physical

antimon

1-5. Exp

A

and anti

excess a

ternary phases such as $Yb_{1.1}Ni_3Al_{8.9}$ and $Yb_3Ni_5Al_{19}$, we also found we might be able to modify the magnetic states of Yb ions in $Yb_3Ni_5Al_{19}$ by applying chemical pressure.

Chapter 6 deals with the work when we extended the tetrelides (Si, Ge) to Group V element — Sb. There has been increasing interest on the Zintl phases composed of an alkaline earth metal (Ca, Sr, Ba) or rare earth metal (Eu, Yb), a transition metal (Mn, Zn) or a group 13 element (Al, Ga, In) and a pnicogen element (P, As, Sb, Bi). In the 9-4-9 family, $A_9Zn_{4+x}Pn_9$ (x = 0 for A= Yb, Pn = Bi, x = 0.5 for A = Ca & Yb, Pn = Sb), the discovery of mixed valence of Yb in $Yb_9Zn_4Bi_9$ [69] and extra Zn component in $A_9Zn_{4.5}Sb_9$[70] opens the opportunity to reexamine the parental compound $Ca_9Zn_4Bi_9$. In the 14-1-11 family, $Eu_{14}MnSb_{11}$ shows colossal magnetoresistance effects;[71] while $Eu_{14}MnBi_{11}$ orders antiferromagnetically and shows a large negative magnetoresistance.[72] The single crystals used for structural characterization and physical properties measurements in most of these systems, were obtained from Sn flux. Here our studies on the Yb/Al/Sb system using Al as the flux led to the discovery of two new valence-precise phases: $Yb_9Al_3Sb_9$ and Yb_3AlSb_3. Although these two compounds have the same stoichiometry, they belong to different structure types and show different chemical and physical behaviors. Our work indicates that Al is a reactive flux in the synthesis of antimonides and this study might be extended to the quaternary systems RE/TM/Al/Sb.

1-5. Experimental Techniques

All the reagents including rare earth metal, transition metal, aluminum, tetrelides and antimony were stored and handled in a nitrogen-filled dry box. Usually a ten-fold excess amount of Al was used. Since the rare earth metal and Al will attack the silica

tube at

The mi

(13mm

10^{-4} Tor

Temperature

Figure 1

T

for Al f

higher th

ensure h

was slow

°C). Du

could gr

After the

excess A

tube at high temperatures, an inert container such as alumina crucible had to be used. The mixtures were combined into alumina crucibles which were put into silica tubes (13mm in diameter). The silica ampoules were then flame-sealed under the vacuum of 10^{-4} Torr to avoid oxygen contamination.

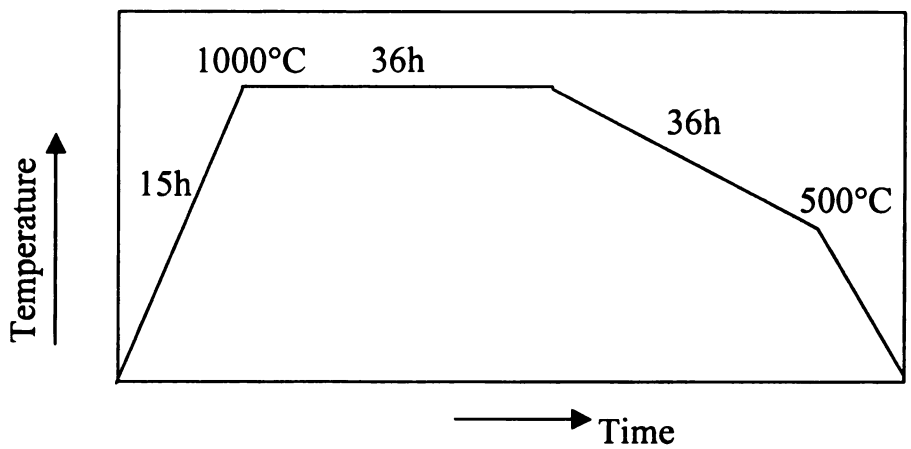

Figure 1-1. A typical temperature heating profile used for Al flux synthesis.

The samples were then subjected to heat treatment. A typical heating profile used for Al flux synthesis is shown in Figure 1-1. The system was brought to a temperature higher than the melting point of Al metal and kept at this temperature for some time to ensure homogeneous melting of the constituents in liquid Al. Subsequently the system was slowly cooled to a temperature lower than the melting point of Al metal (here 500 °C). During the slow-cooling stage, the solution became supersaturated so that crystals could grow out. Finally the system was quickly brought down to room temperature. After the reaction, the products were usually embedded in a Al matrix. To get rid of excess Al, either a physical or chemical method can be utilized. Since Al melts at 660

°C, the

Howev

melting

impract

conveni

tempera

And the

solution

to stand

to be the

°C, the excess Al can be removed via centrifuge at temperatures higher than 660 °C. However this method is more applicable to Ga, In and Sn fluxes which have much lower melting point, since taking the samples out at as high as 700 °C is dangerous and impracticable. On the contrary, the chemical way to remove Al is much easier and more convenient: the product was treated with 5M NaOH solution overnight at room temperature. During this process, Al reacted with NaOH solution by this reaction:

$$2Al + 2NaOH + 2H_2O \longrightarrow 2NaAlO_2 + 3H_2\uparrow$$

And the products were attacked by NaOH solution at a much slower rate. Dilute HCl solution is another way to get rid of excess Al; however some crystals are too vulnerable to stand acid solution, therefore for isolation of Al flux reactions, NaOH solution seems to be the best choice. Finally the products were rinsed and dried by acetone and ether.

Referen

[1] A) Sur
b) Chen
Rev. **20**
Metall.
Microci

[2] Sauth

[3] Sauth

[4] Gerhar
Sons, In

[5] a) Fitz
Berezhn
Ukrain.
J.; Schm

[6] Viswa
A, **2002**,

[7] a) Izun
c) Waym

[8] A15 is
Pm-3n.

[9] Hardy,

[10] a) Mo
Testardi,
Rehwald

[11] Cava,
Batlogg,

[12] Jones,

[13] Nagam
410, 63.

References:

[1] A) Surdoval, W. A.; Singhal, S. C.; McVay, G. L. *P. Electrochem. Soc.* **2001**, *16*, 53. b) Chen, G.; Dresselhaus, M. S.; Dresselhaus, G.; Fleurial, J.-P.; Caillat, T. *Int. Mater. Rev.* **2003**, *48*, 45. c) Datta, S. K.; Tewari, S. N.; Gatica, J. E.; Shih, W.; Bentsen, L. *Metall. Mater. Trans. A* **1999**, *30A*, 175. d) Cadenhead, R. L.; Frazier, A. B. *Int. J. Microcircuits Electron. Packaging* **1995**, *18*, 51.

[2] Sauthoff, G. *Intermetallics* **2000**, ***8***, 1101.

[3] Sauthoff, G. *Intermetallics*, VCH Verlagsgesellschaft, Weinheim 1995.

[4] Gerhard Sauthoff in "Ullmann's Encyclopedia of Industrial Chemistry", John Wiley & Sons, Inc., 7th, 2005.

[5] a) Fitzer, E. *Plansee Proc.* **1956**, 56-79. b) Krockel, O. *Silikattechnik* **1960**, *11*, 108. c) Berezhnoi, A. S.; Repenko, K. N.; German, I. A.; Gul'ko, N. V. *Sbornik Nauch. Trudov Ukrain. Nauch.-Issledovatel. Inst. Ogneuporov* **1960**, *4*, 296. d) Fitzer, F.; Schlichting, J.; Schmidt, F. K. *High Temperatures - High Pressures* **1970**, *2*, 553.

[6] Viswanathan, G. B.; Karthikeyan, S.; Hayes, R. W.; Mills, M. *J. Metall. Mater. Trans. A*, **2002**, *32A*, 329.

[7] a) Izuno, S. J. *Electron. Eng.* **1983**, *20*, 89. b) Huang, W. *Mater. Design* **2002**, *23*, 11. c) Wayman, C. M. *J. Met.* **1980**, *32*, 129.

[8] A15 is the *Strukturbericht* designation for the Cr_3Si structure type with the space group *Pm-3n*. Other members with this structure: Nb_3Al, Cr_3O, Ti_3Sb, Ti_3Au.

[9] Hardy, G. F.; Hulm, J. K. *Phys. Rev.* **1953**, *89*, 884.

[10] a) Morin, F. J.; Maita, J. P. *Phys. Rev.* **1963**, *129*, 1115. b) Dynes, R. C.; Poate, J. M.; Testardi, L. R.; Storm, A. R.; Hammond, R. H. *IEEE T. Magn.* **1977**, *13*, 640. c) Rehwald, W.; Rayl, M.; Cohen, R. W.; Cody, G. D. *Phys. Rev. B: Solid St.* **1972**, *6*, 363.

[11] Cava, R. J.; Takagi, H.; Zandbergen, H. W.; Krajewski, J. J.; Peck, W. F.; Siegrist, T.; Batlogg, B.; Van Dover, R. B.; Felder, R. J. *Nature* **1994**, *367*, 252.

[12] Jones, M.E.; Marsh, R.E. *J. Am. Chem. Soc.* **1954**, *76*, 1434.

[13] Nagamatsu, J.; Nakagawa, N; Muranaka, T.; Zenitani, Y.; Akimitsu, J. *Nature* **2001**, *410*, 63.

[14] a) Zl
M.; Sc
Schonh
Takaba

[15] Schul

[16] a) Ho
Prog. M

[17] Muni

[18] Olive

[19] Gurin
Korsuk
1995.

[20] Rowe

[21] a) Ha
b) Picka
Boston 1

[22] Millic
State Ch

[23] Canfi

[24] Holm
Grandje
S. *Inorg.*

[25] Kanat

[26] a) Ke
B. C. *Tr*
Metallic

[27] Latturn

[28] Kawai
Electron.

[29] Okada

[14] a) Zlatic, V.; Freericks, J. K. Acta Physica Polonica, B 2001, 32, 3253. b) Getzlaff, M.; Schmied, B.; Wilhelm, M.; Kubler, U.; Fecher, G. H.; Bansmann, J.; Lu, L.; Schonhense, G. *Phys. Rev. B* **1998**, *58*, 9670. c) Hossain, Z.; Hamashima, S.; Umeo, K.; Takabatake, T.; Geibel, C.; Steglich, F. *Phys. Rev. B* **2000**, *62*, 8950.

[15] Schulze, G. E. R. *Metallphysik* Akademie-Verlag: Berlin, 1967.

[16] a) Holt, J. B.; Munir, Z. A. *J. Mater. Sci.* **1986,** *21,* 251. b) Moore, J. J.; Feng, H. J. *Prog. Mater. Sci.* **1995,** *39,* 275.

[17] Munir, Z. A. *Ceram. Bull.* **1988,** *67,* 342.

[18] Oliveira, A. A. M.; Kaviany, M. *Int. J. Heat Mass Tran.* **1999,** *42,* 1059.

[19] Gurin, V. N.; Obukhov, A. P.; Mazina, T. I.; Terent'eva, Z. P.; Kozlova, I. R.; Korsukova, M. M. *Izvestiya Akademii Nauk SSSR, Neorganicheskie Materialy* **1969**, *5*, 1995.

[20] Rowcliffe, D. J.; Warren, W. J. *J. Mater. Sci.* **1970**, *5*, 345.

[21] a) Halden, F. A. Silicon Carbide, Proc. Conf., Boston, 1960, Volume Date 1959, 115. b) Pickar, Paul B., Jr. U.S. 1967, 5 pp. c) Ellis, R. C., Jr. *Silicon Carbide, Proc. Conf. Boston* **1960**, *1959*, 420.

[22] Millican, J. N.; Macaluso, R. T.; Young, D. P.; Moldovan, M.; Chan, J. Y. *J. Solid State Chem.* **2004,** *177,* 4695.

[23] Canfield, P. C.; Fisk, Z. *Philos. Mag. B* **1992**, *65*, 1117.

[24] Holm, A. P. P., Park, S.; Condron, C. L.; Olmstead, M.; Kim, H.; Klavins, P.; Grandjean, F.; Hermann, R. P.; Long, G. J.; Kanatzidis, M. G.; Kauzlarich, S. M.; Kim, S. *Inorg. Chem.* **2003**, *42*, 4660.

[25] Kanatzidis, M. G.; Pöttgen, R.; Jeitschko, W. *Angew. Chem. Int. Ed.* **2005,** *44,* 6996.

[26] a) Kevorkijan, V. *Aluminum* **2002,** *78,* 469. b) Satyanarayana, K. G.; Pillai, R. M.; Pai, B. C. *Trans. Indian Inst. Metals* **2002**, *55,* 115. c) Ochiai, S. *Mechanical Properties of Metallic Composite,* Marcel Dekker, Inc., New York, 1994.

[27] Latturner, S. E.; Kanatzidis, M. G. *Inorg. Chem.* **2004,** *43,* 2.

[28] Kawai, S.; Takaho, T.; Shigetoshi, M.; Masakazu, A.; Oshima, C. *Kinet. Prop. Electron. Magn. Ceram., Proc. U. S. – Jpn. Semin. Basic Sci. Ceram.* **1976**, 125.

[29] Okada, S.; Tetsuzo, A. *Nippon Kagaku kaishi* **1984**, *3*, 416.

[30] Okada, S.; Tetsuzo, A.; Iwami, H.; Yasuo, T. *Nippon Kagaku kaishi* **1985**, *1*, 1.

[31] Okada, S.; Tetsuzo, A. *Kanagawa Daigaku Kogakubu Kenkyu Hokoku* **1985**, *23*, 37.

[32] Zhang, Y.; Shigeru, O.; Tetsuzo, A.; Takeo, Y.; Yasumori, I. *Yogyo Kyokaishi* **1987**, *95*, 374.

[33] Shigeru, O.; Kudou, K .; Yu, Y.; Lundstroem, T. *JJAP Series* **1994**, *10*, 136.

[34] a) Niemann, S.; Jeitschko, W. *Z. Metallkd.* **1994**, *85*, 345. b) Niemann, S.; Jeitschko, W. *J. Solid State Chem.* **1995**, *114*, 337.

[35] a) Fehrmann, B.; Jeitschko, W. *Inorg. Chem.* **1999**, *38*, 3344. b) Thiede, V. M. T.; Jeitschko, W. *Zeitschrift fuer Naturforschung, B: Chemical Sciences* **1998**, *53*, 673.

[36] a) Thiede, V. M. T.; Ebel, T.; Jeitschko, W. *J. Mater. Chem.* **1998**, *8*, 125. b) Reehuis, M.; Wolff, M. W.; Krimmel, A.; Scheidt, E. W.; Stusser, N.; Loidl, A.; Jeitschko, W. *J. Phys Condens. Matt.* **2003**, *15*, 1773.

[37] Fehrmann, B.; Jeitschko, W. Z. *Naturforschung, B: Chemical Sciences* **1999**, *54*, 1277.

[38] a) Chen, X. Z.; Sportouch, S.; Sieve, B.; Brazis, P.; Kannewurf, C. R.; Cowen, J. A.; Patschke, R.; Kanatzidis, M. G. *Chem. Mater.* **1998**, *10*, 3202. b) Sieve, B.; Chen, X. Z.; Cowen, J.; Larson, P.; Mahanti, S. D.; Kanatzidis, M. G. *Chem. Mater.* **1999**, *11*, 2451. c) Sieve, B.; Chen, X. Z.; Henning, R.; Brazis, P.; Kannewurf, C. R.; Cowen, J. A.; Schultz, A. J.; Kanatzidis, M. G. *J. Am. Chem. Soc.* **2001**, *123*, 7040. d) Latturner, S. E.; Bilc, D.; Mahanti, S. D.; Kanatzidis, M. G. *Chem. Mater.* **2002**, *14*, 1695.

[39] Vasudevan, A. K.; Petrovic, J. *J. Mater. Sci. Eng.* **1992**, *A155*, 1.

[40] Williams, J. J.; Akinc, M. *Oxid. Met.* **2002**, *58*, 57.

[41] Lohfeld, S.; Schuetze, M. *Mater. Corros.* **2005**, *56*, 93.

[42] Kurokawa, K.; Matsuoka, H.; Nagai, T. *T. Mater. Res. Soc. Jpn.* **1994**, *14A*, 255.

[43] Liu, X. B.; Yu, L. G.; Wang, H. M. *J. Mater. Sci. Lett.* **2001**, *20*, 1489.

[44] Wang, H. M.; Lu, X. D.; Liu, Y. F.; Duan, G.; Cai, L. X.; Wang, C. M. *Mater. Sci. Foru*, **2003**, *426-432*, 2551.

[45] Gross, Erwin. *Int. J. Powder Metall.* **1995**, *31*, 239.

[46] a) Kishimoto, Y.; Kawasaki, Y.; Ohno, T. *Phys. Lett. A*, **2003**, *317*, 308. b) Kim, S. J.; Salvador, J.; Bilc, D.; Mahanti, S. D.; Kanatzidis, M. G. *J. Am. Chem. Soc.* **2001**, *123*,

12704.
Kauzla

[47] a) H
Mydos
Hossai
K.; Ko

[48] a) B
Magn.
Hoffma

[49] a) Jul
63. b) T
W.; Ro
Phys. R

[50] Sieve
Papaefti

[51] Lattu
7959.

[52] Brevn

[53] Lattu

[54] Lattu
M. G. *J.*

[55] Sieve,

[56] Shah,

[57] Vaz, F
Technol

[58] a) Oht
M.; Suzu

[59] Yoshio

[60] Shecht

[61] Ma, Y.

12704. c) Fisher, I. R.; Bud'ko, S. L.; Song, C.; Canfield, P. C.; Ozawa, T. C.; Kauzlarich, S. M. *Phys. Rev. Lett.* **2000**, *85,* 1120.

[47] a) Hossain, Z.; Schmidt, M.; Schnelle, W.; Jeevan, H. S.; Geibel, C.; Ramakrishnan, S.; Mydosh, J. A.; Grin, Y. *Phys. Rev. B,* **2005**, *71,* 060406. b) Singh, Y.; Ramakrishnan, S.; Hossain, Z.; Geibel, C. *Phys. Rev. B,* **2002**, *66,* 014415. c) He, J.; Tsujii, N.; Yoshimura, K.; Kosuge, K. *J. Alloy Compd.* **1998**, *268,* 221.

[48] a) Baranov, N. V.; Hilscher, G.; Markin, P. E.; Michor, H.; Yermakov, A. A. *J. Magn. Magn. Mater.* **2004**, *272-276,* 637. b) Taremba, V. I.; Kaczorowski, D.; Rodewald, U.; Hoffmann, R. D.; Poettgen, R. *Chem. Mater.* **2004**, *16,* 466.

[49] a) Julian, S. R.; Tautz, F. S.; McMullan, G. J.; Lonzarich, G. G. *Phys. B* **1994**, *199-200,* 63. b) Tanatar, M. A.; Paglione, J.; Nakatsuji, S.; Hawthorn, D. G.; Boaknin, E.; Hill, R. W.; Ronning, F.; Sutherland, M.; Taillefer, L.; Petrovic, C.; Canfield, P. C.; Fisk, Z. *Phys. Rev. Lett.* **2005,** *95,* 067002.

[50] Sieve, B.; Sportouch, S.; Chen, X. Z.; Cowen, J. A.; Brazis, P.; Kannewurf, C. R.; Papaefthymiou, V.; Kanatzidis, M. G. *Chem. Mater.* **2001**, *13,* 273.

[51] Latturner, S. E.; Bilc, D.; Mahanti, S. D.; Kanatzidis, M. G. *Inorg. Chem.* **2003**, *42,* 7959.

[52] Brevnov, D. A.; Bungay, C. *J. Phys. Chem. B* **2005**, *109,* 14529.

[53] Latturner, S. E.; Kanatzidis, M. G. *Chem. Commun.* **2003**, *18,* 2340.

[54] Latturner, S. E.; Bilc, D.; Ireland, J. R.; Kannewurf, C. R.; Mahanti, S. D.; Kanatzidis, M. G. *J. Solid State Chem.* **2003**, *170,* 48.

[55] Sieve, B. Ph. D. Dissertation, Michigan State University, 2002.

[56] Shah, D. M.; Anton, D. L. *Mater. Sci. Eng. A* **1992**, *A153,* 402.

[57] Vaz, F.; Rebouta, L.; Da Silva, M. F.; Soares, J. C. *NATO ASI Series, Series 3: High Technology* **1997**, *21*, 501.

[58] a) Ohta, Y.; Miura, S.; Mishima, Y. *Intermetallics* **1999**, *7,* 1203. b) Ono, K.; Kado, M.; Suzuki, R. O. *Steel Res.* **1998**, *69,* 387.

[59] Yoshida, S.; Sato, M.; Sugawara, E.; Shimada, Y. *J. Appl. Phys.* **1999**, *85,* 4636.

[60] Shechtman, D.; Blech, I.; Gratias, D.; Cahn, J. W. *Phys. Rev. Lett.* **1984**, *53,* 1951.

[61] Ma, Y.; Stern, E. A.; Bouldin, C. E. *Phys. Rev. Lett.* **1986**, *57*, 1611.

[62] Wu, L. M.; Seo, D. K. *J. Am. Chem. Soc.* **2004**, *126,* 4398.

[63] Surikov, V. I.; Borzhitskaya, M. K.; Shtol'ts, A. K.; Zagryazhskii, V. L.; Gel'd, P. V. *Fiz. Met. Metalloved. 1970*, **30**, 1167.

[64] German, N. V. *Vestn. L'VoV. UniV. Chim.* **1981**, *23*, 61.

[65] Mushnikov, N. V.; Goto, T.; Kolomiets, A. V.; Yoshimura, K.; Zhang, W.; Kageyama, H. *J. Phys: Condens. Mat.* **2004**, *16*, 2395.

[66] Avila, M. A.; Sera, M.; Takabatake, T. *Phys. Rev. B* **2004**, *70*, 100409.

[67] Muro, Y.; Haizaki, Y.; Kim, M. S.; Umeo, K.; Tou, H.; Sera, M.; Takabatake, T. *Phys. Rev. B* **2004**, *69*, 020401.

[68] Salvador, J.; Guo, F.; Hogan, T.; Kanatzidis, M. G. *Nature* **2003**, *425*, 702.

[69] Kim, S. J.; Salvador, J.; Bilc, D.; Mahanti, S. D.; Kanatzidis, M. G. *J. Am. Chem. Soc.* **2001**, *123*, 12704.

[70] Bobev, S.; Thompson, J. D.; Sarrao, J. L.; Olmstead, M. M.; Hope, H.; Kauzlarich, S. M. *Inorg. Chem.* **2004**, *43*, 5044.

[71] Chan, J. Y.; Kauzlarich, S. M.; Klavins, P.; Shelton, R. N.; Webb, D. J. *Chem. Mater.* **1997**, *9*, 3132.

[72] Chan, J. Y.; Wang, M. E.; Rehr, A.; Kauzlarich, S. M.; Webb, D. J. *Chem. Mater.* **1997**, *9*, 2131.

REA

2-1. Int

synthes
quality
physica
RE TM
by our
compou
properti
as Fe, C
compou
parallel
$_yTr_y)(Al$
and Ge,
l. The
was four
why rare
the trans
the disc
Fe),[4] wh

CHAPTER TWO

$REAuAl_4Ge_2$ and $REAuAl_4(Au_xGe_{1-x})_2$ (RE = rare earth element): New Quaternary Intermetallics Grown from Aluminum Flux

2-1. Introduction

Recently, Al has been suggested as a high temperature solvent for the exploratory synthesis of new intermetallic phases.[1, 2, 3] Liquid Al facilitates the growth of large high quality single crystals of complex intermetallic compounds, and this makes structural and physical characterization easier and more reliable. Synthetic explorations of the system RE/TM/Al/Si(Ge) (RE = rare earth element, TM = first row transition metal) conducted by our former group members led to the discovery of a number of new multinary compounds, many with novel structures and interesting magnetic and electronic properties.[4] Interestingly, this system is very effective for the late transition metals such as Fe, Co and Ni. Moreover, both Si- and Ge-containing systems tend to form quaternary compounds from Al flux; sometimes isostructural analogues are obtained indicating parallel chemistry between Si and Ge. For example, the families $RE_{2-x}TMAl_4Tr_2(Al_{1-y}Tr_y)(Al_{1-z}Tr_z)_2$ (RE = Sm, Dy, Er; TM = Ni, Co; Tr = Si, Ge) can be formed with both Si and Ge,[5] when the reaction ratio of the rare earth metal to transition metal is smaller than 1. The rare earth-rich family $RE_2Ni(Ni_xSi_{1-x})Al_4Si_6$ (RE = Pr, Nd, Sm, Gd, Dy and Tb) was found to be isostructural analogue of $Sm_2Co(Co_xAl_{1-x})Al_4Ge_{6-y}$,[5] although the reason why rare earth metals show different reaction reactivity is not clear at this point. When the transition metal was moved to the earlier ones such as Mn and Fe, the results led to the discovery of the novel series $RE_4TM_{2+x}Al_{7-x}Si_8$ (RE = Ce, Pr, Nd, Sm; TM = Mn, Fe),[4] while an isostructural Ge-analogue has not been found so far.

interest

numbe

$REAu_3$

antiflu

RE_2Au

YNiAl

be redu

$BaHg_{11}$

Ge, but

using A

Sm, Eu

Eu). Th

when w

characte

2-2. Exp

Reagent

Th

Sm, Eu,

bullion,

The results obtained with the first and second row transition metals stimulated interest in the third row. Gold is particularly active in Al flux and has resulted in a number of new phases such as the $Th_2(Au_xSi_{1-x})[AuAl_2]_nSi_2$ homologous series,[6] $REAu_4Al_8Si$,[7] $RE_2AuAl_6Si_4$[8] and $REAu_3Al_7$.[9] These compounds feature hexagonal antifluorite-type slabs which can be regarded as fragments of the bulk $AuAl_2$ structure. $RE_2AuAl_6Si_4$ is comprised of two different layers — a $CaAl_2Si_2$-type layer and a $YNiAl_4Ge_2$-type layer. The perovskites $MTiO_3$ (M = Ca, Sr, Ba) combined with Au can be reduced by aluminum to form quaternary compounds $M_3Au_{6+x}Al_{26}Ti$ with a stuffed $BaHg_{11}$ structure type.[10] The rich chemistry of the Si systems appears to be parallel to Ge, but not in an identical fashion. Our systematic studies in the system RE/Au/Al/Ge using Al as the flux led to two new quaternary families: $REAuAl_4Ge_2$ (RE = Ce, Pr, Nd, Sm, Eu, Gd, Tb, Dy, Er, Tm and Yb) and $REAuAl_4(Au_xGe_{1-x})_2$ (x = 0.4) (RE = Ce and Eu). The Cu-analogue of the second family $CeCuAl_4(Cu_xGe_{1-x})_2$ (x = 0.62) was obtained when we studied the system RE/Cu/Al/Ge. In this chapter, synthesis, structural characterization and magnetic measurements of these families are described.

2-2. Experimental Section

Reagents:

The following reagents were used as obtained: rare earth metal (RE = Ce, Pr, Nd, Sm, Eu, Gd, Tb, Dy, Er, Tm and Yb) (Cerac, 99.9%), Au (shavings from 1 ounce gold bullion, 99.99%), Al pellets (Cerac, 99.99%), Ge (Cerac, 99.999%).

nitrog

mmol

crucib

vacuu

temper

d. foll

down t

mmol

and 2 n

placed

Torr).

h, then

(0.140

combin

in diam

1000 °C

They w

Finally

Synthesis:

$REAuAl_4Ge_2$ (RE = Ce, Pr, Nd, Sm, Eu, Gd, Tb, Dy, Er, Tm and Yb): In a nitrogen-filled glove box, 1 mmol RE metal (0.14-0.18 g), 1 mmol Au (0.197 g), 10 mmol Al (0.270 g) and 5 mmol Ge (0.36 g) were combined in an alumina crucible. The crucible was then placed into a silica tube (13 mm in diameter), which was sealed under vacuum (~10^{-4} Torr). The samples were heated to 1000 °C in 12 h, maintained at this temperature for 30 h, then cooled to 850 °C in 24 h. They were annealed at 850 °C for 3 d, followed by cooling down to 500 °C in 72 h. Finally the temperature was brought down to 50 °C in 12 h.

$REAuAl_4(Au_xGe_{1-x})_2$ (x = 0.4) (RE = Ce, Eu): In a nitrogen-filled glove box, 1 mmol RE metal (Ce 0.140 g, Eu 0.152 g), 1 mmol Au (0.197 g), 10 mmol Al (0.270 g) and 2 mmol Ge (0.1466 g) were combined in an alumina crucible. The crucible was then placed into a silica tube (13 mm in diameter), which was sealed under vacuum (~10^{-4} Torr). The samples were heated to 1000 °C in 12 h, maintained at this temperature for 5 h, then cooled to 850 °C in 24 h, finally slowly cooled down to 50 °C in 72 h.

$CeCuAl_4(Cu_xGe_{1-x})_2$ (x = 0.62): In a nitrogen-filled glove box, 1 mmol Ce metal (0.140 g), 1 mmol Cu (0.064 g), 10 mmol Al (0.270 g) and 5 mmol Ge (0.36 g) were combined in an alumina crucible. The crucible was then placed into a silica tube (13 mm in diameter), which was sealed under vacuum (~10^{-4} Torr). The samples were heated to 1000 °C in 12 h, maintained at this temperature for 30 h, then cooled to 860 °C in 24 h. They were annealed at 850 °C for 3 d, followed by cooling down to 500 °C in 72 h. Finally the temperature was brought down to 50 °C in 12 h.

Isolati

NaOH
rinsed
for RE
the init
elemen

Elemen

sample
Energy
with a
voltage
CeAuA
determi
: Ge) a
the resu

X-ray C

Nd, Gd
tempera

Isolation:

The excess aluminum was removed by soaking the crucibles in aqueous 5M NaOH solution overnight. The solid product remaining after the isolation procedure was rinsed with water and acetone. The yields of each were ~80% for $REAuAl_4Ge_2$, ~90% for $REAuAl_4(Au_xGe_{1-x})_2$ (x = 0.4) and ~90% for $CeCuAl_4(Cu_xGe_{1-x})_2$ (x = 0.62) based on the initial amount of RE metal used in the reaction. Single crystals were selected for elemental analysis, X-ray diffraction and magnetic susceptibility measurements.

Elemental Analysis:

The crystals were picked and placed on a Scanning Electron Microscope (SEM) sample stub using carbon tape. Chemical composition of the products was determined by Energy Dispersive Spectroscopy (EDS) performed on a JEOL JSM-35C SEM equipped with a NORAN EDS detector. Spectra were acquired by applying a 25 kV accelerating voltage with an accumulation time of 30 s. The atomic ratios in the compounds $CeAuAl_4Ge_2$, $EuAuAl_4(Au_xGe_{1-x})_2$ (x = 0.4) and $CeCuAl_4(Cu_xGe_{1-x})_2$ (x = 0.62) were determined to be 1 : 1.25 : 4.87 : 2.1 (Ce : Au : Al : Ge), 1 : 1.76 : 3.73 : 1.1 (Eu : Au : Al : Ge) and 1 : 1.86 : 3.84 : 0.86 (Ce : Cu : Al : Ge) respectively, which agreed well with the results derived from single crystal X-ray analysis.

X-ray Crystallography:

Single crystal X-ray diffraction data were collected for $REAuAl_4Ge_2$ (RE = Ce, Nd, Gd, Er), $EuAuAl_4(Au_xGe_{1-x})_2$ (x = 0.4) and $CeCuAl_4(Cu_xGe_{1-x})_2$ (x = 0.62) at room temperature on a Bruker AXS SMART CCD X-ray diffractometer. A data collection

(Mo K

hemisp

softwa

SADA

and re

anisotr

EDS.

NdAu.

listed

displac

and 2-

0.4) an

displac

compo

INEL

Experi

crystal

and pur

(Mo Kα radiation, λ = 0.71073 Å) was acquired covering either a full sphere or hemisphere of reciprocal space. Data processing was performed with the SAINTPLUS software package.[11] An empirical absorption correction was applied to the data using the SADABS program.[12] The structures were solved straight forwardly using direct methods and refined with the SHELXTL package program.[13] All atomic positions were refined anisotropically. The resulting stoichiometry agreed well with the elemental analysis from EDS. Data collection parameters and refinement details for $CeAuAl_4Ge_2$ and $NdAuAl_4Ge_2$ can be found in Table 2-1. The refinement details for Gd and Er analog are listed in Table 2-2. Atomic positions, displacement parameters and anisotropic displacement parameters for $REAuAl_4Ge_2$ (RE = Ce, Nd, Gd, Er) are listed in Tables 2-3 and 2-4. Data collection parameters and refinement details for $EuAuAl_4(Au_xGe_{1-x})_2$ (x = 0.4) and $CeCuAl_4(Cu_xGe_{1-x})_2$ (x = 0.62) can be found in Table 2-5; atomic positions, displacement parameters and anisotropic displacement parameters for these two compounds are listed in Tables 2-6 and 2-7.

X-ray powder diffraction data were collected at room temperature on a CPS 120 INEL X-ray diffractometer (Cu Kα) equipped with position-sensitive detector. Experimental powder patterns were compared to the patterns calculated from the single crystal structure solution (by the CrystalDiffract software) to determine the phase identity and purity.

Table 2

Empi
Form
Temp
Wav
Spac
Latti
Volu
Z
Calc
Abso
F(00
Crys
θ ran
Limi
Refl
Uniq
R_{int}
Comp
Refi
Vari
Good
Final
R ind
Extin
High

$R1 = \Sigma($

Table 2-1. Crystal data and structure refinements for $REAuAl_4Ge_2$ (RE = Ce, Nd).

Empirical formula	$CeAuAl_4Ge_2$	$NdAuAl_4Ge_2$
Formula weight	590.19	594.31
Temperature	293(2) K	293(2) K
Wavelength	0.71073 Å	0.71073 Å
Space Group	*R* -3 *m* (#166)	*R* -3 *m* (#166)
Lattice constants (Å)	a = 4.2384(7) Å	a = 4.2258(4) Å
	c = 31.613(7) Å	c = 31.359(5) Å
Volume	491.81(16) $Å^3$	484.97(10) $Å^3$
Z	3	3
Calculated density, (g/cm^3)	5.978	6.105
Absorption coefficient, (mm^{-1})	38.598	40.132
F(000)	759	765
Crystal size, (mm^3)	0.63 × 0.21 × 0.32	0.43 × 0.26 × 0.33
θ range, (°)	1.93 to 27.63	11.22 to 37.15
Limiting indices	$-5 \le h \le 5$	$-7 \le h \le 7$
	$-5 \le k \le 5$	$-7 \le k \le 7$
	$-40 \le l \le 39$	$-52 \le l \le 52$
Reflections collected	1650	2487
Unique reflections	186	347
R_{int}	0.0454	0.0628
Completeness to θ	100.0 %	93.3 %
Refinement method	Full-matrix least-squares on F^2	
Variables	15	15
Goodness-of-fit on F^2	1.111	1.128
Final R indices [$I>2\sigma(I)$][a]	$R_1 = 0.0214$ $wR_2 = 0.0514$	$R_1 = 0.0235$ $wR_2 = 0.0634$
R indices (all data)	$R_1 = 0.0214$ $wR_2 = 0.0514$	$R_1 = 0.0235$ $wR_2 = 0.0634$
Extinction coefficient	0.0121(7)	0.0111(7)
Highest residual peak ($e/Å^3$)	1.412 and -2.365	2.920 and -4.494

$R1 = \Sigma(|F_o|-|F_c|)/\Sigma|F_o|$; $wR2 = [\Sigma[w(F_o^2 - F_c^2]/ [\Sigma(w|F_o|^2)^2]]^{1/2}$

Table

Emp
For
Tem
Wav
Spac
Latti
Volu
Z
Calc
Abs
F(00
Crys
θ ran
Limi
Refle
Uniq
R_{int}
Comp
Refin
Varia
Good
Final
R ind
Extin
High

$R1 = \Sigma($

Table 2-2. Crystal data and structure refinements for $REAuAl_4Ge_2$ (RE = Gd, Er).

Empirical formula	$GdAuAl_4Ge_2$	$ErAuAl_4Ge_2$
Formula weight	581.11	671.29
Temperature	293(2) K	293(2) K
Wavelength	0.71073 Å	0.71073 Å
Space Group	*R* -3 *m* (#166)	*R* -3 *m* (#166)
Lattice constants (Å)	a = 4.2123(6) Å	a = 4.2074(4) Å
	c = 30.994(6) Å	c = 30.717(5) Å
Volume	476.26(14) $Å^3$	470.91(9) $Å^3$
Z	3	3
Calculated density, (g/cm^3)	6.352	6.531
Absorption coefficient, (mm^{-1})	43.133	46.427
F(000)	777	789
Crystal size, (mm^3)	0.27 × 0.19 × 0.28	0.33 × 0.28 × 0.11
θ range, (°)	11.25 to 37.25	11.27 to 37.00
Limiting indices	$-7 \leq h \leq 7$	$-7 \leq h \leq 6$
	$-7 \leq k \leq 7$	$-7 \leq k \leq 7$
	$-49 \leq l \leq 48$	$-51 \leq l \leq 51$
Reflections collected	2472	2448
Unique reflections	332	338
R_{int}	0.0635	0.0793
Completeness to θ	91.0 %	94.4 %
Refinement method	Full-matrix least-squares on F^2	
Variables	15	15
Goodness-of-fit on F^2	1.168	1.108
Final R indices [$I>2\sigma(I)$][a]	$R_1 = 0.0299$ $wR_2 = 0.0696$	$R_1 = 0.0283$ $wR_2 = 0.0772$
R indices (all data)	$R_1 = 0.0305$ $wR_2 = 0.0708$	$R_1 = 0.0297$ $wR_2 = 0.0780$
Extinction coefficient	0.0104(8)	0.0134(10)
Highest residual peak ($e/Å^3$)	5.815 and -3.885	2.732 and -4.754

$R1 = \Sigma(|F_o|-|F_c|)/\Sigma|F_o|$; $wR2 = [\Sigma[w(F_o^2 - F_c^2]/ [\Sigma(w|F_o|^2)^2]]^{1/2}$

Table 2-3. Atomic coordinates and equivalent isotropic displacement parameters ($Å^2 \times 10^3$) for $REAuAl_4Ge_2$ (RE = Ce, Nd, Gd, Er).

Atom	Wyk. Symbol	x	y	z	$U_{(eq)}$*
Ce	3*b*	-0.6667	0.6667	0.1667	8(1)
Au	3*a*	0	0	0	7(1)
Ge	6*c*	-0.3333	0.3333	0.1081(1)	8(1)
Al(1)	6*c*	-0.3333	0.3333	0.0245(1)	7(1)
Al(2)	6*c*	0	0	0.0820(1)	9(1)
Nd	3*b*	-0.6667	0.6667	0.1667	7(1)
Au	3*a*	0	0	0	5(1)
Ge	6*c*	-0.3333	0.3333	0.1091(1)	8(1)
Al(1)	6*c*	-0.3333	0.3333	0.0250(1)	7(1)
Al(2)	6*c*	0	0	0.0823(1)	6(1)
Gd	3*b*	-0.6667	0.6667	0.1667	5(1)
Au	3*a*	0	0	0	7(1)
Ge	6*c*	-0.3333	0.3333	0.1105(1)	6(1)
Al(1)	6*c*	-0.3333	0.3333	0.0255(1)	6(1)
Al(2)	6*c*	0	0	0.0832(1)	8(1)
Er	3*b*	-0.6667	0.6667	0.1667	5(1)
Au	3*a*	0	0	0	6(1)
Ge	6*c*	-0.3333	0.3333	0.1121(1)	4(1)
Al(1)	6*c*	-0.3333	0.3333	0.0260(1)	8(1)
Al(2)	6*c*	0	0	0.0842(1)	6(1)

* $U_{(eq)}$ is defined as one third of the trace of the orthogonalized U_{ij} tensor.

Table 2-4. Anisotropic displacement parameters ($Å^2 \times 10^3$) for $REAuAl_4Ge_2$ (RE = Ce, Nd, Gd, Er).

Atom	U^{11}	U^{22}	U^{33}	U^{23}	U^{13}	U^{12}
Ce	9(1)	9(1)	6(1)	0	0	5(1)
Au	7(1)	7(1)	5(1)	0	0	4(1)
Ge	9(1)	9(1)	6(1)	0	0	4(1)
Al(1)	7(1)	7(1)	7(2)	0	0	4(1)
Al(2)	11(1)	11(1)	5(1)	0	0	6(1)
Nd	7(1)	7(1)	7(1)	0	0	4(1)
Au	6(1)	7(1)	3(1)	0	0	3(1)
Ge	9(1)	9(1)	7(1)	0	0	4(1)
Al(1)	6(1)	7(1)	8(1)	0	0	5(1)
Al(2)	5(1)	5(1)	7(1)	0	0	4(1)
Gd	5(1)	6(1)	5(1)	0	0	3(1)
Au	7(1)	7(1)	7(1)	0	0	4(1)
Ge	7(1)	6(1)	7(1)	0	0	4(1)
Al(1)	6(1)	7(1)	7(1)	0	0	4(1)
Al(2)	9(1)	8(1)	8(1)	0	0	5(1)
Er	4(1)	4(1)	7(1)	0	0	2(1)
Au	6(1)	6(1)	6(1)	0	0	4(1)
Ge	5(1)	3(1)	7(1)	0	0	3(1)
Al(1)	6(1)	5(1)	12(1)	0	0	5(1)
Al(2)	6(1)	6(1)	8(1)	0	0	3(1)

The anisotropic displacement factor exponent takes the form:
$-2\pi^2[h^2a^{*2}U^{11}+\ldots+2hka^*b^*U^{12}]$

Table

CeCu

Em

For

Ter

Wa

Spa

Lat

Vo

Z

Ca

Ab

F(

Cr

θ r

Lir

Re

Ur

R_{in}

Co

Re

Va

Go

Fir

R i

Ex

Hi

R1 =

Table 2-5. Crystal data and structure refinements for $EuAuAl_4(Au_xGe_{1-x})_2$ (x = 0.4) and $CeCuAl_4(Cu_xGe_{1-x})_2$ (x = 0.62).

Empirical formula	$EuAuAl_4(Au_xGe_{1-x})_2$ (x = 0.4)	$CeCuAl_4(Cu_xGe_{1-x})_2$ (x = 0.62)
Formula weight	726.4	671.29
Temperature	293(2) K	293(2) K
Wavelength	0.71073 Å	0.71073 Å
Space Group	*P4/mmm* (#123)	*P4/mmm* (#123)
Lattice constants (Å)	a = 4.3134(8) Å	a = 4.2207(4) Å
	c = 8.371(3) Å	c = 7.9504(11) Å
Volume	155.75(7) $Å^3$	141.63(3) $Å^3$
Z	1	1
Calculated density, (g/cm^3)	7.745	9.286
Absorption coefficient, (mm^{-1})	62.085	42.176
F(000)	305	354
Crystal size, (mm^3)	0.046 × 0.064 × 0.052	0.033 × 0.058 × 0.071
θ range, (°)	2.43 to 28.25	14.63 to 39.73
Limiting indices	$-5 \le h \le 5$	$-7 \le h \le 7$
	$-5 \le k \le 5$	$-7 \le k \le 7$
	$-10 \le l \le 10$	$-14 \le l \le 14$
Reflections collected	1745	2341
Unique reflections	146	283
R_{int}	0.0533	0.0401
Completeness to θ	96.7 %	91.3 %
Refinement method	Full-matrix least-squares on F^2	
Variables	14	14
Goodness-of-fit on F^2	1.151	1.498
Final R indices [$I>2\sigma(I)$][a]	$R_1 = 0.0276$ $wR_2 = 0.0634$	$R_1 = 0.0321$ $wR_2 = 0.0849$
R indices (all data)	$R_1 = 0.0289$ $wR_2 = 0.0642$	$R_1 = 0.0323$ $wR_2 = 0.0849$
Extinction coefficient	0.141(9)	0.12(2)
Highest residual peak ($e/Å^3$)	2.923 and -4.569	2.545 and -1.697

$R1 = \Sigma(|F_o|-|F_c|)/\Sigma|F_o|$; $wR2 = [\Sigma[w(F_o^2 - F_c^2]/ [\Sigma(w|F_o|^2)^2]^{1/2}$

Table 2-6. Atomic coordinates and equivalent isotropic displacement parameters ($Å^2 \times 10^3$) for $EuAuAl_4(Au_xGe_{1-x})_2$ (x = 0.4) and $CeCuAl_4(Cu_xGe_{1-x})_2$ (x = 0.62).

	Wyk.Symbol	x	y	z	U(eq)	Occu.
Au(1)	1*a*	0.0000	0.0000	0.0000	10(1)	1
Au(2)	2*h*	-0.5000	-0.5000	0.3462(1)	11(1)	0.411(4)
Ge	2*h*	-0.5000	-0.5000	0.3462(1)	11(1)	0.590(4)
Eu	1*b*	0.0000	0.0000	0.5000	13(1)	1
Al	4*i*	0.0000	-0.5000	0.1739(4)	12(1)	1
Cu(1)	1*a*	0.0000	0.0000	0.0000	6(1)	1
Cu(2)	2*h*	-0.5000	-0.5000	0.3523(1)	8(1)	0.620(3)
Ge	2*h*	-0.5000	-0.5000	0.3523(1)	8(1)	0.380(3)
Ce	1*b*	0.0000	0.0000	0.5000	6(1)	1
Al	4*i*	0.0000	-0.5000	0.1721(2)	9(1)	1

* $U_{(eq)}$ is defined as one third of the trace of the orthogonalized U_{ij} tensor.

Table 2-7. Anisotropic displacement parameters ($Å^2 \times 10^3$) for $EuAuAl_4(Au_xGe_{1-x})_2$ (x = 0.4) and $CeCuAl_4(Cu_xGe_{1-x})_2$ (x = 0.62).

Atom	U^{11}	U^{22}	U^{33}	U^{23}	U^{13}	U^{12}
Au(1)	12(1)	12(1)	7(1)	0	0	0
Au(2)	14(1)	14(1)	6(1)	0	0	0
Ge	14(1)	14(1)	6(1)	0	0	0
Eu	14(1)	14(1)	10(2)	0	0	0
Al	17(2)	12(2)	7(2)	0	0	0
Cu(1)	7(1)	7(1)	7(1)	0	0	0
Cu(2)	7(1)	7(1)	8(1)	0	0	0
Ge	7(1)	7(1)	8(1)	0	0	0
Ce	5(1)	5(1)	7(1)	0	0	0
Al	13(1)	7(1)	7(1)	0	0	0

The anisotropic displacement factor exponent takes the form:
$-2\pi^2[h^2a^{*2}U^{11}+...+2hka^*b^*U^{12}]$

Magnetic Characterization:

Magnetic measurements were conducted on the polycrystalline samples of $CeAuAl_4Ge_2$, $EuAuAl_4Ge_2$, $DyAuAl_4Ge_2$, $CeAuAl_4(Au_xGe_{1-x})_2$ and $EuAuAl_4(Au_xGe_{1-x})_2$ ($x = 0.4$) using a Quantum Design MPMS SQUID magnetometer. EDS-analyzed crystals were ground into powder, and then sealed in kapton tape and placed into the magnetometer. The data were collected in the temperature range of 3-300 K at 1000 G, while field dependent magnetic measurements, conducted at 3 K, were carried out in fields up to ± 55000 G. A diamagnetic correction was applied to the data to account for core diamagnetism.

2-3. Results and Discussion

Synthesis:

The compounds $REAuAl_4Ge_2$ were obtained with most rare earth elements and they tend to crystallize as plates or pyramidal crystals. Figure 2-1 shows the SEM images of typical single crystals of $CeAuAl_4Ge_2$ and $EuAuAl_4(Au_xGe_{1-x})_2$ ($x = 0.4$). The yields of the reactions were generally > 80% based on the rare earth elements used. Side products were mainly recrystallized Ge and Au. Reactions with longer annealing times at 1000 °C did not improve the yields. Use of Yb as the RE metal produced the ternary compound $YbAl_2Ge_2$ instead of the target phase. Only when the amount of Yb was increased (from elemental ratio 1 : 1 : 10 : 5 to 3 : 1 : 10 : 5 for Yb : Au : Al : Ge), could $YbAuAl_4Ge_2$ be obtained as the main phase.

For Ce and Eu, when a much shorter heating profile was used, the phase $REAuAl_4(Au_xGe_{1-x})_2$ ($x = 0.4$) was found as the major product. When Sm was used under the same heating profile, only $SmAuAl_4Ge_2$ could be obtained.

A

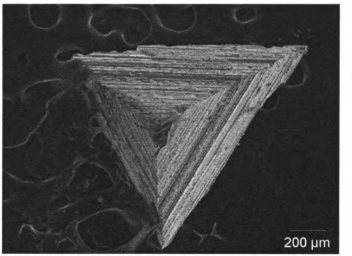

B

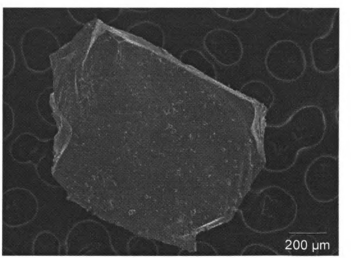

Figure 2-1. SEM images of typical crystals of (A) $CeAuAl_4Ge_2$. (B) $EuAuAl_4(Au_xGe_{1-x})_2$ ($x = 0.4$).

Crystal Structure of $REAuAl_4Ge_2$:

The $REAuAl_4Ge_2$ compounds crystallize in a rhombohedral structure with space group *R*-3*m*. These compounds are isostructural to $YNiAl_4Ge_2$,[1] which suggests that this structure type is robust and can accommodate a wide variety of non-isoelectronic transition metals. The difference between the Ni and Au analogs is that $RENiAl_4Ge_2$ forms readily only with late RE metals, whereas almost all RE metals can form the Au analogs. That the $RENiAl_4Ge_2$ compounds form only with late RE metals could be due to the smaller size of $[NiAl_4Ge_2]$ slab (compared to $[AuAl_4Ge_2]$ slab) which permits only the small RE ions to pack in the available space.[5] When the Ni atoms are replaced by the larger Au atoms in this structure, a cell parameter expansion is observed as expected, with the *a*-axis being much more expanded than the *c*-axis. This allows the larger rare earth elements to fit into the interlayer space. The cell volume for Ce, Nd, Gd and Er analogs, exhibit the sequential contraction as expected (Figure 2-2).

The structure of $CeAuAl_4Ge_2$ can be described as alternating layers of Ce atoms and $[AuAl_4Ge_2]$ slabs, Figure 2-3. The bonds between Ce atoms and the other atoms were omitted in order to emphasize different layers in the structure. The Ce atoms on the *ab* plane are close-hexagonally packed and form regular equilateral triangles with Ce-Ce distance of 4.2384(7) Å, corresponding to the length of the unit cell, *a* (Figure 2-4A). Each Ce atom is sandwiched by two puckered layers composed of Ge and Al(2) atoms, see Figure 2-4B.

The $[AuAl_4Ge_2]$ slab consists of distorted Al_8 cubes, with the lengths of the cube sides being 2.897(3) Å and 3.048 Å. Au atoms (as shown in Figure 2-5A), held in the center of the cube, are surrounded by six Al(1) and two Al(2) atoms above and below to

achieve an eight-coordinate environment. The Au-Al bond distances are 2.5668(9) Å and 2.591(3) Å, respectively, comparable to those in gold aluminides such as $AuAl_2$ (2.597 Å). These cubes are connected to each other via face sharing along the *ab*-plane.

The Ge atoms form puckered layers with Al(2) atoms which are in chair geometries when viewed down the *c*-direction. Each Ge atom is surrounded by three Al(2) atoms and one Al(1) atom forming an umbrella like geometry (shown in Figure 2-5B). A similar coordination environment for Ge atoms is found in $AEAl_2Ge_2$ (AE = Ca, Sr) and $REAl_2Ge_2$ in which the Ge atom is bonded to three Al atoms and one AE or RE atom.[14]

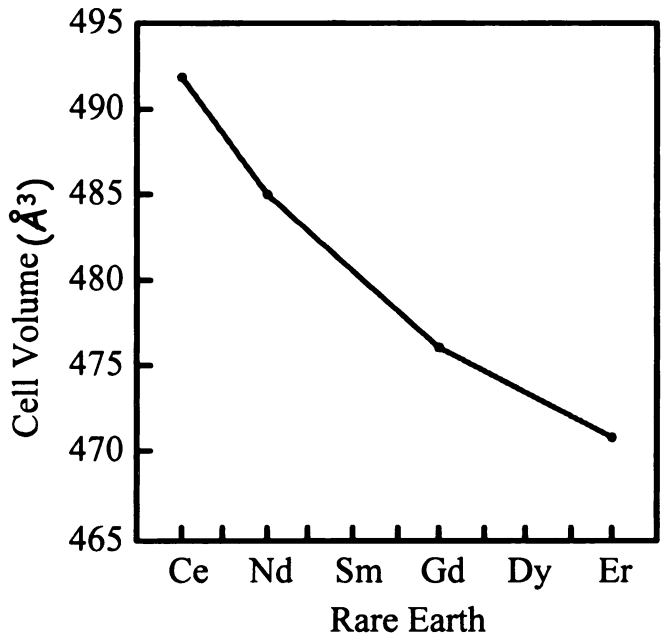

Figure 2-2. Cell volume variation of different rare earth metals in $REAuAl_4Ge_2$.

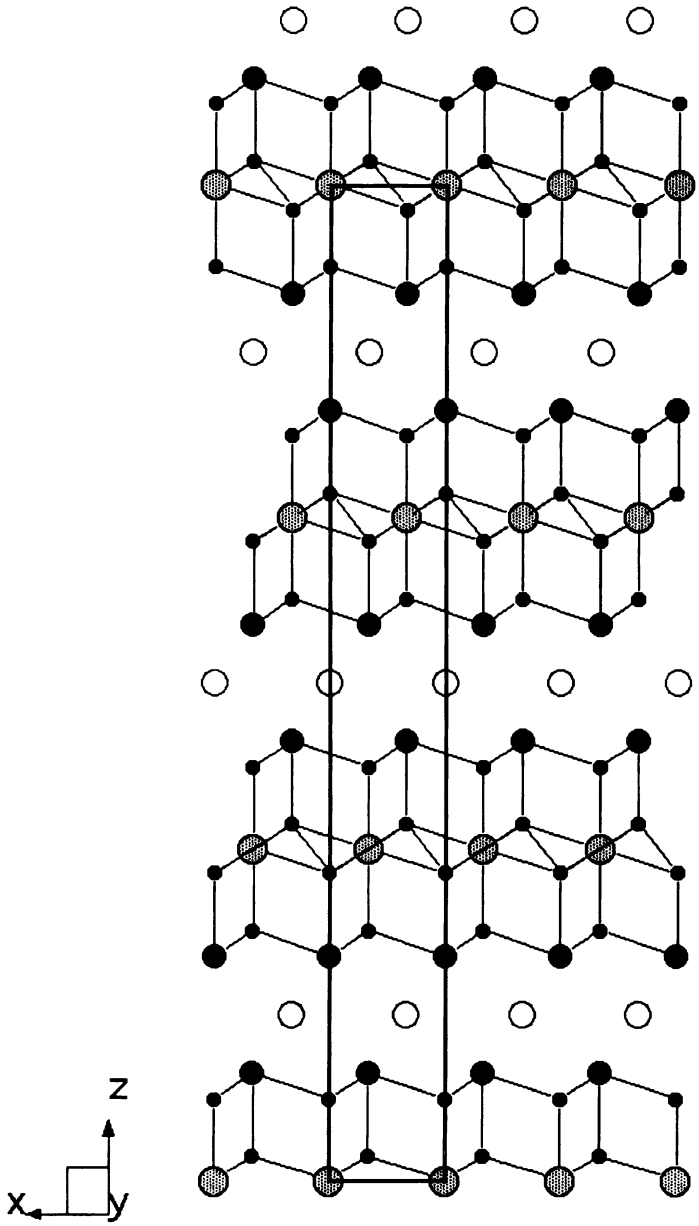

Figure 2-3. Structure of $CeAuAl_4Ge_2$ viewed down the [010] direction. Large empty circles: Ce; black dots: Al; lighter shaded circles: Au; darker shaded circles: Ge.

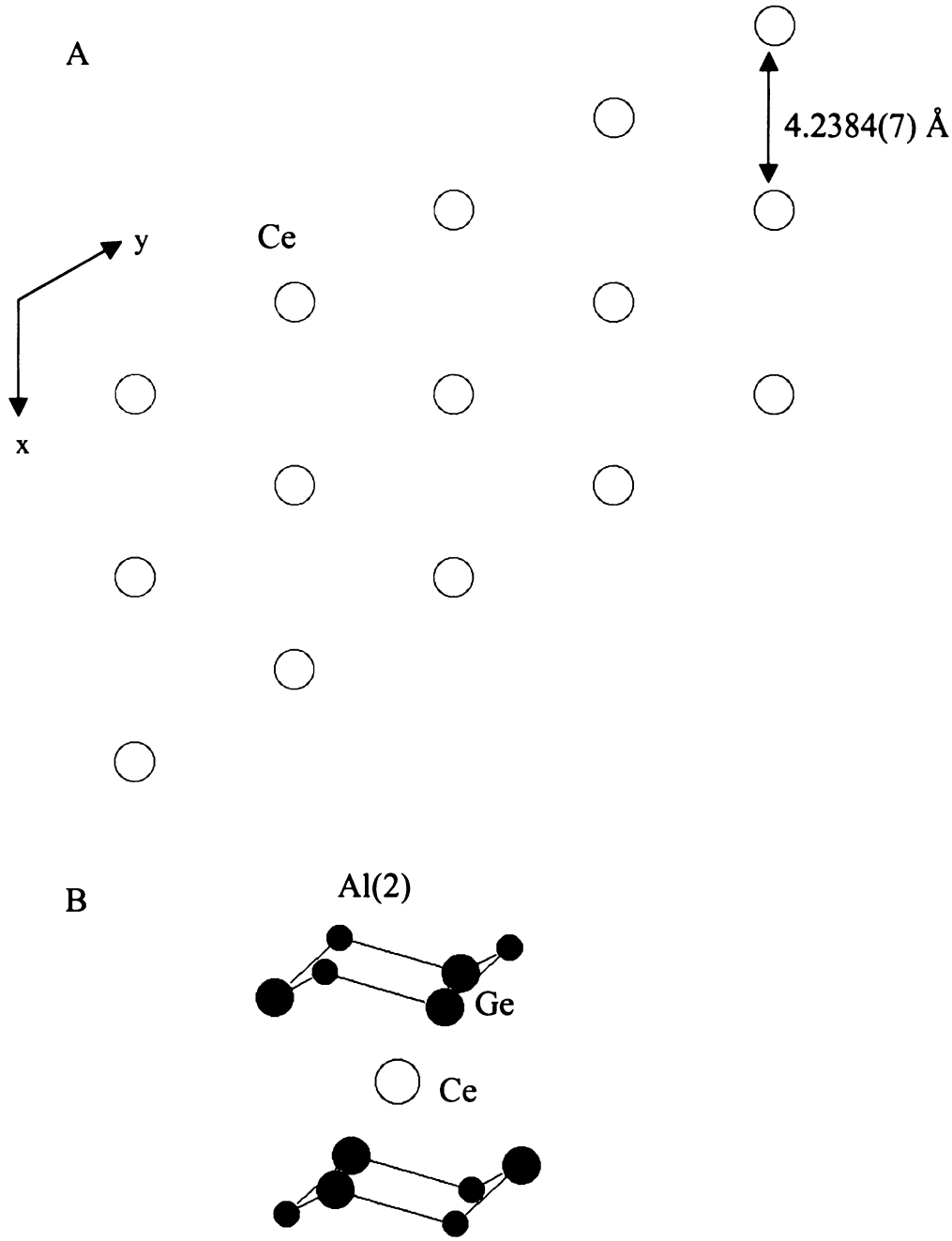

Figure 2-4. Structure of $CeAuAl_4Ge_2$. A) Trigonal pattern of Ce atoms in *ab* plane. B) Coordination environment of Ce atom.

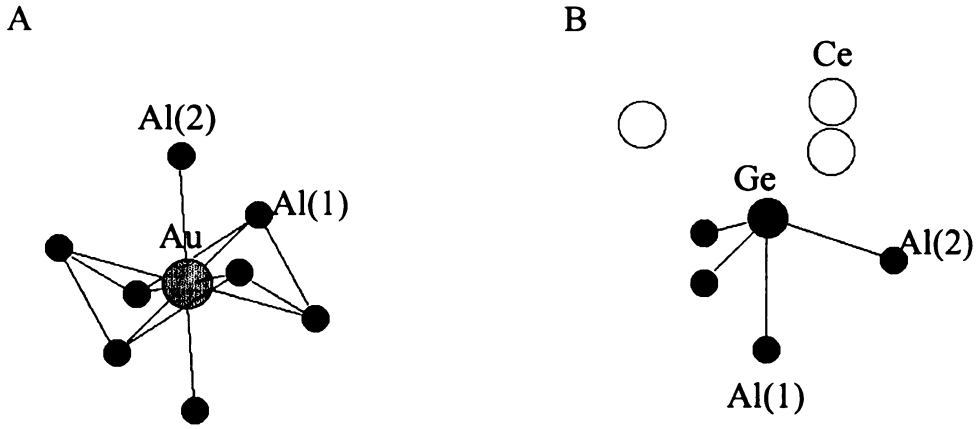

Figure 2-5. Structure of $CeAuAl_4Ge_2$. A) Coordination environment of Au atom. B) Coordination environment of Ge atom.

Table 2-8. Bond lengths (Å) for $REAuAl_4Ge_2$ (RE = Ce, Nd, Gd, Er).

	$CeAuAl_4Ge_2$	$NdAuAl_4Ge_2$	$GdAuAl_4Ge_2$	$ErAuAl_4Ge_2$
RE-Ge ×5	3.0692(7)	3.0342(4)	2.9901(6)	2.9516(5)
Au-Al(1) ×6	2.5668(9)	2.5629(6)	2.5575(8)	2.5568(8)
Au-Al(2) ×2	2.591(3)	2.5820(19)	2.578(3)	2.585(3)
Ge-Al(1)	2.5824(10)	2.638(2)	2.635(2)	2.645(3)
Ge-Al(2) ×3	2.641(3)	2.5806(7)	2.5757(9)	2.5761(9)
Al(1)-Al(1) ×3	2.897(3)	2.901(2)	2.902(3)	2.906(3)

Crystal Structure of $REAuAl_4(Au_xGe_{1-x})_2$ (x = 0.4):

The compound $REAuAl_4(Au_xGe_{1-x})_2$ (x = 0.4) crystallizes in space group *P4/mmm* with the KCu_4S_3 structure type. The same structure forms with other transition metals including Ni, Cu and Pd when Ge is replaced by Si.[5] As shown in Figure 2-6, the $AuAl_4(Au_xGe_{1-x})_2$ layers stack along the *c*-axis, and the Eu atoms reside in cages formed by eight Ge/Au atoms and eight Al atoms (Figure 2-7B), similar to those of the Ba atoms in the $BaAl_4$ structure type.[15] When viewed on the *ab* plane, as shown in Figure 2-7A, the Eu atoms are arranged in a flat square-net, with an Eu-Eu distance of 4.3134(8)Å, which is equal to the *a*-cell parameter.

The structure type of the $AuAl_4(Au_xGe_{1-x})_2$ layer contains a stable unit which occurs frequently in many intermetallic compounds, such as $LaGa_6Ni_{1-x}$,[16] $Tb_2NiAl_4Ge_2$,[4] and Sm_2NiGa_{12}.[17] This layer can be described as follows: Au atoms are arranged in a square network with each Au atom sitting inside a distorted Al_8 cube, shown in Figure 2-7C. These cubes share edges with the Al-Al bond distance of 2.912(6) Å to form an infinite slab. The slab is then completed by capping Ge/Au atoms on both sites. Analysis of the X-ray data shows that the capping atomic sites are in fact occupied by a mixture of Au and Ge atoms with a ratio of 2 : 3.[18] The resulting $AuAl_4(Au_xGe_{1-x})_2$ layers stack and link to each other via Ge-Ge bonding between capping Ge atoms along the *c*-direction. The distance between Au/Ge atoms across neighboring $AuAl_4(Au_xGe_{1-x})_2$ layers is 2.575(2) Å.

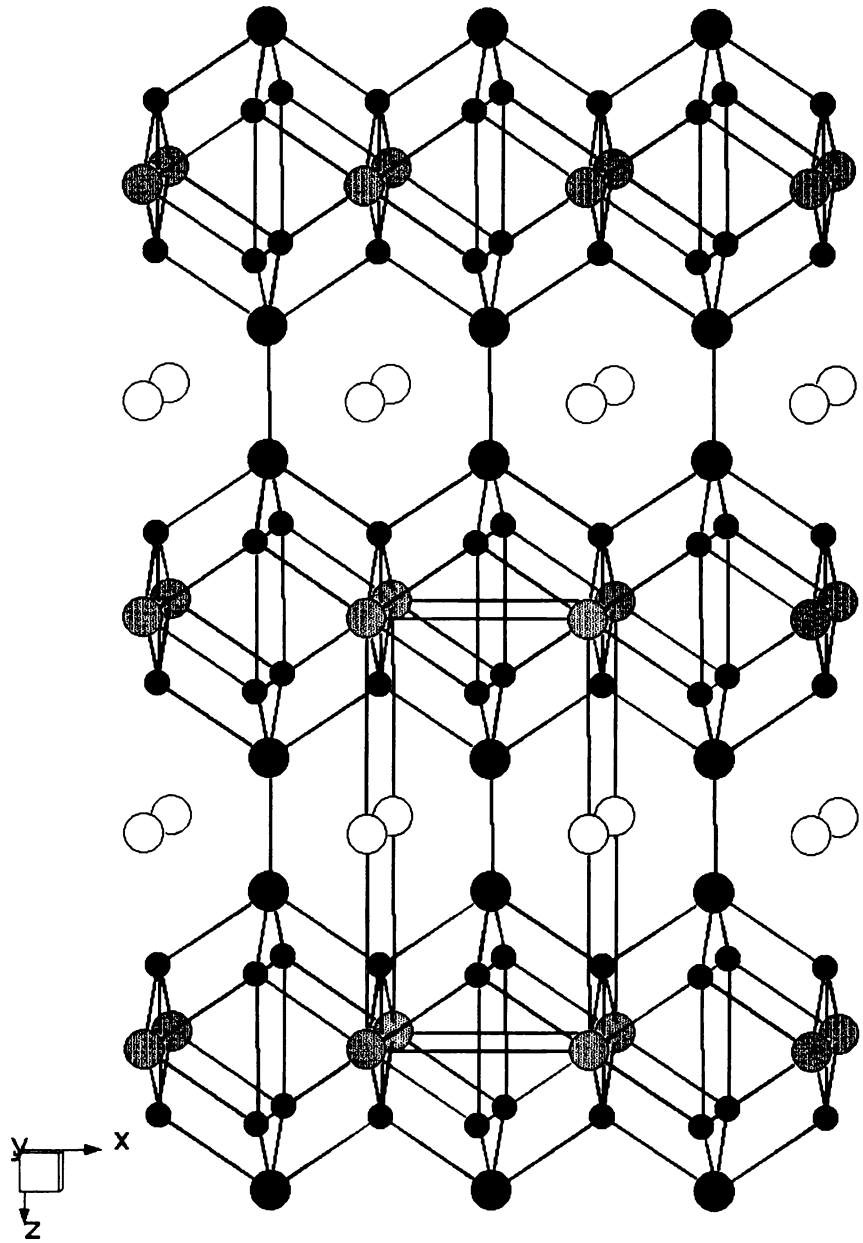

Figure 2-6. Structure of $EuAuAl_4(Au_xGe_{1-x})_2$ viewed down the [010] direction. Large empty circles: Eu; black dots: Al; lighter shaded circles: Au; darker shaded circles: Ge/Au.

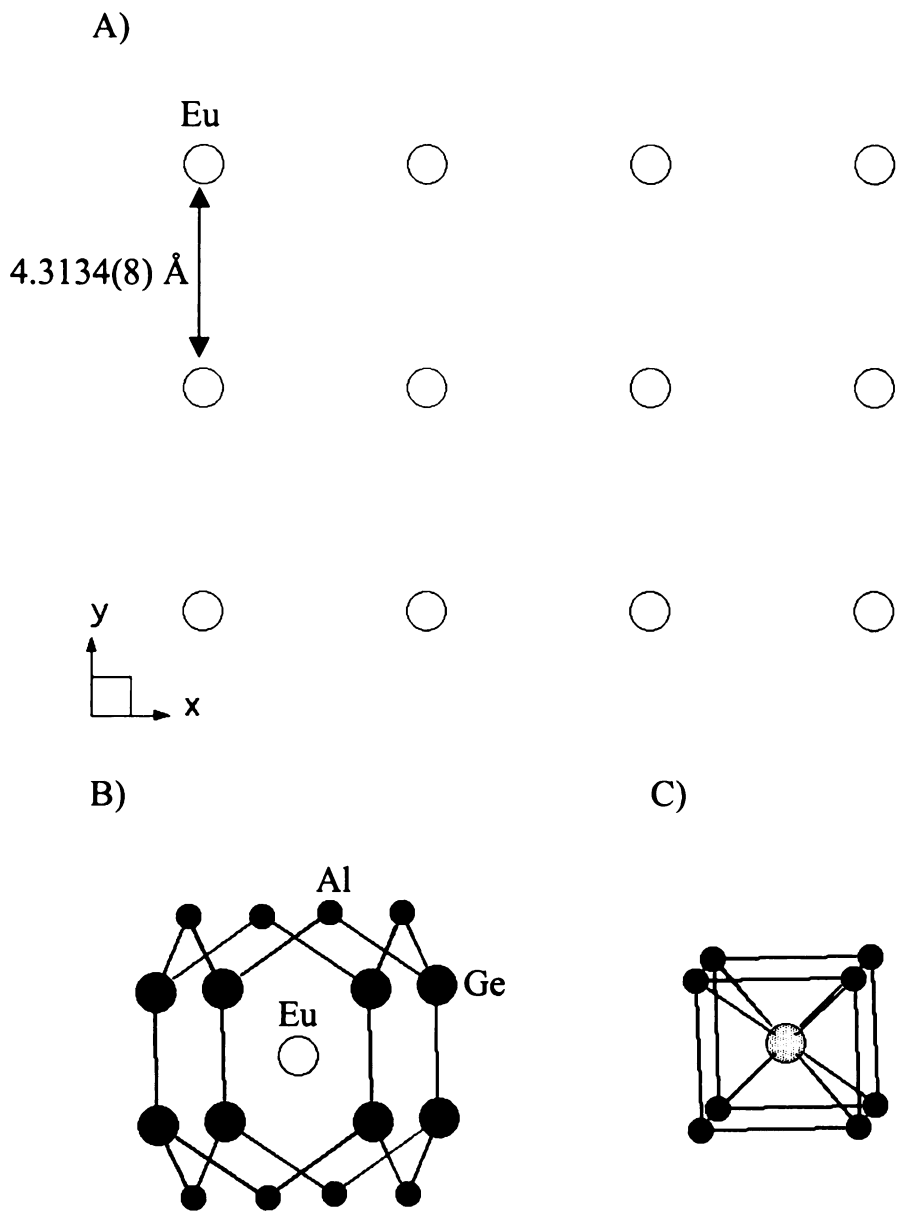

Figure 2-7. Structure of $EuAuAl_4(Au_xGe_{1-x})_2$. (A) The square net formed by Eu atoms in *ab* plane. (B) (C) Local coordination environments of Eu and Au(1) atoms.

Table 2-9. Bond lengths (Å) for $EuAuAl_4(Au_xGe_{1-x})_2$ (x = 0.4) and $CeCuAl_4(Cu_xGe_{1-x})_2$ (x = 0.62).

	$EuAuAl_4(Au_xGe_{1-x})_2$ (x = 0.4)		$CeCuAl_4(Cu_xGe_{1-x})_2$ (x = 0.62)
Eu-Ge ×10	3.3107(7)	Ce-Ge ×10	3.2071(4)
Eu-Al ×2	3.479(2)	Ce-Al ×2	3.3536(13)
Au(1)-Al ×8	2.6021(17)	Cu(1)-Al ×8	2.2154(9)
Ge-Al ×4	2.5944(18)	Ge-Al ×4	2.5507(10)
Al-Al	2.912(6)	Al-Al	2.9845(3)
Ge-Ge ×2	2.575(2)	Ge-Ge ×2	2.3475(17)

Magnetic Properties:

Crystals were picked from the products and analyzed by EDS. Magnetic measurements were performed on polycrystalline samples ground from those selected crystals.

Magnetism of $CeAuAl_4Ge_2$, $EuAuAl_4Ge_2$ and $DyAuAl_4Ge_2$

The magnetic susceptibility as a function of temperature for $CeAuAl_4Ge_2$ is plotted in Figure 2-8A. Up to 300 K, $CeAuAl_4Ge_2$ does not obey Curie-Weiss Law at any temperature range which indicates possible mixed Ce^{3+}/Ce^{4+} valence in this compound. The mixed or intermediate valence behavior, which is generally induced by the hybridization between 4f electrons and conduction electrons, has also been seen in other Ce-containing compounds such as $CeNiAl_4(Si_{2-x}Ni_x)$ and $Ce_2NiAl_{6-x}Ge_{4-y}$.[5] We have calculated the magnetic moment of this compound from its susceptibility value χ_m measured at T = 280 K according to the equation $\mu_{exp} = 2.83(T\chi_m/6)^{1/2}(4\pi x10^{-6})\ \mu_B$. The

resulting value $\mu_{exp} = 0.78\ \mu_B$ is between the theoretical value of $\mu_{eff} = 0\ \mu_B$ for Ce^{4+} and $\mu_{eff} = 2.54\ \mu_B$ for Ce^{3+}. However, the temperature dependent magnetic behavior of $CeAuAl_4Ge_2$ is different from well known mixed valence systems such as $CeRu_3Si_2$,[19] the weakly mixed valence system $CeSn_3$[20] and the strongly mixed valence system $CeRu_2$[21]. In these typical mixed valence compounds, χ_m is almost constant at low temperatures, then increases with increasing temperature and tends to obey the Curie-Weiss Law at high temperatures. The reason why $CeAuAl_4Ge_2$ shows different magnetic behavior from typical mixed valence compounds might be that, it is a very weakly mixed valence system that has a much lower fluctuation temperature. Figure 2-8B shows the magnetization of $CeAuAl_4Ge_2$ as a function of field. The magnetization increases linearly up to 10000 G without saturation.

The magnetic susceptibility of $EuAuAl_4Ge_2$ obeys the Curie-Weiss Law above 50 K, Figure 2-8C. The μ_{eff} value, obtained from the data, is 3.34 μ_B, while that of a free-ion for Eu^{3+} is 3.40 μ_B. Therefore, we can regard the oxidation state of the Eu ion as 3+, while Au is in a diamagnetic state. Because of the slightly enhanced stability of half filled 4f shells of Eu^{2+}, most europium compounds show divalent europium or mixed valence of Eu^{2+}/Eu^{3+}. To further determine the oxidation state of Eu atoms, ^{151}Eu Mössbauer Spectroscopy might be needed. The field dependent data (Figure 2-8D) shows a gradual increase of the magnetization until saturation which occurs at about 30000 G. However magnetization per Eu ion at this point is only 30% of the maximum value calculated according to the formula $\mu_{Eu(calc)} = gJ\ \mu_B$ (for a free atom the g factor is defined by the Landé equation, the total angular momentum J is the sum of the orbital L and spin S angular momenta).

The molar magnetic susceptibility data of $DyAuAl_4Ge_2$ *vs* temperature is plotted in Figure 2-8E. This material exhibits an antiferromagnetic transition at low temperature around 11 K and conforms to the Curie-Weiss Law behavior above the transition temperature. The calculated μ_{eff} (9.17 μ_B), is somewhat lower than the theoretical value for Dy^{3+}(10.63 μ_B), as is frequently observed, and the difference might be ascribed to the crystal-field effects.[22] The measured magnetic moment is entirely attributed to Dy atoms with the Au atoms being diamagnetic. $DyAuAl_4Ge_2$ exhibits field-induced metamagnetic behavior at 3K, as shown in Figure 2-8F. A gradual increase in magnetization is observed until the field reaches 5000 G where a dramatic increment occurs, indicating spin reorientation. Then the magnetization begins to saturate and does not change much up to 55000 G. However, the moment per Dy^{3+} ion at this point is only 60% of its maximum value (10.60 μ_B) which is calculated from $\mu_{Dy(calc)} = gJ\ \mu_B$. The sharp jump occurring at 5000 G suggests a possible transition to a more ferromagnetically ordered state, which can also be supported by the positive sign of the Weiss constant θ. Similar spin complexity has been observed in other intermetallic compounds including $Dy_2AuAl_6Si_4$[8] and β-$DyNiGe_2$[23]. It has been suggested that a trigonal arrangement of rare earth ions on a plane could create frustration in antiferromagnetic coupling.[24] A field higher than 55000 G may be required to achieve complete saturation of the magnetization.

Magnetism of $CeAuAl_4(Au_xGe_{1-x})_2$ and $EuAuAl_4(Au_xGe_{1-x})_2$ ($x = 0.4$)

Figure 2-9A gives the thermal dependence of the magnetic susceptibility χ_m measured for $CeAuAl_4(Au_xGe_{1-x})_2$. The μ_{eff} values, calculated by fitting to the Curie-

Weiss Law in the temperature range of 50~140 K and 160~300 K, are 1.54 μ_B and 1.18 μ_B, respectively, which are between the theoretical ones of $\mu_{eff} = 0$ μ_B for Ce^{4+} and $\mu_{eff} = 2.54$ μ_B for Ce^{3+}. The change in the slope of inverse susceptibility plot may be due to changes in the Ce valence state over the whole temperature range. This behavior is different from those compounds with intermediate valence of Ce atoms, which also obey the Curie-Weiss Law at high temperature while Ce atoms are in 3+ oxidation state.[25] The Au atoms are likely diamagnetic as in the other Al-grown intermetallic compounds described above.

For $EuAuAl_4(Au_xGe_{1-x})_2$, the temperature dependent magnetic susceptibility data at 1000 G show an antiferromagnetic transition at about 4 K, as shown in the inset of Figure 2-9 C. When the high temperature (above 20 K) data are fit to the Curie-Weiss Law, a μ_{eff} of 6.03 μ_B is obtained. The calculated effective magnetic moment for Eu^{2+} $4f^7$ ions is predicted to be equal to the value of Gd^{3+} ions, which is 7.94 μ_B. Thus we suggest that Eu ions in this compound $EuAuAl_4(Au_xGe_{1-x})_2$ are in a divalent $4f^7$ ground state and the difference might due to the crystal-field effects. This observation is consistent with the statement that Eu is often found to be divalent in the noble-metal compounds with a broad *s* band. Examples include $EuAg_5$[26], $EuAu_5$[27], EuAuMg[28], $Eu(Pd_{1-x}Au_x)_2Si_2$[29] and $EuAu_4Al_8Si$[7]. The magnetization increases gradually with increasing applied field. No magnetization saturation is observed up to 55000 G (Figure 2-9D).

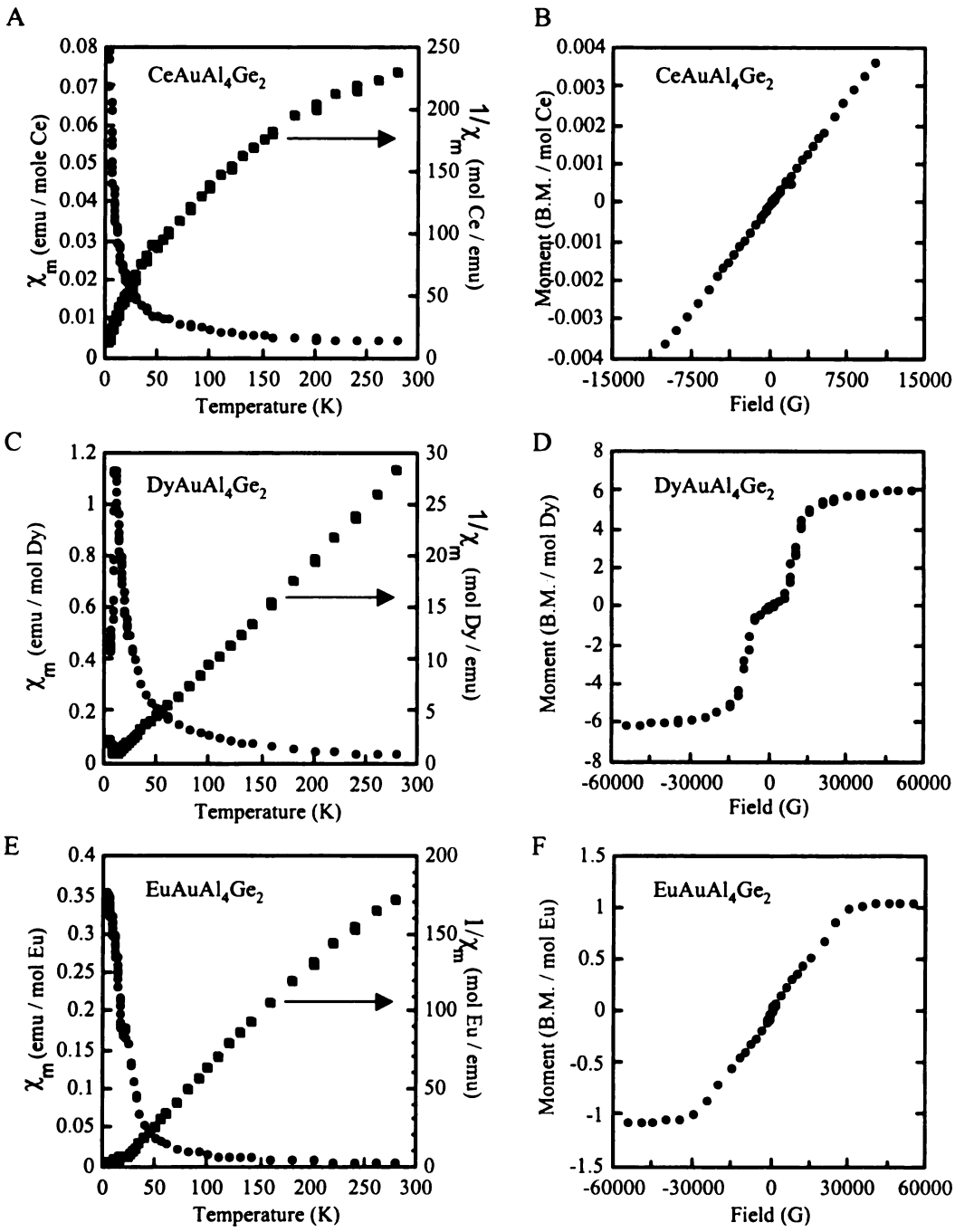

Figure 2-8. (A) Temperature dependent magnetic susceptibility of $CeAuAl_4Ge_2$. (B) Field dependent magnetization at 3K for $CeAuAl_4Ge_2$. (C) Temperature dependent magnetic susceptibility of $EuAuAl_4Ge_2$. (D) Field dependent magnetization at 3K for $EuAuAl_4Ge_2$. (E) Temperature dependent magnetic susceptibility of $DyAuAl_4Ge_2$. (F) Field dependent magnetization at 3K for $DyAuAl_4Ge_2$.

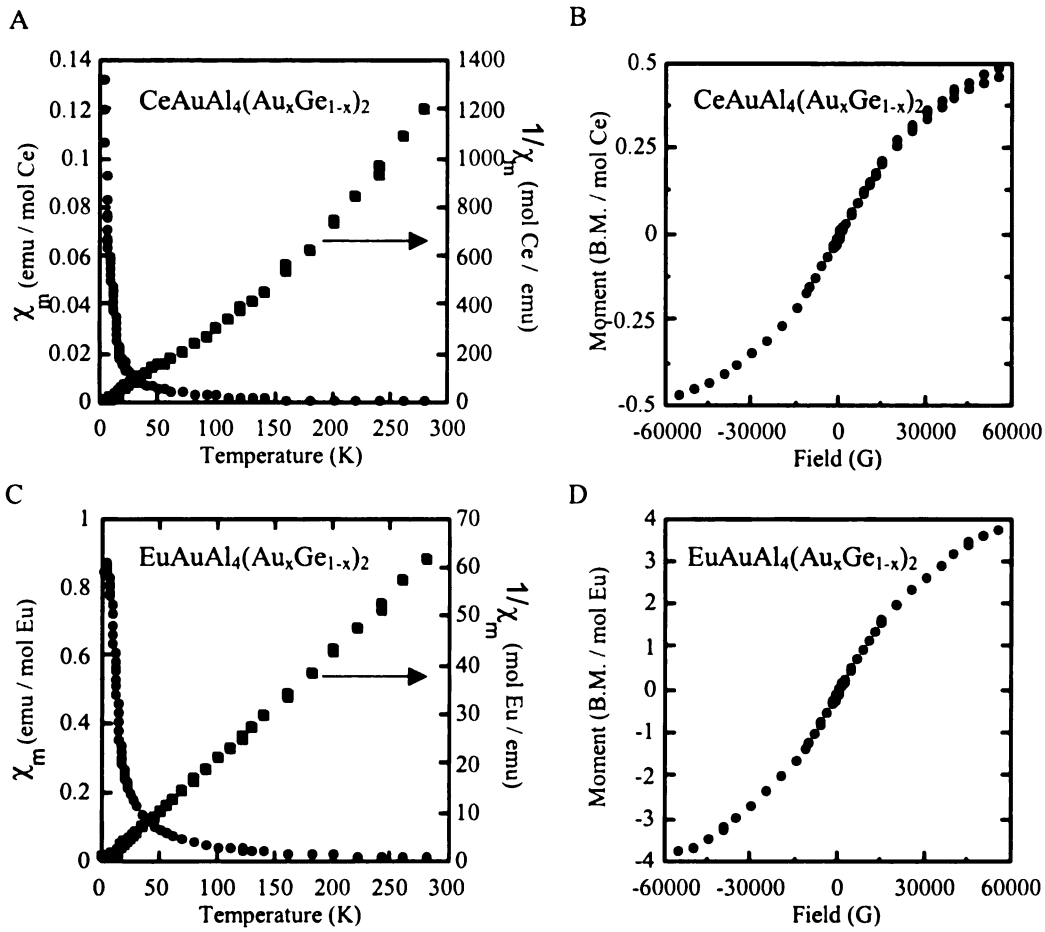

Figure 2-9. (A) Temperature dependent magnetic susceptibility of $CeAuAl_4(Au_xGe_{1-x})_2$. (B) Field dependent magnetization at 3K for $CeAuAl_4(Au_xGe_{1-x})_2$. C) Temperature dependent magnetic susceptibility of $EuAuAl_4(Au_xGe_{1-x})_2$. (D) Field dependent magnetization at 3K for $EuAuAl_4(Au_xGe_{1-x})_2$.

2-4. Conclusions

The exploratory reaction chemistry in the system RE/Au/Al/Ge using Al as a flux led to two types of intermetallic phases $REAuAl_4Ge_2$ (RE = Ce, Pr, Nd, Sm, Eu, Gd, Tb, Dy, Er, Tm and Yb) and $REAuAl_4(Au_xGe_{1-x})_2$ (x = 0.4) (RE = Ce and Eu). These two families crystallize in different structure types and were characterized by single crystal X-ray diffraction. However these two structures are related and both can be represented as consequent stacking of RE layers and $AuAl_4Ge_2$ (or $AuAl_4(Au_xGe_{1-x})_2$) slabs along the *c*-axis. Single crystal X-ray diffraction analysis reveals that the Ge atoms in $REAuAl_4(Au_xGe_{1-x})_2$ are in a mixed occupancy site with 40% of Au and 60% of Ge, while for the Cu-analogue, the mixed site is occupied by 62% Cu and 38% Ge.

The discovery of these two families suggests the parallel chemistry between the third row transition metal and the first row transition metal, especially Ni. For example, the hexagonal phase $RETMAl_4Ge_2$ can be formed both with Au and Ni; $REAuAl_4(Au_xGe_{1-x})_2$ and $RENiAl_4(Si_{2-x}Ni_x)$ are isostructural phases which have transition metal and tetrelide on the mixed occupied site.

Magnetic measurements indicate that the magnetic moments are localized on the RE atoms and Au atoms are in a non-magnetic state. Antiferromagnetic ordering transitions are observed in $DyAuAl_4Ge_2$ and $EuAuAl_4(Au_xGe_{1-x})_2$ with Néel temperatures of 11 K and 4 K respectively, and $DyAuAl_4Ge_2$ exhibits metamagnetic behavior at 3K. The Ce analogs may exhibit valence fluctuations in the temperature range measured.

References:

[1] a) Chen, X. Z.; Sportouch, S.; Sieve, B.; Brazis, P.; Kannewurf, C. R.; Cowen, J. A.; Patschke, R.; Kanatzidis, M. G. *Chem. Mater.* **1998**, *10*, 3202. b) Sieve, B.; Chen, X. Z.; Cowen, J.; Larson, P.; Mahanti, S. D.; Kanatzidis, M. G. *Chem. Mater.* **1999**, *11*, 2451.

[2] a) Thiede, V. M. T.; Fehrmann, B.; Jeitschko, W. *Z. Anorg. Allg. Chem.* **1999**, *625*, 1417. b) Fehrmann, B.; Jeitschko, W. *J. Alloys Compd.* **2000**, *298*, 153.

[3] Kanatzidis, M. G.; Pöttgen, R.; Jeitschko, W. *Angew. Chem. Int. Edit.* **2005**, *44*, 6996.

[4] a) Sieve, B.; Sportouch, S.; Chen, X. Z.; Cowen, J. A.; Brazis, P.; Kannewurf, C. R.; Papaefthymiou, V.; Kanatzidis, M. G. *Chem. Mater.* **2001**, *13*, 273. b) Sieve, B.; Chen, X. Z.; Henning, R.; Brazis, P.; Kannewurf, C. R.; Cowen, J. A.; Schultz, A. J.; Kanatzidis, M. G. *J. Am. Chem. Soc.* **2001**, *123*, 7040. c) Sieve, B.; Trikalitis, P. N.; Kanatzidis, M. G. *Z. Anorg. Allg. Chemie* **2002**, *628*, 1568.

[5] Sieve, B. Ph. D. Dissertation, Michigan State University, 2002.

[6] Latturner, S. E.; Bilc, D.; Mahanti, S. D.; Kanatzidis, M. G. *Chem. Mater.* **2002**, *14*, 1695.

[7] Latturner, S. E.; Kanatzidis, M. G. *Chem. Commun.* **2003**, *18*, 2340.

[8] Latturner, S. E.; Kanatzidis, M. G. *Inorg. Chem.* **2003**, *42*, 7959.

[9] Latturner, S. E.; Bilc, D.; Ireland, J. R.; Kannewurf, C. R.; Mahanti, S. D.; Kanatzidis, M. G. *J. Solid State Chem.* **2003**, *170*, 48.

[10] Latturner, S. E.; Kanatzidis, M. G. *Inorg. Chem.* **2004**, *43*, 2.

[11] Saint, version 4; Simens Analytical X-ray Instruments, Inc., Madison, WI.

[12] SADABS, Sheldrick, G. M.; University of Göttingen, Göttingen, Germany.

[13] Sheldrick, G. M. 1995, SHELXTL. Structure Determination Programs, Version 5.0. Siemens Analytical X-ray Instruments, Inc. Madison, WI.

[14] Kranenberg, C.; Johrendt, D.; Mewis, A. *Solid State Sci.* **2002**, *4*, 261.

[15] Andress, K. R.; Alberti, E. *Z. Metallkunde* **1935**, *27*, 126.

[16] Grin, Yu. N.; Yarmolyuk, Ya. P.; Rozhdestvenskaya, I. V.; Gladyshevskii, E. I.; *Kristallografiya* **1982**, *27*, 693.

[17] Chen, X. Z.; Small, P.; Sportouch, S.; Zhuravleva, M.; Brazis, P.; Kannewurf, C. R.; Kanatzidis, M. G. *Chem. Mater.* **2000**, *12*, 2520.

[18] The Si analogues grown from Al flux such as $REAu_4Al_8Si$ also has the mixed occupied site of Au and Si with the ratio 1 : 1. Our assignment in the compound $EuAuAl_4(Au_xGe_{1-x})_2$ supports the assignment that the mixed occupied site in $REAu_4Al_8Si$ is in fact between Au and Si instead of Au and Al.

[19] Kishimoto, Y.; Kawasaki, Y.; Ohno, T. *Phy. Lett.* **2003**, *317*, 308.

[20] a) Lawrence, J. M.; Riseborough, P. S.; Parks, R. D. *Rep. Prog. Phys.* **1981**, *44*, 1. b) Lawrence, J. M.; Riseborough, P. S.; Parks, R. D. in: L.M. Falicov, W. Hanke, M.B. Maple(Eds.), Valence Fluctuations in Solids, North-Holland, Amsterdam, 1981.

[21] Tsvyashchenko, A. V.; Fomicheva, L. N.; Sorokin, A. A.; Ryasny, G. K.; Komissarova, B. A.; Shpinkova, L. G.; Klementiev, K. V.; Kuznetsov, A. V.; Menushenkov, A. P.; Trofimov, V. N.; Primenko, A. E.; Cortes, R. *Phys. Rev. B* **2002**, *65*, 174513.

[22] Kittel, C. Introduction to Solid State Physics, 7th Ed. John Wiley & Sons, New York, 1996, p. 426.

[23] Salvador, J. R.; Gour, J. R.; Bilc, D.; Mahanti, S. D.; Kanatzidis, M. G. *Inorg. Chem.* **2004**, *43*, 1403.

[24] Gignoux, D.; Schmitt, D. *J. Alloys Compd.* **2001**, *326*, 143.

[25] a) Chevalier, B.; Bobet, J. L.; Gaudin, E.; Pasturel, M.; Etourneau, J. *J. Solid State Chem.* **2002**, *168*, 28. b) Tang, J.; Gschneidner, K. A. *Phy. Rev. B* **1995**, *52*, 7328.

[26] Sampathkumaran, E. V.; Perscheid, B.; Kaindl, G. *Solid State Commun.* **1984**, *51*, 701.

[27] Van Steenwijk, F. J.; Huiskamp, W. J.; Lefever, H. T.; Thiel, R. C.; Buschow, K. H. J. *Physica B & C* **1997**, *86-88B*, 89.

[28] Pottgen, R.; Hoffmann, R.; Renger, J.; Rodewald, U. C.; Moller, M. H. *Z. Anorg. Allg. Chem.* **2000**, *626*, 2257.

[29] Abd-Elmeguid, M. M.; Sauer, C.; Koebler, U.; Zinn, W. *Z. Phys. B: Cond. Matter* **1985**, *60*, 239.

CHAPTER THREE

$V_2Al_5Ge_5$: First Ternary Intermetallic in the V-Al-Ge system Accessible in Liquid Aluminum

3-1. Introduction

Recently Al flux has been proven by the Kanatzidis group, Jeitschko group and others to be a powerful method to study the multinary systems including RE/Al/Tr, RE/TM/Al, RE/TM/Al/Tr (RE = rare earth metal, TM = transition metal, Tr = Si or Ge).[1,2] Surprisingly rich chemistry was found from these systems in liquid aluminum: explorations of the new multinary systems led to the discovery of a number of new series of intermetallics such as $RENiAl_4Ge_2$,[3] $RE_4Fe_{2+x}Al_{7-x}Si_8$,[4] and $REAu_3Al_7$[5]. In addition, new phases were obtained by reinvestigation of some old systems. For example, there are a few ternary rare earth aluminum silicides reported in the literature, such as RE_6Al_3Si (RE = Ho, Tm),[6] Tm_2AlSi_2,[7] and $DyAl_2Si_2$.[8] Re-inspection of this system using Al as the flux produced a new family of intermetallics $RE_2Al_3Si_2$ (RE = Ho, Er, Tm).[9] The single crystal form of these phases obtained from liquid aluminum made the structural determination easier and physical properties measurements more reliable.

The success on these rare earth-containing systems stimulated us to start inspecting the systems without rare earth metals, e.g. TM/Al/Tr, TM_1/TM_2/Al/Tr. There have been some reports in the literature on ternary transition metal silicides with the transition metal mainly Mn, Fe, Co, Ni, such as $FeAl_2Si$[10] and $Ni_{16}AlSi_9$.[11] Many of them are pseudo-binary compounds with Al and Si sitting on the same site, such as $Mo_3Al_{0.8}Si_{0.2}$,[12] $Ni_3Al_{0.6}Si_{0.4}$.[13] These systems are of particular interest due to the remarkable thermal oxidation resistance of silicides. Since 1980s, a large number of

quasicrystalline approximants have been discovered in the Al-rich region of the Al/TM and related ternary systems. One well-known example is α-MnAlSi, which is a prototype of approximants presenting Mackay-type clusters.[14]

As to the systems containing Ge, there are even less examples reported in the literature, MnAlGe,[15] $Ni_3Al_{0.8}Ge_{0.2}$[16] to name a few. In the system V/Al/Ge, as far as we know, only a few pseudo-binary phases were reported, such as $V_3Al_{0.25}Ge_{0.75}$,[17] $V_3Al_{0.3}Ge_{0.7}$[18] and $V_3Al_{0.5}Ge_{0.5}$.[19] All these phases belong to the A15 structure type with Al and Ge atoms occupying the same site.[20] The parent compound V_3Ge is a superconductor with Tc = 6.104 K, and it was found that in the system $V_3Al_xGe_{1-x}$, the substitution of Al for Ge expands the lattice and dramatically increases T_c (T_c = 11.17 K when x = 0.3).[21] Our studies on the system V/Al/Ge using Al as the flux led to the discovery of a new ternary compound $V_2Al_5Ge_5$ with all the atoms sitting on independent atomic sites. In this chapter, synthesis, crystal structure, thermal analysis, magnetic measurements and electronic structure calculations for $V_2Al_5Ge_5$ are reported.

3-2. Experimental Section

Reagents:

The following reagents were used as obtained without further purification: V (-325 mesh, Cerac, 99.7%), Al pellets (Cerac, 99.99%), Ge (Cerac, 99.999%).

Synthesis:

In a nitrogen-filled glove box, 2 mmol V metal (0.102 g), 5 mmol Ge (0.36 g) and 10 mmol Al (0.270 g) were combined in an alumina crucible. The crucible was then

placed into a silica tube (13 mm in diameter), which was sealed under vacuum (~10^{-4} Torr). The sample was heated to 850 °C in 12 h, maintained at this temperature for 3d, slowly cooled down to 200 °C at the rate of 15 °C h^{-1}, and finally brought down to 50 °C in 5 h. This compound can also be obtained as a pure phase by combining 2mmol V metal (0.102 g), 5mmol Al (0.135 g) and 5mmol Ge (0.36 g) using the same heating profile.

Isolation:

The excess aluminum was removed by soaking the crucible in aqueous 5M NaOH solution overnight. The solid product remaining after the isolation procedure was rinsed with water and dried with acetone. The yield of the reaction was ~90% based on the initial amount of V metal used. Single crystals were selected for elemental analysis, X-ray diffraction, thermal analysis and magnetic susceptibility measurements.

Elemental Analysis:

The crystals were fixed on a Scanning Electron Microscope (SEM) sample plate using carbon tape. Chemical composition of the products was determined by Energy Dispersive Spectroscopy (EDS) performed on a JEOL JSM-35C SEM equipped with a NORAN EDS detector. Data were acquired by applying a 25 kV accelerating voltage with an accumulation time of 60 s. The atomic ratio averaged from ten crystals was determined to be 1 : 2.85 : 2.73 (V : Al : Ge), which agreed well with the results derived from the single crystal X-ray data analysis.

X-ray Crystallography:

Single crystal X-ray diffraction data of $V_2Al_5Ge_5$ was collected at room temperature on a Bruker AXS SMART CCD X-ray diffractometer. A data collection (Mo Kα radiation, λ = 0.71073 Å) was acquired covering a full sphere of reciprocal space. Data processing was performed with the SAINTPLUS software package.[22] An empirical absorption correction was applied to the data using the SADABS program.[23] The structure was solved by direct method and refined with the SHELXTL package program.[24] Systematic absences conditions led to three *c*-centered space groups: *Cmc*2, *Cmcm* and *Ama*2. *Cmcm* is the only centrosymmetric one and has the lowest CFOM value thus was chosen. Later structure refinement confirmed this choice. All atomic positions were refined with anisotropic thermal displacement parameters. The resulting stoichiometry agreed well with the elemental analysis from EDS. Data collection parameters and refinement details for $V_2Al_5Ge_5$ can be found in Table 3-1. Atomic positions, displacement parameters and anisotropic displacement parameters for this compound are listed in Table 3-2 and Table 3-3.

The X-ray powder diffraction data were collected at room temperature on a CPS 120 INEL X-ray diffractometer (Cu Kα) equipped with position-sensitive detector. Experimental powder patterns were compared to the patterns calculated from the single crystal structure solution (by the CrystalDiffract program) to determine the phase identity and purity.

Thermal Analysis:

Differential thermal analysis (DTA) was performed on a Shimadzu DTA-50 differential thermal analyzer with α-Al_2O_3 as a standard reference. The sample was heated to 1000 °C at a rate of 10 °C/min, then cooled to 150 °C at the same rate. The cycle was then repeated to determine if the compound melted congruently.

Thermal gravimetric analysis (TGA) was performed on a Shimadzu TGA-50 thermal gravimetric analyzer. The sample was heated to 1000 °C at a rate of 10 °C/min under flowing air, held at 1000 °C for 10 min, and then cooled down to room temperature at the same rate.

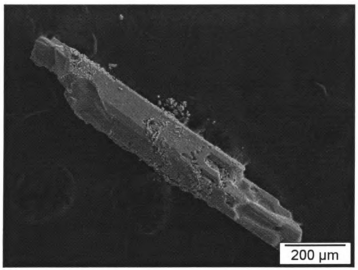

Figure 3-1. SEM image of a typical crystal of $V_2Al_5Ge_5$.

Table 3-1. Crystal data and structure refinements for $V_2Al_5Ge_5$.

Empirical formula	$V_2Al_5Ge_5$
Formula weight	599.73
Temperature	298(2) K
Wavelength	0.71073 Å
Space Group	Cmcm (#63)
Lattice constants (Å)	a = 5.4072(10) Å
	b = 12.978(2) Å
	c = 11.363(2) Å
Volume	797.4(3) $Å^3$
Z	4
Calculated density, (g/cm^3)	4.996
Absorption coefficient, (mm^{-1})	21.293
F(000)	1084
Crystal size, (mm^3)	0.22 × 0.17 × 0.15
θ range, (°)	11.48 to 37.92
Limiting indices	$-9 \leq h \leq 9$
	$-22 \leq k \leq 22$
	$-19 \leq l \leq 19$
Reflections collected	6346
Unique reflections	1133
R_{int}	0.0965
Completeness to θ	93.9 %
Refinement method	Full-matrix least-squares on F^2
Variables	40
Goodness-of-fit on F^2	1.064
Final R indices [$I>2\sigma(I)$][a]	R_1 = 0.0486 wR_2 = 0.0895
R indices (all data)	R_1 = 0.0828 wR_2 = 0.0996
Extinction coefficient	0.0099(7)
Highest residual peak ($e/Å^3$)	2.207 and –1.843

$R1 = \Sigma(|F_o|-|F_c|)/\Sigma|F_o|$; $wR2 = [\Sigma[w(F_o^2 - F_c^2]/ [\Sigma(w|F_o|^2)^2]^{1/2}$

Table 3-2. Atomic coordinates and equivalent isotropic displacement parameters ($Å^2 \times 10^3$) for $V_2Al_5Ge_5$.

Atom	Wyk. Symbol	x	y	z	$U_{(eq)}$*
V	8*g*	0.2526(2)	0.3903(1)	0.7500	3(1)
Ge(1)	4*c*	0.0000	0.2208(1)	0.7500	6(1)
Ge(2)	4*c*	0.5000	0.3430(1)	0.5566(1)	6(1)
Ge(3)	8*f*	0.0000	0.5322(1)	0.6321(1)	8(1)
Al(1)	4*c*	-0.5000	0.2095(2)	0.7500	11(1)
Al(2)	4*c*	0.0000	0.3331(2)	0.5451(2)	9(1)
Al(3)	8*f*	0.0000	0.0425(2)	0.6273(2)	9(1)

* $U_{(eq)}$ is defined as one third of the trace of the orthogonalized U_{ij} tensor.

Table 3-3. Anisotropic displacement parameters ($Å^2 \times 10^3$) for $V_2Al_5Ge_5$.

Atom	U^{11}	U^{22}	U^{33}	U^{23}	U^{13}	U^{12}
V	4(1)	4(1)	3(1)	0	0	0
Ge(1)	6(1)	4(1)	8(1)	0	0	0
Ge(2)	6(1)	8(1)	4(1)	-1(1)	0	0
Ge(3)	7(1)	8(1)	9(1)	3(1)	0	0
Al(1)	8(1)	7(1)	18(1)	0	0	0
Al(2)	11(1)	10(1)	6(1)	-3(1)	0	0
Al(3)	9(1)	8(1)	8(1)	3(1)	0	0

The anisotropic displacement factor exponent takes the form:
$-2\pi^2[h^2a^{*2}U^{11}+...+2hka^*b^*U^{12}]$

Magnetic Characterization:

Magnetic measurements were conducted on the polycrystalline samples of $V_2Al_5Ge_5$ using a Quantum Design MPMS SQUID magnetometer. EDS-analyzed crystals were ground into powder, which was then sealed in kapton tape and placed into the magnetometer. The data were collected in the temperature range 3-300 K at 1000 G, while field dependent magnetic measurements, conducted at 3 K, were carried out in fields up to ± 55000 G. A diamagnetic correction was applied to the data to account for core diamagnetism. The magnetic contribution from kapton tape was also subtracted for correction.

Electronic Structure Calculation:

Band structure calculations for $V_2Al_5Ge_5$ were performed using the self-consistent full-potential linearized augmented plane wave method (LAPW) within density functional theory (DFT). For the exchange and correlation parts of the potential, the generalized gradient approximation (GGA) was used. Scalar relativistic corrections were added and spin-orbital interaction (SOI) was incorporated using a second variational procedure. The calculations were performed using the WIEN97 program.

3-3. Results and Discussion

Synthesis:

$V_2Al_5Ge_5$ was originally found as we were exploring the system V/Co/Al/Ge using Al as the flux. After excess Al was removed by NaOH solution, $V_2Al_5Ge_5$ was obtained in the form of elongated needles, frequently aggregated in bundles. The SEM

image of a typical crystal of $V_2Al_5Ge_5$ is shown in Figure 3-1. Elemental analysis and single crystal X-ray data revealed that Co did not go into the product and a new ternary compound $V_2Al_5Ge_5$ formed. This result is surprising since Co is very reactive in liquid aluminum and several new Co-containing quaternary intermetallics had been discovered by the Al flux method, such as $CeCoAl_4Si_2$, $RE_2CoAl_4Ge_2$ (RE = Sm, Gd, Tb) and $Sm_2Co(Co_xAl_{1-x})Al_4Ge_{6-y}$.[25] Later flux synthesis only incorporating V, Al and Ge was also successful to produce the title compound as single crystals with the reaction yield ~90%. $V_2Al_5Ge_5$ can also be obtained as a pure phase by combining stoichiometric amount of V, Al and Ge using the same heating profile; however only microcrystalline products were obtained. This again shows the effectiveness of Al flux to grow single crystals of intermetallics.

We have also tried to apply the same conditions to the system V/Al/Si expecting to obtain Si-analogue of the title compound. Various conditions led to the same product V_3AlSi_5, which is a variant of the known compound VSi_2 with Al and Si atoms sitting on the same site.[26]

Crystal Structure of $V_2Al_5Ge_5$:

$V_2Al_5Ge_5$ crystallizes in the orthorhombic space group *Cmcm* (#63) in what appears to be a new structure type (Figure 3-2). In this structure a total of seven crystallographically distinct atomic sites were identified: V atoms at *8g* sites, Al and Ge atoms occupying three atomic sites: two at *8f* and one at *4c*. A recognizable building block in this structure is a distorted pentagonal prismatic column made of stacked pentagonal prisms defined by Al and Ge atoms with V atoms in the center. The

pentagonal prisms have been seen in other compounds such as CeGaMg, in which Ga and Mg atoms build a three dimensional network with Ce atoms filling in the pentagonal channels.[27] These pentagonal columns are close-packed hexagonally throughout the whole structure. To show the structural organization of $V_2Al_5Ge_5$ more clearly, all Al atoms were removed as shown in Figure 3-3. These pentagons form layered structure stacking along the *c*-axis; on the neighboring layer, the pentagons are rotated 180° pointing to the opposite direction.

In $V_2Al_5Ge_5$ the pentagonal prism is not regular, as described in Figure 3-4A: one of its pentagonal faces contains one Al(1) atom, two symmetry-related Al(3) atoms and two symmetry-related Ge(2) atoms, while on the opposite face, correspondingly, there are one Ge(1) atom, two Ge(3) atoms and two Al(2) atoms. The pentagonal prisms stack along the *a*-axis to make a column by sharing the top and bottom faces with two other prisms. Therefore each V atom is not only surrounded by five Al atoms and five Ge atoms, but also bonded with other two V atoms inside the column forming a vanadium chain, which is rarely seen in other vanadium-containing intermetallic compounds.[28] Another interesting feature of this structure is long–short alternation of the V–V bond distances in the chain at 2.732(2) Å and 2.676(2) Å, respectively. Both distances imply V–V bonding and are comparable to those found in other intermetallic compounds such as AlV_3 and V_4Al_{23}.[29] The difference in bond distance indicates that the V atom is not located exactly at the center of the prism. In fact, the V atom is closer to the face containing two Ge atoms and three Al atoms (plane Al(1) – Al(3) – Ge(2), Figure 3-4A). The local coordination environments of Ge and Al atoms within 3.0 Å are presented in Figure 3-4B-D and Figure 3-4E-G respectively. Each Al/Ge atom is surrounded by eight

atoms, and they exhibit similar coordination geometry. The Ge(1) atom is sitting at the cross-section of two planes: one plane is defined by atoms Al(1)–V–V–Al(1), the other plane is perpendicular and defined by atoms Al(2)–Al(3)–Al(3)–Al(2). Ge(1), Al(2) and V atoms are connected to form a triangular pyramid. The Ge(2) atom shows a similar geometry as Ge(1), but in this case, those two Al(3) atoms are from different pentagonal clusters, so there is no bonding between them, as shown in Figure 3-4C. Another noteworthy point is that the two triangles Al(2)–V–Ge(2) connected by Ge(2) atom are not co-planar. Ge(3) atom also presents a similar coordination environment, but it is different from those of Ge(1) and Ge(2) atoms, particularly in the triangular pyramid. One of the Al atoms in the apex positions is replaced by one Ge(3) atom, with the Ge(3)–Ge(3) bond distance of 2.6791(15) Å. The Al atoms show very similar coordination geometries to the Ge atoms (shown in Figure 3-4E-G) and will not be discussed here in detail.

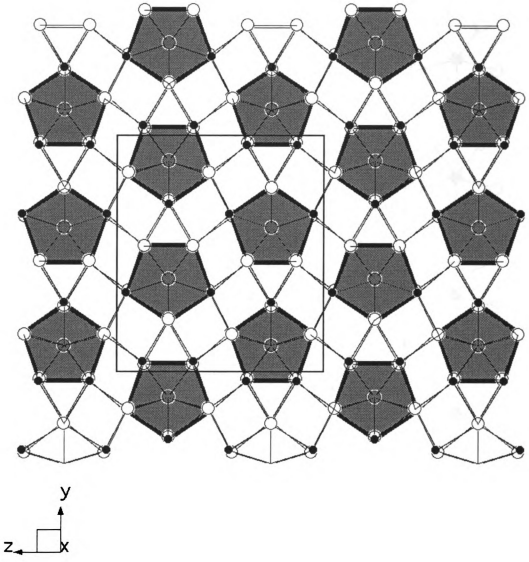

Figure 3-2. Structure of $V_2Al_5Ge_5$ in polyhedra of V atoms viewed down the [100] direction. Large empty circles: Ge; black circles: Al; gray circles: V.

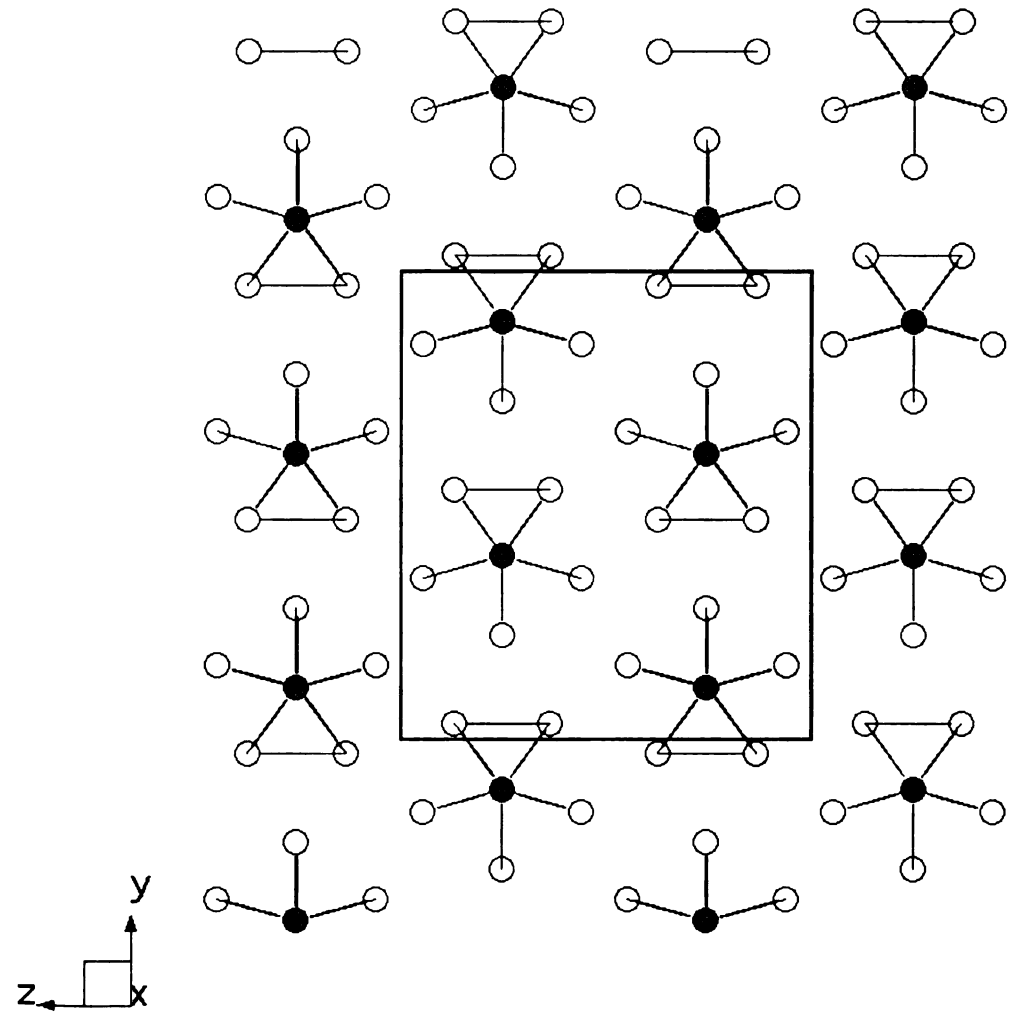

Figure 3-3. Structure of $V_2Al_5Ge_5$ viewed down the *a*-axis with all Al atoms omitted for clarity.

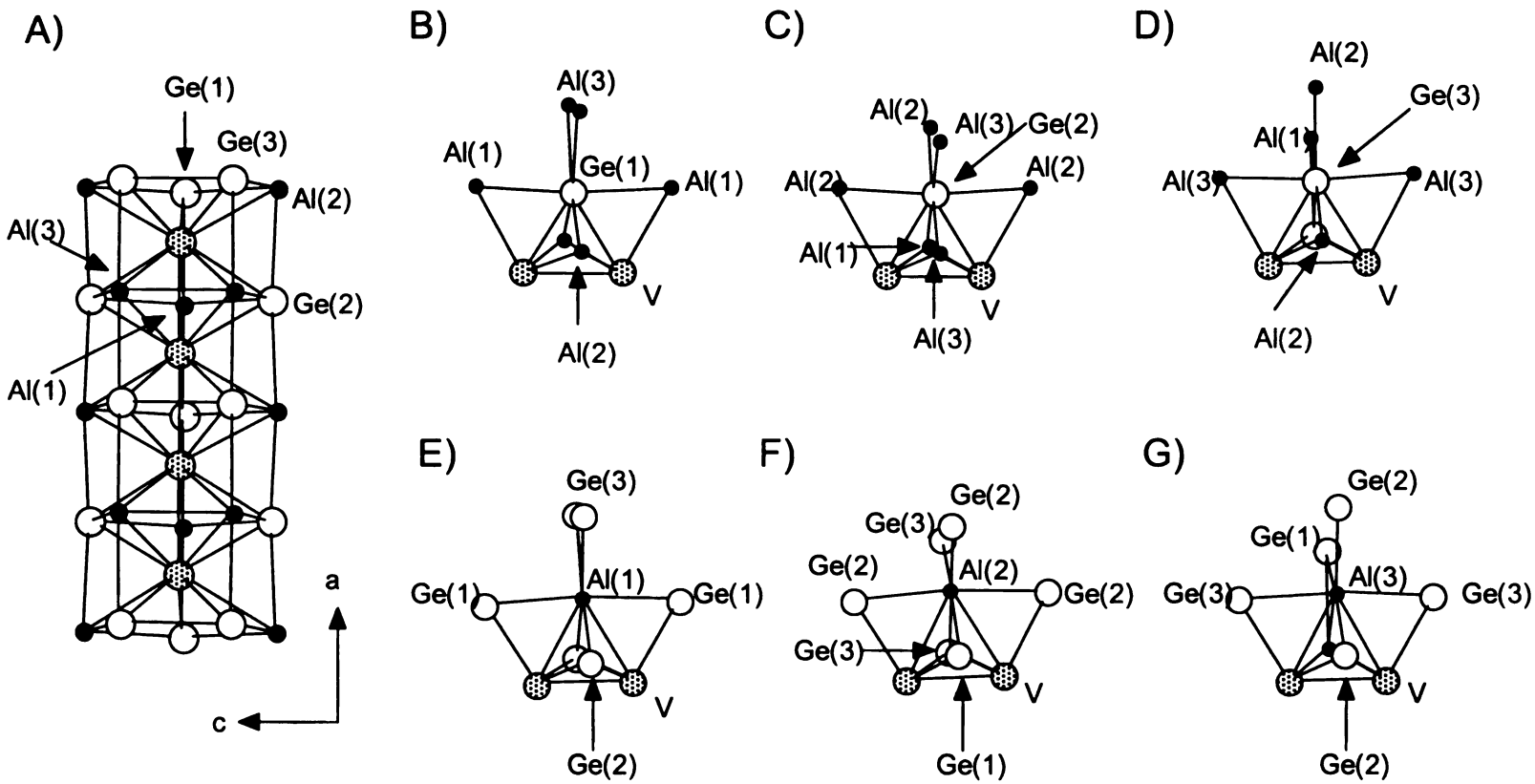

Figure 3-4. Structure of $V_2Al_5Ge_5$. A) Pentagonal column composed of Al and Ge atoms with V-chaining sitting in the center. B) - G) Coordination environments of Ge and Al atoms.

Table 3-4. Bond lengths (Å) for $V_2Al_5Ge_5$.

Bond	Distance	Bond	Distance
V-Ge(1)	2.5890(13)	Ge(1)-Al(1)	2.7076(5)
V-Ge(2) ×2	2.6447(9)	Ge(1)-Al(2)	2.747(2)
V-Ge(3) ×2	2.6558(11)	Ge(1)-Al(3)	2.701(2)
V-Al(1)	2.701(3)	Ge(2)-Al(1)	2.799(2)
V-Al(2) ×2	2.799(2)	Ge(2)-Al(2)	2.562(2)
V-Al(3) ×2	2.764(2)	Ge(2)-Al(2) ×2	2.7098(5)
V-V	2.676(2)	Ge(2)-Al(3)	2.564(2)
V-V	2.732(2)	Ge(2)-Al(3)	2.711(2)
Ge(3)-Ge(3)	2.6791(15)	Ge(3)-Al(1)	2.662(3)
Al(3)-Al(3)	2.788(4)	Ge(3)-Al(2)	2.666(2)
Ge(3)-Al(3) ×2	2.7075(5)	Ge(3)-Al(2)	2.766(2)

Magnetic Properties:

Magnetic measurements were performed on polycrystalline samples ground from selected single crystals and from direct combination to check the reproducibility of the result. Originally, the temperature dependent magnetic measurements show ferromagnetic behavior of the title compound with Tc around 280 K. However the magnetization at 3 K is as low as 0.005 μ_B when the applied field is 10000 G. Although powder X-ray diffraction analysis shows that it is pure phase of $V_2Al_5Ge_5$, careful elemental analysis on the sample detects a very small amount of adventitious iron which might come from reduction of the crucible cement (a mixture of metal oxides) by Al flux. To avoid this problem, the reaction was conducted in a one-side-ended crucible as obtained, so no cement was used. The result confirmed our assumption: as shown in Figure 3-5, this material was almost temperature independent during the whole

temperature range of 3 to 300 K which indicates that $V_2Al_5Ge_5$ exhibits Pauli paramagnetic behavior. The very small amount of ferromagnetic fragment at low temperatures might be from impurities.

Thermal Analysis:

Differential thermal analysis shows that $V_2Al_5Ge_5$ melts congruently with the melting point 709 °C and it recrystallizes at 641 °C. Figure 3-6 shows the thermal gravimetric analysis of single crystals of $V_2Al_5Ge_5$ under flowing air up to 1000 °C. This material was resistant to air oxidation until 520 °C, and no weight gain or loss was observed. Above this temperature, however, the weight increased gradually and up to 1000 °C a total of 30% of weight was gained. PXRD shows that this material was finally fully oxidized to the mixture of oxides: Al_2O_3, V_2O_5 and GeO_2. The oxidation resistance properties of germanides are generally not so good as those of silicides, which have been studied extensively as wear and corrosion resist coating materials.

Band Structure Calculations:

Electronic structure calculations using the linearized augmented plane wave method within density functional theory show metallic behavior of $V_2Al_5Ge_5$, as shown in Figure 3-7. The Fermi level is at 0 eV with a density of states of about 8 states/eV/2[$V_2Al_5Ge_5$] (Figure 3-7A). The Ge p states are in the energy range -7 to 10 eV, and they hybridize with the Al p and s orbitals indicating the covalent interaction between Ge and Al atoms (Figure 3-7B, C). The DOS diagram of V d-orbitals, Figure 3-7D, reveals two bands evidently: one is located between –4 to 0 eV and the other is 0 to 3

eV, showing that the d-orbitals of V atoms are partially occupied. Comparison between the occupied partial DOS diagrams implies that the d-states of V atoms (in the range -4 to 0 eV) hybridize more with Ge p states than Al p and s states, suggesting that the covalent interaction between V and Ge is stronger than that of V and Al atoms.

3-4. Conclusions

By studying the ternary system V-Al-Ge in liquid aluminum, we obtained single crystals of a new phase $V_2Al_5Ge_5$, which is the first real ternary compound in this system. It crystallizes in a new structure type with the pentagonal column composed of Al and Ge atoms as the unique building block. The V atoms form a long-short alternating chain residing in the center of the pentagonal column.

Magnetic measurements show that this material is Pauli paramagnetic, which is consistent with metallic behavior predicted from band structure calculations. The partial DOS diagrams reveal covalent bonding between Ge and Al atoms; the d-orbitals of V atoms are partially occupied and the covalent bonding between V and Ge atoms is stronger than that between V and Al atoms. $V_2Al_5Ge_5$ is resistant to air oxidation up to 520 °C; up to 1000 °C this material is fully oxidized to the mixture of metal oxides.

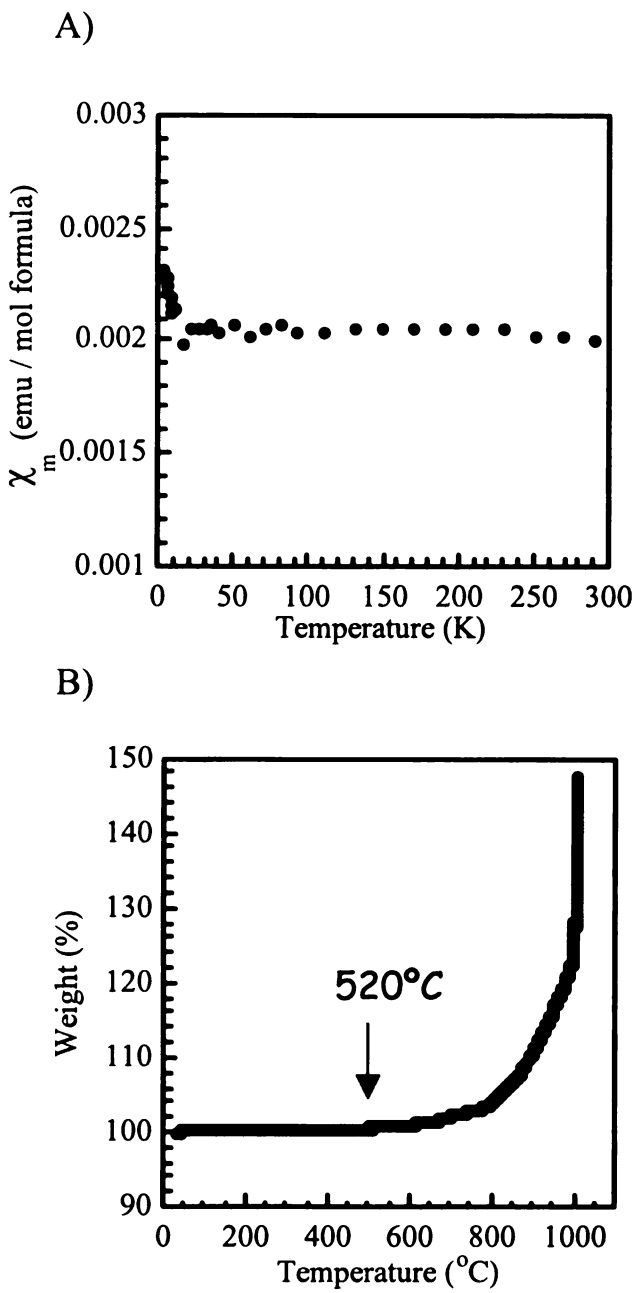

Figure 3-5. A)Temperature dependent magnetic behavior of $V_2Al_5Ge_5$ at 1000G.
B). Thermal gravimetric analysis of $V_2Al_5Ge_5$ under air.

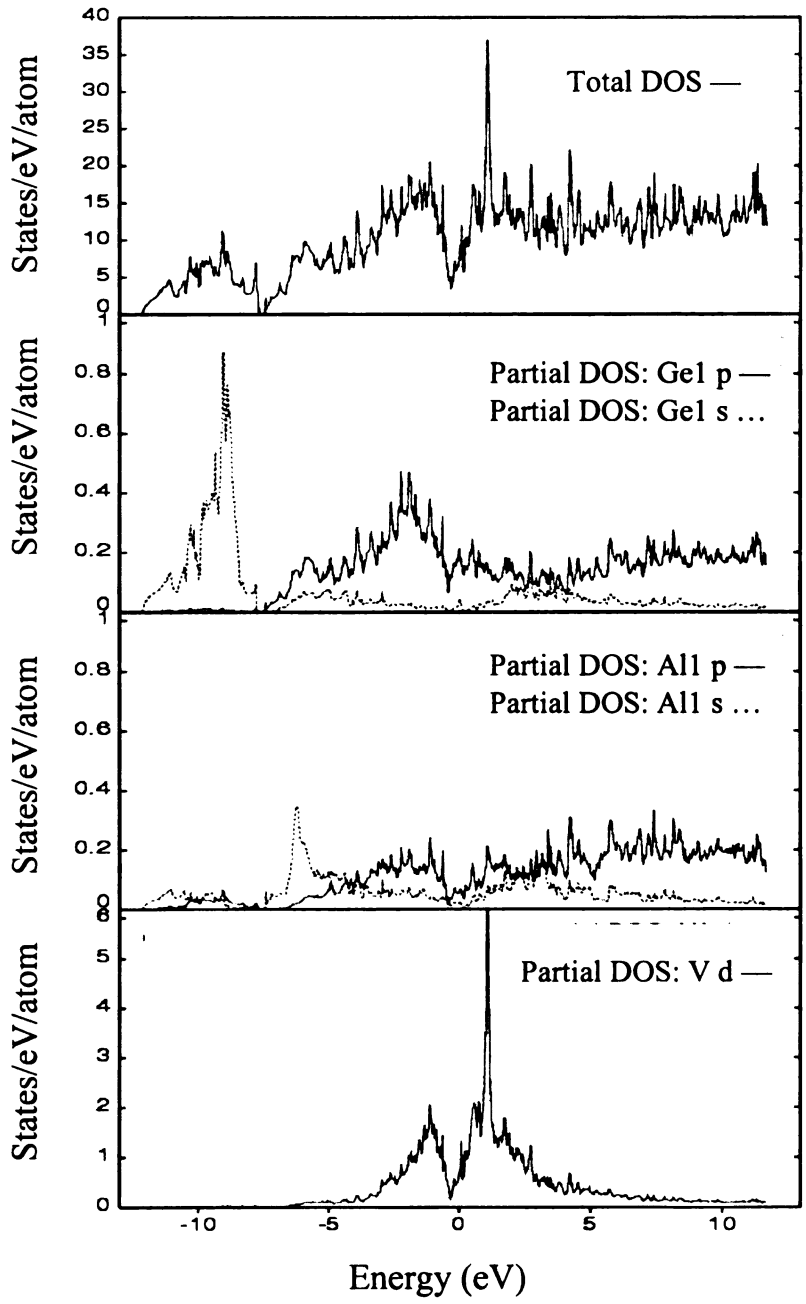

Figure 3-7. Density functional theory calculated for $V_2Al_5Ge_5$.

References:

[1] a) Chen, X. Z.; Sportouch, S.; Sieve, B.; Brazis, P.; Kannewurf, C. R.; Cowen, J. A.; Patschke, R.; Kanatzidis, M. G. *Chem. Mater.* **1998**, *10*, 3202. b) Sieve, B.; Chen, X. Z.; Henning, R.; Brazis, P.; Kannewurf, C. R.; Cowen, J. A.; Schultz, A. J.; Kanatzidis, M. G. *J. Am. Chem. Soc.* **2001**, *123*, 7040. c) Kanatzidis, M. G.; Pöttgen, R.; Jeitschko, W. *Angew. Chem. Int. Edit.* **2005**, *44*, 6996.

[2] a) Thiede, V. M. T.; Fehrmann, B.; Jeitschko, W. *Z. Anorg. Allg. Chem.* **1999**, *625*, 1417. b) Fehrmann, B.; Jeitschko, W. *J. Alloys Compd.* **2000**, *298*, 153.

[3] Sieve, B.; Chen, X. Z.; Cowen, J. A.; Larson, P.; Mahanti, S. D.; Kanatzidis, M. G. *Chem. Mater. 1999*, *11*, 2451.

[4] Sieve, B.; Sportouch, S.; Chen, X. Z.; Cowan, J. A.; Brazis, P.; Kannewurf, C. R.; Papaefthymiou, V.; Kanatzidis, M. G. *Chem. Mater.* **2001**, *13*, 273.

[5] Latturner, S. E.; Bilc, D.; Ireland, J. R.; Kannewurf, C. R.; Mahanti, S. D.; Kanatzidis, M. G. *J. Solid State Chem.* **2003**, *170*, 48.

[6] Dubenko, I. S.; Evdokimov, A. A.; Ionov, V. M. *Kristallografiya* **1987**, *32*, 347.

[7] Kranenberg, C.; Mewis, A. *Z. Anorg. Allg. Chem.* **2000**, *626*, 1448.

[8] Schobinger-Papamantellos, P.; Hulliger, F. *J. Less-Common Met.* **1989**, *146*, 327.

[9] Chen, X. Z.; Sieve, B.; Henning, R.; Schultz, A. J.; Brazis, P.; Kannewurf, C. R.; Cowen, J. A.; Crosby, R.; Kanatzidis, M. G. *Angew. Chem. Int. Edit.* **1999**, *38*, 693.

[10] Geman, N. V.; Zavodnik, V. E.; Yanson, T. I.; Zarechnyuk, O. S. *Kristallografiya* **1989**, *34*, 738.

[11] Richter, K.W.; Prots, Yu.; Grin, Yu. N. *Z. Anorg. Allg. Chem.* **2004**, *630*, 417.

[12] Holleck, H.; Benesovsky, F.; Laube, E.; Nowotny, H. *Monatsh. Chem.* **1962**, *93*, 1075.

[13] Mohan Rao, P. V.; Satyanarayana Murthy, K.; Suryanarayana, S. V.; Nagender Naidu, S.V. *Phys. Status Solidi, A* **1992**, *133*, 231.

[14] Frank, F. C.; Kasper, J. S. *Acta Cryst.* **1996**, *A52*, 125.

[15] Pearson, W. B. *Z. Kristallogr.* **1985**, *171*, 23.

[16] Ul-Haq, I.; Booth, J. G. *J. Magn. Magn. Mater.* **1986**, *62*, 256.

[17] Holleck, H.; Benesovsky, F.; Novotny, H. *Monatsh. Chem.* **1963**, *94*, 477.

[18] Luo, H. LP.; Vielhaber, E.; Corenzwit, E. *Z. Phys.* **1970**, *230*, 443.

[19] Kodess, B. N. *Phys. Status Solidi, A* **1971**, *4*, 109.

[20] A15 is the Strukturbericht designation of the structure type with the space group Pm-3n. The prototype compound is Cr_3Si.

[21] Smith, T. F. *Solid State Comm.* **1971**, *9*, 903.

[22] Saint, version 4; Simens Analytical X-ray Instruments, Inc., Madison, WI.

[23] SADABS, Sheldrick, G. M.; University of Göttingen, Göttingen, Germany.

[24] Sheldrick, G. M. 1995, SHELXTL. Structure Determination Programs, Version 5.0. Siemens Analytical X-ray Instruments, Inc. Madison, WI.

[25] Sieve, B. Ph. D. Dissertation, Michigan State University, 2002.

[26] Structural information of V_3AlSi_5: hexagonal, space group: $P6_{(2)}22$ (#180), a = 4.6173(8) Å, c = 6.4445(15) Å, V = 118.99(4) $Å^3$, Z = 1, Dc = 4.857 g cm^{-3}, μ = 9.715 mm^{-1}; index range –7<=h<=7, -7<=k<=7, -10<=l<=8; total reflections 1153, independent reflections 203 (R_{int} = 3.48%), and 11 parameters; R_1 = 2.59, wR_2 = 6.63, GOF = 1.131. The *6j* site M (occupied by Si in VSi_2) was refined to be mixed occupied by Al and Si: Al 17%, Si 83%. What first brought to attention was the bond distance of M-M, which ranges from 2.5145(5) Å to 2.6922(8) Å, much longer than the bond distance of Si-Si (2.3~2.5 Å), while shorter than that of normal bond distance of Al-Al (2.7~2.9 Å). Moreover, this mixed occupany of Al and Si lowers the R value from 2.68% (fully occupied by Si) to 2.59%; the refinement result is consistent with the elemental analysis by EDS (V : Al : Si 3 : 1 : 5), which also confirms this refinement.

[27] Kraft, R.; Pöttgen, R. *Chem. Mater.* **2003**, *15*, 2998.

[28] Kuzma, Y. B.; Starodub, P. K.; *Izv. Akad. Nauk SSSR, Neorg. Mater.* **1973**, *9*, 337.

[29] (*a*) Kodess, B. N. *Phys. Status Solidi A* **1971**, *4A*, 109. (*b*) Ray, A. E.; Smith, J. F. *Acta Cryst.* **1960**, *13*, 876.

CHAPTER FOUR

Structurally Complex Cobalt Intermetallics Grown from Liquid Aluminum: $Co_{19}Al_{45}Si_{10-x}$ (x = 0.13) & $Co_5Al_{14}Si_2$

4-1. Introduction

Aluminum matrix alloys are technologically useful materials because of their light weight, special mechanical strength, high thermal and electrical conductivity, etc.[1] For example, aluminum metal-matrix composites (Al-MMCs) have emerged as a critical class of material for applications in lightweight automotive structures, forgings for suspension and drive trains as well as aerospace development products.[2] The addition of transition metals and silicon into an Al matrix contributes to the desirable properties of these materials such as high temperature wear and corrosion resistant coatings[3] and even thermoelectric energy conversion[4]. Moreover, a large number of quasicrystal approximants occur in the Al-rich region of the Al-TM (TM = transition metal) and related ternary systems.[5] One well known example is α-MnAlSi which is a prototype of approximants presenting Mackay-type clusters.[6] Since the quasicrystalline phases are often found with a composition in the vicinity of crystalline approximant phases, the detection of new approximants often helps to find new quasicrystals and aid in the understanding of the local order of the latter compounds.

In the ternary phase diagram of Co-Al-Si system, very little information is known about the structural chemistry of ternary compounds. Nowotny and his coworkers identified two ternary phases $Co_3Al_3Si_4$ and Co_2AlSi_2;[7] German has had a tentative study on this ternary system and found five ternary phases.[8] He confirmed the existence of

$Co_3Al_3Si_4$ and Co_2AlSi_2 and labeled them as α and β phase. The other three phases were designated as γ, δ and ε and their crystal structures were not determined. In 2005 Grin and his coworkers reported the structure of another ternary compound $Co_4Al_{7+x}Si_{2-x}$, which shows a covalently bonded Al/Si 3D polyanion presenting ionic interactions with Co atoms.[9] $Co_4Al_{7+x}Si_{2-x}$ was assigned by Grin *et al.* as χ phase. In this chapter we present two new members in the Al-rich region — $Co_{19}Al_{45}Si_{10-x}$ (x = 0.13) and $Co_5Al_{14}Si_2$ grown from aluminum flux.[10] Among them, $Co_{19}Al_{45}Si_{10-x}$ (x = 0.13) was designated by German as γ phase however he could not characterize its crystal structure.[8] We were able to grow single crystals of these phases by Al flux and determine their crystal structures by single crystal X-ray diffraction analysis. Both phases exhibit surprisingly large unit cell parameters and complex structures; $Co_5Al_{14}Si_2$ shows remarkable thermal oxidation resistance in air up to 1000°C. Herein the synthesis, crystal structure, thermal stability and magnetic properties of the title compounds are reported.

4-2. Experimental Section

Reagents:

The following reagents were used as obtained without further purification: Co (-325 mesh, Cerac, 99.9%), V (-325 mesh, Cerac, 99.7%), Al pellets (Cerac, 99.99%), Si (-325 mesh amorphous powder, Cerac, 99.999%).

Synthesis:

$Co_{19}Al_{45}Si_{10-x}$ (x=0.13): In a nitrogen-filled glove box, 1 mmol vanadium (0.051 g), 2 mmol cobalt (0.118 g), 10 mmol Al (0.270 g) and 5 mmol Si (0.14 g) were combined in an

alumina crucible. The crucible was put into a silica tube, which was sealed under a vacuum of 10^{-4} Torr. The sample was then heated to 1000°C in 15 h, maintained at this temperature for 5 h, followed by cooling to 850°C in 2 h. It was annealed at 850°C for 3 d, cooled to 200°C in 36 h, and finally cooled down to 50°C in 2 h.

$Co_5Al_{14}Si_2$: In a nitrogen-filled glove box, 3 mmol cobalt (0.177 g), 15 mmol Al (0.405 g) and 5 mmol Si (0.14 g) were combined in an alumina crucible. The crucible was put into a silica tube, which was sealed under a vacuum of 10^{-4} Torr. The sample was then heated to 1000°C in 15 h, maintained at this temperature for 5 h, followed by cooling to 850°C in 2 h. It was annealed at 850°C for 3 d, and then cooled to 200°C in 36 h.

The excess aluminum was removed by soaking the crucible in aqueous 5M NaOH solution overnight. The resulting crystalline product was rinsed with water and dried with acetone. The yield for $Co_{19}Al_{45}Si_{10-x}$ (x = 0.13) was ~70% based on the initial amount of cobalt used. $Co_5Al_{14}Si_2$ was obtained as a pure phase with the yield 90%. Single crystals were selected for elemental analysis, X-ray diffraction, thermal gravimetric analysis and magnetic measurements. When we tried to produce the phase $Co_{19}Al_{45}Si_{10-x}$ by arc-melting the stoichiometric amount of the elements (ratio 1.9 : 4.5 : 1.0), the phase $Co_5Al_{14}Si_2$ formed instead. Arc-melting reactions were run under an Ar atmosphere on a water-cooled copper plate and the pellets were flipped and remelted three times to ensure a homogeneous distribution of the reactants.

Elemental Analysis:

Selected crystals were fixed on a SEM stub using carbon tape. Chemical composition of the products was determined by Energy Dispersive Spectroscopy (EDS) performed on a scanning electron microscope (SEM) JEOL JSM-35C equipped with NORAN EDS detector. Data were acquired by applying a 25 kV accelerating voltage with an accumulation time of 30 s. The atomic ratio in the compounds $Co_{19}Al_{45}Si_{10-x}$ (x = 0.13) and $Co_5Al_{14}Si_2$ were determined to be 18.4 : 41.5 : 10 (Co : Al : Si) and 5.27 : 13.6 : 2 (Co : Al : Si) respectively, in good agreement with the results derived from the single crystal X-ray analysis.

X-ray Crystallography:

Single crystal X-ray diffraction data of $Co_{19}Al_{45}Si_{10-x}$ (x = 0.13) and $Co_5Al_{14}Si_2$ were collected at room temperature on a Bruker AXS SMART CCD X-ray diffractometer with graphite monochromatized Mo Kα (λ = 0.71073 Å) radiation. Data processing was performed with the SAINTPLUS software package.[11] The face-indexing procedure was used to analytically correct for absorption; and an empirical absorption correction was applied to the data using the SADABS program.[12] The structure was solved using direct methods and refined with the SHELXTL package programs.[13] Since Al and Si could not be distinguished directly from the collected X-ray scattering data, the assignment of Al and Si positions were made based on the bond distances. All atomic positions were refined anisotropically. Tables 4-1 shows the crystallographic refinement data for $Co_{19}Al_{45}Si_{10-x}$ (x = 0.13) and $Co_5Al_{14}Si_2$. Tables 4-2, 4-3, 4-4, 4-5, 4-6 and 4-7 list

fractional atomic positions, equivalent isotropic thermal displacement parameters and selected bond distances for $Co_{19}Al_{45}Si_{10-x}$ (x = 0.13) and $Co_5Al_{14}Si_2$ respectively.

Table 4-1. Selected crystal data and structure refinement details for $Co_{19}Al_{45}Si_{10-x}$ (x = 0.13) and $Co_5Al_{14}Si_2$.

Empirical formula	$Co_{19}Al_{45}Si_{10-x}$ (x = 0.13)	$Co_5Al_{14}Si_2$
Formula weight	2614.67	728.55
Crystal system	Monoclinic	Orthorhombic
Space group	*C2/c* (#15)	*Pnma* (#62)
Unit cell dimensions	a = 19.991(2) Å	a = 13.8948(19) Å
	b = 19.143(2) Å	b = 23.039(3) Å
	c = 12.8137(2) Å	c = 7.3397(10) Å
	β = 123.583(2)°	
Volume	4085.1(8) $Å^3$	2349.6(6) $Å^3$
Z	4	8
Density (calculated)	4.251 Mg/m^3	4.119 Mg/m^3
Absorption coefficient	8.773 mm^{-1}	8.130 mm^{-1}
F(000)	4952	2760
Crystal size	0.23 × 0.13 × 0.09 mm^3	0.22 × 0.18 × 0.26 mm^3
Theta range for data collection	1.62 to 28.10°	1.77 to 28.14°
Reflections collected	21558	24268
Independent reflections	4644 [R(int) = 0.0429]	2789 [R(int) = 0.0328]
Completeness to theta = 37.00°	92.9 %	94.7 %
Refinement method	Full-matrix least-squares on F^2	
Data / restraints / parameters	4644 / 0 / 338	2789 / 0 / 200
Goodness-of-fit on F^2	1.030	1.066
Final R indices [I>2sigma(I)]	R_1 = 0.0326	R_1 = 0.0268
	wR_2 = 0.0705	wR_2 = 0.0640
R indices (all data)	R_1 = 0.0446	R_1 = 0.0316
	wR_2 = 0.0746	wR_2 = 0.0686
Largest diff. peak and hole	1.588 and –0.979 $e.Å^{-3}$	3.007 and -1.111 $e.Å^{-3}$

$R1 = \Sigma(|F_o|-|F_c|)/\Sigma|F_o|$; $wR2 = [\Sigma[w(F_o^2 - F_c^2]/ [\Sigma(w|F_o|^2)^2]^{1/2}$

Table 4-2. Atomic coordinates ($\times 10^4$) and equivalent isotropic displacement parameters ($Å^2 \times 10^3$) for $Co_{19}Al_{45}Si_{10-x}$ (x = 0.13). Estimated standard deviations are in parentheses.

	Wyckoff site	x	y	z	U(eq)
Co(1)	8*f*	752(1)	4023(1)	5417(1)	7(1)
Co(2)	8*f*	1790(1)	5896(1)	8002(1)	5(1)
Co(3)	8*f*	6144(1)	9017(1)	9009(1)	5(1)
Co(4)	8*f*	3150(1)	7111(1)	6806(1)	7(1)
Co(5)	8*f*	3158(1)	4800(1)	6845(1)	8(1)
Co(6)	8*f*	4223(1)	5238(1)	9509(1)	8(1)
Co(7)	8*f*	4343(1)	2922(1)	9487(1)	10(1)
Co(8)	4*e*	5000	5969(1)	7500	7(1)
Co(9)	8*f*	1374(1)	7814(1)	9263(1)	5(1)
Co(10)	8*f*	3327(1)	4063(1)	8855(1)	10(1)
Al(1)	8*f*	2163(1)	7874(1)	6744(1)	7(1)
Al(2)	8*f*	4651(1)	7124(1)	8210(1)	8(1)
Al(3)	8*f*	-300(1)	4113(1)	3249(1)	7(1)
Al(4)	8*f*	2204(1)	3966(1)	6668(1)	6(1)
Al(5)	8*f*	1290(1)	7129(1)	7360(1)	8(1)
Al(6)	8*f*	1244(1)	3321(1)	7368(1)	8(1)
Al(7)	8*f*	2892(1)	6026(1)	10162(1)	9(1)
Al(8)	8*f*	3833(1)	6653(1)	5789(1)	7(1)
Al(9)	8*f*	2937(1)	6781(1)	8451(1)	8(1)
Al(10)	8*f*	3816(1)	5201(1)	5826(1)	8(1)
Al(11)	8*f*	4659(1)	4812(1)	8210(1)	7(1)
Al(12)	8*f*	1190(1)	3510(1)	4091(1)	8(1)
Al(13)	8*f*	1209(1)	4736(1)	7299(1)	8(1)
Al(14)	8*f*	4453(1)	6320(1)	10624(1)	13(1)
Al(15)	8*f*	1705(1)	4804(1)	4757(1)	15(1)
Al(16)	8*f*	-473(1)	3295(1)	5210(1)	10(1)
Al(17)	8*f*	3877(1)	3600(1)	7569(1)	9(1)
Al(18)	8*f*	6860(1)	7887(1)	9747(1)	16(1)
Al(19)	8*f*	477(1)	5325(1)	4826(1)	10(1)
Al(20)	4*e*	0	7681(1)	7500	16(1)

Table 4-2. (Continued) Atomic coordinates ($\times 10^4$) and equivalent isotropic displacement parameters ($Å^2 \times 10^3$) for $Co_{19}Al_{45}Si_{10-x}$ (x = 0.13). Estimated standard deviations are in parentheses.

	Wyckoff site	x	y	z	U(eq)
Al(21)	8*f*	2047(1)	6031(1)	6316(1)	12(1)
Al(22)	8*f*	619(1)	2684(1)	5059(1)	13(1)
Al(23)	8*f*	3722(1)	5964(1)	7587(1)	7(1)
Si(1)	8*f*	7485(1)	9093(1)	9607(1)	25(1)
Si(2)	4*e*	5000	8339(1)	7500	6(1)
Si(3)	8*f*	2516(1)	7828(1)	9157(1)	6(1)
Si(4)	4*e*	5000	9678(1)	7500	6(1)
Si(5)	8*f*	2814(1)	5184(1)	8259(1)	8(1)
Si(6)	8f	5249(1)	5928(1)	9655(1)	7(1)

$U_{(eq)}$ is defined as one third of the trace of the orthogonalized U_{ij} tensor.

Table 4-3. Anisotropic displacement parameters ($Å^2 \times 10^3$) for $Co_{19}Al_{45}Si_{10-x}$ (x = 0.13).

	U^{11}	U^{22}	U^{33}	U^{23}	U^{13}	U^{12}
Co(1)	10(1)	6(1)	7(1)	0(1)	6(1)	1(1)
Co(2)	7(1)	6(1)	6(1)	0(1)	4(1)	0(1)
Co(3)	5(1)	5(1)	5(1)	0(1)	2(1)	0(1)
Co(4)	7(1)	8(1)	9(1)	2(1)	5(1)	1(1)
Co(5)	9(1)	8(1)	10(1)	-2(1)	7(1)	-2(1)
Co(6)	8(1)	8(1)	9(1)	1(1)	5(1)	-1(1)
Co(7)	12(1)	7(1)	6(1)	0(1)	2(1)	4(1)
Co(8)	7(1)	7(1)	6(1)	0	4(1)	0
Co(9)	4(1)	5(1)	5(1)	1(1)	3(1)	1(1)
Co(10)	10(1)	10(1)	10(1)	0(1)	6(1)	1(1)
Al(1)	7(1)	6(1)	9(1)	0(1)	6(1)	1(1)
Al(2)	8(1)	8(1)	7(1)	0(1)	3(1)	0(1)
Al(3)	6(1)	8(1)	5(1)	-1(1)	2(1)	0(1)

Table 4-3. (Continued) Anisotropic displacement parameters ($Å^2 \times 10^3$) for $Co_{19}Al_{45}Si_{10-x}$ (x = 0.13).

	U^{11}	U^{22}	U^{33}	U^{23}	U^{13}	U^{12}
Al(4)	6(1)	6(1)	5(1)	1(1)	4(1)	-1(1)
Al(5)	8(1)	7(1)	6(1)	1(1)	4(1)	-1(1)
Al(6)	8(1)	7(1)	8(1)	1(1)	5(1)	0(1)
Al(7)	12(1)	8(1)	7(1)	1(1)	4(1)	-2(1)
Al(8)	8(1)	9(1)	6(1)	-1(1)	5(1)	0(1)
Al(9)	10(1)	8(1)	8(1)	0(1)	6(1)	1(1)
Al(10)	10(1)	8(1)	8(1)	0(1)	6(1)	0(1)
Al(11)	8(1)	7(1)	6(1)	1(1)	3(1)	0(1)
Al(12)	10(1)	7(1)	8(1)	1(1)	6(1)	1(1)
Al(13)	11(1)	6(1)	8(1)	-1(1)	6(1)	-1(1)
Al(14)	10(1)	12(1)	13(1)	-4(1)	5(1)	4(1)
Al(15)	22(1)	8(1)	12(1)	3(1)	8(1)	7(1)
Al(16)	11(1)	11(1)	9(1)	-2(1)	6(1)	3(1)
Al(17)	9(1)	8(1)	8(1)	0(1)	4(1)	0(1)
Al(18)	25(1)	8(1)	8(1)	1(1)	5(1)	7(1)
Al(19)	11(1)	10(1)	13(1)	1(1)	9(1)	-2(1)
Al(20)	8(1)	16(1)	14(1)	0	-1(1)	0
Al(21)	12(1)	15(1)	6(1)	0(1)	4(1)	-2(1)
Al(22)	18(1)	11(1)	23(1)	-3(1)	18(1)	0(1)
Al(23)	8(1)	7(1)	9(1)	0(1)	6(1)	0(1)
Si(1)	11(1)	34(1)	30(1)	2(1)	12(1)	0(1)
Si(2)	6(1)	8(1)	5(1)	0	3(1)	0
Si(3)	7(1)	5(1)	6(1)	0(1)	4(1)	1(1)
Si(4)	7(1)	6(1)	6(1)	0	4(1)	0
Si(5)	8(1)	7(1)	8(1)	-1(1)	5(1)	1(1)
Si(6)	8(1)	7(1)	9(1)	0(1)	6(1)	-1(1)

The anisotropic displacement factor exponent takes the form:
$-2\pi^2[h^2a^{*2}U^{11}+...+2hka^*b^*U^{12}]$

Table 4-4. Selected bond distances for $Co_{19}Al_{45}Si_{10-x}$ (x = 0.13).

Bond	Length, Å	Bond	Length, Å
Co(3)-Si(1)	2.3498(16)	Al(5)-Co(7)	2.4880(13)
Co(3)-Al(6)	2.5884(13)	Al(5)-Al(17)	2.8434(17)
Co(5)-Al(11)	2.5013(14)	Si(2)-Si(4)	2.562(2)
Co(5)-Co(6)	2.9744(8)	Si(3)-Co(9)	2.3587(12)
Al(2)-Al(23)	2.7160(17)	Si(3)-Al(7)	2.6517(17)
Al(2)-Si(6)	2.7666(17)	Si(4)-Co(3)	2.3825(10)

Table 4-5. Selected bond distances for $Co_5Al_{14}Si_2$.

Bond	Length, Å	Bond	Length, Å
Co(1)-Al(7)	2.4518(12)	Si(1)-Al(9)	2.6347(15)
Co(2)-Al(11)	2.5148(13)	Si(2)-Al(14)	2.5721(16)
Co(3)-Si(2)	2.3686(11)	Si(3)-Co(6)	2.6895(19)
Co(4)-Al(14)	2.4538(12)	Al(1)-Al(12)	2.9093(16)
Co(5)-Si(1)	2.3715(16)	Al(3)-Si(2)	2.6162(15)
Co(5)-Co(6)	2.8075(11)	Al(5)-Co(4)	2.4934(12)

Table 4-6. Atomic coordinates ($\times 10^4$) and equivalent isotropic displacement parameters ($Å^2 \times 10^3$) for $Co_5Al_{14}Si_2$. Estimated standard deviations are in parentheses.

	Wyckoff site	x	y	z	U(eq)
Co(1)	8*d*	7853(1)	3393(1)	956(1)	8(1)
Co(2)	8*d*	5213(1)	6648(1)	1010(1)	8(1)
Co(3)	8*d*	4393(1)	5755(1)	5767(1)	5(1)
Co(4)	8*d*	6560(1)	5021(1)	-918(1)	8(1)
Co(5)	4*c*	5460(1)	2500	3877(1)	8(1)
Co(6)	4*c*	7092(1)	2500	6132(1)	12(1)
Si(1)	4*c*	8753(1)	2500	1136(2)	9(1)
Si(2)	8*d*	4360(2)	4720(1)	5850(1)	7(1)
Si(3)	4*c*	4769(1)	7500	2858(2)	15(1)
Al(1)	4*c*	6942(1)	2500	2206(2)	10(1)
Al(2)	8*d*	6201(1)	5796(1)	1113(2)	6(1)
Al(3)	8*d*	7672(1)	4218(1)	-968(1)	6(1)
Al(4)	8*d*	4352(1)	5818(1)	2223(2)	8(1)
Al(5)	8*d*	2984(1)	5256(1)	4086(2)	9(1)
Al(6)	4*c*	5110(1)	7500	-778(2)	5(1)
Al(7)	8*d*	8365(1)	3134(1)	4048(2)	10(1)
Al(8)	8*d*	4655(1)	5307(1)	8726(2)	11(1)
Al(9)	8*d*	9607(1)	3415(1)	-287(2)	12(1)
Al(10)	8*d*	523(1)	3104(1)	1052(2)	8(1)
Al(11)	8*d*	8225(1)	3133(1)	-2400(2)	14(1)
Al(12)	8*d*	4395(1)	6352(1)	-1920(2)	13(1)
Al(13)	8*d*	3495(1)	6616(1)	4896(2)	17(1)
Al(14)	8*d*	8918(1)	4173(1)	2089(2)	11(1)
Al(15)	8*d*	2900(1)	5708(1)	7494(2)	16(1)

$U_{(eq)}$ is defined as one third of the trace of the orthogonalized U_{ij} tensor.

Table 4-7. Anisotropic displacement parameters ($Å^2 \times 10^3$) for $Co_5Al_{14}Si_2$.

	U^{11}	U^{22}	U^{33}	U^{23}	U^{13}	U^{12}
Co(1)	10(1)	5(1)	10(1)	0(1)	-1(1)	0(1)
Co(2)	8(1)	7(1)	10(1)	2(1)	-1(1)	-1(1)
Co(3)	5(1)	4(1)	7(1)	0(1)	0(1)	0(1)
Co(4)	7(1)	9(1)	9(1)	-2(1)	1(1)	-2(1)
Co(5)	8(1)	5(1)	10(1)	0	1(1)	0
Co(6)	11(1)	8(1)	15(1)	0	-2(1)	0
Si(1)	8(1)	6(1)	13(1)	0	2(1)	0
Si(2)	7(1)	5(1)	9(1)	0(1)	0(1)	1(1)
Si(3)	21(1)	9(1)	16(1)	0	-3(1)	0
Al(1)	8(1)	7(1)	15(1)	0	1(1)	0
Al(2)	5(1)	4(1)	8(1)	-1(1)	0(1)	1(1)
Al(3)	8(1)	4(1)	6(1)	1(1)	0(1)	1(1)
Al(4)	8(1)	6(1)	10(1)	0(1)	0(1)	-2(1)
Al(5)	7(1)	10(1)	9(1)	1(1)	1(1)	-1(1)
Al(6)	7(1)	1(1)	7(1)	0	0(1)	0
Al(7)	10(1)	10(1)	10(1)	-2(1)	-1(1)	2(1)
Al(8)	14(1)	11(1)	9(1)	4(1)	-1(1)	-1(1)
Al(9)	13(1)	7(1)	15(1)	-2(1)	1(1)	-1(1)
Al(10)	5(1)	12(1)	9(1)	-1(1)	0(1)	0(1)
Al(11)	11(1)	18(1)	12(1)	-4(1)	2(1)	-6(1)
Al(12)	20(1)	8(1)	12(1)	-2(1)	-3(1)	0(1)
Al(13)	15(1)	15(1)	21(1)	0(1)	-4(1)	5(1)
Al(14)	6(1)	9(1)	18(1)	-5(1)	1(1)	-1(1)
Al(15)	9(1)	19(1)	20(1)	-9(1)	7(1)	-5(1)

The anisotropic displacement factor exponent takes the form:
$-2\pi^2[h^2a^{*2}U^{11}+...+2hka^*b^*U^{12}]$

Thermal Analysis:

Thermal gravimetric analysis (TGA) was performed on a Shimadzu TGA-50 thermal gravimetric analyzer. The sample was heated to 900 °C at a rate of 10 °C/min under flowing air, held at 900 °C for 10 min, and then cooled down to room temperature at the same rate.

Magnetic Characterization:

Magnetic susceptibility measurements were conducted on the polycrystalline samples of $Co_{19}Al_{45}Si_{10-x}$ (x = 0.13) and $Co_5Al_{14}Si_2$ using a Quantum Design MPMS SQUID magnetometer. EDS-analyzed crystals were ground into powder, which was sealed in kapton tape and placed into the magnetometer. The data were collected in the temperature range 3-300 K at 1000 G, while field dependent magnetic measurements, conducted at 5 K, were carried out in fields up to ± 55000 G. The magnetic contribution from kapton tape was subtracted for correction.

4-3. Results and Discussion

Synthesis:

$Co_{19}Al_{45}Si_{10-x}$ (x = 0.13) was found in an effort to explore the system V-Co-Al-Si using Al as the flux. Vanadium did not incorporate into the product and a new ternary phase $Co_{19}Al_{45}Si_{10-x}$ (x = 0.13) formed instead. The yield of the reaction was 70% based on the initial amount of cobalt element used. The side products were mainly unreacted vanadium and recrystallized Si. Several attempts to make this compound with only Co and Si in Al flux or by direct combination with an arc-welder were not successful. These attempts resulted in $Co_5Al_{14}Si_2$ which is also described here.

Crystal Structure of $Co_{19}Al_{45}Si_{10-x}$ (x = 0.13):

$Co_{19}Al_{45}Si_{10-x}$ (x = 0.13) crystallizes in the monoclinic space group *C2/c*, and its large unit cell contains 10 Co, 23 Al and 6 Si independent sites with a total of 296 atoms. All the atomic sites are ordered except for Si(1) which is only 90% occupied.

The very high structural complexity presents difficulties in describing this structure in a straightforward fashion. A careful examination reveals that no high-symmetry first-neighbor polyhedron can be found around any atomic site. One way to understand the structure is to inspect the Co(3), Co(8), Co(9), Si(3) and Si(6)-based polyhedra which are interpenetrating into each other (Figure 4-1). The Si-based framework, shown in Figure 4-2, is composed of alternating Si(3) and Si(6)-centered slabs along the *a*-axis. In order to simplify the description and obtain a better view of the structure, only the bonds between the center atoms (Si(3) and Si(6) atoms) and the surrounding atoms are shown. On the local scale two types of structural fragments are noteworthy. In the first fragment, the Si(3) atom is bonded to another Si(3) atom forming a Si dimer (Figure 4-3A), with the Si(3)-Si(3) bond distance of 2.528(2) Å. Although this Si-Si bond distance is longer than the sum of the metallic radii of silicon, it is comparable to those in the other intermetallics (2.523 Å in $Re_{24}Al_{102}Si_{12}$,[14] 2.518 Å in $FeAl_2Si$[15]). These two Si(3) atoms, together with two Co(9) atoms, form a Co_2Si_2 rhombus. This rhombus is surrounded by Al atoms, some serving to bridge the Si and Co atoms (Al(5), Al(7), Al(9), Al(12) and Al(17)), while others serving as links to the rest of the structure (Figure 4-3A).

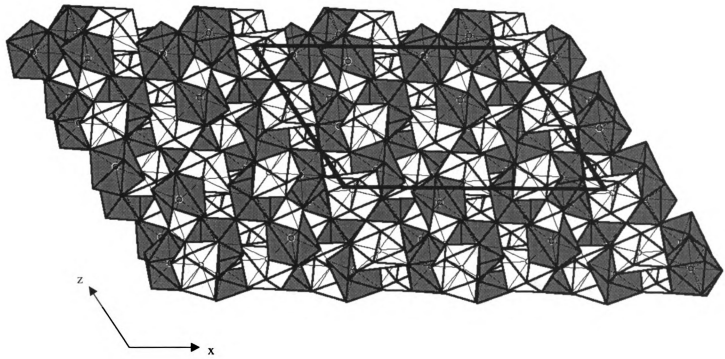

Figure 4-1. The structure of $Co_{19}Al_{45}Si_{10-x}$ (x = 0.13) in polyhedral representation viewed down the *b*-axis.

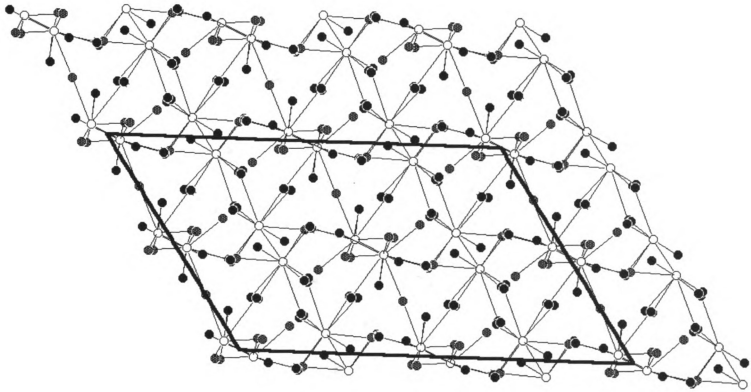

Figure 4-2. Structure of $Co_{19}Al_{45}Si_{10-x}$ (x = 0.13): framework composed of Si(3) and Si(6)-centered slabs. Black circle: Al; empty circle: Si; gray circle: Co.

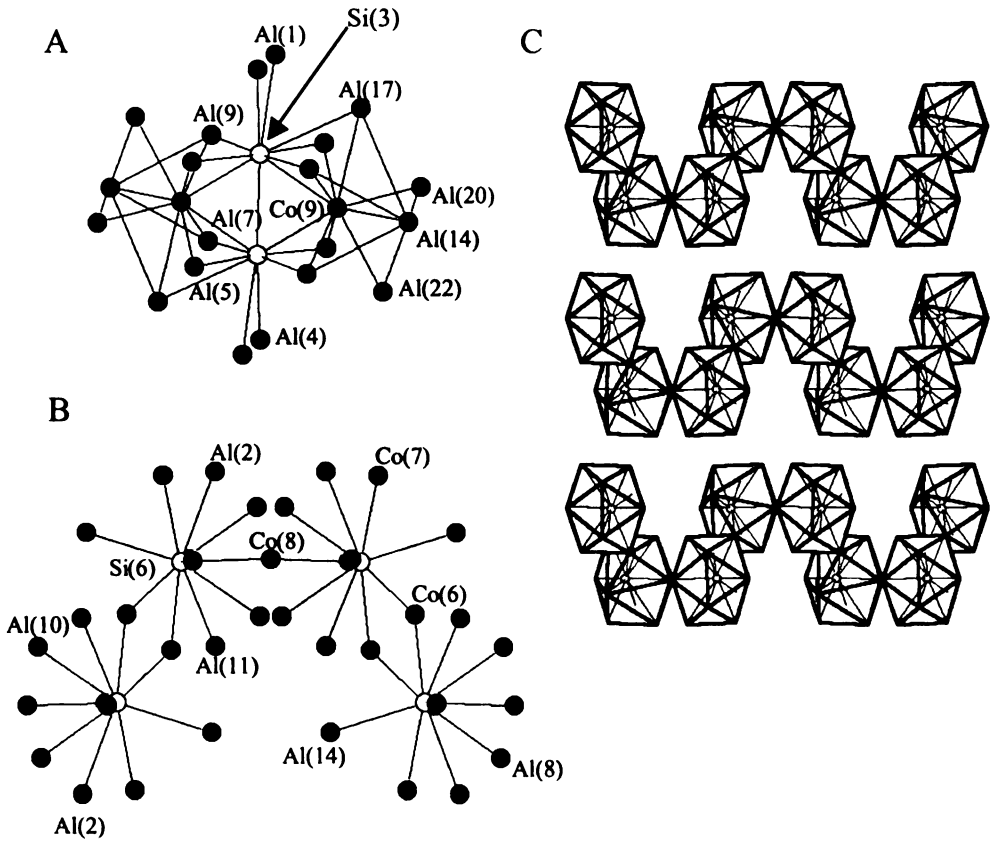

Figure 4-3. Structure of $Co_{19}Al_{45}Si_{10-x}$ (x = 0.13): (A) Two Si(3)-centered polyhedra joined via bridging Co(9) atoms to form a dimer. Si(3)-Si(3) distance: 2.528(2) Å. (B) The connectivity mode of Si(6)-centered dimers. (C) Extended organization of Si(6)-centered polyhedra forming a strongly correlated layer.

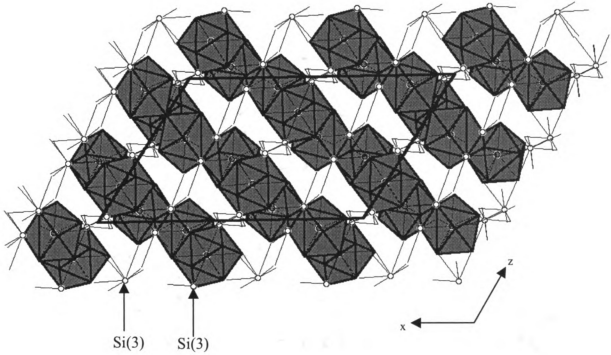

Figure 4-4. Structure of $Co_{19}Al_{45}Si_{10-x}$ (x = 0.13): the polyhedral view of Co(3), Co(8) and Co(9) atoms connected by Si-based wire framework.

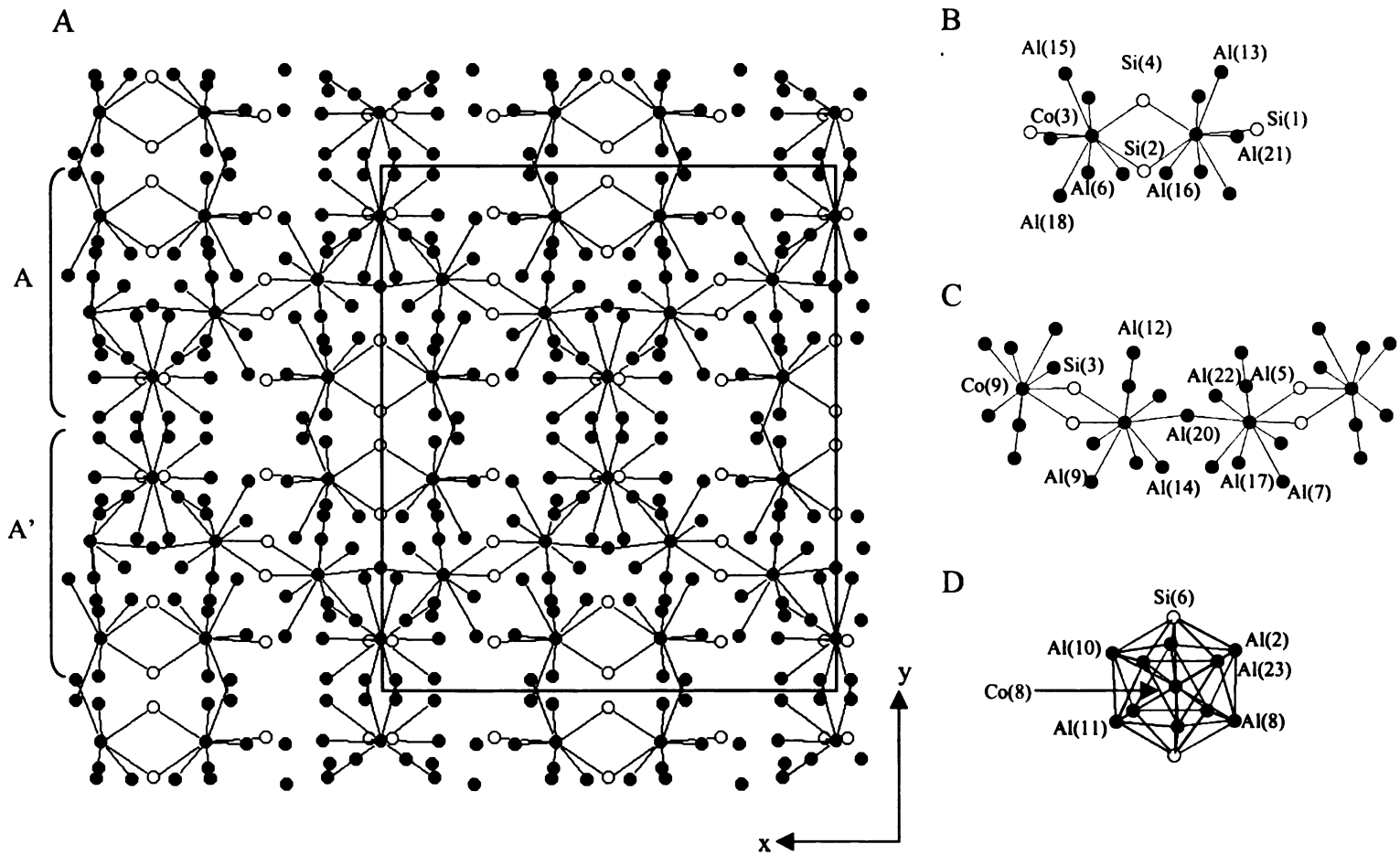

Figure 4-5. Structure of $Co_{19}Al_{45}Si_{10-x}$ (x = 0.13). (A) The layered sub-structure of Co(3), Co(8) and Co(9) polyhedra viewed down the *c*-axis. (B) The connectivity mode of Co(3)-centered clusters. (C) The connectivity mode of Co(9)-centered polyhedra. (D) The coordination environment of Co(8) atom.

Figure 4-3B depicts the Si(6)-centered polyhedra which conjoin with each other in similar but not identical fashion to Si(3). In this fragment, two Si(6) and two Co(6) atoms also form a Co_2Si_2 rhombus, however no Si-Si bonding exits with a Si(6)-Si(6) distance at 3.929 Å. The Si(6)-based dimeric polyhedra are linked to each other by bridging Co(8) atoms; when viewed down the *a*-axis, these Si(6)-centered polyhedra form infinite puckered layers, Figure 4-3C.

The overall organization of the structure of $Co_{19}Al_{45}Si_{10-x}$ (x = 0.13) can be described as layers defined by Co(3), Co(8) and Co(9) polyhedra and linked with each other by a Si(3) and Si(6)-based wire framework, Figure 4-4. The slabs composed of Co(3), Co(8) and Co(9) polyhedra, when viewed down the [001] direction, stack in A-A' fashion where layer A' is shifted relative to layer A along the *a* direction by a/2 (Figure 4-5A). The center of the layer is occupied by Co(9) polyhedra form a chain by vertex-linking. Both ends of the layer are capped by Co(3) and Co(8) polyhedra alternatively. Two Co(3) polyhedra are conjoined by bridging Si(2) and Si(4) atoms forming a Co_2Si_2 rhombus, Figure 4-5B. As seen in Figure 4-5C, the connectivity mode of Co(9) polyhedra is very similar to that of Si(6): the Co_2Si_2 rhombi composed of two Co(9) and Si(3) atoms are connected by bridging Al(20) atoms. Each Co(8) atom, is sitting on a site of icosahedral geometry which contains two Si(6), Al(8), Al(10), Al(11), Al(23) and Al(2) atoms (Figure 4-5D).

Crystal Structure of $Co_5Al_{14}Si_2$:

$Co_5Al_{14}Si_2$ has a different structure type which appears to be new and is also highly elaborate as in $Co_{19}Al_{45}Si_{10-x}$ (x = 0.13). This compound adopts the orthorhombic space group *Pnma*, which has 6 Co, 3 Si and 15 Al independent sites with a total of 168 atoms in the unit cell. Although $Co_{19}Al_{45}Si_{10-x}$ (x = 0.13) and $Co_5Al_{14}Si_2$ exhibit totally different structure types, they show notable similarities in the way the various polyhedra connect to each other. Both structural frameworks derive from the vertex-linkage of polyhedra with the Co_2Si_2 rhombus as the common feature in the structure.

Figure 4-6 depicts this structure in polyhedra of Al(1), Al(11), Al(15), Co(2), Co(3) and Co(5) atoms. One layer is based on Co polyhedra and the second is based on Al polyhedra. To have a clearer view of the layered structure character of $Co_5Al_{14}Si_2$, only the polyhedra of Co(2) and Co(3) are shown in Figure 4-7. This figure shows dimeric units linked to each other by sharing Al(4), Al(9) and Al(12) atoms along the *c* direction. The local structure around these units is shown in Figure 4-8. The manner in which the Co clusters connect with each other is very similar: two Co(2) polyhedra are connected by Si(3) and Al(6) atom; while two Co(3) polyhedra are bridged by two Si(2) atoms. Such linking patterns show resemblance to those of the Co(3) and Co(9) atoms formed in the structure of $Co_{19}Al_{45}Si_{10-x}$ (x = 0.13), which is an indication of the close structural relation of these two phases. Co(5) atoms, shown in Figure 4-8C, link the Co(2)-based dimers to form a "ribbon" running along the *c*-axis, using two Al(12) and one Al(6) atom as bridges.

The Al-based layer is shown in Figure 4-9. Interestingly, the Al(11) and Al(15)-based polyhedra form a similar layered structure as Co(2) and Co(3). However, a closer

view of Al(15)-based polyhedra reveals that they are different from those described before. As shown in Figure 4-10A, Al(15) polyhedra are linked by Al(5) atoms to form zig-zag chains along the *c* axis. The Al(11) polyhedra are condensed into dimers by Al(11)-Al(11) bonding (distance 2.9280(24) Å) with Co(6) atoms acting as bridging atoms, Figure 4-10B. This unit is surrounded by more Al atoms to form a cluster. Furthermore, Al(1) polyhedra are connected to this cluster to form a larger trimer-based cluster.

The local coordination geometries of Co(3), Co(8) and Co(10) in $Co_{19}Al_{45}Si_{10-x}$ (x = 0.13), Co(2), Co(3) and Al(11) in $Co_5Al_{14}Si_2$ are presented in Figure 4-11A & B. As we can see, the Co atoms are surrounded in a cage composed of Al and Si atoms. Such disposition is common in a variety of Al/Ga-rich binaries such as V_8Ga_{41},[16] WAl_{12}[17] and Co_2Al_9[18] which also exhibit large and complex structures. Compared to another ternary intermetallic $Co_4Al_{7+x}Si_{2-x}$,[9] the only significant connection with the title compounds is the trigonal prismatic coordination geometries of Co atoms. Another interesting feature about the structure of $Co_{19}Al_{45}Si_{10-x}$ and $Co_5Al_{14}Si_2$ is that, although there is no obvious evidence showing that they are approximants themselves, they show structural features that are reminiscent to some known quasicrystal approximants. For example, Figure 4-11C shows the first-neighbor coordination polyhedra of transition metals in the Mackay-type approximants $MnAl_6$,[19] α-FeAlSi[20] and o-Co_4Al_{13}.[21] It is evident that for most polyhedra in the structure of $Co_{19}Al_{45}Si_{10-x}$ and $Co_5Al_{14}Si_2$, we can find corresponding ones in the approximants, except that they are very distorted from ideal. In this sense, we might be able to consider these two phases as distorted Mackay-type approximants.

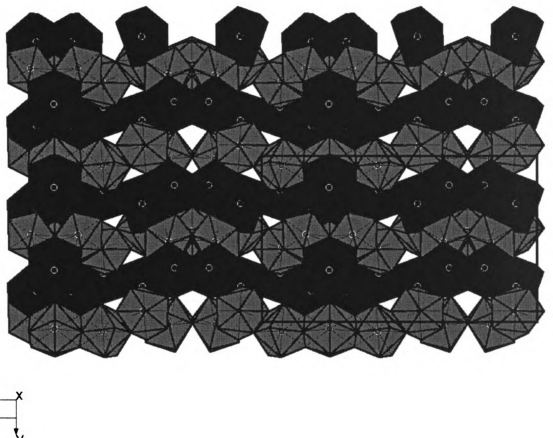

Figure 4-6. Structure of $Co_5Al_{14}Si_2$ in polyhedral representation down the *a*-axis. Black polyhedra: Al; gray polyhedra: Co.

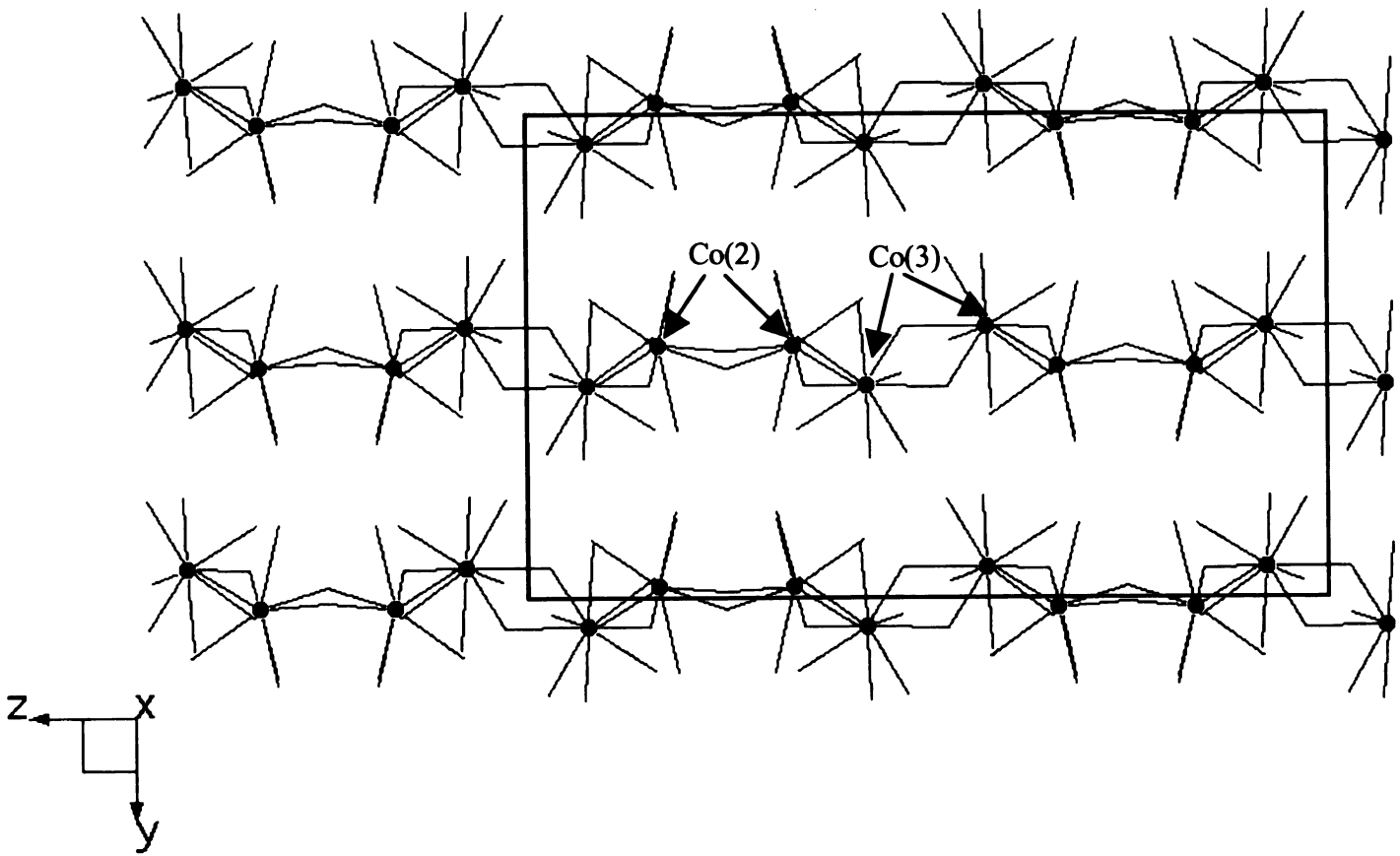

Figure 4-7. Structure of $Co_5Al_{14}Si_2$: the layered sub-structure of Co(2) and Co(3) polyhedra along the *b*-axis.

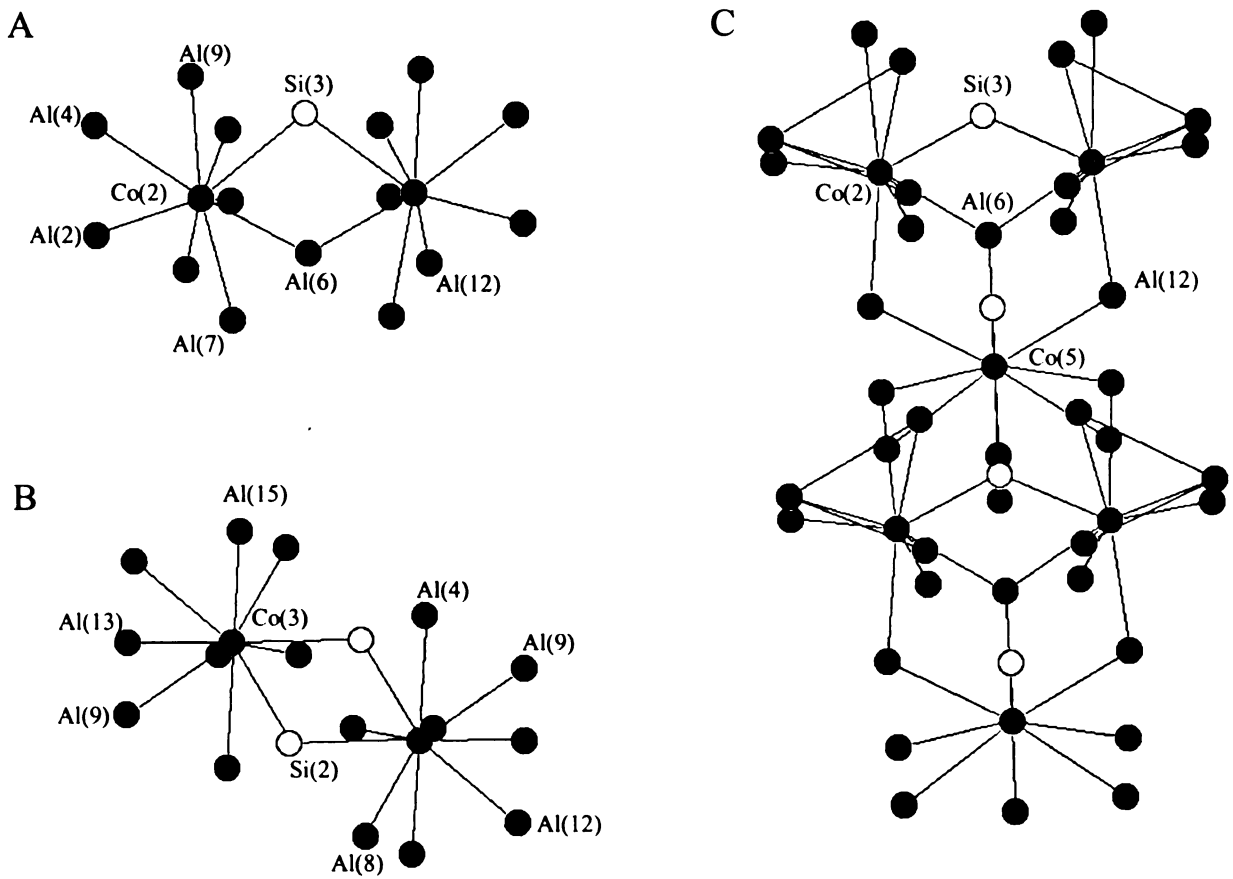

Figure 4-8. (A) Structure of the Co(2)-based dimeric fragment. (B) Structure of the Co(3)-based dimeric fragment. (C) The connectivity mode of Co(2) and Co(5) polyhedra along the *a*-axis.

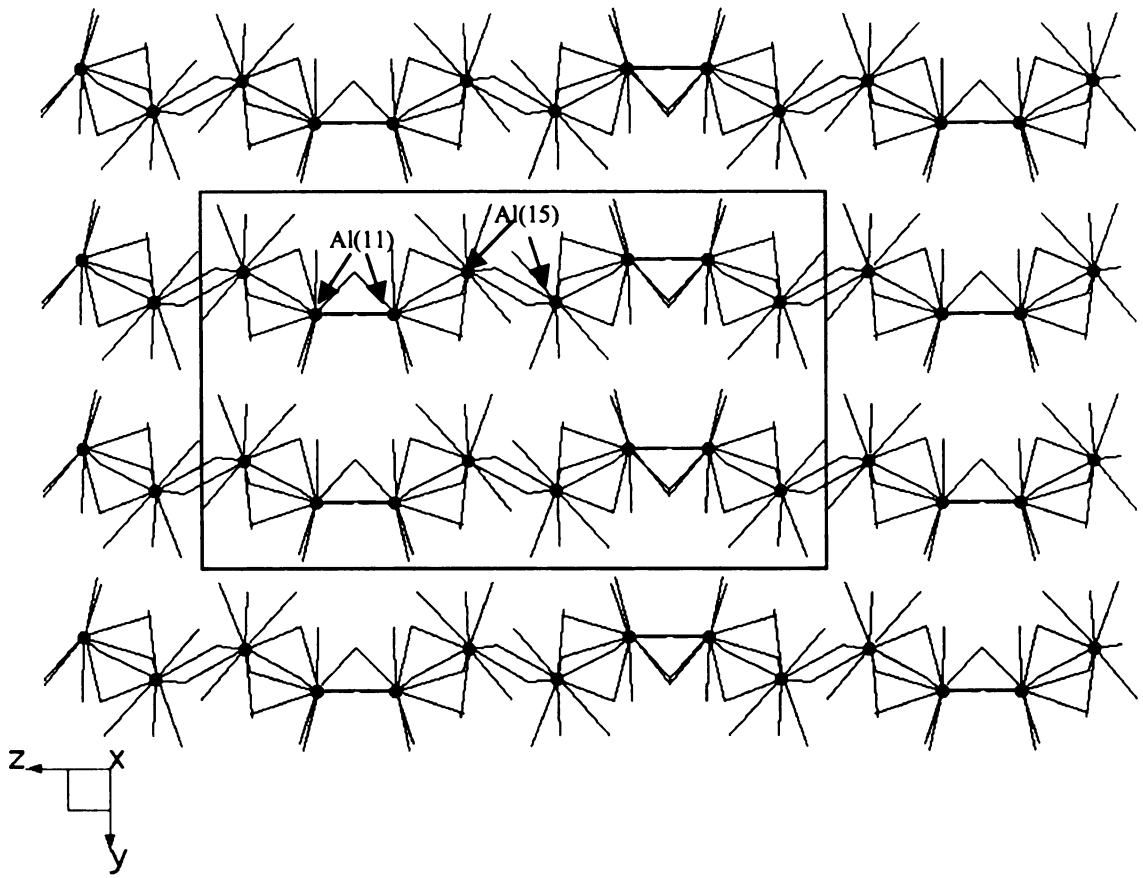

Figure 4-9. The layered sub-structure of Al(11) and Al(15) polyhedra in $Co_5Al_{14}Si_2$ along the *b*-axis.

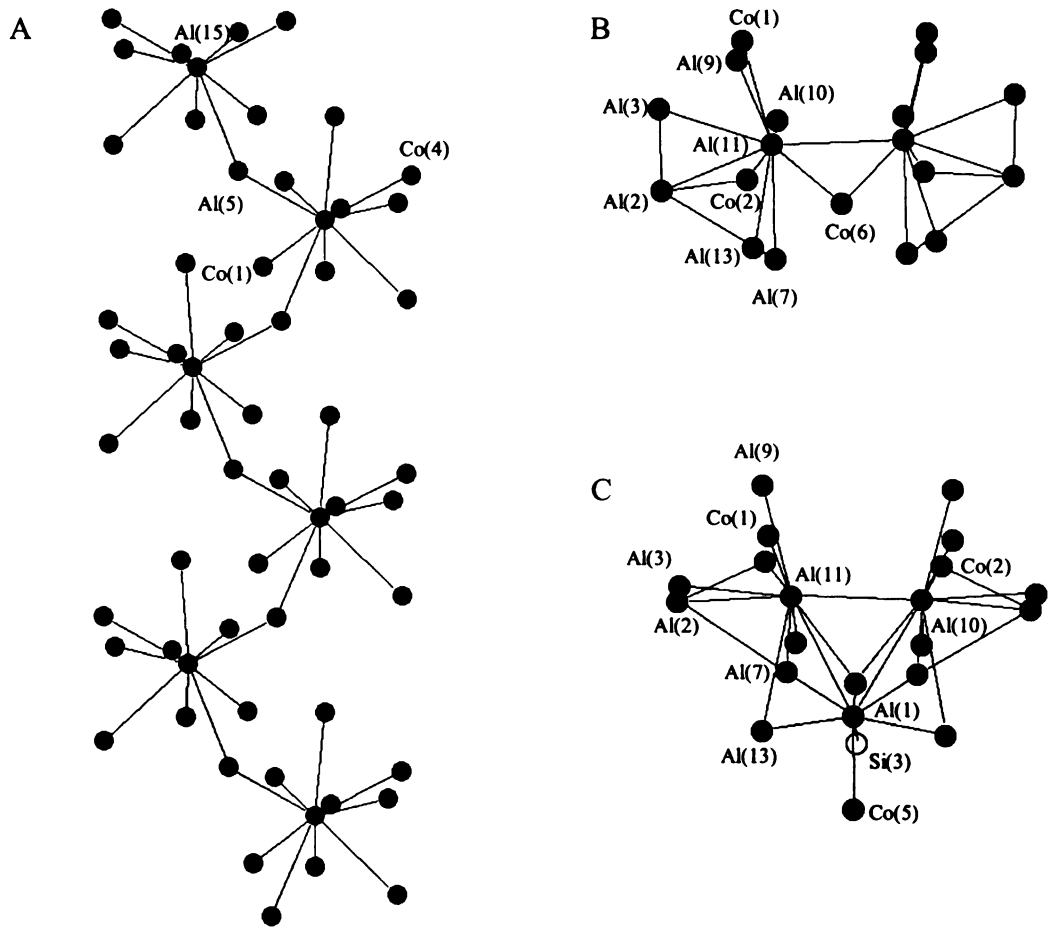

Figure 4-10. (A) The linkage of Al(15)-based polyhedra along the *a* axis. (B) Structure of the Al(11)-based dimer. (C) The fragment composed of Al(1) and Al(11) dimer.

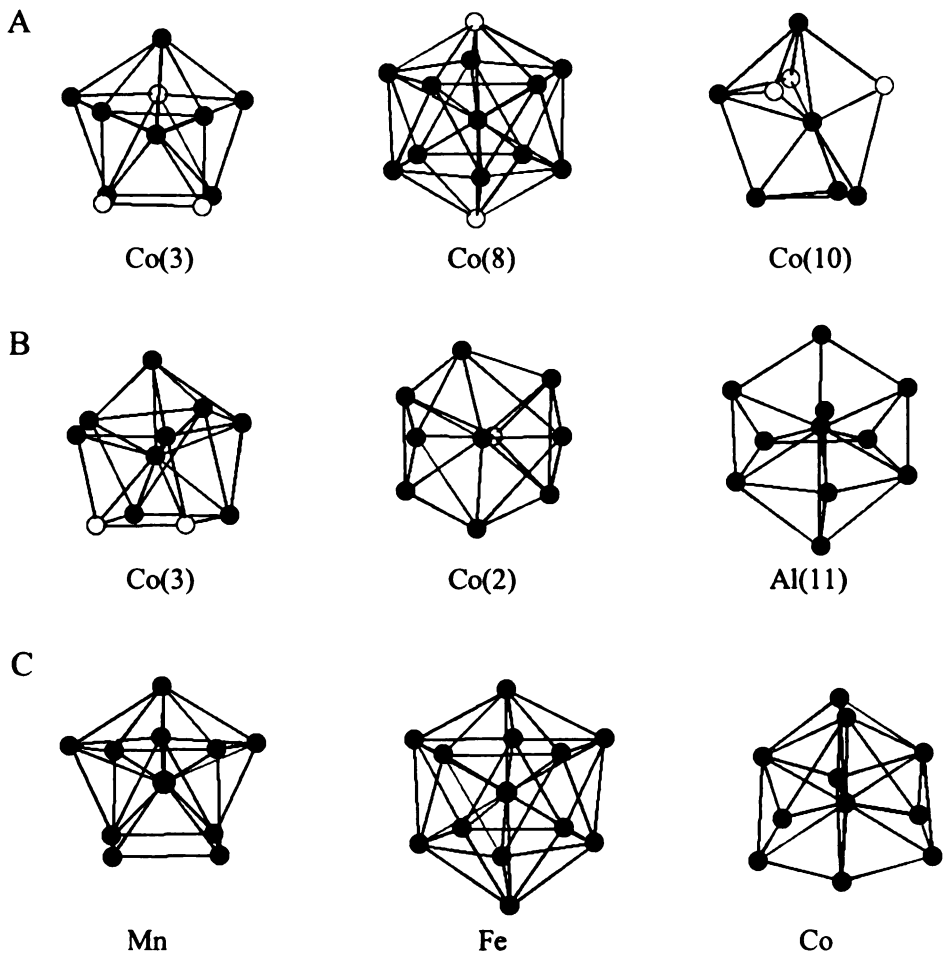

Figure 4-11. Coordination environments of (A) Co(3), Co(8), and Co(10) in $Co_{19}Al_{45}Si_{10-x}$ (x = 0.13). (B) Co(3), Co(2) and Al(11) in $Co_5Al_{14}Si_2$. (C) Selected transition metals in $MnAl_6$, α-FeAlSi and o-Co_4Al_{13}.

Physicochemical Properties:

A noteworthy property of $Co_5Al_{14}Si_2$ is its inertness to thermal attack. When crystals of this compound were exposed to air in a thermal gravimetric furnace environment, there was no obvious ignition point, and up to 900 °C only about 3% weight gain was observed (Figure 4-12A). To further investigate the oxidation resistance properties of this material, single crystals of $Co_5Al_{14}Si_2$ were loaded into an alumina crucible and annealed in air at 1000 °C for 5 hours. The shiny and clean surface of the crystals was covered by an oxide layer which is evidently seen by comparing the SEM images of $Co_5Al_{14}Si_2$ before and after annealing (Figure 4-12B, C & D). Elemental analysis by energy dispersive spectroscopy showed highly elevated levels of Al on the surface of the air-annealed crystals and the amount of Co and Si was less than 3%. This indicates that Al diffused outward and reacted with oxygen on the surface of the material to form Al_2O_3, which was not spallable and blocked further oxygen transportation into the material.

In aluminides, it is usually found that Al preferentially forms Al_2O_3 on the surfaces of alloys, such as NiAl and TiAl.[22] It has also been reported that addition of Al into $ZrSi_2$ and $MoSi_2$ helps to improve the oxidation resistance properties by forming a protective Al_2O_3 layer.[23] However, the presence of Al_2O_3 was not detected by the X-ray diffraction analysis of the material after annealing. Instead all observed Bragg peaks corresponded to the starting compound which implies that the structural integrity of $Co_5Al_{14}Si_2$ was not compromised by annealing at 1000 °C. Similar thermal resistant properties have been found in $RE_5Co_4Si_{14}$ (RE = Ho, Er, Tm and Yb)[24] in which a protective SiO_2 layer was formed and this intriguing behavior is due to the Si-rich nature

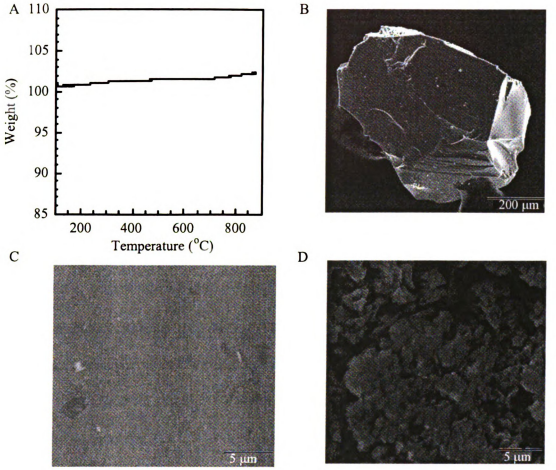

Figure 4-12. (A) Thermal gravimetric analysis of $Co_5Al_{14}Si_2$ in air. (B) Scanning electron micrograph of $Co_5Al_{14}Si_2$ before annealing. (C) (D) Close up view of $Co_5Al_{14}Si_2$ before and after annealing at 1000 °C for 5 hours.

of the crystal framework. The difference in the protecting layer between $Co_5Al_{14}Si_2$ and $RE_5Co_4Si_{14}$ might suggest higher oxygen affinity of aluminum than Co and Si. Although it has been observed that additions of Si to some aluminide alloys such as Ti_3Al result in a considerable reduction in the oxidation rate,[25] this fact does not explain why $Co_5Al_{14}Si_2$ shows better thermal properties than $Co_{19}Al_{45}Si_{10-x}$ (x = 0.13), since in $Co_5Al_{14}Si_2$ the Si level is lower.

Magnetic Properties:

Crystals were picked from the products and analyzed by EDS. Magnetic measurements were performed on polycrystalline samples ground from those selected crystals. Magnetic susceptibility measurements showed that both compounds exhibit ferromagnetic behavior with T_c around 260K, however very low χ_m values were observed (~0.015 emu / mol formula at 5K). In addition, although the magnetization determined at 5K does show hysteresis, the low saturation magnetic moment (0.025 B.M. / mol formula at 10000 Oe) indicates that the ferromagnetic behavior is probably caused by magnetic impurities. These may be nanocrystals of an unidentified compound occluding the grains of single crystals, however we could not identify any distinct phase by SEM analysis or X-ray diffraction analysis. Therefore we conclude that the pure bulk compounds are probably paramagnetic.

4-4. Conclusions

The Al flux method is a powerful tool to synthesize new intermetallic compounds. The compounds $Co_{19}Al_{45}Si_{10-x}$ (x = 0.13) and $Co_5Al_{14}Si_2$, grown from liquid Al, show exceptionally complex structures and large unit cells. The extended structures can be described in terms of distorted polyhedra of Co, Al and Si atoms. The resemblance of the current structures to the quasicrystal approximants, especially in the first-neighbor coordination environments, might be helpful in discovering new quasicrystals in the ternary Co-Al-Si system. $Co_5Al_{14}Si_2$ shows interesting thermal oxidation resistance up to 1000°C which is due to the formation of Al_2O_3 layer on the surface of the crystals.

References:

[1] (a) Kevorkijan, V. *Aluminum* **2002**, *78*, 469. (b) Satyanarayana, K. G.; Pillai, R. M.; Pai, B. C. *Trans. Indian Inst. Metals* **2002**, *55*, 115.

[2] (a) Suresh, S.; Mortensen, A.; Needleman, A. *Fundamentals of Metal-Matrix Composite*, Butterworth-Heinemann, Boston, 1993. (b) Ochiai, S. *Mechanical Properties of Metallic Composite*, Marcel Dekker, Inc., New York, 1994.

[3] Wang, H. M.; Lu, X. D.; Liu, Y. F.; Duan, G.; Cai, L. X.; Wang, C. M. *Mater. Sci. Forum* **2003**, *426-432*, 2551.

[4] Tokita, S.; Amano, T.; Okabayashi, M.; Nishida, I. A. *Mater. Sci. Forum* **1993**, *12*, 197.

[5] Tamura, N. *Phil. Mag. A* **1997**, *76*, 337.

[6] Frank, F. C.; Kasper, J. S. *Acta Cryst.* **1996**, *A52*, 125.

[7] Burger, K. O.; Wittmann, A.; Nowotny, H. *Monatsh. Chem.* **1962**, *93*, 9.

[8] German, N. V. *Bestn. L'vov. Univ. Chim.* **1981**, *23*, 61.

[9] Richter, K. W.; Prots, Y.; Grin, Yu. *Inorg. Chem.* **2005**, *44*, 4576.

[10] Kanatzidis, M. G.; Pöttgen, R.; Jeitschko, W. *Angew. Chem. Int. Edit.* **2005**, *44*, 6996.

[11] Saint, Version 4; Simens Analytical X-ray Instruments Inc., Madison, WI.

[12] SADABS, Sheldrick, G. M.; University of Göttingen, Göttingen, Germany.

[13] G.M. Sheldrick, 1995, SHELXTL. Structure Determination Programs, Version 5.0. Siemens Analytical X-ray Instruments, Inc. Madison, WI.

[14] Onogi, T.; Takeuchi, T.; Sato, H.; Mizutani, U. *J. Alloys Compd.* **2002**, *342*, 397.

[15] Geman, N. V.; Zavodnik, V. E.; Yanson, T. I.; Zarechnyuk, O. S. *Kristallografiya* **1989**, *34*, 738.

[16] Girgis, K.; Petter, W.; Pupp, G. *Acta Crystallogr., Sect. B: Struct. Sci.* **1975**, *B31*, 113.

[17] Adam, J.; Rich, J. B. *Acta Cryst.* **1954**, *7*, 813.

[18] Bostroem, M.; Rosner, H.; Prots, Y.; Burkhardt, U.; Grin, Yu. Z. *Anorg. Allg. Chem.* **2005**, *631*, 534.

[19] Stenberg, L.; Sjövall, R.; Lidin, S. *J. Solid State Chem.* **1996,** *124*, 65.

[20] Corby, R. N.; Black, P. J. *Acta Crystallogr.* **1977,** *33B,* 3468.

[21] Grin, J.; Burkhardt, U.; Ellner, M.; Peters, K. *J. Alloy Compd.* **1994,** *206,* 243.

[22] Grabke, H. J. *Mater. Sci. Forum* **1997,** *251-254,* 149.

[23] Perez, P.; Lopez, M. F.; Jimenez, J. A.; Adeva, P. *Intermetallics* **2000,** *8*, 1393.

[24] Salvador, J. R.; Malliakas, C.; Gour, J. R.; Kanatzidis, M. G. *Chem. Mater.* **2005,** *17,* 1636.

[25] Jazayeri-G, A.; Buckley, R. A.; Davies, H. A. *Mater. Sci. Tech.* **2002,** *18*, 1485.

CHAPTER FIVE

Exploratory Studies on the Ternary System RE/Ni/Al Employing Al as a Flux

PART I. Synthesis, Crystal Structure and Magnetic Properties of $RE_3Ni_5Al_{19}$ (RE = Sm, Dy, Er, Yb)

5-1-1. Introduction

The use of liquid Al as a high temperature solvent for exploratory synthesis has led to the discovery of many novel multinary intermetallics.[1] These phases exhibit complex structures and interesting physical properties. Examples include $RE_2TM_3Al_9$ (TM = Rh, Ir, Pd),[2] $YNiAl_4Ge_2$,[3] $RE_4Fe_{2+x}Al_{7-x}Si_8$ (RE = Ce, Pr, Nd, Sm),[4] $RE_8Ru_{12}Al_{49}Si_9(Al_xSi_{12-x})$ (RE = Pr, Nd, Sm, Gd, Tb, Er),[5] and $RE_2TMAl_6Si_4$ (RE = Gd, Tb, Dy; TM = Au, Pt).[6] The rich chemistry possible in the liquid metal environment can be exemplified by the family $RETM_2Al_{10}$ (TM = Mn, Re, Fe, Ru, Os). It has a homogeneous composition while four different crystal structure types are present which can be considered as stacking variants of each other. $REMn_2Al_{10}$ (RE = Y, La-Nd, Sm, Gd-Dy) and $RERe_2Al_{10}$ (RE = Ce, Pr, Sm) crystallize in the tetragonal $CaCr_2Al_{10}$ structure type;[7] $RETM_2Al_{10}$ (RE = Y, La-Nd, Sm, Gd-Lu; TM = Fe, Ru, Os) have the orthorhombic $YbFe_2Al_{10}$ structure type;[8] and the middle rare earth (Gd, Tb) and late rare earth (Ho-Lu) analogues of $RERe_2Al_{10}$ crystallize in a different stacking variant of the $YbFe_2Al_{10}$ type structure.[7a,9]

The ternary system RE/Ni/Al is probably one of the most extensively studied intermetallic systems. There are quite a few ternary families in this system reported in

the literature, examples include $RE_4Ni_6Al_{23}$ (RE = Ce, Sm),[10] $RENiAl_2$ (RE = Gd, Dy, Ho, Er),[11] $RENiAl_4$ (RE = La, Ce, Sm, Tb, Dy, Ho, Er, Tm),[11, 12] $RE_3Ni_6Al_2$ (RE = Y, Sm, Gd, Dy, Ho, Er),[13] $RENi_2Al_5$ (RE = Ce, Pr),[14] $RENi_4Al$ (RE = La, Ce, Pr, Nd, Sm, Gd, Dy, Ho, Er),[15] RENiAl (RE = Ce, Gd, Tb, Ho),[16] $RENi_3Al_9$ (RE = Gd, Dy, Er),[17] $RENi_2Al_3$ (RE = Pr, Nd)[18] and $RE_3Ni_5Al_{19}$ (RE = Gd, Yb).[19] RENiAl crystallizes in the hexagonal ZrNiAl structure type, and for most rare earth metals, low temperature ferromagnetic ordering has been observed.[20] Interestingly, it was found that the incorporation of hydrogen into the crystal lattice of RENiAl drastically reduced the magnetic ordering temperatures due to modification of the density of electronic states at the Fermi level.[21] YbNiAl was shown to be the first Yb-based example of a heavy-Fermion antiferromagnet with a Neel temperature T_N of 3 K.[22] Ferromagnetic ordering at low temperature was also observed for the $RENi_4Al$ family, and the location of the magnetic moments was identified to be within the hexagonal plane.[23] In the case of $CeNi_4Al$, mixed-valence behavior was observed by X-ray photoemission spectroscopy (XPS) and magnetic susceptibility measurements.[24]

Most of these RE/Ni/Al compounds were obtained by direct combination reactions using an arc-welder, and this stimulated us to study the RE/Ni/Al system using the less common Al flux method. Based on our experience, Al tends to serve as a reactive solvent, so ternary compounds are expected from this RE/Ni/Al system. In addition, the metal flux method facilitates the growth of high quality large single crystals, which not only make the structure determination relatively easier, they also allow anisotropic measurements of physical properties. Our investigations of the RE/Ni/Al system employing Al flux led to the discovery of compounds $RE_3Ni_5Al_{19}$ (RE = Sm, Dy,

Er, Yb) which crystallize in the orthorhombic $Gd_3Ni_5Al_{19}$ structure type.[19a] Among these compounds $Yb_3Ni_5Al_{19}$ was reported by Bauer and coworkers in 2004 using Al flux method and it exhibits intermediate valence behavior.[19b] We used different reaction conditions to form $Yb_3Ni_5Al_{19}$ from that of Bauer *et al*; additionally, our studies showed different magnetic behavior of this compound. In this section, we will describe the crystal growth, structure characterization and physical properties of $RE_3Ni_5Al_{19}$ (RE = Sm, Dy, Er, Yb).

5-1-2. Experimental Section

Reagents:

The following reagents were used as obtained: rare earth metals (RE = Sm, Dy, Er, Yb) (Cerac, 99.9%), Ni (99%, 325 mesh, Sargent, Buffalo Grove, IL), Al (Cerac, 99.5%, -20 mesh).

Synthesis:

In a nitrogen-filled glove box, 1 mmol RE metal (0.15 — 0.18 g), 2 mmol Ni (0.118 g) and 10 mmol Al (0.270 g) were combined in alumina crucibles. The crucibles were then placed into silica tubes (13 mm in diameter), which were sealed under vacuum (~10^{-4} Torr). The samples were heated to 1000 °C in 15 h, maintained at this temperature for 5 h, then cooled to 850 °C in 2 h. They were annealed at 850 °C for 3 d, followed by cooling down to 500 °C in 36 h. Finally the temperature was brought down to 50 °C in 10 h. The yield of the reaction for the Yb-analogue was ~50% with the side products

mainly $YbAl_3$ and $Yb_{1.1}Ni_3Al_{8.9}$[25]; while for the Sm-analogue the yield was 90% and $Sm_4Ni_6Al_{23}$ was the side product.[26]

Isolation:

The excess aluminum was removed by soaking the crucible in aqueous 5M NaOH solution overnight. The crystalline product remaining after the isolation procedure was rinsed with water and acetone. The crystals of $RE_3Ni_5Al_{19}$ crystallized in the form of needles. Single crystals were selected for elemental analysis, X-ray diffraction, and physical properties measurements.

Scanning Electron Microscopy and Elemental Analysis:

The crystals were picked and placed on a Scanning Electron Microscope (SEM) sample plate using carbon tape. Chemical compositions of the products were determined by Energy Dispersive Spectroscopy (EDS) performed on a JEOL JSM-35C SEM equipped with a NORAN EDS detector. Data were acquired by applying a 25 kV accelerating voltage with an accumulation time of 60 s. The atomic ratio for $Yb_3Ni_5Al_{19}$ was determined to be 3 : 5.55 : 19.61 for Yb : Ni : Al, which agreed well with the results derived from single crystal X-ray analysis. The SEM images of typical crystals of $Sm_3Ni_5Al_{19}$, $Er_3Ni_5Al_{19}$ and $Yb_3Ni_5Al_{19}$ are shown in Figure 5-1-1. The crystals were formed with rod or needle morphology, sometimes bundled together.

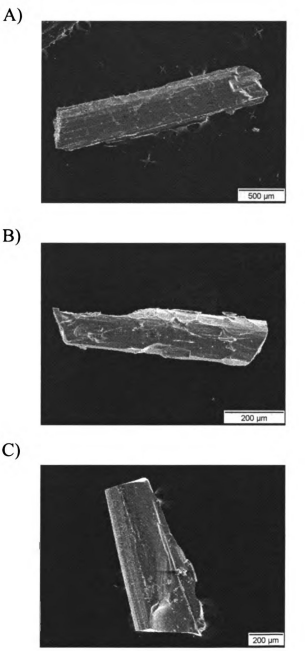

Figure 5-1-1. SEM images of typical crystals of $Sm_3Ni_5Al_{19}$, $Er_3Ni_5Al_{19}$ and $Yb_3Ni_5Al_{19}$ grown from Al flux.

X-ray Crystallography:

Single crystal X-ray diffraction data were collected for $RE_3Ni_5Al_{19}$ (RE = Sm, Dy, Er and Yb) at room temperature on a Bruker AXS SMART CCD X-ray diffractometer. The data collections (Mo Kα radiation, λ = 0.71073 Å) were acquired covering a full sphere of reciprocal space. Data acquisition and cell reduction were done with the SMART[27] software package and data processing was performed with the SAINTPLUS program.[28] An empirical absorption correction was applied to the data using the SADABS program.[29] The structures were solved using direct methods and refined with the SHELXTL package program.[30] Systematic absence conditions led to three possible space groups: $Cmc2_1$, *Cmcm* and *Ama*2. The $|E^2 - 1|$ value was 0.876 suggesting a centrosymmetric space group. So *Cmcm* was chosen and later structural refinement confirmed this choice. All atomic positions were refined anisotropically. Data collection parameters and refinement details for $Sm_3Ni_5Al_{19}$ and $Dy_3Ni_5Al_{19}$ can be found in Table 5-1-1. The refinement details for Er and Yb analogs are listed in Table 5-1-2. Atomic positions, displacement parameters and anisotropic displacement parameters for $RE_3Ni_5Al_{19}$ (RE = Sm, Dy, Er and Yb) are listed in Tables 5-1-3 and 5-1-4.

X-ray powder diffraction data were collected at room temperature on a CPS 120 INEL X-ray diffractometer (Cu Kα) equipped with position-sensitive detector. Experimental powder patterns were compared with the patterns calculated from the single crystal structure solution (by the CrystalDiffract software program[31]) to determine the phase purity.

Table 5-1-1. Selected crystal data and structure refinement details for $Sm_3Ni_5Al_{19}$ and $Dy_3Ni_5Al_{19}$.

Empirical formula	$Sm_3Ni_5Al_{19}$	$Dy_3Ni_5Al_{19}$
Formula weight	1257.22	1293.67
Crystal system	Orthorhombic	Orthorhombic
Space group	*Cmcm* (#63)	*Cmcm* (#63)
Unit cell dimensions	a = 4.1013(9) Å	a = 4.0747(4) Å
	b = 16.050(4) Å	b = 15.9632(16) Å
	c = 27.105(6) Å	c = 27.029(3) Å
Volume	1784.2(7) $Å^3$	1758.1(3) $Å^3$
Z	4	4
Density (calculated)	4.680 Mg/m^3	4.887 Mg/m^3
Absorption coefficient	15.783 mm^{-1}	18.747 mm^{-1}
F(000)	2292	2340
Crystal size	0.24 × 0.032 × 0.05 mm^3	0.22 × 0.18 × 0.26 mm^3
Theta range for data collection	1.50 to 28.05°	1.51 to 27.96°
Limiting indices	$-5 \le h \le 5$ $-20 \le k \le 20$ $-35 \le l \le 34$	$-5 \le h \le 5$ $-20 \le k \le 19$ $-35 \le l \le 35$
Reflections collected	9577	8481
Independent reflections	1228 [R(int) = 0.0380]	1169 [R(int) = 0.0313]
Completeness to theta = 37.00°	97.4 %	94.7 %
Refinement method	Full-matrix least-squares on F^2	
Data / restraints / parameters	1228 / 0 / 86	1169 / 0 / 86
Goodness-of-fit on F^2	1.328	1.440
Final R indices [I>2sigma(I)]	R_1 = 0.0256	R_1 = 0.0270
	wR_2 = 0.0577	wR_2 = 0.0675
R indices (all data)	R_1 = 0.0296	R_1 = 0.0280
	wR_2 = 0.0615	wR_2 = 0.0713
Largest diff. peak and hole	1.720 and –2.209 $e.Å^{-3}$	2.114 and -2.371 $e.Å^{-3}$

$R1 = \Sigma(|F_o|-|F_c|)/\Sigma|F_o|$; $wR2 = [\Sigma[w(F_o^2 - F_c^2]/ [\Sigma(w|F_o|^2)^2]^{1/2}$

Table 5-1-2. Selected crystal data and structure refinement details for $Er_3Ni_5Al_{19}$ and $Yb_3Ni_5Al_{19}$.

Empirical formula	$Er_3Ni_5Al_{19}$	$Yb_3Ni_5Al_{19}$
Formula weight	1307.95	1325.29
Crystal system	Orthorhombic	Orthorhombic
Space group	*Cmcm* (#63)	*Cmcm* (#63)
Unit cell dimensions	a = 4.0523(8) Å	a = 4.0573(2) Å
	b = 15.878(3) Å	b = 15.8745(9) Å
	c = 27.927(5) Å	c = 26.9365(15) Å
Volume	1732.6(6) $Å^3$	1734.92(16) $Å^3$
Z	4	4
Density (calculated)	5.014 Mg/m^3	5.074 Mg/m^3
Absorption coefficient	20.617 mm^{-1}	22.249 mm^{-1}
F(000)	2364	2388
Crystal size	0.20 × 0.12 × 0.15 mm^3	0.23 × 0.16 × 0.09 mm^3
Theta range for data collection	1.50 to 28.36°	1.51 to 28.23°
Limiting indices	$-5 \le h \le 5$	$-5 \le h \le 5$
	$-20 \le k \le 20$	$-20 \le k \le 20$
	$-35 \le l \le 35$	$-34 \le l \le 35$
Reflections collected	8740	9907
Independent reflections	1231 [R(int) = 0.0764]	1228 [R(int) = 0.0332]
Completeness to theta = 37.00°	97.5 %	98.2 %
Refinement method	Full-matrix least-squares on F^2	
Data / restraints / parameters	1231 / 0 / 86	1228 / 0 / 86
Goodness-of-fit on F^2	1.739	1.209
Final R indices [I>2sigma(I)]	R_1 = 0.0499	R_1 = 0.0217
	wR_2 = 0.1172	wR_2 = 0.0428
R indices (all data)	R_1 = 0.0533	R_1 = 0.0243
	wR_2 = 0.01371	wR_2 = 0.0434
Largest diff. peak and hole	5.790 and –2.757 $e.Å^{-3}$	1.335 and -2.178 $e.Å^{-3}$

$R1 = \Sigma(|F_o|-|F_c|)/\Sigma|F_o|$; $wR2 = [\Sigma[w(F_o^2 - F_c^2]/ [\Sigma(w|F_o|^2)^2]]^{1/2}$

Table 5-1-3. Atomic coordinates (Å × 10^4) and equivalent isotropic displacement parameters (Å^2 × 10^3) for $Sm_3Ni_5Al_{19}$ and $Dy_3Ni_5Al_{19}$.

Atom	Wyk.	x	y	z	$U_{(eq)}$*
Sm(1)	4*c*	0	3865(1)	2500	7(1)
Sm(2)	8f	-5000	6685(1)	3649(1)	6(1)
Ni(1)	8*f*	0	6597(1)	4581(1)	6(1)
Ni(2)	8*f*	-5000	5531(1)	5835(1)	8(1)
Ni(3)	4*c*	-5000	5450(1)	2500	7(1)
Al(1)	8*f*	0	5949(1)	5370(1)	9(1)
Al(2)	8*f*	0	5780(1)	2982(1)	9(1)
Al(3)	8*f*	0	7917(1)	4118(1)	8(1)
Al(4)	8*f*	-5000	7345(1)	4717(1)	8(1)
Al(5)	8*f*	0	3702(1)	3654(1)	9(1)
Al(6)	8*f*	-5000	2758(1)	3067(1)	10(1)
Al(7)	8*f*	-5000	4321(1)	5302(1)	9(1)
Al(8)	4*c*	-5000	6929(2)	2500	9(1)
Al(9)	8*f*	0	5364(1)	4001(1)	9(1)
Al(10)	8*f*	-5000	4649(1)	3265(1)	10(1)
Dy(1)	4*c*	0	3883(1)	2500	7(1)
Dy(2)	8*f*	-5000	6659(1)	3648(1)	6(1)
Ni(1)	8*f*	0	6595(1)	4575(1)	6(1)
Ni(2)	8*f*	-5000	5537(1)	5845(1)	8(1)
Ni(3)	4*c*	-5000	5454(1)	2500	7(1)
Al(1)	8*f*	0	5941(2)	5368(1)	9(1)
Al(2)	8*f*	0	5799(2)	2983(1)	9(1)
Al(3)	8*f*	0	7909(2)	4112(1)	8(1)
Al(4)	8*f*	-5000	7343(2)	4716(1)	8(1)
Al(5)	8*f*	0	3702(2)	3651(1)	9(1)
Al(6)	8*f*	-5000	2766(2)	3064(1)	9(1)
Al(7)	8*f*	-5000	4325(2)	5310(1)	9(1)
Al(8)	4*c*	-5000	6939(2)	2500	9(1)
Al(9)	8*f*	0	5369(2)	3993(1)	9(1)
Al(10)	8*f*	-5000	4650(2)	3259(1)	10(1)

$U_{(eq)}$ is defined as one third of the trace of the orthogonalized U_{ij} tensor.

Table 5-1-4. Atomic coordinates (Å × 10^4) and equivalent isotropic displacement parameters (Å^2 × 10^3) for $Er_3Ni_5Al_{19}$ and $Yb_3Ni_5Al_{19}$.

Atom	Wyk.	x	y	z	$U_{(eq)}$*
Er(1)	4*c*	0	3892(1)	2500	4(1)
Er(2)	8*f*	-5000	6663(1)	3647(2)	4(1)
Ni(1)	8*f*	0	6586(1)	4573(2)	4(1)
Ni(2)	8*f*	-5000	5540(1)	5853(2)	5(1)
Ni(3)	4*c*	-5000	5454(2)	2500	4(1)
Al(1)	8*f*	0	5930(3)	5373(2)	6(1)
Al(2)	8*f*	0	5801(3)	2984(2)	5(1)
Al(3)	8*f*	0	7907(3)	4110(2)	4(1)
Al(4)	8*f*	-5000	7348(3)	4713(2)	5(1)
Al(5)	8*f*	0	3698(3)	3645(2)	6(1)
Al(6)	8*f*	-5000	2770(2)	3063(2)	6(1)
Al(7)	8*f*	-5000	4334(2)	5316(2)	5(1)
Al(8)	4*c*	-5000	6941(4)	2500	6(1)
Al(9)	8*f*	0	5364(3)	3986(2)	6(1)
Al(10)	8*f*	-5000	4649(3)	3253(2)	6(1)
Yb(1)	4*c*	0	3912(1)	2500	5(1)
Yb(2)	8*f*	-5000	6664(1)	3646(1)	4(1)
Ni(1)	8*f*	0	6591(1)	4581(1)	4(1)
Ni(2)	8*f*	-5000	5534(1)	5850(1)	5(1)
Ni(3)	4*c*	-5000	5473(1)	2500	5(1)
Al(1)	8*f*	0	5937(1)	5377(1)	6(1)
Al(2)	8*f*	0	5826(1)	2983(1)	6(1)
Al(3)	8*f*	0	7904(1)	4105(1)	6(1)
Al(4)	8*f*	-5000	7347(1)	4710(1)	6(1)
Al(5)	8*f*	0	3700(1)	3642(1)	7(1)
Al(6)	8*f*	-5000	2785(1)	3062(1)	7(1)
Al(7)	8*f*	-5000	4327(1)	5317(1)	6(1)
Al(8)	4*c*	-5000	6968(2)	2500	7(1)
Al(9)	8*f*	0	5381(1)	3983(1)	7(1)
Al(10)	8*f*	-5000	4662(1)	3253(1)	6(1)

$U_{(eq)}$ is defined as one third of the trace of the orthogonalized U_{ij} tensor.

Table 5-1-5. Anisotropic displacement parameters ($Å^2$ x 10^3) for $Sm_3Ni_5Al_{19}$ and $Dy_3Ni_5Al_{19}$.

Atom	U^{11}	U^{22}	U^{33}	U^{23}	U^{13}	U^{12}
Sm(1)	8(1)	7(1)	6(1)	0	0	0
Sm(2)	6(1)	6(1)	5(1)	0(1)	0	0
Ni(1)	7(1)	6(1)	6(1)	0(1)	0	0
Ni(2)	8(1)	7(1)	9(1)	-1(1)	0	0
Ni(3)	8(1)	7(1)	6(1)	0	0	0
Al(1)	12(1)	10(1)	5(1)	3(1)	0	0
Al(2)	7(1)	14(1)	6(1)	-2(1)	0	0
Al(3)	9(1)	6(1)	9(1)	1(1)	0	0
Al(4)	7(1)	8(1)	8(1)	-2(1)	0	0
Al(5)	11(1)	8(1)	9(1)	0(1)	0	0
Al(6)	5(1)	5(1)	7(1)	0	0	4(1)
Al(7)	10(1)	12(1)	7(1)	2(1)	0	0
Al(8)	12(1)	8(1)	8(1)	0	0	0
Al(9)	9(1)	8(1)	11(1)	1(1)	0	0
Al(10)	10(1)	11(1)	7(1)	0(1)	0	0
Dy(1)	9(1)	5(1)	6(1)	0	0	0
Dy(2)	8(1)	5(1)	6(1)	0(1)	0	0
Ni(1)	8(1)	5(1)	6(1)	0(1)	0	0
Ni(2)	10(1)	5(1)	9(1)	0(1)	0	0
Ni(3)	10(1)	5(1)	6(1)	0	0	0
Al(1)	14(1)	8(1)	5(1)	2(1)	0	0
Al(2)	8(1)	13(1)	5(1)	-1(1)	0	0
Al(3)	9(1)	4(1)	9(1)	1(1)	0	0
Al(4)	8(1)	7(1)	9(1)	-3(1)	0	0
Al(5)	12(1)	6(1)	9(1)	1(1)	0	0
Al(6)	11(1)	9(1)	7(1)	2(1)	0	0
Al(7)	10(1)	6(1)	12(1)	0(1)	0	0
Al(8)	12(1)	6(1)	11(2)	0	0	0
Al(9)	10(1)	6(1)	12(1)	2(1)	0	0
Al(10)	12(1)	9(1)	9(1)	1(1)	0	0

The anisotropic displacement factor exponent takes the form:
$-2\pi^2[h^2a^{*2}U^{11}+...+2hka^*b^*U^{12}]$

Table 5-1-6. Anisotropic displacement parameters ($Å^2 \times 10^3$) for $Er_3Ni_5Al_{19}$ and $Yb_3Ni_5Al_{19}$.

Atom	U^{11}	U^{22}	U^{33}	U^{23}	U^{13}	U^{12}
Er(1)	6(1)	6(1)	0(1)	0	0	0
Er(2)	6(1)	6(1)	0(1)	0(1)	0	0
Ni(1)	5(1)	6(1)	0(1)	0(1)	0	0
Ni(2)	7(1)	6(1)	1(1)	-1(1)	0	0
Ni(3)	8(1)	5(1)	0(1)	0	0	0
Al(1)	10(2)	9(2)	0(2)	4(2)	0	0
Al(2)	6(2)	10(2)	0(2)	-1(2)	0	0
Al(3)	6(2)	6(2)	0(2)	1(2)	0	0
Al(4)	6(2)	8(2)	0(2)	-2(2)	0	0
Al(5)	7(3)	10(3)	0(3)	0	0	0
Al(6)	8(2)	7(2)	4(2)	2(2)	0	0
Al(7)	7(2)	7(2)	2(2)	-2(2)	0	0
Al(8)	7(3)	10(3)	0(3)	0	0	0
Al(9)	8(2)	7(2)	4(2)	2(2)	0	0
Al(10)	9(2)	7(2)	0(2)	1(2)	0	0
Yb(1)	6(1)	5(1)	3(1)	0	0	0
Yb(2)	5(1)	5(1)	4(1)	0(1)	0	0
Ni(1)	4(1)	4(1)	4(1)	0(1)	0	0
Ni(2)	6(1)	5(1)	5(1)	0(1)	0	0
Ni(3)	6(1)	5(1)	4(1)	0	0	0
Al(1)	10(1)	8(1)	1(1)	4(1)	0	0
Al(2)	5(1)	10(1)	4(1)	-1(1)	0	0
Al(3)	7(1)	6(1)	6(1)	0(1)	0	0
Al(4)	6(1)	6(1)	6(1)	-1(1)	0	0
Al(5)	8(1)	7(1)	6(1)	-1(1)	0	0
Al(6)	9(1)	7(1)	5(1)	0(1)	0	0
Al(7)	6(1)	4(1)	7(1)	0(1)	0	0
Al(8)	7(1)	7(1)	6(1)	0	0	0
Al(9)	7(1)	7(1)	8(1)	1(1)	0	0
Al(10)	8(1)	5(1)	7(1)	1(1)	0	0

The anisotropic displacement factor exponent takes the form:
$-2\pi^2[h^2a^{*2}U^{11}+...+2hka^*b^*U^{12}]$

Table 5-1-7. Bond distances (Å) for $RE_3Ni_5Al_{19}$ (RE = Sm, Dy, Er, Yb).

Bond	Distance	Bond	Distance
Sm(1)-Al(5) ×2	3.139(2)	RE(2)-Al(4)	3.099(2)
Dy(1)-Al(5)	3.125(3)		3.086(3)
Er(1)-Al(5)	3.099(4)		3.068(4)
Yb(1)-Al(5)	3.095(2)		3.063(2)
RE(1)-Al(6) ×4	3.1187(16)	RE(2)-Ni(1)	2.379(2)
	3.1066(18)		3.2296(9)
	3.095(3)		3.2137(16)
	3.1002(15)		3.2353(7)
RE(1)-Al(8)	3.107(3)	Ni(1)-Al(1)	2.379(2)
	3.103(4)		2.386(3)
	3.097(6)		2.393(5)
	3.086(3)		2.382(2)
RE(1)-Al(10) ×4	3.1762(17)	Ni(1)-Al(7) ×2	2.5433(14)
	3.139(2)		2.5308(16)
	3.108(3)		2.516(3)
	3.1048(16)		2.5128(13)
RE(1)-Ni(3)	3.2679(12)	Ni(2)-Al(5) ×2	2.7638(16)
	3.2320(12)		2.7349(19)
	3.203(2)		2.719(3)
	3.2023(10)		2.7322(15)
RE(2)-Al(2)	3.0742(12)	Ni(2)-Al(9) ×2	2.5429(14)
	3.044(2)		2.5360(16)
	3.028(3)		2.520(3)
	3.0126(15)		2.5356(13)

Table 5-1-7. (Continued) bond distances (Å) for $RE_3Ni_5Al_{19}$ (RE = Sm, Dy, Er, Yb).

Bond	Distance	Bond	Distance
RE(2)-Al(3)	3.1486(17)	Ni(3)-Al(2) ×4	2.4885(13)
	3.1157(19)		2.4819(15)
	3.092(3)		2.471(3)
	3.0844(15)		2.4747(12)
Ni(3)-Al(10) ×2	2.439(2)	Al(3)-Al(4) ×2	2.772(2)
	2.419(3)		2.763(3)
	2.396(4)		2.743(4)
	2.402(2)		2.7477(19)
Al(4)-Al(4) ×2	2.609(3)	Al(3)-Al(5) ×2	2.715(2)
	2.600(3)		2.702(2)
	2.594(5)		2.693(4)
	2.606(3)		2.6964(19)
Al(7)-Al(7)	2.725(4)	Al(4)-Al(7)	2.675(3)
	2.731(5)		2.664(3)
	2.714(8)		2.673(6)
	2.735(4)		2.657(3)
Al(7)-Al(9) ×2	2.834(2)	Al(5)-Al(10) ×2	2.762(2)
	2.817(3)		2.751(2)
	2.805(4)		2.739(4)
	2.809(2)		2.7473(19)
Al(6)-Al(8) ×2	2.888(2)		
	2.866(2)		
	2.852(4)		
	2.8433(19)		

Physical Properties Characterization:

Magnetic measurements were conducted on a single crystal of $Sm_3Ni_5Al_{19}$ and polycrystalline samples of $Er_3Ni_5Al_{19}$ and $Yb_3Ni_5Al_{19}$. Field-cooled and zero-field cooled dc magnetization measurements were performed for the above samples using a Quantum Design MPMS SQUID magnetometer. For polycrystalline samples, EDS-analyzed crystals were ground into powder, sealed in a kapton tape and placed into the magnetometer by using a straw. Thermal dependent data were collected in the temperature range of 5 ~ 400 K at 1000 G, while field dependent magnetic measurements, conducted at 5 K, were carried out in fields up to ± 55000 G. The magnetic contributions from the core diamagnetism and kapton tape were subtracted for correction.

Electrical resistivity was measured over the temperature range 5 K ~ 300 K using a four-probe dc technique with contacts made using silver paste on a pressed-pellet sample of $Sm_3Ni_5Al_{19}$. Single crystals of $Sm_3Ni_5Al_{19}$ were selected, ground into powder and pressed into a pellet of 3 mm length, 2 mm width and 0.2 mm thickness. The pellet sample was annealed at 350 °C for 3h. Thermopower data were collected on single crystals of $Sm_3Ni_5Al_{19}$ from 300 K to 400 K with a MMR Technologies, Inc. Seebeck measurement system.

5-1-3. Results and Discussion

Synthesis:

$Gd_3Ni_5Al_{19}$ — the first member belonging to the $RE_3Ni_5Al_{19}$ family, was synthesized by arc-melting stoichiometric amounts of the elements followed by annealing

at 800 °C for two weeks.[19a] Our systematic explorations on the system Yb/Ni/Al using Al as a flux led to the discovery of the second member of this family — $Yb_3Ni_5Al_{19}$. This phase is very stable and it was formed with a variety of Yb : Ni ratios from 1:1 to 1:2 to 2:1. The reaction with equal amount of Yb and Ni produced $Yb_3Ni_5Al_{19}$ in 70% yield, and the side products were mainly $YbAl_3$. Bauer has shown that $Yb_3Ni_5Al_{19}$ could be synthesized by loading equal amount of Yb and Ni in liquid Al, then heating the samples up to 1100 °C and slowly cooling down to 600 °C at which point excess Al was removed by centrifuging.[19b] However no yield or phase purity was given in the paper. Our experimental studies show that larger single crystals of $Yb_3Ni_5Al_{19}$ could be obtained when the ratio of Yb : Ni was 1 : 2 or 2 : 1, however under these conditions another ternary compound formed — $Yb_{1.1}Ni_3Al_{8.9}$, which is a new phase and will be described in Part II of this chapter.

The synthesis of the Sm-analogue is noteworthy. Reactions with equal amount of Sm and Ni (1 : 1) led to the formation of a pure phase of $Sm_4Ni_6Al_{23}$, which belongs to the family $RE_{2n+m}T_{4n+m}Al_{15n+4m}$ with $m = 2$, $n = 1$.[26] This family will be described in more detail in the crystal structure section. When extra amount of Ni was added to have a ratio of Sm : Ni as 1 : 2, powder X-ray diffraction indicated that the major phase was $Sm_3Ni_5Al_{19}$, shown in Figure 5-1-2A. Most experimental Bragg peaks match fairly well with the ones calculated from single crystal X-ray data of $Sm_3Ni_5Al_{19}$ except for a weak peak at 22° in 2θ. This peak belongs to $Sm_4Ni_6Al_{23}$, the other peaks of which overlap with the ones of $Sm_3Ni_5Al_{19}$. Even the reaction with stoichiometric amount of Sm and Ni (1:1.67) could not avoid this problem. $Sm_3Ni_5Al_{19}$ and $Sm_4Ni_6Al_{23}$ could not be distinguished by their crystal habits because both of them crystallize in needles.

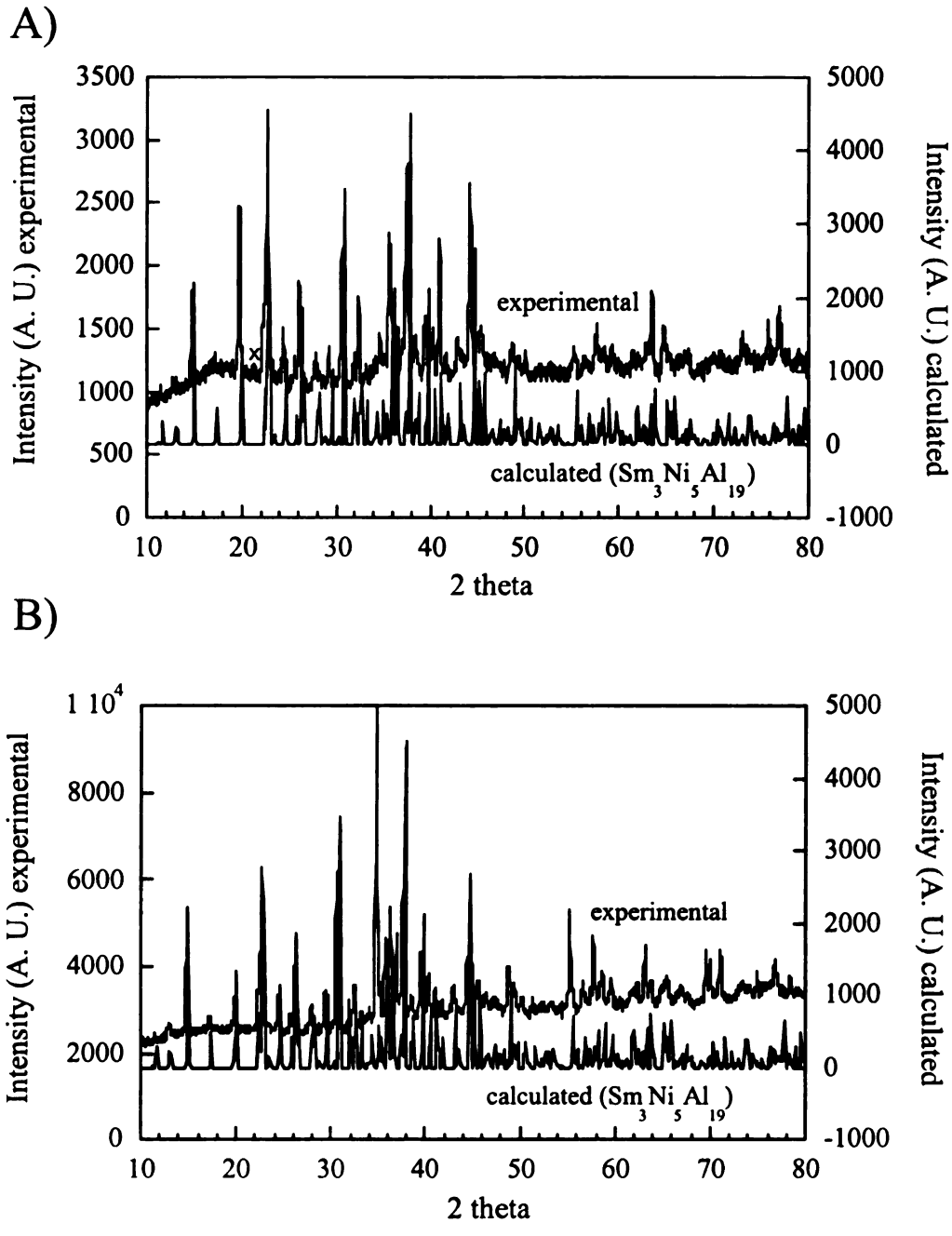

Figure 5-1-2. A) Powder X-ray diffraction pattern of $Sm_3Ni_5Al_{19}$ compared with the calculated pattern. B) Powder X-ray diffraction pattern of a single crystal of $Sm_3Ni_5Al_{19}$ compared with the calculated pattern.

Attempts to make the other rare earth analogs of $RE_3Ni_5Al_{19}$ were not successful so far; instead stable binaries such as $REAl_3$ and $Ni_{86}Al_{14}$ formed.

Crystal Structure:

All four compounds — $Sm_3Ni_5Al_{19}$, $Dy_3Ni_5Al_{19}$, $Er_3Ni_5Al_{19}$ and $Yb_3Ni_5Al_{19}$ crystallize in the $Gd_3Ni_5Al_{19}$ structure type.[19a] According to Gladyshevskii, $Gd_3Ni_5Al_{19}$ belongs to the series $RE_{2n+m}T_{4n+m}Al_{15n+4m}$, where n is the number of the $RE_2T_4Al_{15}$ slab and m is the number of the $RENiAl_4$ slab. The monoclinic structure of $RE_2T_4Al_{15}$, shown in Figure 5-1-3A, is hypothetical since no crystallographic data has been observed. The $RENiAl_4$ slab crystallizes in the $YNiAl_4$ structure type and is depicted in Figure 5-1-3D.[32] Both the $RE_2T_4Al_{15}$ slabs and the $YNiAl_4$ slabs can be considered to form from the stacking of RE-centered pentagonal prisms and T-centered trigonal prisms. $Gd_3Ni_5Al_{19}$ is the simplest member in this family with $m = 1$, $n = 1$. So the structure of $Gd_3Ni_5Al_{19}$ can be considered as intergrowth of two kinds of slabs, one deriving from the orthorhombic $YNiAl_4$ lattice and the other one corresponding to the translation unit of a hypothetical $RE_2T_4Al_{15}$ lattice. Another member of this family was identified as monoclinic $Y_4Ni_6Al_{23}$ with $n = 1$, $m = 2$, shown in Figure 5-1-3B.[33]

$RE_3Ni_5Al_{19}$ crystallizes in an orthorhombic space group *Cmcm* with two crystallographically independent RE sites, three Ni sites and ten Al sites. All atomic sites are fully occupied and no disorder is observed in the structure. It is evident from Tables 5-1-1 and 5-1-2 that from Sm to Dy to Er, the unit cell parameters decrease as expected (known as "Lanthanide Contraction"). However an anomaly is found in the Yb analogue

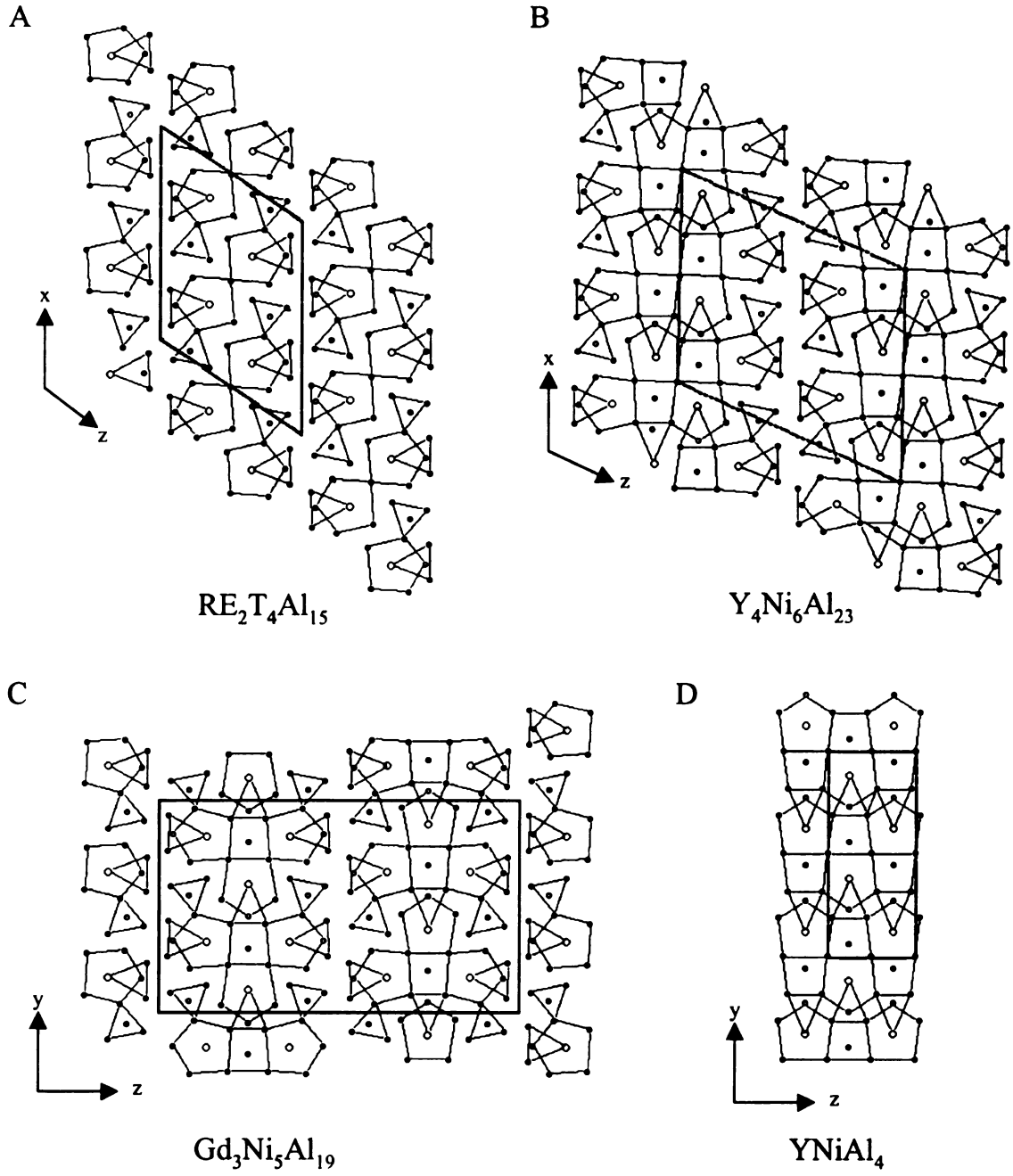

Figure 5-1-3. A) Structure of $RE_2Ni_4Al_{15}$ (hypothetical) along the *b*-axis. B) Structure of $Y_4Ni_6Al_{23}$ along the *b*-axis. C) Structure of $Gd_3Ni_5Al_{19}$ along the *a*-axis. D) Structure of $YNiAl_4$ along the *a*-axis. Large empty circles: rare earth element; medium gray circles: Ni; black circles: Al.

i. e. the cell volume of the Yb-analogue is larger than that of the Er analogue, suggesting that the Yb ions are in a divalent or at least an intermediate valence state which will be discussed in detail in the physical properties section.

For the structure description of $RE_3Ni_5Al_{19}$ we will use the Yb analogue as an example. The whole structure can be viewed in polyhedra of three Ni sites with Yb atoms sitting in the channels down the *a*-axis (Figure 5-1-4). The channel is composed of two Ni(1) polyhedra, four Ni(2) polyhedra and two Ni(3) polyhedra. These channels form columns along the *b*-direction by sharing Ni polyhedra. Each unit cell contains two such columns, rotated by 180° with respect to each other. Inside the channel, the polyhedra of Ni atoms are interconnected by bridging Al(6) atoms with Al(6)-Al(6) bond distance of 2.939(3) Å.

The local coordination environments of three Ni sites and two Yb sites are shown in Figure 5-1-5. All three Ni sites are sitting in matrixes composed of Al atoms with coordination numbers of 8, 9 and 7, respectively. The Ni(1) atom is bonded to eight Al atoms with Ni-Al bond distance ranging from 2.382(2) to 2.548(2) Å. The Ni(2) atom is sitting in a tri-capped trigonal prism composed of nine Al atoms with Ni-Al bond distance in a similar range as the Ni(1) atom. This tri-capped trigonal prism geometry is often seen in other transition metal aluminides, such as Co_2Al_5.[34] The Ni(3) atom is coordinated by seven Al atoms with one trianglular face composed of one Al(8) and two Al(2) atoms, the other face being a parallelogram containing two Al(2) and two Al(10) atoms.

The two Yb sites have similar coordination geometry: both of them are in a penta-capped pentagonal prism composed of thirteen Al atoms and two Ni atoms. The

geometry of Yb(2) atom, however is slightly more distorted than the Yb(1) atom (Figure 5-1-5D & E). The distance between Yb(1) and Al atoms ranges from 3.085(3) to 3.306(2) Å, while for Yb(2) atoms, the range is slightly broader which is from 3.0126(15) to 3.3516(20) Å. Obviously in this compound we cannot assess a size difference for the two Yb ions by comparing Yb-Al bond distances.

Physical Properties:

Initially magnetic measurements of $Sm_3Ni_5Al_{19}$ were conducted on polycrystalline samples ground from single crystals. Ferromagnetic behavior was found with magnetic susceptibility $\chi_m = 0.35\ \mu_B$ at 5 K. This behavior was also supported by the fact that single crystals were attracted to a magnet. To confirm this observation, a large crystal of $Sm_3Ni_5Al_{19}$ about 3 mg was selected for the magnetic measurements. Powder X-ray diffraction analysis on this crystal showed that every Bragg peak matched with the calculated one for $Sm_3Ni_5Al_{19}$ (Figure 5-1-2B). The magnetic measurements obtained from this single crystal indicated paramagnetic instead of ferromagnetic behavior. Thus the observed ferromagnetic behavior of the ground sample was most likely caused by impurities. To avoid Ni particles attaching on the surface of the crystals, the crystals were sonicated in acetone for ten minutes. After the crystals were dry, we found that fewer of them were attracted to the magnet. Attempts to further clean the crystals with aqua-regia failed since acid attacked the sample.

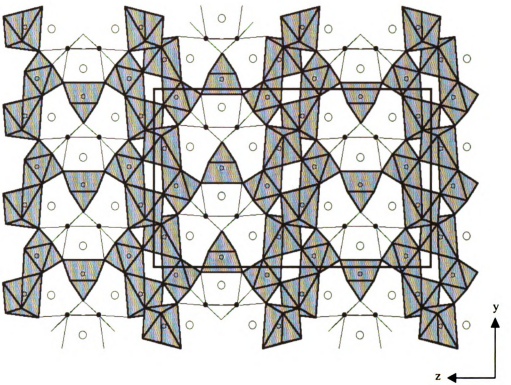

Figure 5-1-4. The structure of $Yb_3Ni_5Al_{19}$ in polyhedral view down the *a*-axis. Large circles: Yb; black circles: Al; gray circles: Ni.

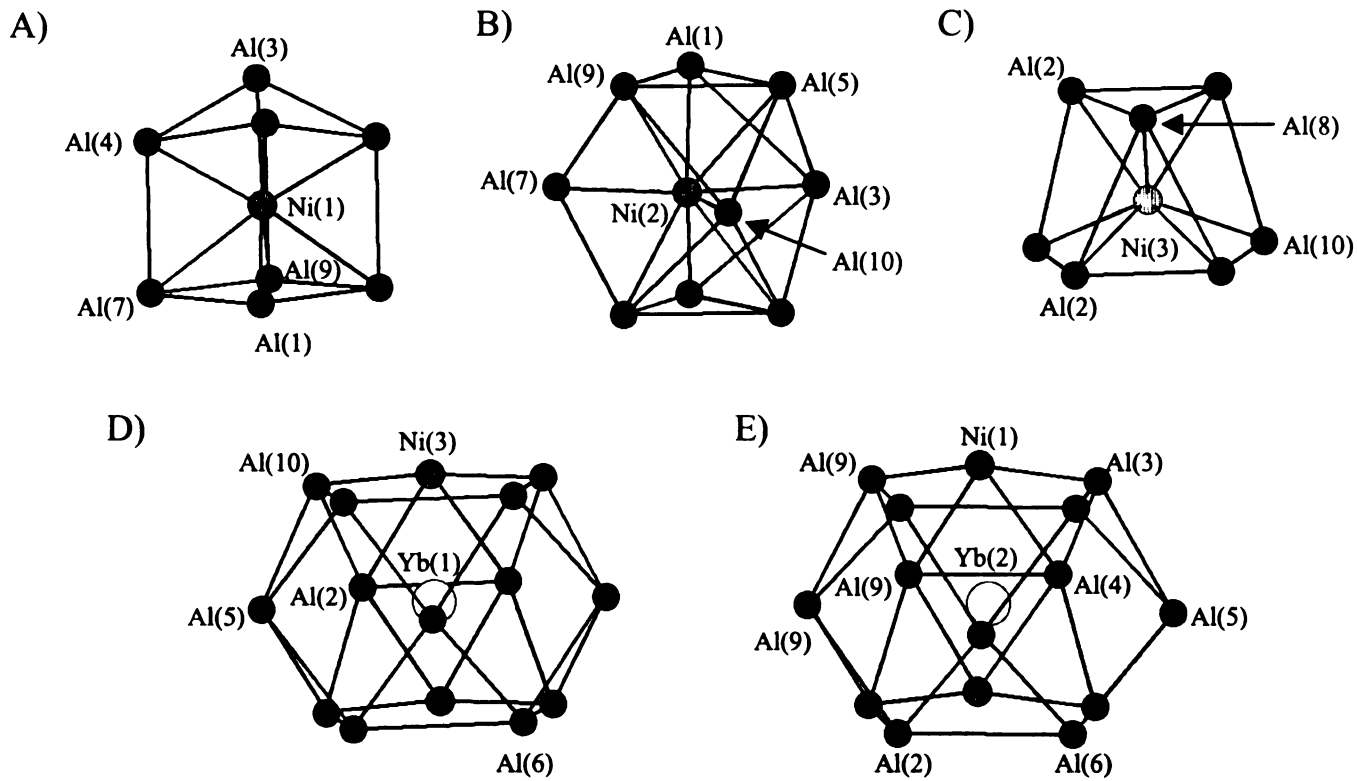

Figure 5-1-5. Coordination environments of Ni atoms (within 3.0 Å) and Yb atoms (within 4.0 Å).

The temperature dependent magnetic susceptibility of $Sm_3Ni_5Al_{19}$ measured on a single crystal sample with the *a*-axis perpendicular and parallel to the external magnetic field are shown in Figures 5-1-6A and 5-1-7A, respectively. With the applied field perpendicular to the *a*-axis, $Sm_3Ni_5Al_{19}$ first undergoes a ferromagnetic transition at ~150 K and then an antiferromagnetic transition at the low temperature about 5 K. Interestingly we did not observe the curvy feature in the inverse magnetic susceptibility data due to the close spacing of the $^6H_{5/2}$ and $^6H_{7/2}$ multiplet levels.[35] Instead, above 300 K, this material follows the Curie-Weiss Law with an effective magnetic moment of 2.36 μ_B. This number is much larger than the theoretical value for Sm^{3+} ions (μ_{eff} = 1.46 μ_B per formula), and the reason might be due to the effect of the low-lying excited levels.

The transition from ferromagnetic to antiferromagnetic state is supported by the field dependent magnetization data, Figure 5-1-6B. The moments are rapidly aligned with the applied field indicating a ferromagnetic state until 2000 G; then the magnetization increases more slowly in a linear function until 55000 G which is not enough to saturate the spins.

When the field is applied parallel to the *a*-axis of $Sm_3Ni_5Al_{19}$, no antiferromagnetic transition is found at low temperature; besides, the hump at 150 K indicates that the ferromagnetic interaction is much weaker (Figure 5-1-7A). However the higher temperature data is very similar to those obtained with the field perpendicular to the *a*-axis: a Curie-Weiss behavior is found between 320 K to 400 K with an effective magnetic moment of 2.45 μ_B. This orientation dependent behavior implies that the magnetic spins are confined to the *bc*-plane. When the external field is parallel to the *a*-

axis, i.e. perpendicular to the magnetically ordered spins, the spins are forced out of the plane by the external field which suppresses the ferro- or antiferromagnetic ordering.

Figure 5-1-8A shows the temperature dependence of the electrical resistivity $\rho(T)$ of $Sm_3Ni_5Al_{19}$, which indicates metallic behavior of this material. The resistivity value at room temperature is about 550 $\mu\Omega$·cm, and it decreases with decreasing temperature until it reaches a plateau of 400 $\mu\Omega$·cm below 20 K. The thermoelectric power, shown in Figure 5-1-8B, is about 3 μV/K at room temperature. The small magnitude of thermopower is also indicative of the metallic system of $Sm_3Ni_5Al_{19}$; and the positive values suggest a p-type material.

The temperature dependent magnetic susceptibility for $Er_3Ni_5Al_{19}$ is plotted in Figure 5-1-9A. This material shows Curie-Weiss behavior from 50 K to 400 K without obvious magnetic ordering at low temperatures. The μ_{eff} value, obtained from fitting the data to the Curie-Weiss law, is 16.2 μ_B (per formula), in excellent agreement with the theoretical value for Er^{3+} (16.6 μ_B). This indicates that Ni atoms do not contribute to the magnetic moment. The very low θ value (-1.85 K) implies weak antiferromagnetic interaction between the Er atoms. Figure 5-1-9B shows the isothermal magnetization behavior of $Er_3Ni_5Al_{19}$ at different temperatures (5 K and 100 K). In both cases, the magnetization increases gradually with applied external field which is characteristic of the paramagnetic material; and no sign of saturation is observed up to 55000 G.

The temperature dependent magnetic susceptibility for $Yb_3Ni_5Al_{19}$ is shown in Figure 5-1-10A. From the temperature range 5~300 K, this compound shows paramagnetic behavior; above 80 K, the magnetic susceptibility follows the Curie-Weiss law with an effective magnetic moment μ_{eff} = 6.77 μ_B. This value is smaller than the

theoretical value for Yb^{3+} ion (7.86 μ_B per formula), which could be an indication of mixed valent behavior of the Yb ions. This observation is also supported by the comparison of the unit cell parameters between $Er_3Ni_5Al_{19}$ and $Yb_3Ni_5Al_{19}$. If the Yb ions were in a 3+ oxidation state as the Er ions, we would expect to see a unit cell parameter contraction from the Er analogue to the Yb analogue; however the cell volume of the Yb analogue is larger than that of the Er analogue, implying either a divalent or an intermediate valence state of the Yb ions. The unusual negative large Weiss constant θ (-551.2 K) indicates strong antiferromagnetic interaction between the Yb ions; however, no magnetic ordering was observed down to 5 K. Bauer and his coworkers also claimed to observe intermediate valence behavior of Yb ions in $Yb_3Ni_5Al_{19}$:[19b] the calculated effective magnetic moment was found to be 7.36 μ_B, lower than the theoretical value of Yb^{3+} (7.86 μ_B); a broad hump in the temperature dependent magnetic susceptibility data was present at ~100 K, which is typical of intermediate valence system.[36] Our experimental results did not show the broad hump at low temperatures; and our effective magnetic moments (μ_{eff} = 6.77 μ_B, θ = -551.2 K) are slightly different from the results reported by Bauer ((μ_{eff} = 7.36 μ_B, θ = -731 K). These differences might be due to experimental error or differences in the samples because of different reaction conditions employed in the synthesis; however they all support the argument that Yb atoms in $Yb_3Ni_5Al_{19}$ are in intermediate valence states.

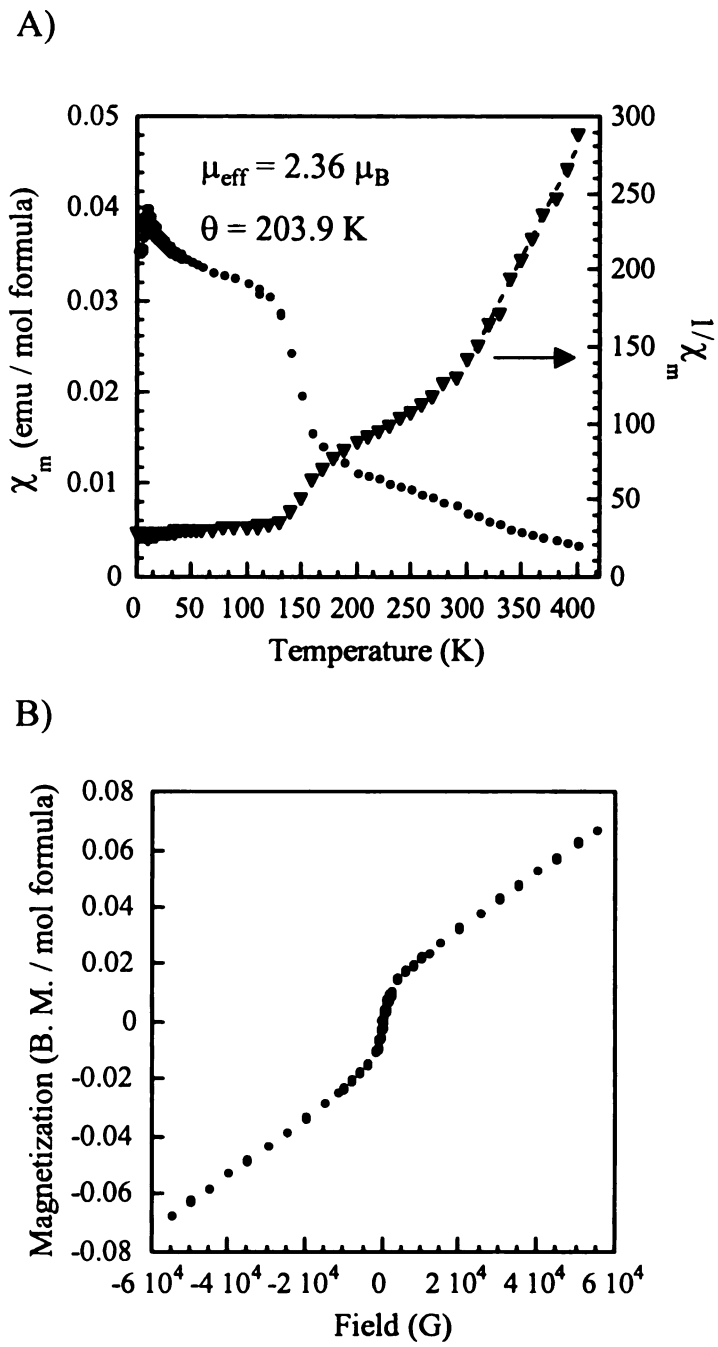

Figure 5-1-6. (A) Temperature dependent molar magnetic susceptibility and inverse magnetic susceptibility of $Sm_3Ni_5Al_{19}$. The susceptibility was measured with an applied magnetic field 1000 Gauss; (B) Field dependent magnetization for $Sm_3Ni_5Al_{19}$ at 5 K. The single crystal sample was oriented with the *a*-axis perpendicular to the external magnetic field.

A)

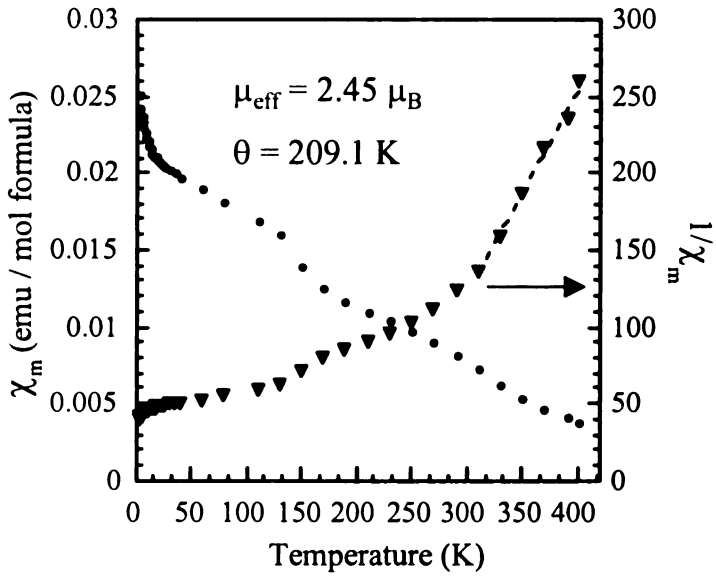

B)

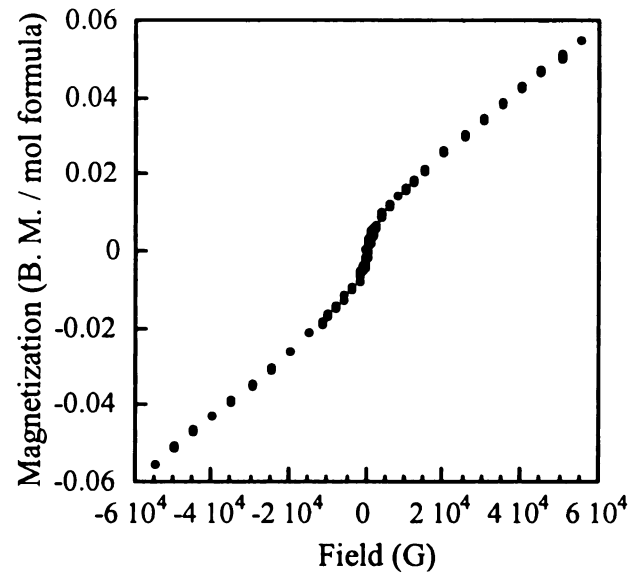

Figure 5-1-7. (A) Temperature dependent molar magnetic susceptibility and inverse magnetic susceptibility of $Sm_3Ni_5Al_{19}$. The susceptibility was measured with an applied magnetic field 1000 Gauss; (B) Field dependent magnetization for $Sm_3Ni_5Al_{19}$ at 5 K. The single crystal sample was oriented with the *a*-axis parallel to the external magnetic field.

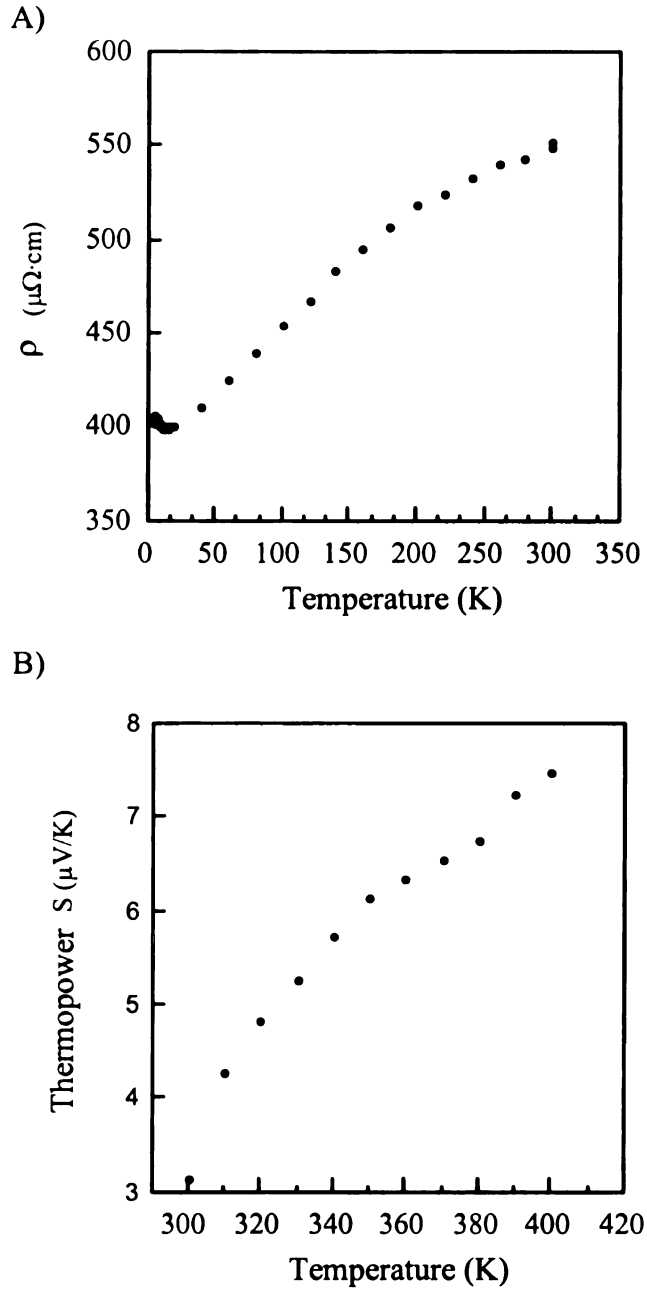

Figure 5-1-8. A) Temperature dependence of the electric resistivity for a polycrystalline pellet of $Sm_3Ni_5Al_{19}$. B) Temperature dependence of the thermoelectric power for a single crystal of $Sm_3Ni_5Al_{19}$.

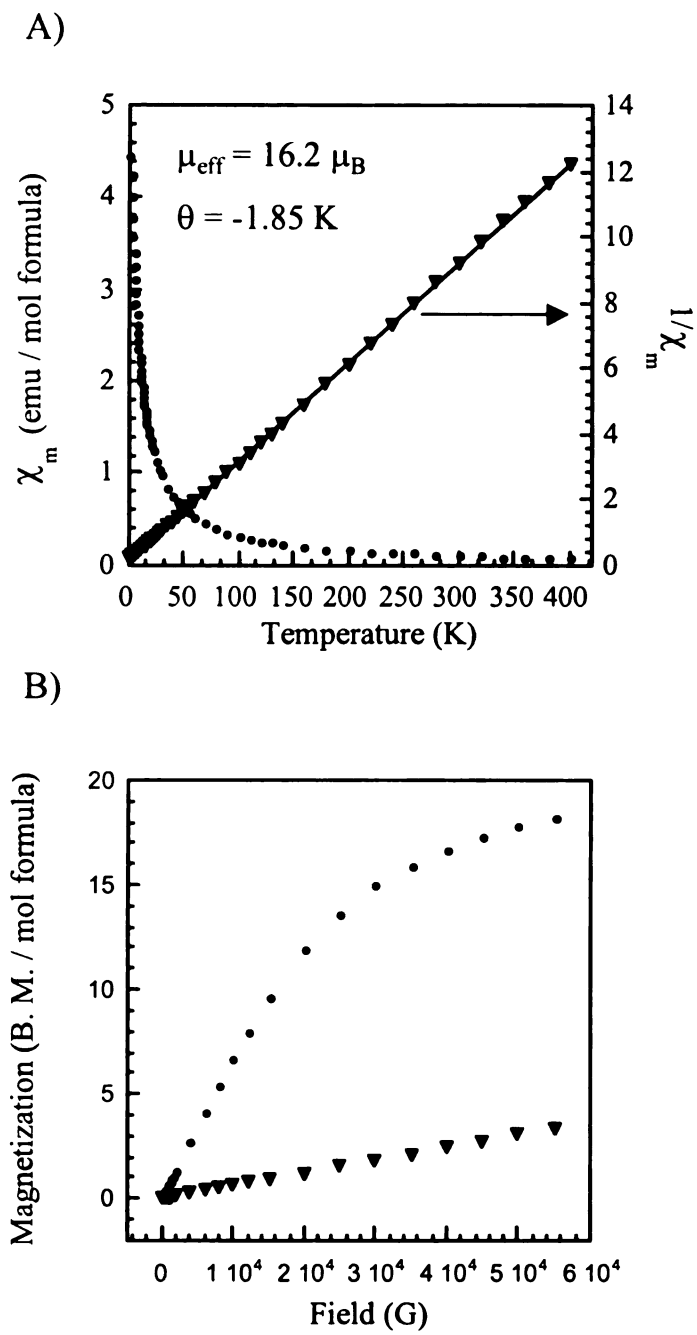

Figure 5-1-9. (A) Temperature dependent molar magnetic susceptibility and inverse magnetic susceptibility of a polycrystalline sample of $Er_3Ni_5Al_{19}$. The susceptibility was measured with an applied magnetic field 1000 Gauss; (B) Field dependent magnetization for $Er_3Ni_5Al_{19}$ at 5 K and 100 K.

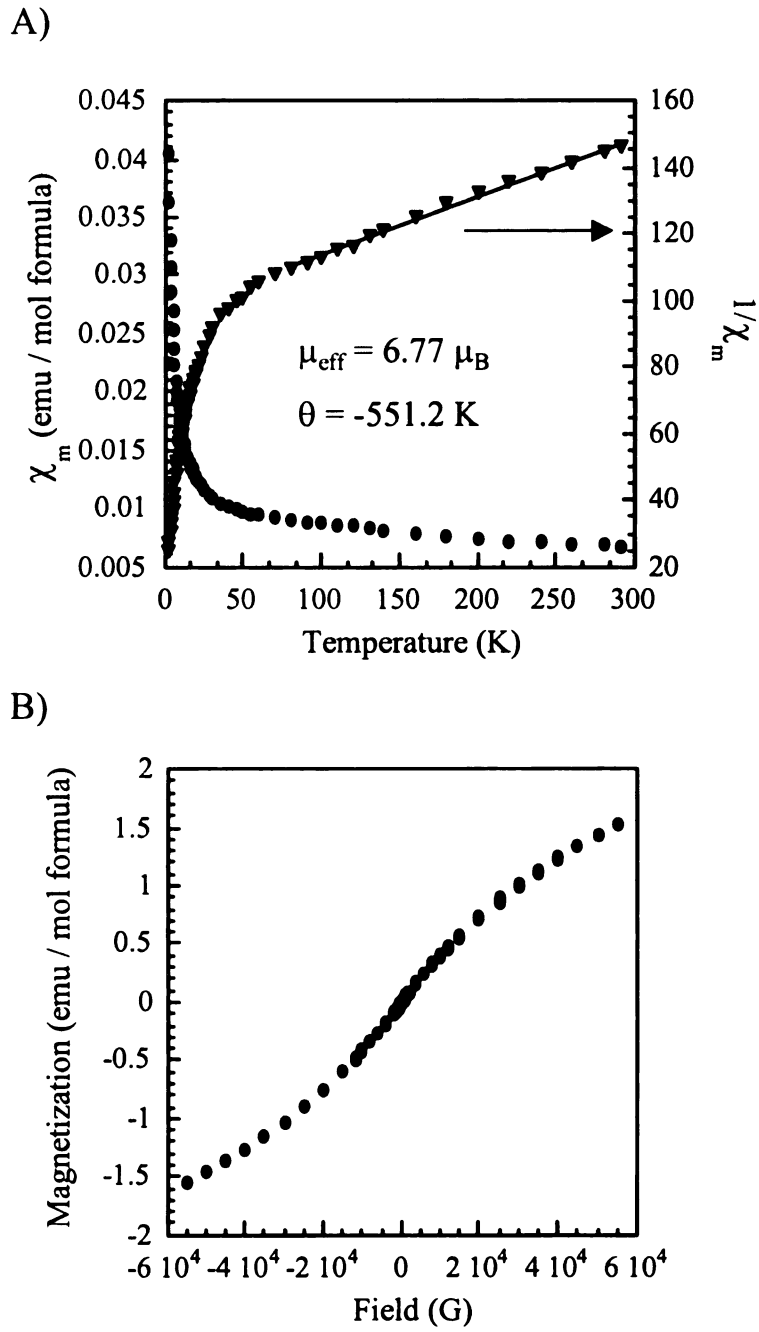

Figure 5-1-10. (A) Temperature dependent molar magnetic susceptibility and inverse magnetic susceptibility of polycrystalline sample of $Yb_3Ni_5Al_{19}$. The susceptibility was measured with an applied magnetic field 1000 Gauss; (B) Field dependent magnetization for $Yb_3Ni_5Al_{19}$ at 5 K.

5-1-4. Conclusions

We have presented in this part the compounds $RE_3Ni_5Al_{19}$ (RE = Sm, Dy, Er and Yb) synthesized by the molten Al method. This series of compounds crystallize in the *Cmcm* space group with the $Gd_3Ni_5Al_{19}$ structure type. The discovery of these compounds proves the power of the metal flux method to grow high quality large single crystals of intermetallics.

For all the compounds the magnetic moments are from the RE ions and the Ni atoms have filled d-orbitals. The Sm-analogue shows interesting magnetic properties: it has two different magnetic orderings occurring at 5 K (antiferro-) and 150 K (ferro-) with the applied magnetic field perpendicular to the *a*-axis. When the applied field is parallel to the *a*-axis, these transitions are much less obvious and we argue that this effect is because the spins are confined to the *bc*-plane. In the case of Er and Yb analogues, negative Weiss constant θ values imply antiferromagnetic interactions although no magnetic ordering is observed in both cases. Magnetic susceptibility measurements indicate that the Yb ions of $Yb_3Ni_5Al_{19}$ are in intermediate oxidation state of Yb^{2+} and Yb^{3+} which is in agreement with a previous report by Bauer.

References:

[1] Kanatzidis, M. G.; Pöttgen, R.; Jeitschko, W. *Angew. Chem. Int. Edit.* **2005**, *44*, 6996.

[2] Niermann, J.; Fehrmann, B.; Wolff, M. W.; Jeitschko, W. *J. Solid State Chem.* **2004**, *177*, 2600.

[3] Sieve, B.; Chen, X. Z.; Cowen, J.; Larson, P.; Mahanti, S. D.; Kanatzidis, M. G. *Chem. Mater.* **1999**, *11*, 2451.

[4] Sieve, B.; Sportouch, S.; Chen, X. Z.; Cowen, J. A.; Brazis, P.; Kannewurf, C. R.; Papaefthymiou, V.; Kanatzidis, M. G. *Chem. Mater.* **2001**, *13*, 273.

[5] Sieve, B.; Chen, X. Z.; Henning, R.; Brazis, P.; Kannewurf, C. R.; Cowen, J. A.; Schultz, A. J.; Kanatzidis, M. G. *J. Am. Chem. Soc.* **2001**, *123*, 7040.

[6] Latturner, S. E.; Bilc, D.; Mahanti, S. D.; Kanatzidis, M. G. *Inorg. Chem.* **2003**, *42*, 7959.

[7] a) Fehrmann, B.; Jeitschko, W. *Inorg. Chem.* **1999**, *38*, 3344. b) Thiede, V. M. T.; Jeitschko, W. *Z. Naturforsch. B* **1998**, *53*, 673.

[8] a) Thiede, V. M. T.; Ebel, T.; Jeitschko, W. *J. Mater. Chem.* **1998**, *8*, 125. b) Reehuis, M.; Wolff, M. W.; Krimmel, A.; Scheidt, E. W.; Stusser, N.; Loidl, A.; Jeitschko, W. *J. Phys Condens. Matt.* **2003**, *15*, 1773.

[9] Fehrmann, B.; Jeitschko, W. *Z. Naturforsch. B* **1999**, *54*, 1277.

[10] Gout, D.; Benbow, E.; Gourdon, O.; Miller, G. J. *J. Solid State Chem.* **2003**, *174*, 471.

[11] Rykhal', R. M.; Zarechnyuk, O. S.; Pyshchik, A. V. *Dopov. Akad. Nauk A* **1973**, *6*, 568.

[12] a) Mizushima, A.; Isikawa, Y.; Maeda, A.; Oyabe, K.; Mori, K.; Sato, K.; Kamigaki, K. *J. Phys. Soc. Jpn.* **1991**, *60*, 753. b) Fornasini, M. L.; Raggio, R.; Borzone, G. *Z. Krist. – New Cryst. St.* **2004**, *219*, 75.

[13] Yartys', V. A.; Pavlenko, V. V. *Koordinats. Khim.* **1992**, *18*, 424.

[14] Yarmolyuk, Y. P.; Rykhal', R. M.; Aksel'rud, R. D.; Zarechnyuk, O. S. *Dopov. Akad. Nauk A* **1981**, *43*, 86. b) Sikawa, Y.; Mizushima, A.; Sakurai, J.; Mori, K.; Munoz, A.; Givord, F.; Boucherle, J. X.; Voiron, J.; Oliveira, I. S.; Flouquet, J. *J. Phys. Soc. Jpn.* **1994**, *63*, 2349.

[15] a) Takeshita, T.; Malik, S. K.; Wallace, W. E. *J. Solid State Chem.* **1978**, *23*, 271. b) Achard, J. C.; Givord, F.; Percheron-Guegan, A.; Soubeyroux, J. L.; Tasset, F. *J. Phys. Paris* **1979**, *40*, 218.

[16] Dwight, A. E.; Mueller, M. H.; Conner, R. A. jr.; Downey, J. W.; Knott, H. *T. Metall. Soc. Aime* **1968**, *242*, 2075. b) Oesterreicher, H. *J. Less-Common Met.* **1973**, *30*, 225. c) Maletta, H.; Sechovsky, V. *J. Alloys Compd.* **1994**, *207*, 254.

[17] Gladyshevskii, R. E.; Cenzual, K.; Flack, H. D.; Parthe, E. *Acta Crystallogr. B* **1993**, *49*, 468.

[18] Rykhal', R. M.; Zarechnyuk, O. S.; Kuten', Y. I. *Dopov. Akad. Nauk A* **1978**, *40*, 1136. b) Rykhal', R. M.; Zarechnyuk, O. S.; Yanson, T. I. *Dopov. Akad. Nauk A* **1979**, *41*, 1057.

[19] a) Gladyshevskii, R. E.; Cenzual, K.; Parthé, E. *J. Solid State Chem.* **1992**, *100*, 9. b) Bauer, E. D.; Bobev, S.; Thompson, J. D.; Hundley, M. F.; Sarrao, J. L.; Lobos, A.; Aligia, A. A. *J. Phys.: Condens. Matter* **2004**, *16*, 4025.

[20] Tuan, N. C.; Sechovsky, V.; Divis, M.; Svoboda, P.; Nakotte, H.; de Boer, F. R.; Kim-Ngan, N. H. *J. Appl. Phys.* **1993**, *73*, 5677.

[21] Kolomiets, A. V.; Havela, L.; Yartys, V. A.; Andreev, A. V. *Zh. Fiz. Doslidzhen* **1999**, *3*, 458.

[22] Steglich, F.; Geibel, C.; Gloos, K.; Olesch, G.; Schank, C.; Wassilew, C.; Loidl, A.; Krimmel, A.; Stewart, G. R. *J. Low Temp. Phys.* **1994**, *95*, 3.

[23] a) Tolinski, T.; Schafer, W.; Kockelmann, W.; Kowalczyk, A.; Hoser, A. *Phys. Rev. B* **2003**, *68*, 144403. b) Tolinski, T.; Schafer, W.; Kowalczyk, A.; Andrzejewski, B.; Hoser, A.; Szlaferek, A. *J. Alloys Compd.* **2004**, *385*, 28.

[24] Tolinski, T.; Kowalczyk, A.; Chelkowska, G.; Pugaczowa-Michalska, M.; Andrzejewski, B.; Ivanov, V.; Szewczyk, A.; Gutowska, M. *Phys. Rev. B* **2004**, *70*, 064413.

[25] $YbNi_3Al_{19}$ crystallizes in the $ErNi_3Al_{19}$ structure type; the synthesis, crystal structure and physical properties of this compound will be described in Part II of this chapter.

[26] Fornasini, M. L.; Raggio, R.; Borzone, G. *Z. Krist. - New Cryst. St.* **2004**, *219*, 77.

[27] *SMART*, version 5; Siemens Analytical X-ray Systems, Inc.: Madison, WI, 1998.

[28] Saint, Version 4; Simens Analytical X-ray Instruments Inc., Madison, WI.

[29] SADABS, Sheldrick, G. M.; University of Göttingen, Göttingen, Germany.

[30] G.M. Sheldrick, 1995, SHELXTL. Structure Determination Programs, Version 5.0. Siemens Analytical X-ray Instruments, Inc. Madison, WI.

[31] CrystalDiffract is © 1995-1996, Dr. David C. Palmer.

[32] Rykhal, R. M.; Zarechnyuk, O. S. Yarmolyuk, Y. P. *Sov. Phys. Crystallogr. Sect. C* **1992**, *17*, 453.

[33] Gladyshevskii, R. E.; Cenzual, K.; Parthé, E. *Acta Crystallogr. Sect. C* **1992**, *48*, 232.

[34] Newkirk, J. B.; Black, P. J.; Damjanovic, A. *Acta Crystallogr.* **1961**, *14*, 532.

[35] Bourdreaux, E. A.; Mulay, L. N. In *Theory and Applications of Molecular Paramagnetism*; John Wiley and Sons: New York, 1976.

[36] Sales, B. C.; Wohllebent, D. K. *Phys. Rev. Lett.* **1975**, *35*, 1240.

CHAPTER FIVE

Exploratory Studies on the Ternary System RE/Ni/Al Employing Al as a Flux

PART II. Flux Synthesis and Characterization of a New Ternary Phase $Yb_{1.1}Ni_3Al_{8.9}$

5-2-1. Introduction

In the last two decades, there has been increasing interest in Yb-containing intermetallic compounds due to a variety of interesting properties they display such as heavy fermion,[1] intermediate valence[2] and Kondo lattice behavior.[3] These characteristics are associated with the fact that for this element $4f^{13}$ and $4f^{14}$ electronic states are close in energy and they hybridize very easily with the conduction electrons. In spite of the interesting properties, studies on Yb-based compounds are very limited, possibly because of the difficulty in synthesizing Yb-containing compounds due to the high vapor pressure of this element.[4] To overcome this problem, we suggested using metal (Al, Ga, In) as a flux to synthesize Yb-based compounds.[5] This method allows the reaction to be conducted below 1000 °C, much lower than the traditional method (induction furnace, arc-welder). Besides this high temperature solution facilitates the growth of single crystals; thus allowing the structure determination to be much easier and more reliable.

One of the systems which people have been interested in is the ternary family Yb-TM-X (TM = transition metal, X = Al, Ga, In). Steglich and coworkers have investigated tentatively the Yb-Ni-Al ternary phase diagram which is shown in Figure 5-2-1.[6] A slightly curved line starting near YbNi and passing close to Yb_2Ni_2Al and YbNiAl

separates the region with mixed valent Yb (on the Yb and Al-rich side) from the region with trivalent Yb (on the Ni-rich side). The valence of Yb for Yb_2Ni_2Al is between +3 and +2; studies of Yb_2Ni_2Al indicate that it is a heavy fermion compound without any indication of magnetic ordering down to 2 K.[6] YbNiAl orders antiferromagnetically and shows metamagnetic behavior in a magnetic field.[7] $YbNiAl_2$ shows a magnetically ordered ground state with stable trivalent Yb ions.[6] Although Steglich and his coworkers claimed that they found a simple composition dependence of the Yb-valence in the ternary Yb-Ni-Al system as depicted in Figure 5-4-1, some compounds such as $Yb_3Ni_5Al_{19}$ do not fit into this diagram.[8] $Yb_3Ni_5Al_{19}$ is a member of the $RE_3Ni_5Al_{19}$ family which was described earlier in this dissertation and also reported by Bauer and coworkers. According to the phase diagram by Steglich, the Yb ions in this compound are trivalent (Yb 11.1%, Ni 18.5%, Al 70.4%), however magnetic susceptibility measurements indicated intermediate valence behavior of the Yb ions.

Previous studies employing the Al flux method reveal that Al tends to serve as a reactive solvent which usually incorporates into the product.[9] Therefore Al flux is an appropriate tool to synthesize ternary compounds in the Yb-Ni-Al system. Our exploratory studies on this system led to the discovery of a new ternary compound $Yb_{1.1}Ni_3Al_{8.9}$, which is a disordered variant of the $ErNi_3Al_9$ structure type.[10] Herein we report synthesis, crystal structure and magnetic properties of $Yb_{1.1}Ni_3Al_{8.9}$.

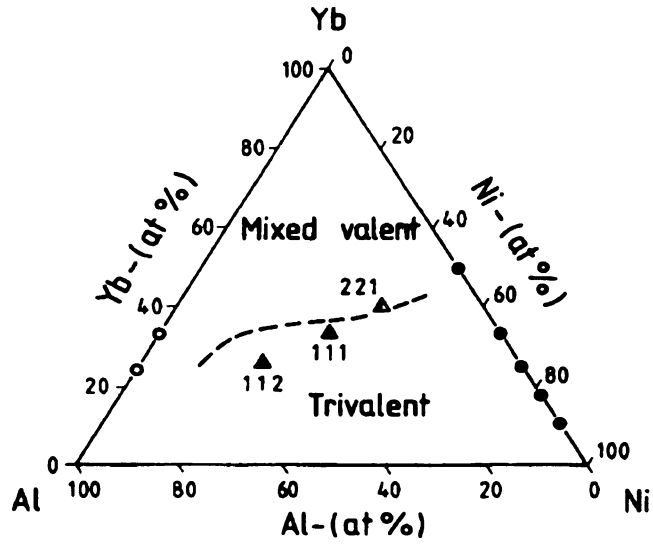

Figure 5-2-1. Valence of binary (circles) and ternary (triangles) compounds in the Yb-Ni-Al phase diagram. Closed symbols: trivalent Yb; open symbols: mixed valent of Yb. Dotted line indicates the border between mixed-valent and trivalent Yb.

5-2-2. Experimental Section

Reagents:

The following reagents were used as obtained: Yb (Cerac, 99.9%), Ni (99%, 325 mesh, Sargent, Buffalo Grove, IL), Al (Cerac, 99.5%, -20 mesh).

Synthesis:

In a nitrogen-filled glove box, the reaction mixture containing 1 mmol Yb metal (0.173 g), 2 mmol Ni (0.118 g), 10 mmol Al (0.270 g) was combined into an alumina crucible. The crucible was then placed into a silica tube (13 mm in diameter), which was sealed under vacuum (~10^{-4} Torr). The sample was subjected to the following treatment: it was heated to 1000 °C in 15 h, maintained at this temperature for 5 h, and then cooled

to 850 °C in 2 h. It was annealed at 850 °C for 3 d, followed by cooling down to 500 °C in 36 h. Finally the temperature was brought down to 50 °C in 10 h. $Yb_{1.1}Ni_3Al_{8.9}$ crystallized as a major phase in 50% yield with $Yb_3Ni_5Al_{19}$ and $YbAl_3$ as minor phases.

The excess aluminum was removed by soaking the crucible in aqueous 5M NaOH solution overnight. The remaining crystalline products after the isolation procedure were rinsed with water and acetone. Single crystals were selected for elemental analysis, X-ray diffraction and magnetic susceptibility measurements.

Scanning Electron Microscopy and Elemental Analysis:

The crystals were picked and affixed on a Scanning Electron Microscope (SEM) sample plate using carbon tape. Chemical compositions of the products were determined by Energy Dispersive Spectroscopy (EDS) performed on a JEOL JSM-35C SEM equipped with a NORAN EDS detector. Data were acquired by applying a 25 kV accelerating voltage with an accumulation time of 30 s. Several crystals were analyzed and averaged with the resulting approximate atomic ratio of 1 : 3.25 : 8.92 for Yb : Ni : Al, which agreed fairly well with the results derived from the single crystal X-ray analysis. The crystals of $Yb_{1.1}Ni_3Al_{8.9}$ are metallic with shiny and smooth surfaces, as shown in Figure 5-2-2.

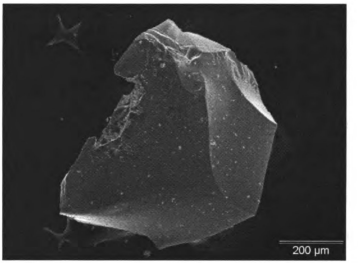

Figure 5-2-2. SEM image of a typical crystal of $Yb_{1.1}Ni_3Al_{8.9}$.

X-ray Crystallography:

X-ray diffraction data were collected at 173 K on a Bruker AXS SMART CCD X-ray diffractometer. A single crystal of $Yb_{1.1}Ni_3Al_{8.9}$ with the size 0.24 × 0.16 × 0.16 mm^3 was cut from a larger crystal and mounted on glass fibers. A data collection (Mo Kα radiation, λ = 0.71073 Å) was acquired covering a full sphere of reciprocal space. The SMART[11] software was used for data acquisition and cell reduction, and the integration was performed with the SAINTPLUS software package.[12] An empirical absorption correction was applied to the data using the SADABS program.[13] The structures were solved using direct methods and refined with the SHELXTL package program.[14]

Five space groups were given by XPREP program as possible candidates: *R*-3, *R*3, *R*3*m*, *R*32, *R*-3*m*. Initially two centrosymmetric space groups *R*-3 and *R*-3*m* were examined which also have the lowest CFOM values. However no satisfactory solutions

could be obtained. So the chiral space group *R*32 was chosen which was consistent with that of $ErNi_3Al_9$ reported by Gladyshevskii.[10] In the structure of $Yb_{1.1}Ni_3Al_{8.9}$ a total of nine atomic sites were identified. The *6c* Yb(1) site, *18f* Ni(1) site, *18f* Al(1), *9d* Al(3), and three *6c* Al sites — Al(4), Al(5) and Al(6) were assigned unambiguously and found fully occupied. Disorder was observed between the Yb(2) and Al(2) atoms: the distance between the Yb(2) and Al(2) atoms was found be to very close at 1.522(2) Å; furthermore, both sites were found partially occupied with Yb(2) 10% and Al(2) 90%. So the Yb(2) and Al(2) sites were constrained to make the occupancy sum of Yb(2) and Al(2) equal to 1. Similar disorder was observed in the isostructural compounds YNi_3Al_9 and $DyNi_3Al_9$, while in both cases an additional Al(7) site was found which also exhibited partially disordered arrangements with RE(1) atom in a triangular mesh.[10] Interestingly the Er and Gd analogues have ordered arrangements of rare earth and aluminum triangles: only one RE site, one Ni site and six Al sites were identified and all were refined fully occupied.

In the structure of $Yb_{1.1}Ni_3Al_{8.9}$, all atomic sites were refined anisotropically. Data collection parameters and refinement details for $Yb_{1.1}Ni_3Al_{8.9}$ can be found in Table 5-2-1. Atomic positions, displacement parameters and anisotropic displacement parameters are listed in Tables 5-2-2 and 5-2-3.

X-ray powder diffraction data were collected at room temperature on a CPS 120 INEL X-ray diffractometer (Cu Kα) equipped with a position-sensitive detector. Experimental powder patterns were compared to the patterns calculated from the single crystal structure solution (by the CrystalDiffract[15] software program) to determine the phase identity and purity.

Table 5-2-1. Selected crystal data and structure refinement details for $Yb_{1.1}Ni_3Al_{8.9}$.

Empirical formula	$Yb_{1.1}Ni_3Al_{8.9}$
Formula weight	591.99
Crystal system	Rhombohedral
Space group	*R*32 (#155)
Unit cell dimensions	a = 7.2314(4) Å
	c = 27.140(3) Å
Volume	1229.11(17) $Å^3$
Z	6
Density (calculated)	4.799 Mg/m^3
Absorption coefficient	18.975 mm^{-1}
F(000)	1626
Crystal size	0.24 × 0.16 × 0.16 mm^3
Theta range for data collection	3.34 to 28.12°
Limiting indices	$-9 \leq h \leq 9$
	$-9 \leq k \leq 9$
	$-36 \leq l \leq 35$
Reflections collected	3654
Independent reflections	635 [R(int) = 0.0522]
Completeness to theta = 28.12	95.5 %
Refinement method	Full-matrix least-squares on F^2
Data / restraints / parameters	635 / 0 / 42
Goodness-of-fit on F^2	1.211
Final R indices [I>2sigma(I)]	R_1 = 0.0260, wR_2 = 0.0606
R indices (all data)	R_1 = 0.0267, wR_2 = 0.0616
Largest diff. peak and hole	2.299 and –1.840 $e.Å^{-3}$

$R1 = \Sigma(|F_o|-|F_c|)/\Sigma|F_o|$; $wR2 = [\Sigma[w(F_o^2 - F_c^2]/ [\Sigma(w|F_o|^2)^2]^{1/2}$

Table 5-2-2. Atomic coordinates ($Å \times 10^4$) and equivalent isotropic displacement parameters ($Å^2 \times 10^3$) for $Yb_{1.1}Ni_3Al_{8.9}$.

Atom	Wyk. Symbol	x	y	z	$U_{(eq)}$*	Occu.
Yb(1)	6*c*	0	0	1668(1)	10(1)	1
Ni	18*f*	3334(2)	48(2)	861(1)	7(1)	1
Al(1)	18*f*	3329(4)	3348(4)	1003(1)	9(1)	1
Al(3)	9*d*	3340(3)	0	0	9(2)	1
Al(4)	6*c*	0	0	522(1)	8(1)	1
Al(5)	6*c*	0	0	2815(1)	8(1)	1
Al(6)	6*c*	0	0	3865(1)	9(1)	1
Yb(2)	3*b*	0	0	5000	3(1)	0.097
Al(2)	9*e*	2105(3)	0	5000	3(1)	0.903

$U_{(eq)}$ is defined as one third of the trace of the orthogonalized U_{ij} tensor.

Table 5-2-3. Anisotropic displacement parameters ($Å^2 \times 10^3$) for $Yb_{1.1}Ni_3Al_{8.9}$.

Atom	U^{11}	U^{22}	U^{33}	U^{23}	U^{13}	U^{12}
Yb(1)	11(1)	11(1)	8(1)	0	0	5(1)
Ni	8(1)	8(1)	5(1)	0(1)	0(1)	4(1)
Al(1)	7(1)	9(1)	13(2)	4(1)	1(1)	4(1)
Al(3)	10(1)	11(2)	8(2)	-1(1)	0(1)	5(1)
Al(4)	9(1)	9(1)	7(1)	0	0	4(1)
Al(5)	8(1)	8(1)	8(1)	0	0	4(1)
Al(6)	9(1)	9(1)	8(1)	0	0	5(1)
Yb(2)	3(1)	3(1)	2(1)	0	0	2(1)
Al(2)	3(1)	3(1)	2(1)	0	0	2(1)

The anisotropic displacement factor exponent takes the form:
$-2\pi^2[h^2a^{*2}U^{11}+\ldots+2hka^*b^*U^{12}]$

Magnetic Characterization:

Magnetic measurements were conducted on polycrystalline samples of $Yb_{1.1}Ni_3Al_{8.9}$. Field-cooled and zero-field cooled dc magnetization measurements were performed for the above samples using a Quantum Design MPMS SQUID magnetometer. EDS-analyzed crystals were ground into powder, which was sealed in kapton tape and placed into the magnetometer. The data were collected in the temperature range 3-300 K at 1000 G, while field dependent magnetic measurements, conducted at 5 K, were carried out in fields up to ± 55000 G. A diamagnetic correction was applied to the data to account for core diamagnetism.

5-2-3. Results and Discussion

Crystal Structure:

The crystal structure of $Yb_{1.1}Ni_3Al_{8.9}$ viewed down the *b*-axis is shown in Figure 5-2-3. This structure is related to the $ErNi_3Al_9$ structure type with a partially disordered triangular arrangement of Yb and Al atoms.[10] As described by Gladyshevskii, this structure can be viewed as three different kinds of triangular layers stacking along the *c*-axis: Al layer, Ni layer and Yb-Al layer. Al(1) and Al(3) atoms form similar triangular arrangements on the *ab* plane with Al-Al distance longer than 4 Å, as shown in Figure 5-2-4A. Al(4), Al(5) and Al(6) atoms also form triangular patterns, with Al(4)-Al(4) bond distance of 2.831(6) Å and Al(5)-Al(6) distance of 2.848 (6) Å. The Ni layer, is inserted between the Al(1) layer and the Al layer composed of Al(4), Al(5) and Al(6) atoms.

What makes this compound interesting and different from the structure of $ErNi_3Al_9$ is the triangular mesh composed of Yb and Al atoms. As shown in Figure 5-2-

5A, in the Er_2Al_3 layer the Er and Al atoms form ordered triangular mesh with regular bond distances between Er and Al atoms of 2.977(2) Å. However for the Y- and Dy-analogues, two additional atomic sites, i.e. one rare earth metal and one Al site, were detected.[10] Figure 5-2-5C depicts the disordered arrangement of RE and Al atom triangles, for the Dy compound the sites RE(1) and RE(2) were found to have the occupation of 80% and 40%, respectively; while for the Y-analogue the corresponding occupation factors were 97% and 6%. While in the present compound $Yb_{1.1}Ni_3Al_{8.9}$, the Yb(1) site is fully occupied and a partly disordered triangular arrangement of Yb-Al atoms is observed, producing unreasonably short distance between Yb(2) and Al(2) atoms: 1.522(2) Å. The occupancy factors of Yb(2) and Al(2) are 10% and 90%, respectively.

The compounds $ErNi_3Al_9$, $DyNi_3Al_9$, YNi_3Al_9 and $Yb_{1.1}Ni_3Al_{8.9}$ crystallize in the same structure type, however with a different type of disorder in the RE-Al triangle layer. It was suggested by Gladyshevskii that this disorder originates from the non-homogeneous stacking of the RE_2Al_3 layer along the *c*-axis.[10] For a structure with maximum disorder of RE and Al atoms triangles, both RE sites would have a occupation of 67% and Al sites 33%. This results in a structure with a space group P-6*m*2 and smaller unit cell: $a = a'/\sqrt{3}$, $c = c'/3$ (a' & c' are the cell parameters of $ErNi_3Al_9$). This argument has been confirmed by $RE_{0.67}Ni_2Ga_{6-x}Tt_x$ (Tt = Si/Ge) in which a complete disorder was observed in the RE-Ga plane. The random stacking of RE-Ga planes along the *c*-axis causes the elongated diffuse streaks along this direction on the *h0l* and *0kl* zone photographs.[16]

The local coordination environments of Yb(1) and Ni atoms are shown in Figure 5-2-5D & E. The Yb atoms are surrounded by 17 atoms which form a bicapped hepta-layer geometry. These five monoatomic layers are in the order of Ni-Al(1)-Al(2)-Al(1)-Ni atoms with Al(4) and Al(5) as capping atoms. The bond distance between Yb(1) and Al(2) is 2.9566(16) Å, slightly shorter than the other Yb-Al distances. The Ni atoms sit in a distorted cubic geometry composed of eight Al atoms with Ni-Al distance ranging from 2.3369(15) Å to 2.6033(17) Å.

Table 5-2-4. Bond lengths (Å) for $Yb_{1.1}Ni_3Al_{8.9}$.

Bond	Distance	Bond	Distance
Yb(1)-Al(1)	3.012(3)	Ni(1)-Al(5)	2.5679(17)
Yb(1)-Al(2)	2.9566(16)	Ni(1)-Al(6)	2.6033(17)
Yb(1)-Ni(1)	3.2386(13)	Al(1)-Al(2)	2.766(3)
Yb(2)-Al(1)	2.999(3)	Al(1)-Al(4)	2.746(4)
Yb(2)-Al(2)	1.522(2)	Al(1)-Al(5)	2.754(3)
Yb(2)-Al(6)	3.082(3)	Al(6)-Al(1)	2.719(3)
Yb(2)-Ni(1)	3.2800(13)	Al(3)-Al(4)	2.800(2)
Ni(1)-Al(1)	2.419(2)	Al(3)-Al(5)	2.7883(18)
Ni(1)-Al(1)	2.451(2)	Al(3)-Al(6)	2.8065(18)
Ni(1)-Al(1)	2.454(2)	Al(4)-Al(4)	2.831(6)
Ni(1)-Al(2)	2.3734(17)	Al(5)-Al(6)	2.848(6)
Ni(1)-Al(3)	2.3369(15)	Al(2)-Al(2)	2.636(4)
Ni(1)-Al(4)	2.5649(17)		

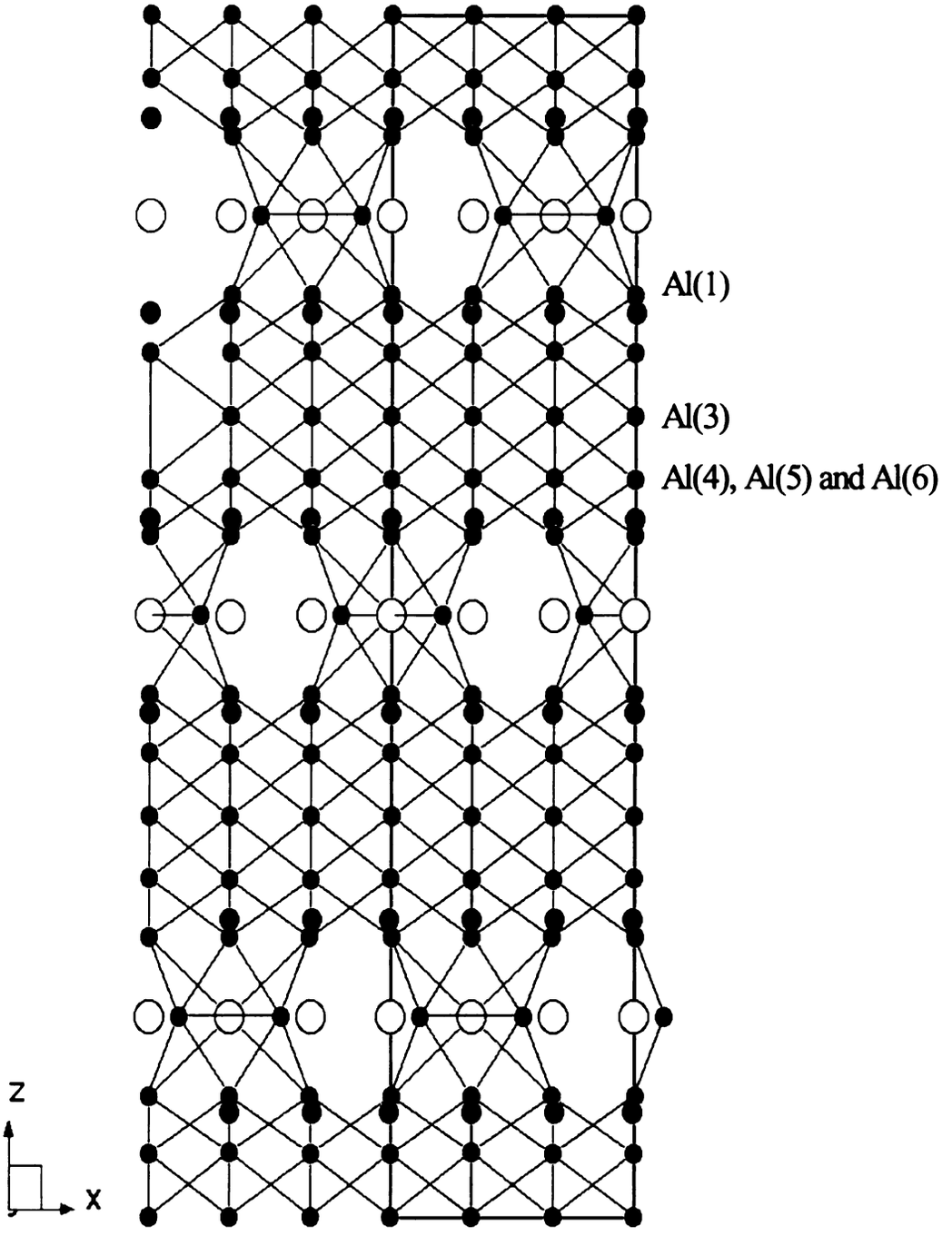

Figure 5-2-3. Crystal structure of $Yb_{1.1}Ni_3Al_{8.9}$ viewed down the [010] direction. Large empty circles: Yb; black circles: Al; gray circles: Ni.

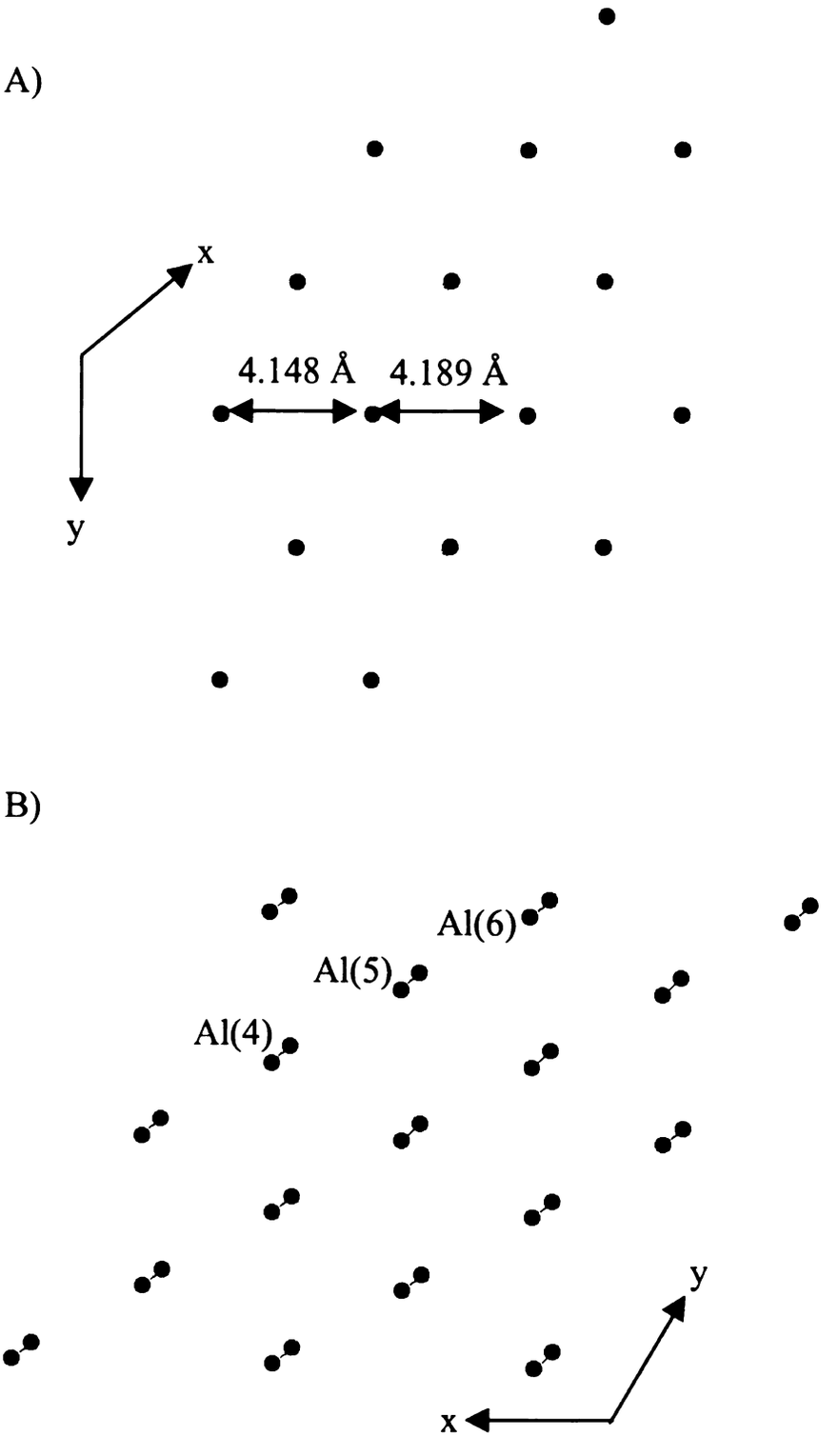

Figure 5-2-4. Structure of $Yb_{1.1}Ni_3Al_{8.9}$. A) Triangular layer composed of Al(1) atoms. B) Triangular layer composed of Al(4), Al(5) and Al(6) atoms down the *c*-axis.

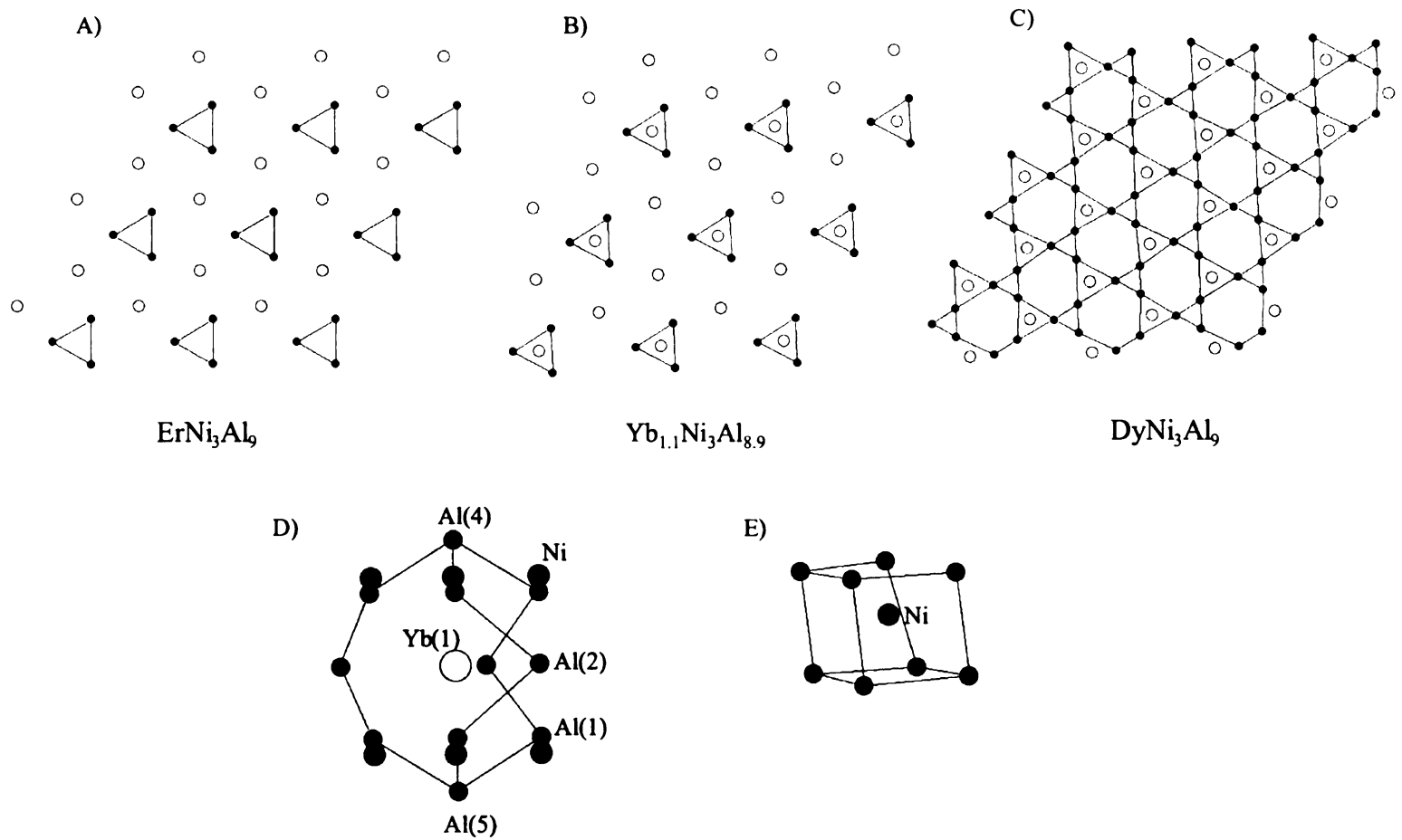

Figure 5-2-5. A) Ordered RE-Al plane in $ErNi_3Al_9$ viewed down the *c*-axis. B) Partially disordered RE-Al plane in $Yb_{1.1}Ni_3Al_{8.9}$ viewed down the *c*-axis. C) Disordered RE-Al plane in $DyNi_3Al_9$ viewed down the *c*-axis. D) & E) Local coordination environments of Yb(1) and Ni atoms in $Yb_{1.1}Ni_3Al_{8.9}$.

Magnetic Properties:

The temperature dependent molar magnetic susceptibility χ_m for $Yb_{1.1}Ni_3Al_{8.9}$ is shown in Figure 5-2-6A. Above 50 K, the magnetic susceptibility can be fit to a Curie-Weiss law yielding an effective magnetic moment μ_{eff} = 4.14 μ_B/mol Yb, slightly lower than the theoretical value for Yb^{3+} (μ_{eff} = 4.54 μ_B). This implies that the Yb ions in $Yb_{1.1}Ni_3Al_{8.9}$ are in an intermediate oxidation state of Yb^{2+} and Yb^{3+}. This compound is another example that does not fit into the diagram suggested by Steglich.[6] The negative Weiss constant (θ = -18.41 K) indicates the presence of weak antiferromagnetic interactions between the Yb ions.

The isothermal magnetization of $Yb_{1.1}Ni_3Al_{8.9}$ conducted at 5 K up to 55000 G is plotted in Figure 5-2-6B. Clear metamagnetic behavior without hysteresis effects is observed. This metamagnetic transition is more obvious when plotting the derivative $(\partial M/\partial B)_T$ *vs* B shown in the inset of Figure 5-2-6B. The sharp peak at 1000 G (T = 5 K) corresponds to the field-induced change in the magnetization. Similar metamagnetic transition is also observed in $Yb_2Rh_3Al_9$ and $Yb_2Ir_3Al_9$; however this transition disappears as T_N is reached.[2] The magnetization value M for $Yb_{1.1}Ni_3Al_{8.9}$ at 55000 G reaches a value of 0.9 μ_B/Yb, which is much lower than the ordered value which is 4.5 μ_B/Yb.

A)

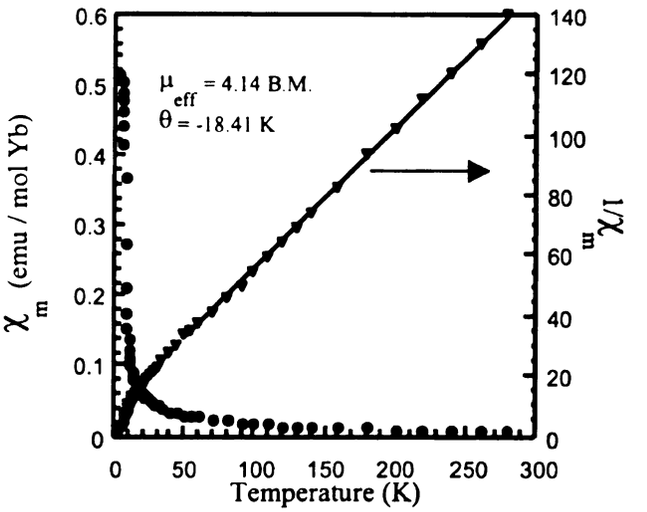

B)

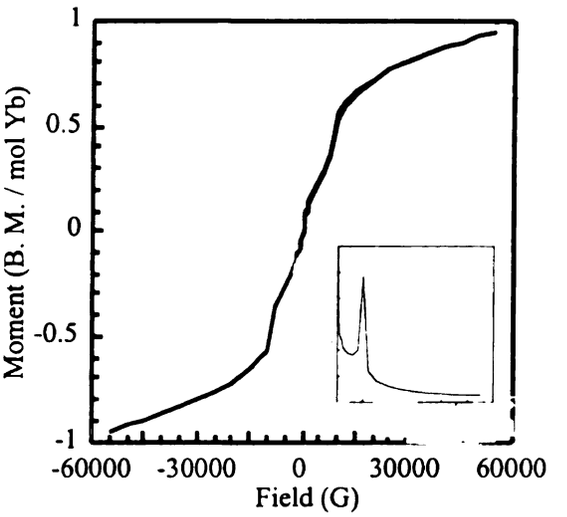

Figure 5-2-6. A) Temperature dependent magnetic susceptibility of a polycrystalline sample of $Yb_{1.1}Ni_3Al_{8.9}$ under the field of 1000 G. B) Molar magnetization of $Yb_{1.1}Ni_3Al_{8.9}$ in fields up to 55000 G measured at 5 K. inset: derivative ($\partial M/\partial B$) as a function of field.

5-2-4. Conclusions

Single crystals of a new ternary intermetallic compound $Yb_{1.1}Ni_3Al_{8.9}$ have been synthesized by the Al flux method. This compound has a crystal structure related to that of $ErNi_3Al_9$ and the whole structure can be viewed as a stack of monoatomic layers along the *c*-axis. As in the isostructural compounds $DyNi_3Al_9$ and YNi_3Al_9, a partially disordered triangle arrangement of Yb and Al atoms was observed for $Yb_{1.1}Ni_3Al_{8.9}$ on the Yb-Al plane. In this disordered model every Yb(2) atom is surrounded by three Al(2) atoms with very close distance of 1.522(2) Å; and the occupancy factors of Yb(2) and Al(2) were found 10%/90%.

Temperature dependent magnetic measurements reveal that the Yb ions in this compound are in an intermediate oxidation state of Yb^{2+} and Yb^{3+}. As in the other intermetallic compounds, transition metal Ni atoms do not contribute to the magnetic moment. The negative Weiss constant θ (-18.41 K) implies weak antiferromagnetic interactions. A clear field-induced metamagnetic transition occurs at 1000 G and a field higher than 55000 G is required to saturate the magnetic moments.

References:

[1] Kaczorowski, D.; Andraka, B.; Pietri, R.; Cichorek, T.; Zaremba, V. I. *Phys. Rev. B* **2000**, *61*, 15255.

[2] Trovarelli, O.; Geibel, C.; Buschinger, B.; Borth, R.; Mederle, S.; Grosche, M.; Sparn, G.; Steglich, F.; Brosch, O. Donnevert, L. *Phys. Rev. B* **1999**, *60*, 1136.

[3] Singh, Y.; Ramakrishnan, S. *Phys. Rev. B* **2003**, *68*, 054419.

[4] Fisk, Z.; Maple, M. B. *J. Alloys Compd.* **1992**, *183*, 303.

[5] Kanatzidis, M. G.; Pöttgen, R.; Jeitschko, W. *Angew. Chem. Int. Ed.* **2005**, *44*, 6996.

[6] Geibel, C.; Klinger, U.; Buschinger, M.; Weiden, M.; Olesch, G.; Thomas, F.; Steglich, F. *Phys. B* **1996**, *223 & 224*, 370.

[7] a) Diehl, J.; Davideit, H.; Klimm, S.; Tegel, U.; Geibel, C.; Steglich, F.; Horn, S. *Phys. B* **1995**, *206 & 207*, 344. b) Schank, C.; Olesch, G.; Kohler, J.; Tegel, U.; Klinger, U.; Diehl, J.; Klimm, S.; Sparn, G.; Horn, S.; Geibel, C.; Steglich, F. *J. Magn. Magn. Mater.* **1995**, *140-144*, 1237.

[8] Bauer, E. D.; Bobev, S.; Thompson, J. D.; Hundley, M. F.; Sarrao, J. L.; Lobos, A.; Aligia, A. A. *J. Phys.: Condens. Matter* **2004**, *16*, 4025.

[9] Sieve, B. Ph. D. Dissertation, Michigan State University, 2002.

[10] Gladyshevskii, R. E.; Cenzual, K.; Flack, H. D.; Parthé, E. *Acta. Cryst.* **1993**, *B49*, 468.

[11] *SMART*, Version 5; Siemens Analytical X-ray Systems, Inc.: Madison, WI, 1998.

[12] *Saint*, Version 4; Simens Analytical X-ray Instruments Inc., Madison, WI.

[13] *SADABS*, Sheldrick, G. M.; University of Göttingen, Göttingen, Germany.

[14] G.M. Sheldrick, 1995, *SHELXTL*. Structure Determination Programs, Version 5.0. Siemens Analytical X-ray Instruments, Inc. Madison, WI.

[15] CrystalDiffract is © 1995-1996, Dr. David C. Palmer.

[16] Zhuravleva, M. A.; Chen, X. Z.; Wang, X.; Schultz, A. J.; Ireland, J.; Kannewurf, C. K.; Kanatzidis, M. G. *Chem. Mater.* **2002**, *14*, 3066.

CHAPTER SIX

PART I. Doping Studies of $Yb_3Ni_5Al_{19}$ with Cu, Fe and Mn Substitutions

6-1-1. Introduction

In the last two decades, the strongly correlated f-electron systems, especially Ce and Yb-based ones, have attracted considerable attention.[1] These compounds often exhibit interesting behavior such as Kondo lattice,[2] heavy fermion[3] and mixed valence.[4] These properties are a result of the competition between the magnetic ordering (Ruderman-Kittel-Kasuya-Yosida interaction) and the Kondo effect.[5] The Kondo effect results from the exchange interaction between the conduction electrons and the local magnetic moments leading to scattering events in which the electron spin is flipped. In a Kondo system, the resistivity drops to a minimum at low temperature and then proceeds to rise at lower temperatures. These two effects (the RKKY interaction and the Kondo effect) are characterized by the hybridization strength J between the 4f electrons and conduction electrons. For the lower J values, i. e. the RKKY interaction dominates, the compound can exhibit magnetic ordering; on the other hand, for the higher J values, the Kondo effect takes over, and the ground state is nonmagnetic. This phenomenon is clearly described in the well-known 'Doniach's magnetic phase diagram'.[5]

The J value (hybridization strength) of a compound can be tuned by applying external pressure or chemical pressure. For Ce-based compounds, applying external pressure (or positive chemical pressure) can cause them to switch from magnetic ordering to intermediate valence behavior (Kondo effect). Generally, with decreasing cell volume the 4f electrons and conduction band hybridization J value increases, favoring the Kondo

effect. This theory is clearly exemplified by $CePd_2Si_2$ and $CeRh_2Si_2$; in both cases the pressure induces a transition from antiferromagnetism to a nonmagnetic state.[6] More interestingly, these compounds become superconductors at pressures close to the critical pressure where magnetic ordering vanishes. The chemical pressure effect on CeNi has been extensively studied by substituting Ni with Cu or Pt.[7] CeNi crystallizes in orthorhombic CrB-type structure with Ce ions in intermediate valence states. Since the size of Cu or Pt is larger than Ni, nonmagnetic to magnetic ordering transition is expected as this "negative pressure" is applied. Indeed, in $CeNi_{1-x}Pt_x$ compounds, a continuous evolution from the intermediate valence behavior in CeNi to a ferromagnetically ordered Ce^{3+} state in CePt was found, passing through a Kondo lattice behavior and heavy fermion state.[8] These properties can be well understood by modifications of 4f-conduction band hybridization driven by cell volume changes.

The Yb-based systems, usually present mirror-like behavior to Ce-compounds due to their hole-electron symmetry: f^1 (Ce^{3+}) vs f^{13} (Yb^{3+}). Therefore, under similar pressure conditions, the opposite effect is expected for Yb-based compounds, which means that external pressure might drive a non-magnetic Yb-system to a magnetically ordered state. This phenomenon has been observed and reported for some Yb-containing intermetallic compounds. For example, Yb_2Ni_2Al is a nonmagnetic heavy fermion compound crystallizing in orthorhombic Mo_2B_2Ni structure type.[9] When the applied pressure is more than 8 GPa and the temperature is below 2 K, a crossover from a nonmagnetic state to magnetically ordered state is observed; however this crossover is not connected with a change of the Yb valence state. $YbCu_2Si_2$ is another well-known nonmagnetic compound with Yb in an intermediate valence state.[10] When the external pressure is higher than 8

GPa, this compound is also converted from a nonmagnetic to magnetic ordered state with localized Yb moments. In this case, the transition is accompanied by a valence change towards the Yb^{3+} state.[11] Chemical substitution may result in a similar effect, such as $Yb(Cu_{1-x}Ni_x)_2Si_2$, in which the chemical pressure obtained by gradual substitution of Cu by Ni changes the nonmagnetic ground state of $YbCu_2Si_2$ to the magnetically ordered one of $YbNi_2Si_2$ (T_N = 2.1 K).[12] Different from the examples described above, Bauer and coworkers found that the substitution of Cu by Al in $YbCu_5$ caused a crossover from non-magnetic $4f^{14}$ state to the magnetic $4f^{13}$ state in $YbCu_3Al_2$.[13] Since the substitution of Cu by Al results in an expansion of the cell volume, chemical pressure might be excluded as a driving force of this change of ground state properties; instead it was suggested that the physical origin was the modification of the electronic structure of the compound which was associated with different number of electrons provided by Al and Cu.

In Part I of Chapter Five, we described a ternary intermetallic compound $Yb_3Ni_5Al_{19}$, in which the Yb ions show intermediate valence behavior.[14] It might be interesting to investigate the magnetic behavior of this Kondo compound by applying chemical pressure, thus we can better understand the correlations between compositions and magnetic states. In this section, we will describe the effects of substitution of Ni by Cu, Fe or Mn on the magnetic properties of $Yb_3Ni_5Al_{19}$. By applying this chemical pressure, two effects are expected. On one hand, the metallic radii of Mn, Cu, Fe and Ni are 1.37 Å, 1.28 Å, 1.26 Å and 1.25 Å, respectively. By substituting Ni with Mn, Fe or Cu, the unit cell volume is expected to expand slightly in all the cases, which corresponds to negative pressure. For the Yb-based systems, it is customary to decrease *J* values by applying external pressure. On the other hand, the number of electrons provided by the

substitutional element (Mn, Fe or Cu) is different from that of Ni, which might change the electronic structure of the parent compound. These two effects can be competing and lead to interesting properties induced by valence fluctuations in the Yb ions.

Here it is noteworthy to mention another important reason that we initiated this study. YbGaGe was reported to show zero thermal expansion (ZTE) between 10 and 300 K.[15] Magnetic measurements indicated that Yb ions were in an intermediate valence state and it was proposed that the ZTE behavior was derived from internal electronic charge transfer of the Yb ions. Later it was found that only when graphite crucibles were used as the reaction container, could the results be repeated. Although Fisher and his coworkers found that lightly C- or B- doped YbGaGe samples tended toward zero volume expansion,[16] we suspect that Fe — which is the second most abundant impurity element in the graphite crucible, might influence the unusual thermal expansion property. It is known that with substitutions of transition metals, the thermal expansion coefficient could be changed. $CeNi_{1-x}Cu_x$ is such an example.[17] Neutron diffraction analysis revealed that the relative changes of the cell parameters for $CeNi_{0.9}Cu_{0.1}$ between 300 K and 1.5 K were smaller than those observed for CeNi. However there has been no discussion about the mechanism behind this observation and no further investigations were reported on the thermal expansion of this system. So we investigated the temperature dependent lattice variation of $Yb_3Ni_{5-x}TM_xAl_{19}$ (TM = Cu, Fe, Mn) as well as their magnetic properties.

6-1-2. Experimental Section

Reagents:

The following reagents were used as obtained: Yb (Cerac, 99.9%), Ni (99%, 325 mesh, Sargent, Buffalo Grove, IL), Cu (99.5%, -325 mesh, Cerac, Milwaukee, WI), Fe (99.99%, fine powder, Aldrich Chemical, Milwaukee, WI), Mn (99.95%, fine powder, Cerac, Milwaukee, WI), Al (Cerac, 99.5%, -20 mesh).

Synthesis:

The elemental starting materials were stored and manipulated in a nitrogen-filled single dry box. All the compounds were synthesized by the Al flux method. The ratios used for Yb : Ni : TM : Al (TM = Cu, Fe, Mn) were summarized in Table 6-1-1. The constitutional metals were combined into alumina crucibles, which were then placed into silica tubes (13 mm in diameter) and sealed under vacuum (~10^{-4} Torr). The samples were heated to 1000 °C in 15 h, maintained at this temperature for 5 h, then cooled to 850 °C in 2 h. They were annealed at 850 °C for 3 d, followed by cooling down to 500 °C in 36 h. Finally the temperature was brought down to 50 °C in 10 h. The yield of the reactions was ~70% with $YbAl_3$ as the side product. When x in $Yb_3Ni_{5-x}Fe_xAl_{19}$ was 1, another side product $YbNi_{2-x}Fe_xAl_8$ appeared which will be described in Part II of this chapter.

Excess aluminum was removed by soaking the crucible in aqueous 5M NaOH solution overnight. The crystalline product remaining after the isolation procedure was rinsed with water and acetone. Single crystals were selected for elemental analysis, single crystal X-ray diffraction analysis and magnetic susceptibility measurements.

Table 6-1-1. Elemental ratios for the flux synthesis of $Yb_3Ni_5Al_{19}$, $Yb_3Ni_{5-x}Cu_xAl_{19}$, $Yb_3Ni_{5-x}Fe_xAl_{19}$ and $Yb_3Ni_{5-x}Mn_xAl_{19}$ (unit: mmol).

Compound	Yb	Ni	Cu/Fe	Al
$Yb_3Ni_5Al_{19}$	1	1	0	10
$Yb_3Ni_{5-x}Cu_xAl_{19}$ (x = 0.5)	1	0.9	0.1	10
$Yb_3Ni_{5-x}Cu_xAl_{19}$ (x = 1)	1	0.8	0.2	10
$Yb_3Ni_{5-x}Fe_xAl_{19}$ (x = 0.5)	1	0.9	0.1	10
$Yb_3Ni_{5-x}Fe_xAl_{19}$ (x = 1)	1	0.8	0.2	10
$Yb_3Ni_{5-x}Mn_xAl_{19}$ (x = 0.5)	1	0.9	0.1	10

Single Crystal X-ray Crystallography:

Single crystal X-ray diffraction data were collected for $Yb_3Ni_{5-x}TM_xAl_{19}$ (TM = Cu, Fe, Mn) at different temperatures (100 K, 173 K and 298 K) on a Bruker AXS SMART CCD X-ray diffractometer. A data collection (Mo Kα radiation, λ = 0.71073 Å) was acquired covering a hemisphere of reciprocal space. The data acquisition and cell reduction were done with the SMART[18] software package and data processing was performed with the SAINTPLUS software package.[19] An empirical absorption correction was applied to the data using the SADABS program.[20] The structure of $Yb_3Ni_5Al_{19}$ was used as the starting model and then refined with the SHELXTL package program.[21]

Magnetic Measurements:

Magnetic measurements were conducted on the polycrystalline samples of $Yb_3Ni_{5-x}TM_xAl_{19}$ (TM = Cu and Fe). Field-cooled and zero-field cooled dc

magnetization measurements were performed on the samples using a Quantum Design MPMS SQUID magnetometer. EDS-analyzed crystals were ground into powder, sealed in a kapton tape and placed into the magnetometer. The data were collected in the temperature range 3-300 K at 1000 G, while field dependent magnetic measurements, conducted at 5 K, were carried out in fields up to ± 55000 G. Diamagnetic corrections were applied to the data to account for core diamagnetism and kapton tape.

6-1-3. Results and Discussion

Synthesis and Compositional Variations:

As was discussed in Part I of Chapter Five, large single crystals of $Yb_3Ni_5Al_{19}$ could be obtained by using a molar ratio of 1 : 2 for Yb : Ni. So the first series of substitutional reactions were conducted based on the following ratios: Yb : Ni : Cu : Al (1 : 2-x : x :10), x = 0.2, 0.4, 0.6 and 0.8. However powder X-ray diffraction pattern showed no presence of $Yb_3Ni_{5-x}Cu_xAl_{19}$. Instead elemental analysis and single crystal X-ray analysis indicated that the products were $YbNi_4Al_8$ and $Yb(NiCu)_4Al_8$ which crystallize in the tetragonal $ThMn_{12}$ structure type.[22] It is obvious that the disruption coming from the large amount of Cu is enough to destabilize the original structure and form different compounds.

When the reactions were conducted with equal amount of Yb and transition metals (Table 6-1-1), we obtained the desired phases $Yb_3Ni_{5-x}TM_xAl_{19}$. Here the values of x were calculated from the ratio of the initial amount of transition metals. Figure 6-1-1 shows the single crystal X-ray data of $Yb_3Ni_{5-x}TM_xAl_{19}$ (TM = Cu, Fe) (x = 0, 0.5, 1) determined at 173 K. In both cases the cell volume expanded with increasing x as

expected since the metallic radii of these transition metals are in the order of $r_{Cu} > r_{Fe} > r_{Ni}$.[23] Therefore the orthorhombic structure of $Yb_3Ni_5Al_{19}$ was retained and Ni had been successfully substituted by small amounts of Cu or Fe. Elemental analysis showed very low level of substitutional element (Cu or Fe): about 1% when x = 0.5 and 3% with x = 1,

The radius of Cu atom is larger than that of Fe, thus the cell parameters of $Yb_3Ni_{5-x}Cu_xAl_{19}$ are larger than the corresponding ones of $Yb_3Ni_{5-x}Fe_xAl_{19}$. Although the relative volume expansion was very similar, a linear Vegard law was observed for the $Yb_3Ni_{5-x}Cu_xAl_{19}$ compounds, Figure 6-1-1A. In the case of $Yb_3Ni_{5-x}Fe_xAl_{19}$, the *a* cell parameter contracted slightly and then increased until x was 1. Since the *b* and *c* edge lengths of $Yb_3Ni_{5-x}Fe_xAl_{19}$ expanded normally, the overall cell volume increased by 0.2%. The orthorhombic structure of $Yb_3Ni_{5-x}Fe_xAl_{19}$ can be stabilized up to x = 1. When x was 1, elemental analysis and XRD showed $Yb_3Ni_{5-x}Fe_xAl_{19}$ was formed along with side products $YbAl_3$ and $YbNi_{2-x}Fe_xAl_8$. $YbNi_{2-x}Fe_xAl_8$ is a new phase also crystallizing in needle morphology; and its crystal structure and physical properties will be described in Part II of this chapter. With more Fe added into the reaction, the percentage of $YbNi_{2-x}Fe_xAl_8$ was higher and finally was the main phase in the product.

The temperature dependent cell parameters of $Yb_3Ni_{5-x}TM_xAl_{19}$ (TM = Mn, Cu, Fe) obtained on single crystals are shown in Figures 6-1-2, 6-1-3, 6-1-4 and 6-1-5. The data were summarized in Tables 6-1-2, 6-1-3, 6-1-4 and 6-1-5. When the temperature increased from 100 K to 298 K, the relative change in cell volume for $Yb_3Ni_5Al_{19}$ was dV/V = 0.57 %. For the Fe and Mn-substituted samples, the corresponding changes were very similar to that of the parent compound. While the cell volume of $Yb_3Ni_{5-x}Cu_xAl_{19}$ changed much more slowly when the temperature increased from 100 K to 298 K, which

were dV/V = 0.32 % (x = 0.5) and dV/V = 0.49 (x = 1). The slow change of the cell volume for $Yb_3Ni_{5-x}Cu_xAl_{19}$ (x = 0.5) came mainly from the *a*-axis. When the temperature increased from 173 K to 298 K, the *a* axis contracted so the overall change from 100 K to 298 K was only 0.03%. As we discussed before, all the cell parameters of $Yb_3Ni_{5-x}TM_xAl_{19}$ are expected to be larger than that of $Yb_3Ni_5Al_{19}$; however this happened only at 173 K (Figure 6-1-2). At higher temperature (298 K), except $Yb_3Ni_{5-x}Cu_xAl_{19}$ (x = 1), the cell volume of all the $Yb_3Ni_{5-x}TM_xAl_{19}$ compounds was equal to or smaller than that of $Yb_3Ni_5Al_{19}$. Although experimental error cannot be excluded as one possible reason, the electronic valence transition between Yb^{2+} and Yb^{3+} ions might also be responsible for this abnormal behavior.

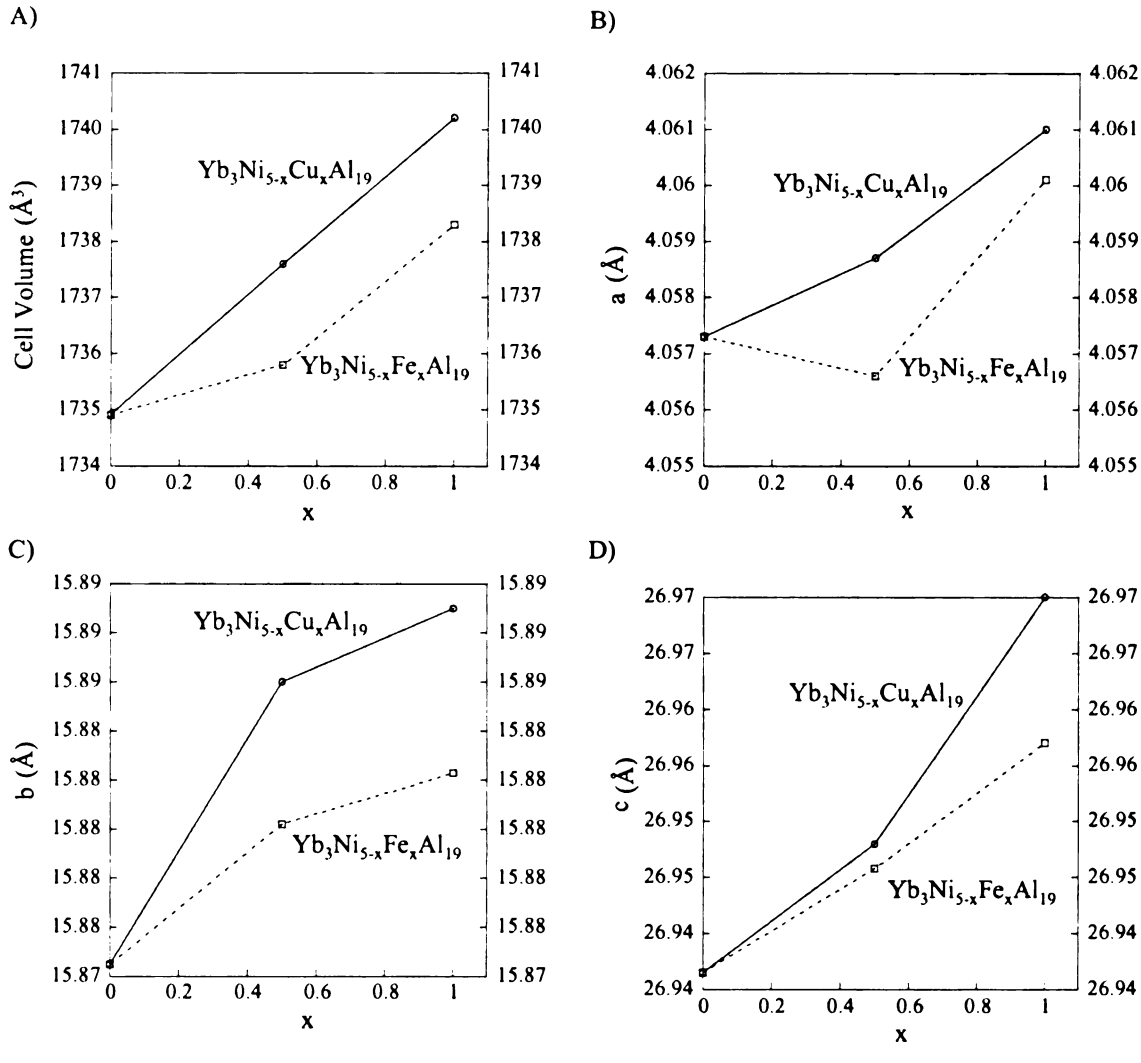

Figure 6-1-1. Cell parameter variations with x for $Yb_3Ni_{5-x}Cu_xAl_{19}$ and $Yb_3Ni_{5-x}Fe_xAl_{19}$ (x = 0, 0.5, 1) at 173 K. A) cell volume; B) *a* cell edge length; C) *b* cell edge length; D) *c* cell edge length.

A)

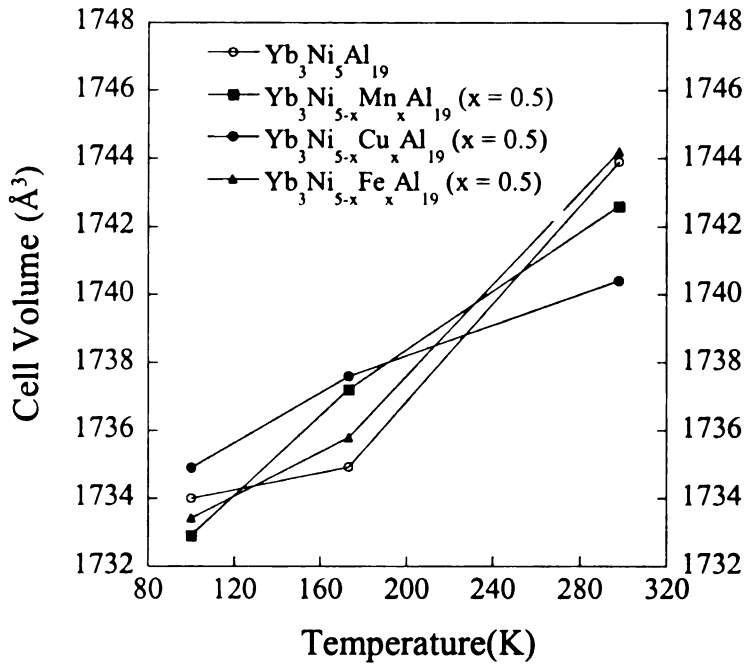

B)

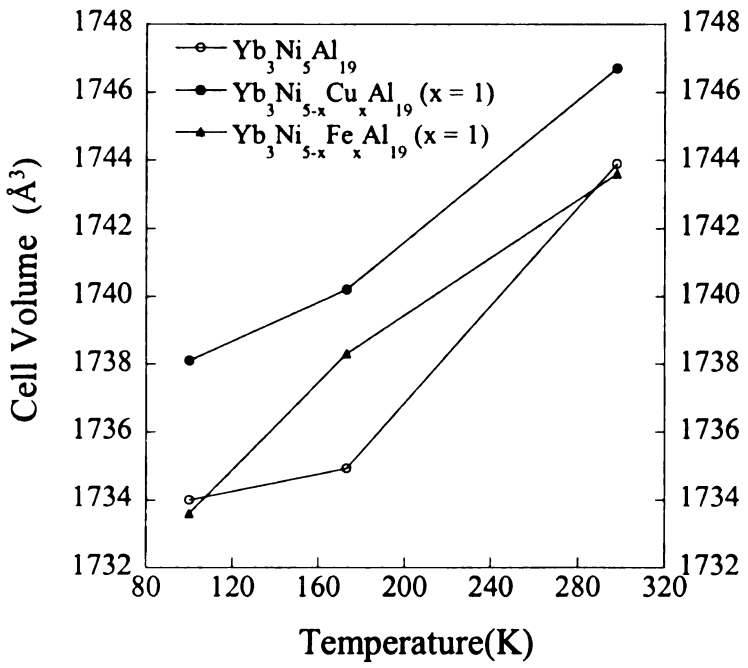

Figure 6-1-2. A) Temperature dependence of the cell volume for $Yb_3Ni_{5-x}TM_xAl_{19}$ (TM = Mn, Cu, Fe; x = 0, 0.5). B) Temperature dependence of cell volume for $Yb_3Ni_{5-x}TM_xAl_{19}$ (TM = Cu, Fe; x = 0, 1).

A)

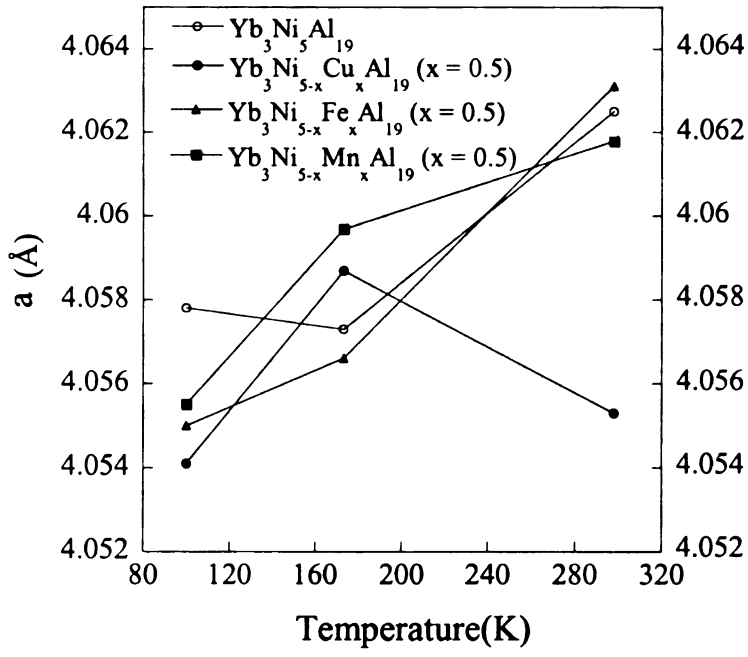

B)

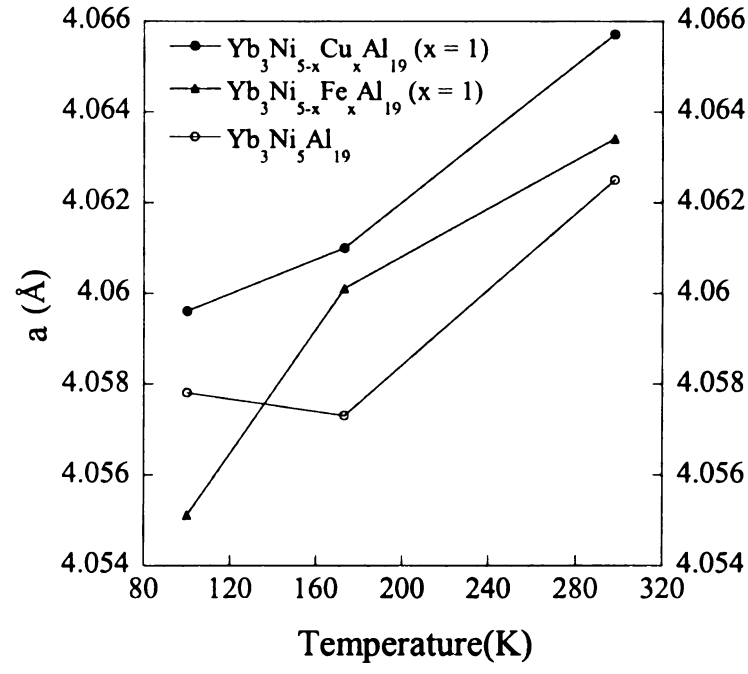

Figure 6-1-3. A) Temperature dependence of the *a* cell edge for $Yb_3Ni_{5-x}TM_xAl_{19}$ (TM = Mn, Cu, Fe; x = 0, 0.5). B) Temperature dependence of the *a* cell edge for $Yb_3Ni_{5-x}TM_xAl_{19}$ (TM = Cu, Fe; x = 0, 1).

A)

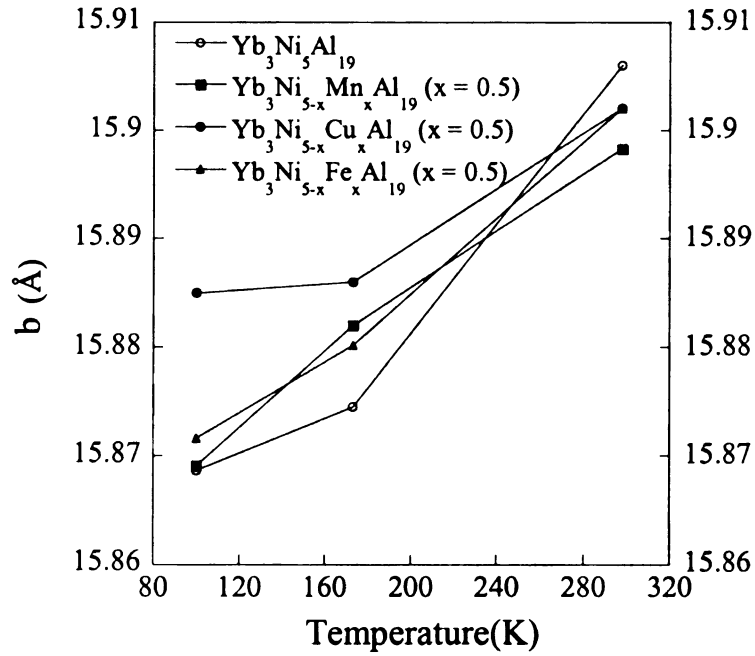

B)

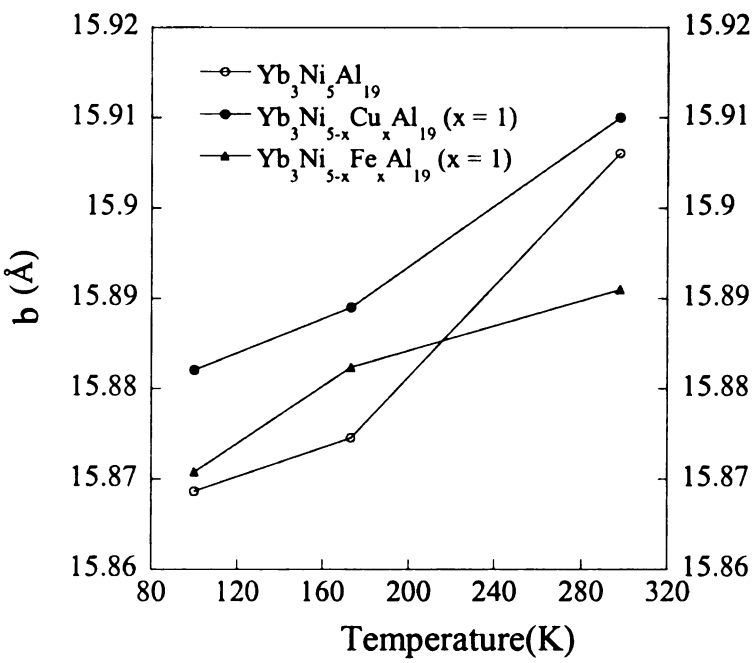

Figure 6-1-4. A) Temperature dependent of *b* cell edge for $Yb_3Ni_{5-x}TM_xAl_{19}$ (TM = Mn, Cu, Fe; x = 0, 0.5). B) Temperature dependent of *b* cell edge for $Yb_3Ni_{5-x}TM_xAl_{19}$ (TM = Cu, Fe; x = 0, 1).

A)

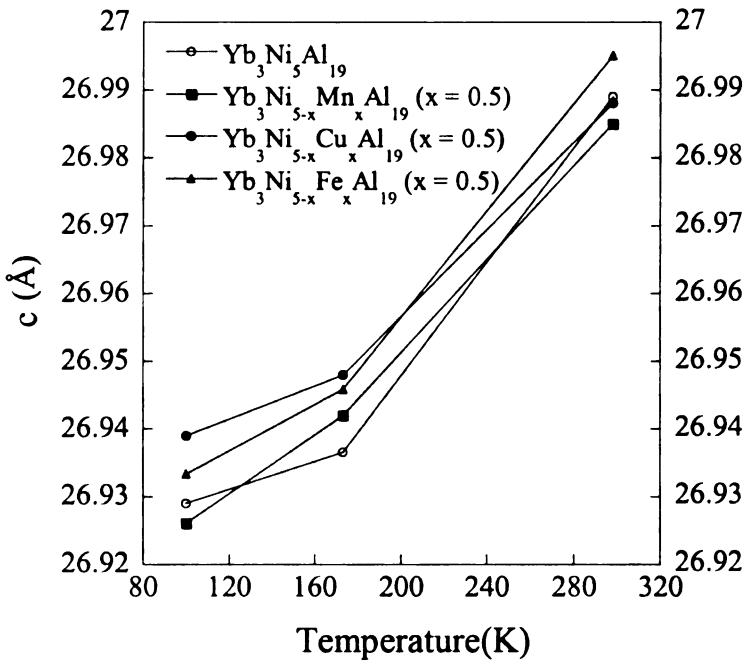

B)

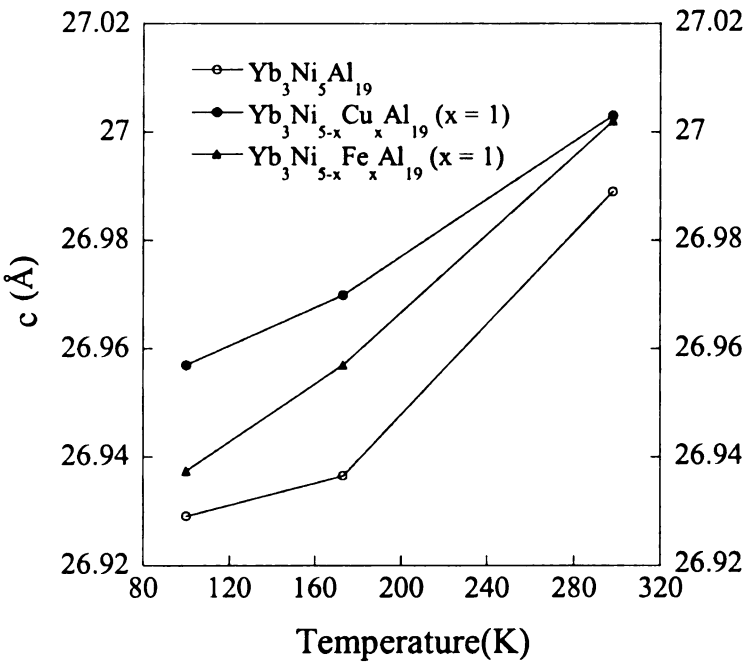

Figure 6-1-5. A) Temperature dependence of the *c* cell edge for $Yb_3Ni_{5-x}TM_xAl_{19}$ (TM = Mn, Cu, Fe; x = 0, 0.5). B) Temperature dependence of the *c* cell edge for $Yb_3Ni_{5-x}TM_xAl_{19}$ (TM = Cu, Fe; x = 0, 1).

Table 6-1-2. Compositional variations of the cell volume for $Yb_3Ni_{5-x}TM_xAl_{19}$ (TM = Cu, Fe, Mn; x = 0, 0.5, 1) obtained on single crystals at temperatures of 100 K, 173 K and 298 K.

$Yb_3Ni_{5-x}TM_xAl_{19}$	V ($Å^3$, 100 K)	V ($Å^3$, 173 K)	V ($Å^3$, 298 K)	% (100 K-298K)
x = 0	1734.0(3)	1734.9(2)	1743.9(7)	0.57
x = 0.5 (TM = Cu)	1734.9(4)	1737.6(4)	1740.4(10)	0.32
x = 1 (TM = Cu)	1738.1(4)	1740.2(4)	1746.7(4)	0.49
x = 0.5 (TM = Fe)	1733.4(2)	1735.8(2)	1744.2(4)	0.62
x = 1 (TM = Fe)	1733.6(2)	1738.3(4)	1743.6(8)	0.58
x = 0.5 (TM = Mn)	1732.9(2)	1737.2(4)	1742.6(4)	0.56

Table 6-1-3. Compositional variations of the *a* cell edge lengths for $Yb_3Ni_{5-x}TM_xAl_{19}$ (TM = Cu, Fe, Mn; x = 0, 0.5, 1) obtained on single crystals at temperatures of 100 K, 173 K and 298 K.

$Yb_3Ni_{5-x}TM_xAl_{19}$	a (Å, 100 K)	a (Å, 173 K)	a (Å, 298 K)	% (100 K-298K)
x = 0	4.0578(4)	4.0573(2)	4.0625(9)	0.12
x = 0.5 (TM = Cu)	4.0541(6)	4.0587(6)	4.0553(13)	0.03
x = 1 (TM = Cu)	4.0596(5)	4.0610(5)	4.0657(5)	0.15
x = 0.5 (TM = Fe)	4.0550(3)	4.0566(3)	4.0631(6)	0.20
x = 1 (TM = Fe)	4.0551(3)	4.0601(5)	4.0634(11)	0.20
x = 0.5 (TM = Mn)	4.0555(3)	4.0597(5)	4.0618(5)	0.16

Table 6-1-4. Compositional variations of the *b* cell edge lengths for $Yb_3Ni_{5-x}TM_xAl_{19}$ (TM = Cu, Fe, Mn; x = 0, 0.5, 1) obtained on single crystals at temperatures of 100 K, 173 K and 298 K.

$Yb_3Ni_{5-x}TM_xAl_{19}$	b (Å, 100 K)	b (Å, 173 K)	b (Å, 298 K)	% (100 K-298K)
x = 0	15.8686(16)	15.8745(9)	15.906(4)	0.24
x = 0.5 (TM = Cu)	15.885(2)	15.886(2)	15.902(5)	0.11
x = 1 (TM = Cu)	15.882(2)	15.889(2)	15.910(2)	0.18
x = 0.5 (TM = Fe)	15.8716(10)	15.8802(10)	15.902(2)	0.19
x = 1 (TM = Fe)	15.8707(11)	15.8823(18)	15.891(4)	0.13
x = 0.5 (TM = Mn)	15.8691(13)	15.882(2)	15.8983(18)	0.18

Table 6-1-5. Compositional variations of the *c* cell edge lengths for $Yb_3Ni_{5-x}TM_xAl_{19}$ (TM = Cu, Fe, Mn; x = 0, 0.5, 1) obtained on single crystals at temperatures of 100 K, 173 K and 298 K.

$Yb_3Ni_{5-x}TM_xAl_{19}$	c (Å, 100 K)	c (Å, 173 K)	c (Å, 298 K)	% (100 K-298K)
x = 0	26.929(3)	26.9365(15)	26.989(6)	0.22
x = 0.5 (TM = Cu)	26.939(4)	26.948(4)	26.988(10)	0.18
x = 1 (TM = Cu)	26.957(3)	26.970(3)	27.003(4)	0.17
x = 0.5 (TM = Fe)	26.9333(17)	26.9458(17)	26.995(4)	0.23
x = 1 (TM = Fe)	26.9374(18)	26.957(3)	27.002(7)	0.24
x = 0.5 (TM = Mn)	26.926(2)	26.942(2)	26.985(3)	0.22

Magnetic Properties:

The temperature dependent magnetic susceptibility data for $Yb_3Ni_{5-x}TM_xAl_{19}$ (TM = Cu, Fe; x = 0, 0.5, 1) are displayed in Figures 6-1-6 & 6-1-7. As the pristine $Yb_3Ni_5Al_{19}$ compound, all the derivatives show paramagnetic behavior and follow Curie-Weiss Law at temperatures above 50 K. As the content of TM — x increases from 0 to 1, the magnitude of the susceptibility increases. The Curie temperature θ and calculated effective magnetic moment μ_{eff} for these samples are summarized in Table 6-1-6. Herein we recall from the first part of this chapter, the parent compound $Yb_3Ni_5Al_{19}$ exhibits intermediate valence behavior and strong antiferromagnetic interactions. As shown in Table 6-1-6, the Curie temperatures θ for $Yb_3Ni_{5-x}Cu_xAl_{19}$ and $Yb_3Ni_{5-x}Fe_xAl_{19}$ are lower than that of $Yb_3Ni_5Al_{19}$. This effect indicates a weakening of the Kondo interaction, since in the scope of single-ion Kondo theories θ is related to T_K by $T_K = m\ |\theta|$, where the coefficient m is usually of the order of 1.[24] Although the Kondo effect is weakening, we have not observed any magnetic ordering in either of the cases until x = 1.

The last column in Table 6-1-6 is the effective magnetic moment μ_{eff} determined by fitting the high temperature data to the Curie-Weiss law. For the Fe-based samples, the μ_{eff} value does not change much. This is possibly because that the Yb valence can change as a function of composition only in materials that undergo a relatively large change in unit cell volume.[25] In $Yb_3Ni_{5-x}Fe_xAl_{19}$ the cell volume expands only 0.19% with x changing from 0 to 1. In the case of $Yb_3Ni_{5-x}Cu_xAl_{19}$, there is no apparent trend with x with regard to the μ_{eff} values. The substitution of Ni by Cu results in the cell volume expansion as confirmed by single crystal X-ray diffraction. Therefore this system is driven by negative chemical pressure toward the Yb^{2+} form while still being in

Yb^{2+}/Yb^{3+} intermediate state. This result is consistent with the fact that the ionic radius of the nonmagnetic Yb ion ($4f^{14}$-state) is larger than that of the magnetic one ($4f^{13}$-state). With more Cu added into the structure, the effective magnetic moment μ_{eff} for $Yb_3Ni_{5-x}Cu_xAl_{19}$ (x = 1) is 7.90 μ_B, which appears to be very close to that of the free Yb^{3+} ion (theoretical value μ_{eff} = 7.86 μ_B per formula). Hence the magnetic $4f^{13}$ configuration is stabilized by the substitution of Ni with Cu. Here the chemical pressure cannot be the reason for this magnetic properties variation, since the substitution causes a volume expansion. The substitution of Ni by Cu should lead to an increment of the number of conduction electrons, and hence to a rise of the Fermi level. Therefore the hybridization between the 4f electrons and the conduction band should decrease causing a quenching of the Kondo effect (indicated by the value of θ). This phenomenon has been observed for the other systems as well, such as $YbCu_5$.[26] The substitution of Cu by Al or Ga shifts the Yb ions from non-magnetic divalent $4f^{14}$ state to localized trivalent $4f^{13}$ state. Since the substitution of Cu by Al/Ga also causes a volume expansion, chemical pressure can be excluded as a driving force of the valence state changes. The number of conduction electrons provided by Al or Ga is more than that of Cu leading to the rise of the Fermi level. For $YbCu_{5-x}Al_x$ ($1.5 \leq x \leq 2$), the 4f band is far below the Fermi level and the s~f *J* mixing is negligible. This example and our experimental observations indicate that in order to explain the changes in the hybridization between 4f electrons and conduction band, both volume and Fermi level modification have to be taken into account.

Table 6-1-6. Magnetic property parameters of $Yb_3Ni_{5-x}Cu_xAl_{19}$ and $Yb_3Ni_{5-x}Fe_xAl_{19}$ (x = 0, 0.5, 1).

Compound	x	c	θ (K)	μ_{eff} (μ_B)
$Yb_3Ni_5Al_{19}$	0	5.73	-551.2	6.77
$Yb_3Ni_{5-x}Cu_xAl_{19}$	0.5	4.59	-276.9	6.06
$Yb_3Ni_{5-x}Cu_xAl_{19}$	1	7.81	-399.0	7.90
$Yb_3Ni_{5-x}Fe_xAl_{19}$	0.5	5.38	-222.5	6.56
$Yb_3Ni_{5-x}Fe_xAl_{19}$	1	6.20	-271.4	7.04

Note: μ_{eff} (theoretical value $Yb_3Ni_5Al_{19}$) = 7.86 μ_B (Yb^{3+})

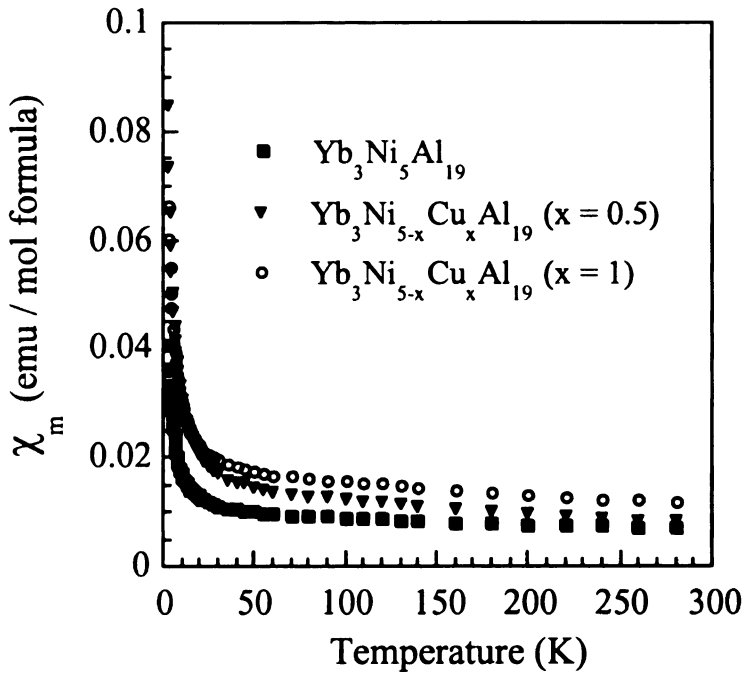

Figure 6-1-6. Magnetic susceptibility of $Yb_3Ni_{5-x}Cu_xAl_{19}$ ($0 \leq x \leq 1$) compounds as a function of temperature from 3 K to 300 K.

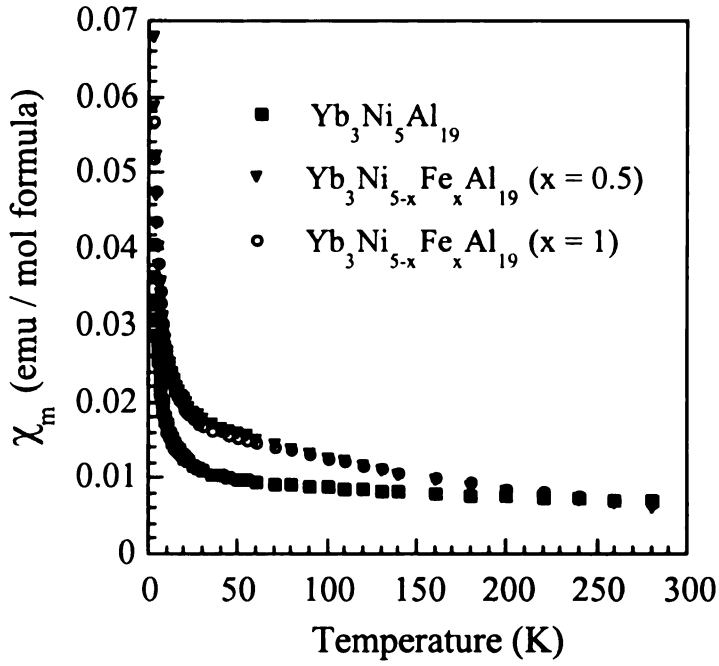

Figure 6-1-7. Magnetic susceptibility of $Yb_3Ni_{5-x}Fe_xAl_{19}$ ($0 \leq x \leq 1$) compounds as a function of temperature from 3 K to 300 K.

6-1-4. Conclusions

The transition metal Ni in $Yb_3Ni_5Al_{19}$ can be substituted to a limited extent by other transition metals such as Mn, Fe or Cu, which are slightly larger and can cause a variation in the number of conduction electrons. Lower cell volume values have been observed for $Yb_3Ni_{5-x}TM_xAl_{19}$ (TM = Mn, Fe) than that of $Yb_3Ni_5Al_{19}$ at 100 K and 298 K; and the electronic valence transition of Yb ions might be one reason causing this abnormal behavior. Substitution of Ni by Mn or Fe does not change significantly the thermal expansion property of $Yb_3Ni_{5-x}TM_xAl_{19}$ from 100 K to 298 K; however the thermal expansion coefficient of $Yb_3Ni_{5-x}Cu_xAl_{19}$ is much lower than that of the parent compound $Yb_3Ni_5Al_{19}$. Magnetic susceptibility measurements indicate that effective magnetic moment can be changed by a modest amount due to the substitution of Ni by Cu, and this may be explained by the effect of cell volume change and fermi level modification.

References:

[1] a) Chandran, L.; Krishna-Murthy, H. R.; Ramakrishnan, T. V. *J. Phys. Condens. Mat.* **1992**, *4*, 7067. b) Zlatic, V.; Costi, T. A.; Hewson, A. C.; Coles, B. R. *Phys. Rev. B* **1993**, *48*, 16152. c) Jaccard, D.; Link, P.; Vargoz, E.; Alami-Yadri, K. *Physica B* **1997**, *230-232*, 297. d) Mushnikov, N. V.; Goto, T.; Kolomiets, A. V.; Yoshimura, K.; Zhang, W.; Kageyama, H. *J. Phys. Condens. Mat.* **2004**, *16*, 2395.

[2] Singh, Y.; Ramakrishnan, S. *Phys. Rev. B* **2003**, *68*, 054419.

[3] Kaczorowski, D.; Andraka, B.; Pietri, R.; Cichorek, T.; Zaremba, V. I. *Phys. Rev. B* **2000**, *61*, 15255.

[4] Trovarelli, O.; Geibel, C.; Buschinger, B.; Borth, R.; Mederle, S.; Grosche, M.; Sparn, G.; Steglich, F.; Brosch, O. Donnevert, L. *Phys. Rev. B* **1999**, *60*, 1136.

[5] a) Doniach, S. *Phy. B* **1977**, *71*, 231. b) Thompson, J. D. and Lawrence, J. L. In *Handbook on the Physics and Chemistry of Rare Earths*; Gschneidner, Jr., K. A., Eyring, L., Lander, G. H., Choppin, G. R., Eds.; North-Holland: Amsterdam, 1994; Vol. 19, p 383.

[6] a) Link, P.; Jaccard, D. *Physica B* **1996**, *223B-224B*, 303. b) Grosche, F. M.; Julian, S. R.; Mathur, N. D.; Carter, F. V.; Lonzarich, G. G. *Physica B* **1997**, *237-238*, 197.

[7] a) Marcano, N.; Paccard, D.; Espeso, J. I.; Allemand, J.; Moreau, J. M.; Kurbakov, A.; Sekine, C.; Paulsen, C.; Lhotel, E.; Gomez-Sal, J. C. *J. Magn. Magn. Mater.* **2004**, *272-276*, 468. b) Garcia, S. J.; Gomez-Sal, J. C.; Rodriguez, F. J.; Espeso, J. I.; Monconduit, L.; Allemand, J.; Paccard, D. *Physica B* **1997**, *230-232*, 117.

[8] Blanco, J. A.; Podesta, M. de; Espeso, J. I.; Gomez-Sal, J. C.; Lester, C.; McEwen, K. A.; Patrikios, N.; Rodriguez, Fernandez, J. *Phys. Rev. B* **1994**, *49*, 15126.

[9] Winkelmann, H.; Abd-Elmeguid, M. M.; Micklitz, H.; Sanchez, J. P.; Geibel, C.; Steglich, F. *Phys. Rev. Lett.* **1998**, *81*, 4947.

[10] Sales, B. C.; Viswanathan, R. *J. Low Temp. Phys.* **1976**, *23*, 449.

[11] Winkelmann, H.; Abd-Elmeguid, M. M.; Micklitz, H.; Sanchez, J. P.; Vulliet, P.; Alami-Yadri, K. Jaccard, D. *Phys. Rev. B* **1999**, *60*, 3324.

[12] Andreica, D.; Amato, A.; Gygax, F.; Pinkpank, M.; Schenck, A. *Physica B* **2000**, *289-290*, 24.

[13] a) Bauer, E.; Hauser, R.; Keller, L.; Fischer, P.; Trovarelli, O.; Sereni, J. G.; Rieger, J. J.; Stewart, G. R. *Phys. Rev. B* **1997**, *56*, 711. b) Bauer, E. *J. Magn. Magn. Mater.* **1999**, *196-197*, 873.

[14] Bauer, E. D.; Bobev, S.; Thompson, J. D.; Hundley, M. F.; Sarrao, J. L.; Lobos, A.; Aligia, A. A. *J. Phys.: Condens. Matter* **2004**, *16*, 4025.

[15] Salvador, J. R.; Guo, F.; Hogan, T.; Kanatzidis, M. G. *Nature* **2003**, *425*, 702.

[16] Drymiotis, F. R.; Lee, Y.; Lawes, G.; Lashley, J. C.; Kimura, T.; Shapiro, S. M.; Migliori, A.; Correa, V.; Fisher, R. A. *Phys. Rev. B* **2005**, *71*, 174304.

[17] a) Gignoux, D.; Givord, F.; Lemaire, R. *J. Less-Common Met.* **1983**, *94*, 165. b) Marcano, N.; Paccard, D.; Espeso, J. I.; Allemand, J.; Moreau, J. M.; Kurbakov, A.; Sekine, C.; Paulsen, C.; Lhotel, E.; Gömez Sal, J. C. *J. Magn. Magn. Mater.* **2004**, *272-276*, 468.

[18] *SMART*, version 5; Siemens Analytical X-ray Systems, Inc.: Madison, WI, 1998.

[19] Saint, Version 4; Simens Analytical X-ray Instruments Inc., Madison, WI.

[20] SADABS, Sheldrick, G. M.; University of Göttingen, Göttingen, Germany.

[21] G.M. Sheldrick, 1995, SHELXTL. Structure Determination Programs, Version 5.0. Siemens Analytical X-ray Instruments, Inc. Madison, WI.

[22] Florio, J. V.; Rundle, R. E.; Snow, A. I. *Acta Crystallogr.* **1952**, *5*, 449.

[23] The metallic radii of Mn, Fe, Ni and Cu are 1.37 Å, 1.26 Å, 1.25 Å and 1.28 Å, respectively. In Wells, A. F. Structural inorganic chemistry, 5th edn, Clarendon Press, Oxford (1984).

[24] Hewson, A. The Kondo Problem to Heavy Fermions, Cambridge Studies in Magnetism, Vol. 2 (Cambridge University Press, 1993).

[25] Bornick, R. M.; Stacy, A. M. *Chem. Mater.* **1994**, *6*, 333.

[26] a) Bauer, E.; Tuan, L.; Hauser, R.; Gratz, E.; Holubar, T.; Hilscher, G.; Yoshimura, K. *J. Magn. Magn. Mater.* **1995**, *140-144*, 1247. b) Bauer, E. *J. Magn. Magn. Mater.* **1999**, *196-197*, 873. c) He, J.; Ling, G.; Ye, Z. *J. Alloys Comd.* **2001**, *325*, 54.

CHAPTER SIX

PART II. Discovery of the New Intermetallic Phases $RENi_{2-x}Fe_xAl_8$ (RE = Eu, Yb) from Liquid Aluminum

6-2-1. Introduction

Yb-containing intermetallics continue to attract considerable attention in the study of interesting behaviors such as Kondo lattice,[1] heavy fermion[2] and mixed valence.[3] In such systems, an array of 4f moments is embedded in a metallic environment, and the nature of the ground state (GS) is determined by the competition between Kondo effect and RKKY (Ruderman-Kittel-Kasuya-Yosida) interactions.[4] The Kondo effect results from the exchange interaction between the conduction electrons and the local magnetic moments leading to scattering events in which the electron spin is flipped. The Kondo effect favors a nonmagnetic GS with a characteristic energy given by the Kondo temperature T_K. The RKKY interaction favors a magnetically ordered GS characterized by T_{RKKY}. In general, the Kondo effect is expected for $T_{RKKY} > T_K$, heavy fermion behavior for $T_{RKKY} \cong T_K$, and mixed valence behavior for $T_K > T_{RKKY}$.

In Part I of Chapter Five, we described crystal growth, structure and physical properties of ternary intermetallics $RE_3Ni_5Al_{19}$ (RE = Sm, Dy, Er, Yb) accessible in liquid Al. In this family $Yb_3Ni_5Al_{19}$ is a Kondo compound with Yb ions showing intermediate valence behavior.[5] We also found that magnetic properties of this compound could be tuned by minor substitutions of Ni by Cu/Fe. The structural integrity of $Yb_3Ni_{5-x}Fe_xAl_{19}$ was retained until x was 1. With more Fe added into the reaction, another new phase appeared in the product and dominated with increasing x — $YbNi_2$.

$_xFe_xAl_8$. This reaction can be optimized by combining stoichiometric amount of Ni and Fe; later we discovered the Eu analogue under the same experimental conditions.

$RENi_{2-x}Fe_xAl_8$ (RE = Eu, Yb) belong to the ternary family $RETM_2X_8$ (TM = Co, Fe; X = Al, Ga) crystallizing in the $CaCo_2Al_8$ structure type.[6] Most compounds reported belonging to this family are ternary with the transition metal mainly Fe, Co or Ni. Among them $CeFe_2Al_8$ is a rare example of the valence fluctuation compound containing element Fe.[7] Mössbauer spectra show that the Fe atoms in $CeFe_2Al_8$ do not carry local magnetic moment.[8] $PrCo_2Al_8$ orders antiferromagnetically at 5 K, with a clear metamagnetic transition occurring at a critical field of 9000 G.[9] Quite a few gallides have also been prepared: the series $REFe_2Ga_8$ (RE = Ce, Pr, Nd, Sm),[10] $RECo_2Ga_8$ (RE = Ce, Pr, Eu, Yb)[10,11] and $RERu_2Ga_8$ (RE = La, Ce, Pr, Nd).[12] The indium-containing isostructural compound $EuRh_2In_8$ was prepared and reported by Pöttgen and co-workers.[13] The compounds $RENi_{2-x}Fe_xAl_8$ (RE = Eu, Yb) we discovered by using Al flux method are the first quaternary examples reported in the literature in this family. In this part of the dissertation, the synthesis, crystal structure, physical properties and ^{57}Fe Mössbauer spectroscopy measurements of $RENi_{2-x}Fe_xAl_8$ (RE = Eu, Yb) will be described.

6-2-2. Experimental Section

Reagents:

The following reagents were used as obtained: rare earth metals (RE = Eu, Yb) (Cerac, 99.9%), Ni (99%, 325 mesh, Sargent, Buffalo Grove, IL), Fe (99.99%, fine powder, Aldrich Chemical, Milwaukee, WI), Al (Cerac, 99.5%, -20 mesh).

Synthesis:

Rare earth metal, Ni and Fe were combined with a large excess of Al in a nitrogen-filled glove box. Alumina crucibles containing the reaction mixture of 1 mmol RE metal (Eu 0.152 g, Yb 0.173 g), 1 mmol Ni (0.059 g), 1 mmol Fe (0.056 g) and 10 mmol Al (0.270 g) were placed into silica tubes (13 mm in diameter), which were then sealed under vacuum (~10^{-4} Torr). The samples were heated to 1000 °C in 15 h, maintained at this temperature for 5 h, and then cooled to 850 °C in 2 h. They were annealed at 850 °C for 3 d, followed by cooling down to 500 °C at a rate of 10 °C/h. Finally the temperature was brought down to 50 °C in 10 h.

The excess aluminum was removed by soaking the crucible in aqueous 5M NaOH solution overnight. The crystalline product remaining after the isolation procedure was rinsed with water and acetone. $RENi_{2-x}Fe_xAl_8$ was the major phase in the product with a yield of 70 %. For RE = Yb, the ternary phase $Yb_3Ni_5Al_{19}$ was also observed.

Scanning Electron Microscopy and Elemental Analysis:

The crystals were picked and placed on a Scanning Electron Microscope (SEM) sample plate using carbon tape. Chemical compositions of the products were determined by Energy Dispersive Spectroscopy (EDS) performed on a JEOL JSM-35C SEM equipped with a NORAN EDS detector. The SEM image of a typical crystal of $YbNi_{2-x}Fe_xAl_8$ is shown in Figure 6-2-1. Data were acquired by applying a 25 kV accelerating voltage with an accumulation time of 40 s. Several crystals were analyzed with the resulting elemental composition corresponding to the ratio 1:1:1:8, which agreed well with the results derived from the single crystal X-ray analysis.

X-ray Crystallography:

Single crystal X-ray diffraction data were collected for $RENi_{2-x}Fe_xAl_8$ (RE = Eu, Yb) at room temperature on a Bruker AXS SMART CCD X-ray diffractometer. A data collection (Mo Kα radiation, λ = 0.71073 Å) was acquired covering a full sphere of reciprocal space using exposure time 20 s/frame. The data acquisition and cell reduction were done with the SMART[14] software package and data processing was performed with the SAINTPLUS program.[15] An empirical absorption correction was applied to the data using the SADABS program.[16] The structures were solved using direct methods and refined with the SHELXTL package program.[17] Systematic absence conditions led to two possible space groups: *Pbam* and *Pba*2. The mean value of $|E^2-1|$ was 0.969 indicating that the structure was likely centrosymmetric. *Pbam* is the centrosymmetric one and has a much lower CFOM value. So *Pbam* was chosen and proved to be correct after final refinement of the structure.

In the structure of $YbNi_{2-x}Fe_xAl_8$, a total of twelve atomic sites including one Yb, two transition metal sites (Ni/Fe) and nine Al sites were identified. Originally the X-ray data was collected at 173 K covering a hemisphere of reciprocal space. Since the atomic numbers of Ni and Fe are very close to each other, different assignments on these two transition metal sites M(1) and M(2) were examined. Two satisfactory solutions were obtained: 1) M(1) site was occupied by Ni and M(2) was occupied by Fe with both sites fully occupied; 2) Both M sites were occupied by a mixture of Ni/Fe: for M(1), Ni and Fe was found to have an occupancy of 84.6 and 15.4%, respectively; while for M(2), the corresponding values were 33.5 and 66.5%. To further confirm the assignment, we collected single crystal X-ray data covering a full sphere of reciprocal space. We found

that if the M(1) site was assigned to Ni and the M(2) assigned to Fe, the occupancy factors were 0.94 and 1.06 respectively, R_1 and wR_2 were 2.39% and 5.72%. If we exchanged these two sites, the occupancy factors were 1.04 and 0.96; R_1 and wR_2 values were 2.40% and 5.77%. As a result of that, M(1) and M(2) sites were refined as a mixed occupancy of Ni and Fe: 42%/58% on M(1) and 62%/38% on M(2) site for Ni/Fe. This refinement gave the lowest R values with R_1 1.86 % and wR_2 3.95 %. And the resulting stoichiometry is in fair agreement with the elemental analysis from EDS.

Data collection parameters and refinement details for $EuNi_{2-x}Fe_xAl_8$ and $YbNi_{2-x}Fe_xAl_8$ can be found in Table 6-2-1. Atomic positions, displacement parameters and anisotropic displacement parameters for $EuNi_{2-x}Fe_xAl_8$ and $YbNi_{2-x}Fe_xAl_8$ are listed in Tables 6-2-2 and 6-2-3.

X-ray powder diffraction data were collected at room temperature on a CPS 120 INEL X-ray diffractometer (Cu Kα) equipped with position-sensitive detector. Experimental powder patterns were compared to the patterns calculated from the single crystal structure solution (by the CrystalDiffract program[18]) to determine the phase identity and purity.

Table 6-2-1. Selected crystal data and structure refinement details for $EuNi_{2-x}Fe_xAl_8$ and $YbNi_{2-x}Fe_xAl_8$.

Empirical formula	$EuNi_{2-x}Fe_xAl_8$	$YbNi_{2-x}Fe_xAl_8$
Formula weight	482.36	503.44
Crystal system	Orthorhombic	Orthorhombic
Space group	*Pbam* (#55)	*Pbam* (#55)
Unit cell dimensions	a = 12.530(2) Å	a = 12.4311(9) Å
	b = 14.503(3) Å	b = 14.4309(10) Å
	c = 4.0326(8) Å	c = 3.9749(3) Å
Volume	732.8(2) $Å^3$	713.06(9) $Å^3$
Z	4	4
Density (calculated)	4.372 Mg/m^3	4.663 Mg/m^3
Absorption coefficient	13.806 mm^{-1}	18.404 mm^{-1}
F(000)	884	912
Crystal size	0.17 × 0.16 × 0.25 mm^3	0.22 × 0.30 × 0.24 mm^3
Theta range for data collection	2.15 to 27.70°	2.82 to 27.79°
Limiting indices	$-16 \le h \le 16$	$-16 \le h \le 16$
	$-18 \le k \le 18$	$-19 \le k \le 18$
	$-5 \le l \le 5$	$-5 \le l \le 5$
Reflections collected	7162	6852
Independent reflections	941 [R(int) = 0.0282]	929 [R(int) = 0.0275]
Completeness to theta = 37.00°	95.4 %	95.6 %
Refinement method	Full-matrix least-squares on F^2	
Data / restraints / parameters	941 / 0 / 70	929 / 0 / 72
Goodness-of-fit on F^2	1.162	1.356
Final R indices [I>2sigma(I)]	R_1 = 0.0186	R_1 = 0.0178
	wR_2 = 0.0395	wR_2 = 0.0397
R indices (all data)	R_1 = 0.0200	R_1 = 0.0186
	wR_2 = 0.0399	wR_2 = 0.0400
Largest diff. peak and hole	0.593 and –0.963 $e.Å^{-3}$	1.064 and –1.407 $e.Å^{-3}$

$R1 = \Sigma(|F_o|-|F_c|)/\Sigma|F_o|$; $wR2 = [\Sigma[w(F_o^2 - F_c^2]/ [\Sigma(w|F_o|^2)^2]]^{1/2}$

Table 6-2-2. Atomic coordinates ($Å \times 10^4$) and equivalent isotropic displacement parameters ($Å^2 \times 10^3$) for $EuNi_{2-x}Fe_xAl_8$ and $YbNi_{2-x}Fe_xAl_8$.

Atom	Wyk. Symbol	x	y	z	Occu.	$U_{(eq)}$*
Eu	4*h*	6592(1)	1811(1)	5000	1.0	8(1)
Ni(1)	4*h*	5342(1)	5913(1)	5000	0.43	7(1)
Fe(1)	4*h*	5342(1)	5913(1)	5000	0.57	7(1)
Ni(2)	4*h*	8505(1)	4015(1)	5000	0.35	6(1)
Fe(2)	4*h*	8505(1)	4015(1)	5000	0.65	6(1)
Al(1)	2*a*	5000	5000	0	1.0	9(1)
Al(2)	4*g*	8399(1)	1197(1)	0	1.0	7(1)
Al(3)	4*g*	7642(1)	3275(1)	0	1.0	8(1)
Al(4)	4*h*	4051(1)	2545(1)	5000	1.0	8(1)
Al(5)	4*g*	4737(1)	1330(1)	0	1.0	7(1)
Al(6)	4*g*	6682(1)	72(1)	0	1.0	8(1)
Al(7)	4*g*	5481(1)	3203(1)	0	1.0	8(1)
Al(8)	2*d*	0	5000	5000	1.0	8(1)
Al(9)	4*h*	6639(1)	4536(1)	5000	1.0	13(1)
Yb	4*h*	6579(1)	1809(1)	5000	1.0	9(1)
Ni(1)	4*h*	5341(1)	5924(1)	5000	0.35	6(1)
Fe(1)	4*h*	5341(1)	5924(1)	5000	0.65	6(1)
Ni(2)	4*h*	8488(1)	4023(1)	5000	0.49	5(1)
Fe(2)	4*h*	8488(1)	4023(1)	5000	0.51	5(1)
Al(1)	2*a*	5000	5000	0	1.0	8(1)
Al(2)	4*g*	8374(1)	1211(1)	0	1.0	8(1)
Al(3)	4*g*	7633(1)	3253(1)	0	1.0	8(1)
Al(4)	4*h*	4027(1)	2546(1)	5000	1.0	7(1)
Al(5)	4*g*	4752(1)	1331(1)	0	1.0	6(1)
Al(6)	4*g*	6678(1)	88(1)	0	1.0	8(1)
Al(7)	4*g*	5481(1)	3188(1)	0	1.0	7(1)
Al(8)	2*d*	0	5000	5000	1.0	6(1)
Al(9)	4*h*	6627(1)	4545(1)	5000	1.0	12(1)

$U_{(eq)}$ is defined as one third of the trace of the orthogonalized U_{ij} tensor.

Table 6-2-3. Anisotropic displacement parameters ($Å^2 \times 10^3$) for $EuNi_{2-x}Fe_xAl_8$ and $YbNi_{2-x}Fe_xAl_8$.

Atom	U^{11}	U^{22}	U^{33}	U^{23}	U^{13}	U^{12}
Eu	8(1)	11(1)	7(1)	0	0	-1(1)
M(1)	8(1)	6(1)	7(1)	0	0	-0(1)
M(2)	6(1)	6(1)	6(1)	0	0	0(1)
Al(1)	12(1)	6(1)	8(1)	0	0	-2(1)
Al(2)	5(1)	8(1)	8(1)	0	0	0(1)
Al(3)	7(1)	10(1)	8(1)	0	0	-2(1)
Al(4)	9(1)	6(1)	10(1)	0	0	0(1)
Al(5)	7(1)	8(1)	7(1)	0	0	-1(1)
Al(6)	9(1)	7(1)	9(1)	0	0	-2(1)
Al(7)	7(1)	6(1)	10(1)	0	0	0(1)
Al(8)	6(1)	6(1)	10(1)	0	0	-2(1)
Al(9)	9(1)	17(1)	13(1)	0	0	4(1)
Yb	8(1)	12(1)	6(1)	0	0	-1(1)
M(1)	7(1)	5(1)	5(1)	0	0	0(1)
M(2)	6(1)	5(1)	4(1)	0	0	0(1)
Al(1)	11(1)	6(1)	6(1)	0	0	-1(1)
Al(2)	6(1)	9(1)	8(1)	0	0	-1(1)
Al(3)	7(1)	10(1)	7(1)	0	0	-2(1)
Al(4)	10(1)	6(1)	7(1)	0	0	0(1)
Al(5)	6(1)	7(1)	6(1)	0	0	-1(1)
Al(6)	10(1)	7(1)	6(1)	0	0	-1(1)
Al(7)	7(1)	7(1)	8(1)	0	0	-1(1)
Al(8)	5(1)	8(1)	6(1)	0	0	-2(1)
Al(9)	8(1)	16(1)	11(1)	0	0	4(1)

The anisotropic displacement factor exponent takes the form:
$-2\pi^2[h^2a^{*2}U^{11}+...+2hka^*b^*U^{12}]$

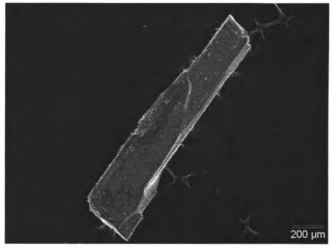

Figure 6-2-1. SEM image of a typical crystal of $YbNi_{2-x}Fe_xAl_8$.

Physical Properties Characterization:

Magnetic measurements were conducted on single crystal and polycrystalline samples of $YbNi_{2-x}Fe_xAl_8$. Field-cooled and zero-field cooled dc magnetization measurements were performed for the above samples using a Quantum Design MPMS SQUID magnetometer. EDS-analyzed crystals were ground into powder, which was sealed in kapton tape and placed into the magnetometer. The data were collected in the temperature range 3-300 K at 1000 G, while field dependent magnetic measurements, conducted at 5 K, were carried out in fields up to ± 55000 G. A diamagnetic correction was applied to the data to account for core diamagnetism.

Electrical resistivity of $YbNi_{2-x}Fe_xAl_8$ was measured over the temperature range 5 K ~ 300 K using a four-probe dc technique with contacts made using silver paste on a pressed-pellet sample. Single crystals of $YbNi_{2-x}Fe_xAl_8$ were selected, ground into powder and pressed into a pellet of 3 mm length, 2 mm width and 0.2 mm thickness. The pellet sample was annealed at 350 °C for 3h. Thermopower data were collected on the

pellet from 300 K to 400 K with a MMR Technologies, Inc. Seebeck measurement system.

Mössbauer Spectroscopy:

The Mössbauer spectra were taken on a polycrystalline sample of $YbNi_{2-x}Fe_xAl_8$ with a constant-acceleration spectrometer, equipped with a ^{57}Co source in a Rh matrix. The spectrometer was calibrated with metallic iron, and the isomer shift values were reported relative to α-Fe. A closed-loop refrigerator system was used for the low temperature measurements. An Oxford Instrument Variox 316 cryostat was used for measurements at liquid-helium temperature.

6-2-3. Results and Discussion

Synthesis:

$YbNi_{2-x}Fe_xAl_8$ was discovered during an attempt to substitute Ni in $Yb_3Ni_5Al_{19}$ with Fe with the molar ratio 0.8 : 0.2 for Ni : Fe. PXRD showed that besides $Yb_3Ni_5Al_{19}$, another phase appeared in the product and elemental analysis indicated almost equal amount of Ni and Fe. Single crystal X-ray diffraction analysis confirmed the existence of $YbNi_{2-x}Fe_xAl_8$ which crystallizes in a different structure from $Yb_3Ni_5Al_{19}$. To optimize this reaction, equal amount of Ni and Fe metals were combined to form $YbNi_{2-x}Fe_xAl_8$ with a yield as high as 70%; however a large percentage of $Yb_3Ni_5Al_{19}$ remained as the side product. Interestingly, when we tried to grow larger single crystals of $YbNi_{2-x}Fe_xAl_8$ by scaling up the reaction, i.e. the molar ratio of Yb : Ni : Fe : Al as 3 : 3 : 3 : 30, the yield was greatly improved (90 %). To make the other rare earth analogs of this phase,

we tried the reactions with equal amount of Ni and Fe metals. So far only $EuNi_{2-x}Fe_xAl_8$ was obtained which will also be described in this section. For the other rare earth metals only $RE_3Ni_5Al_{19}$ was found in the product.

Crystal Structure:

$RENi_{2-x}Fe_xAl_8$ (RE = Eu, Yb) crystallize in a known structure type of $CaCo_2Al_8$ with the space group *Pbam*.[6] This is a rather stable structural arrangement as a number of isotypical ternary phases have been reported which we already described in the introduction section. The $RENi_{2-x}Fe_xAl_8$ family seems to be the first quaternary analogue of the $CaCo_2Al_8$ structure type. Herein we will briefly describe the structure and local coordination geometries with $YbNi_{2-x}Fe_xAl_8$ as an example. In this structure, there are one crystallographically independent Yb site, two M sites (mixed occupied by Ni and Fe) and nine Al sites. Figure 6-2-2 depicts the structure of $YbNi_{2-x}Fe_xAl_8$ in polyhedral view down the *c*-axis. The M(1)- and M(2)-centered polyhedra, composed of Al atoms, form a three-dimensional framework with Yb ions sitting in the channels. Each channel is composed of two M(1)-polyhedra and three M(2)-polyhedra which connect with each other by sharing Al corners. As is shown in Figure 6-2-3, the coordination environments of M(1) and M(2) atoms are similar and best described as tri-capped trigonal prisms composed of Al atoms. On the *ab* plane, the M(1) polyhedra are condensed into dimers by sharing faces containing two Al(1) and two Al(9) atoms. The bond distance between M(1) atoms is 2.8051(12) Å. Along the *c*-direction, these M(1)-centered polyhedra share Al trianglular faces containing Al(1), Al(2) and Al(7) atoms. The distances between these Al atoms range from 2.664(2) Å to 2.997(2) Å. The coordination geometry of the

M(2) atom resembles that of M(1): each M(2) atom is surrounded by nine Al atoms which form a tri-capped trigonal prism. Along the *c*-axis, these trigonal prisms share the Al-based trigonal faces but without forming M(2)-dimers on the *ab*-plane.

The Yb atoms reside in distorted penta-capped pentagonal prisms composed of Al atoms. This geometry is similar as those of the Yb atoms in $Yb_3Ni_5Al_{19}$ which are also in distorted fashion.[5] The distance from Yb to Al(9) atoms is 3.917(2) Å, much longer than the distances from Yb to the other Al neighbors which are between 3.1009(11) Å to 3.2717(3) Å.

Physical Properties:

Because of the explicit needle morphology and the large crystal size of $YbNi_{2-x}Fe_xAl_8$, we were able to study its magnetic properties both isotropically (polycrystalline) and anisotropically (single crystal). The temperature dependent molar magnetic susceptibility data conducted on a polycrystalline sample is shown in Figure 6-2-4A. Above 50 K, the inverse magnetic susceptibility data can be fitted to the Curie-Weiss Law, with calculated $\mu_{eff} = 2.19\ \mu_B$, which is between the theoretical number for Yb^{2+} (0 μ_B) and Yb^{3+} (4.54 μ_B). This suggests that the Yb ions are of mixed valency nature in this compound. It is noteworthy that no broad hump was observed in the susceptibility data which is typical of mixed-valent systems.[19] In some other mixed-valent Yb-containing compounds, this broad hump is not observed either, such as YbGaGe[20] and $Yb_2Ir_3Ge_5$.[21]

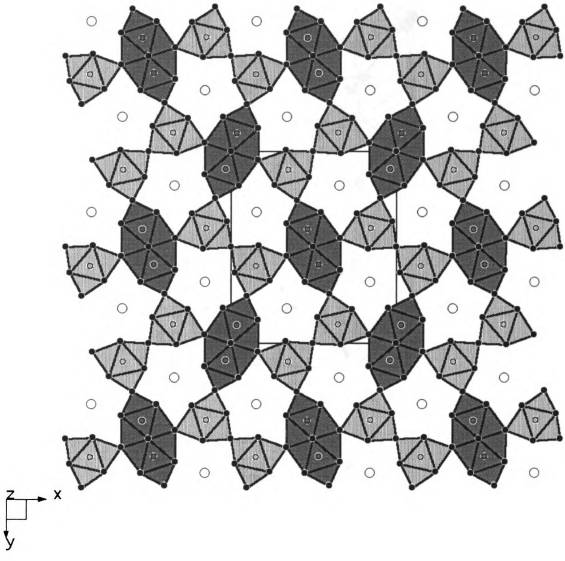

Figure 6-2-2. Crystal structure of $YbNi_{2-x}Fe_xAl_8$ in polyhedra of M(1) and M(2) atoms viewed down the [001] direction. Large circles: Yb; black dots: Al; darker shaded circles: M(1); lighter shaded circles: M(2).

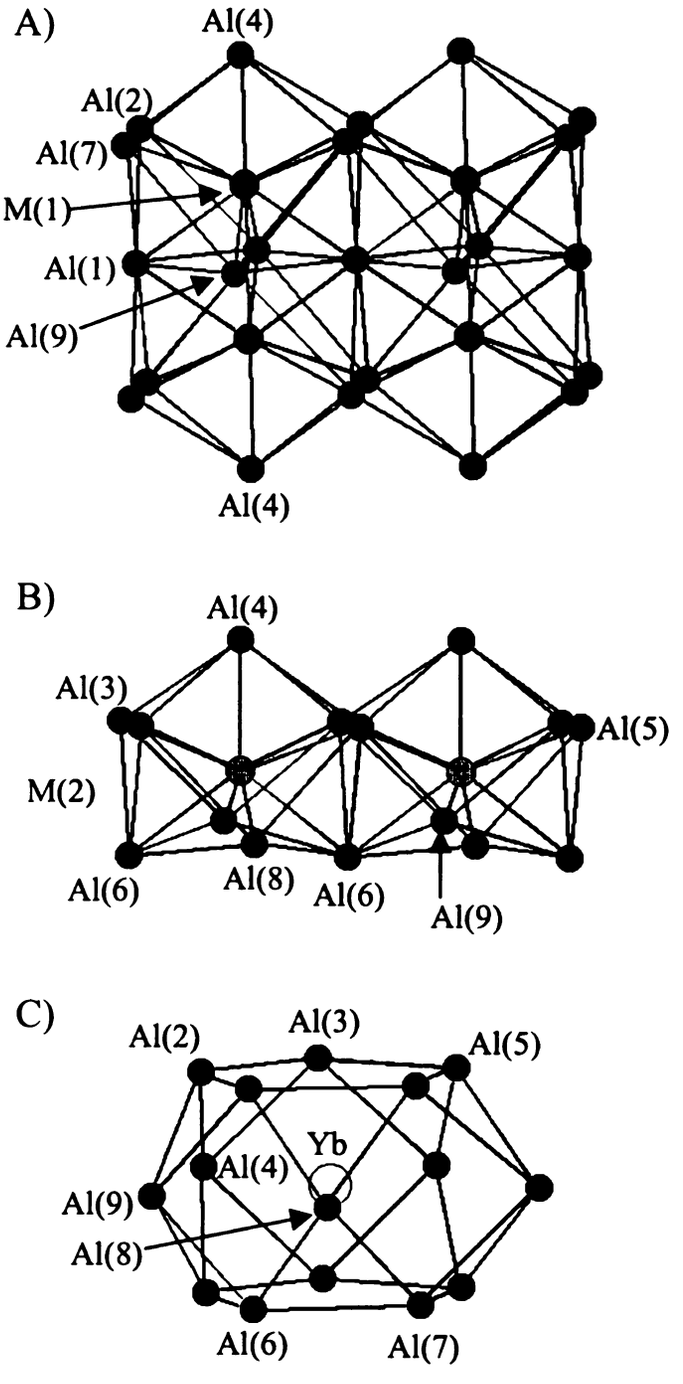

Figure 6-2-3. Coordination environments of M(1), M(2) and Yb atoms.

Table 6-2-4. Bond lengths (Å) for $EuNi_{2-x}Fe_xAl_8$ and $YbNi_{2-x}Fe_xAl_8$.

Bond	Distance	Bond	Distance
Eu-Al(2) ×2	3.1599(11)	M(2)-Al(8)	2.3559(7)
Yb-Al(2) ×2	3.1164(10)		2.3544(6)
RE-Al(3) ×2	3.2102(11)	M(2)-Al(9)	2.4560(16)
	3.1695(11)		2.4380(15)
RE-Al(4) ×2	3.2187(14)	Al(1)-Al(2) ×2	2.6523(14)
	3.1892(14)		2.6768(14)
RE-Al(5) ×2	3.1555(11)	Al(1)-Al(7) ×2	2.6752(14)
	3.1009(11)		2.6870(13)
RE-Al(6) ×2	3.2308(12)	Al(1)-Al(9) ×4	2.9551(11)
	3.1890(11)		2.9162(10)
RE-Al(7) ×2	3.1751(11)	Al(2)-Al(4) ×2	2.8397(14)
	3.1326(10)		2.8028(13)
RE-Al(8)	3.2982(5)	Al(2)-Al(6)	2.7004(19)
	3.2717(3)		2.664(2)
M(1)-Al(1) ×2	2.4497(5)	Al(2)-Al(7)	2.7494(19)
	2.4353(4)		2.7644(19)
M(1)-Al(2) ×2	2.5925(10)	Al(3)-Al(4) ×2	2.9316(14)
	2.5874(9)		2.8834(14)
M(1)-Al(4)	2.3632(15)	Al(3)-Al(5)	2.687(2)
	2.3470(14)		2.708(2)
M(1)-Al(7) ×2	2.6029(10)	Al(3)-Al(6)	2.740(2)
	2.5804(9)		2.7887(19)
M(1)-Al(9) ×2	2.5740(16)	Al(3)-Al(7)	2.710(2)
	2.5576(15)		2.682(2)

Table 6-2-4. (Continued) bond lengths (Å) for $EuNi_{2-x}Fe_xAl_8$ and $YbNi_{2-x}Fe_xAl_8$.

Bond	Distance	Bond	Distance
M(1)-M(1)	2.7825(13)	Al(3)-Al(9) ×2	2.9980(15)
	2.8051(12)		2.997(2)
M(2)-Al(3) ×2	2.5270(9)	Al(4)-Al(5) ×2	2.8125(13)
	2.5177(9)		2.8048(13)
M(2)-Al(4)	2.3638(15)	Al(4)-Al(7) ×2	2.8612(14)
	2.3653(14)		2.8470(14)
M(2)-Al(5)	2.5885(10)	Al(5)-Al(6)	2.7004(19)
	2.5892(10)		2.717(2)
M(2)-Al(6)	2.5432(10)	Al(5)-Al(7)	2.8717(19)
	2.5256(9)		2.8349(19)

The negative value of Weiss constant (θ = -92.2 K) implies strong antiferromagnetic coupling and/or a Kondo effect. However no magnetic ordering was observed down to 3 K. Below 20 K, the inverse magnetic susceptibility deviated from a linear behavior, probably due to thermal depopulation of the crystal field effects.

The magnetization behavior of $YbNi_{2-x}Fe_xAl_8$ with the field perpendicular or parallel to the *c*-axis is shown in Figure 6-2-4B. In both cases there was no sign of magnetic saturation up to 55000 G; and substantial magnetic anisotropy was observed. When the field was perpendicular to the *c*-axis, the magnetization values were higher than those when the field was parallel to the *c*-axis. This orientation dependent behavior implies that the magnetic spins are confined to the *ab* plane. In the case of applied field perpendicular to the *c*-axis, the magnetization reached 0.16 μ_B at 55000 G, which is only about 4% of the saturation value.

Figure 6-2-5A shows the temperature dependent electrical resistivity $\rho(T)$ of $YbNi_{2-x}Fe_xAl_8$, which indicates metallic behavior of this material. The resistivity value at room temperature was ~185 $\mu\Omega$·cm, and it decreased with decreasing temperature tending towards a constant value at low temperatures. A broad shoulder was observed around 160 K, characteristic of intermediate valence systems.[19] The thermoelectric power, shown in Figure 6-2-5B, was about -1 μV/K at room temperature. The small magnitude of the thermopower is also indicative of the metallic system of $YbNi_{2-x}Fe_xAl_8$; and the negative values suggest that it is an n-type material.

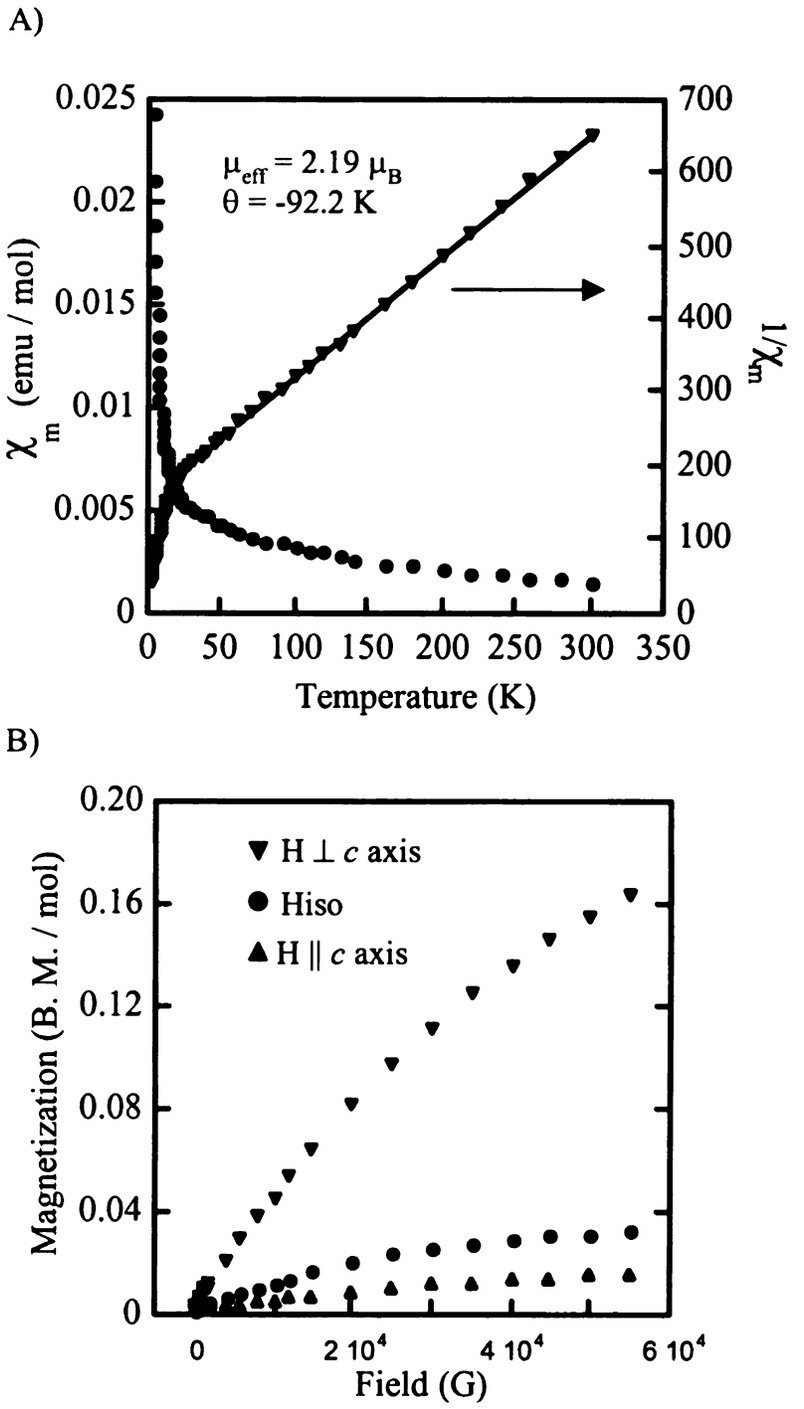

Figure 6-2-4. A) Temperature dependent magnetic susceptibility of a polycrystalline sample of $YbNi_{2-x}Fe_xAl_8$ under the field of 1000 G. B) Molar magnetization of $YbNi_{2-x}Fe_xAl_8$ single crystals oriented with [001] axes perpendicular, parallel to the external magnetic field and isotropic in fields up to 55000 G.

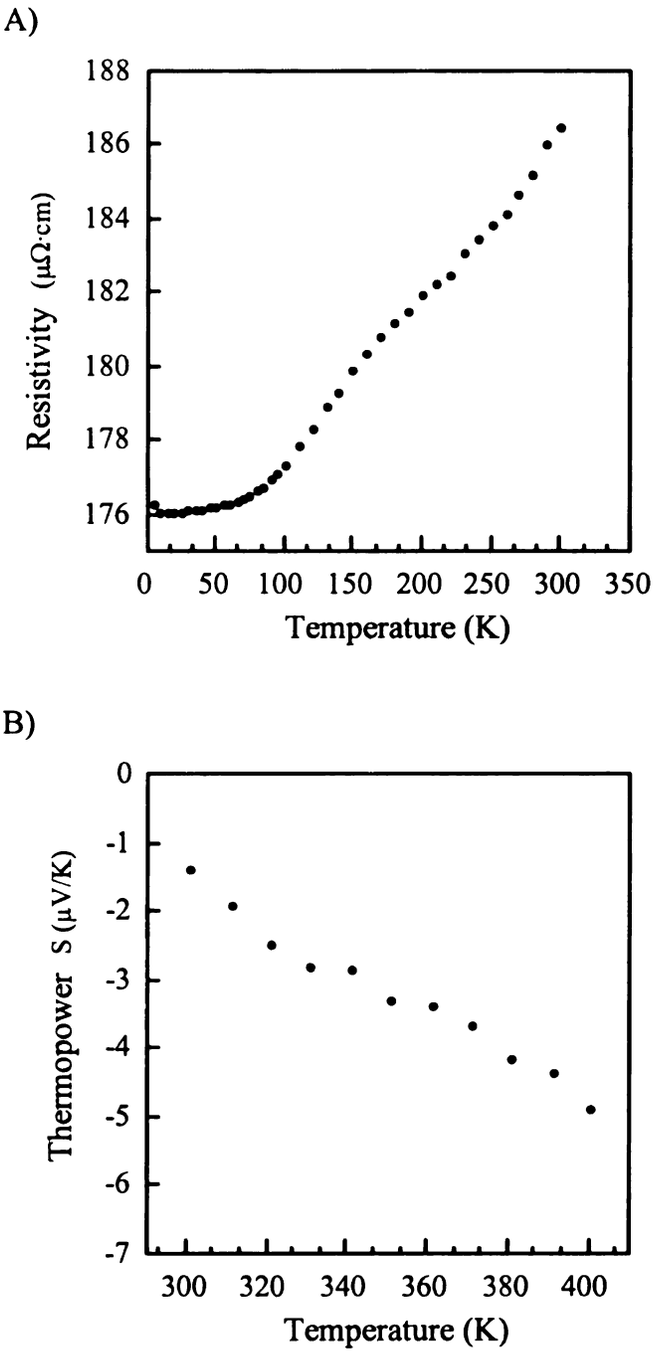

Figure 6-2-5. A) Temperature dependence of the electric resistivity on a polycrystalline pellet of $YbNi_{2-x}Fe_xAl_8$. B) Temperature dependence of the thermoelectric power on a single crystal of $YbNi_{2-x}Fe_xAl_8$.

Mössbauer Spectroscopy:

To further probe the electronic state of Fe in $RENi_{2-x}Fe_xAl_8$, ^{57}Fe Mössbauer spectroscopy was taken at temperatures of 80 K and RT and the spectrum was fitted with Lorentzian form, shown in Figure 6-2-6. The Mössbauer spectrum parameters are listed in Table 6-2-5.

Each spectrum consists of two doublets indicting two Fe atomic sites (M1 and M2) in the structure. The doublet with large quadrupole splitting is assigned to site Fe(1) while the doublet with the smaller quadrupole value is attributed to site Fe(2), because Fe(1) is also bonded to another Fe(1) atom besides nine Al atoms and the principal electric field gradient at Fe(1) is larger than that of Fe(2). For the Fe(1) site, the quadrupole splitting values ΔEq at RT and 80 K are the same — 0.63(2) mm/s; For the Fe(2) site, the ΔEq values are 0.37(2) mm/s and 0.41(2) mm/s at RT and 80 K, respectively. The similarities of the quadrupole splitting values ΔEq at different temperatures suggest the absence of any transition in this temperature range. The isomer shift value of Fe(1) is 0.25(2) mm/s at 80 K, very close to the values of metallic Fe; however the isomer shift value of Fe(2) is much higher — 0.42(2) mm/s which has more ferric character. Similar nonmagnetic character of the Fe atoms was observed in other Fe-containing intermetallic compounds, such as $REFe_2Al_{10}$,[22] $RE_2Fe_3Si_5$,[23] $RE_4Fe_{2+x}Al_{7-x}Si_8$[24] and $RE_4FeGa_{12-x}Ge_x$.[25]

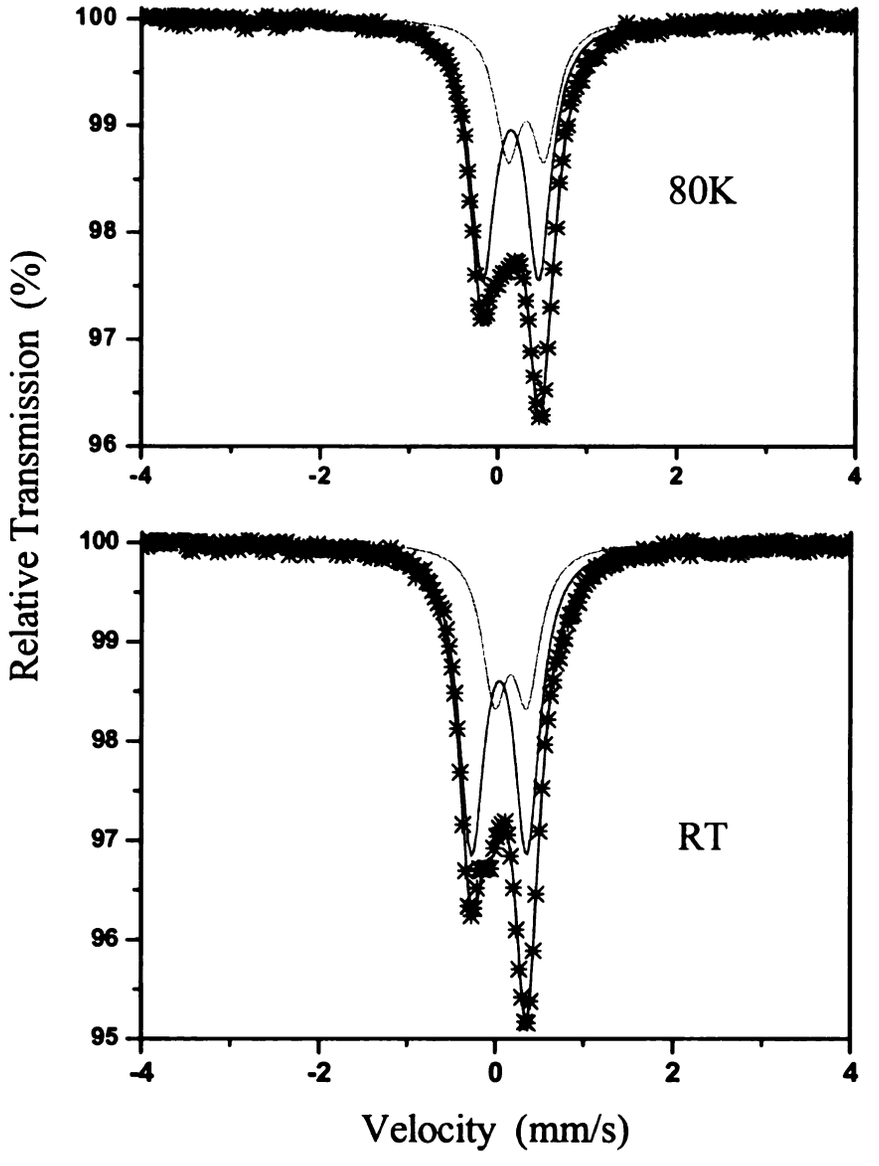

Figure 6-2-6. ^{57}Fe Mössbauer spectrum of $YbNi_{2-x}Fe_xAl_8$ at 80 K and RT.

Table 6-2-5. ^{57}Fe Mössbauer spectra parameters for $YbNi_{2-x}Fe_xAl_8$ at RT and 80 K.

	Site M(1)			Site M(2)		
Temperature (K)	IS_{Fe} (mm/s)	ΔEq (mm/s)	Area (%)	IS_{Fe} (mm/s)	ΔEq (mm/s)	Area (%)
300	0.15(2)	0.63(2)	67(2)	0.28(2)	0.37(2)	33(2)
80	0.25(2)	0.63(2)	66(2)	0.42(2)	0.41(2)	34(2)

6-2-4. Conclusions

New quaternary intermetallic aluminides $RENi_{2-x}Fe_xAl_8$ (RE = Eu and Yb) were synthesized by using Al as a high temperature solvent. The $RENi_{2-x}Fe_xAl_8$ species are the first quaternary analogues of the $CaCo_2Al_8$ structure type. Mixed occupancy is present on both transition metal sites (M1 and M2) by Ni and Fe. Both magnetic properties and Mössbauer spectra show that the Fe atoms do not carry magnetic moments. Temperature dependent magnetic susceptibility indicates that the Yb atoms are in an intermediate oxidation state with effective magnetic moment $\mu_{eff} = 2.19\ \mu_B$. The magnetization behavior studies point out that the *ab* plane is the easy plane on which the magnetic moments are confined. Both resistivity and thermopower measurements exhibit metallic character of $YbNi_{2-x}Fe_xAl_8$. Furthermore ^{57}Fe Mössbauer spectra investigations confirm the absence of magnetic ordering in this material.

References:

[1] Singh, Y.; Ramakrishnan, S. *Phys. Rev. B* **2003**, *68*, 054419.

[2] Kaczorowski, D.; Andraka, B.; Pietri, R.; Cichorek, T.; Zaremba, V. I. *Phys. Rev. B* **2000**, *61*, 15255.

[3] Trovarelli, O.; Geibel, C.; Buschinger, B.; Borth, R.; Mederle, S.; Grosche, M.; Sparn, G.; Steglich, F.; Brosch, O. Donnevert, L. *Phys. Rev. B* **1999**, *60*, 1136.

[4] Doniach, S. *Physica B&C* **1977**, *91B*, 231.

[5] Bauer, E. D.; Bobev, S.; Thompson, J. D.; Hundley, M. F.; Sarrao, J. L.; Lobos, A.; Aligia, A. A. *J. Phys.: Condens. Matter* **2004**, *16*, 4025.

[6] Czech, E.; Cordier, G.; Schaefer, H. *J. Less-Common Met.* **1983**, *95*, 205.

[7] Koterlin, M. D.; Morokhivskii, B. S.; Lapunova, R. V.; Sichevich, O. M. *Sov. Phys. Solild State* **1989**, *31*, 1826.

[8] Tamura, I.; Mizushima, T.; Isikawa, Y.; Sakurai, J. *J. Magn. Magn. Mater.* **2000**, *220*, 31.

[9] Tougait, O.; Kaczorowski, D.; Noel, H. *J. Solid State Chem.* **2005**, *178*, 3639.

[10] Sichevits, O. M.; Lapunova, R. V.; Grin, Yu. N.; Yarmolyuk, Ya. P. *Izv. Akad. Nauk SSSR, Metally* **1985**, *6*, 117.

[11] Gladyshevskii, R. E.; Yarmolyuk, Ya. P.; Grin, Yu. N. *Kristallografiya* **1983**, *28*, 1090.

[12] Schlüter, M.; Jeitschko, W. *Inorg. Chem.* **2001**, *40*, 6362.

[13] Pöttgen, R. Kumann, D. *Z. Anorg. Allg. Chem.* **2001**, *627*, 55.

[14] *SMART*, version 5; Siemens Analytical X-ray Systems, Inc.: Madison, WI, 1998.

[15] *Saint*, Version 4; Simens Analytical X-ray Instruments Inc., Madison, WI.

[16] *SADABS*, Sheldrick, G. M.; University of Göttingen, Göttingen, Germany.

[17] G.M. Sheldrick, 1995, *SHELXTL*. Structure Determination Programs, Version 5.0. Siemens Analytical X-ray Instruments, Inc. Madison, WI.

[18] CrystalDiffract is © 1995-1996, Dr. David C. Palmer.

[19] Sales, B. C.; Wohlleben, D. K. *Phys. Rev. Lett.* **1975**, *35*, 1240.

[20] Salvador, J. R.; Guo, F.; Hogan, T.; Kanatzidis, M. G. *Nature* **2003**, *425*, 702.

[21] Singh, Y.; Ramakrishnan, S. *Phys. Rev. B* **2003**, *68*, 054419.

[22] Tiede, V. M. T.; Ebel, T.; Jeitschko, W. J. *J. Mater.Chem.* **1998**, *8*, 125.

[23] Moodenbaugh, A. R.; Cox, D. E.; Vining, C. B.; Segre, C. U. *Phys. Rev.* **1984**, *B29*, 109.

[24] Sieve, B.; Sportouch, S.; Chen, X. Z.; Cowen, J. A.; Brazis, P.; Kannewurf, C. R.; Papaefthymiou, V.; Kanatzidis, M. G. *Chem. Mater.* **2001**, *13*, 273.

[25] Zhuravleva, M. A.; Wang, X.; Schultz, A. J.; Bakas, T.; Kanatzidis, M. G. *Inorg. Chem.* **2002**, *41*, 6056.

CHAPTER SEVEN

Synthesis and Characterization of New Zintl Phases: Yb_3AlSb_3 and $Yb_9Al_3Sb_9$

7-1. Introduction

In the past decade, there has been increasing interest in Zintl phases composed of an alkaline-earth metal (Ca, Sr, Ba) or divalent rare earth metal (Eu, Yb), a transition metal (Mn, Zn, Cd) or a group 13 element (Al, Ga, In) and a pnicogen element (P, As, Sb, Bi).[1] In these systems, the classic octet rule (8-N) is satisfied and closed shell configuration is achieved. These Zintl phases present a striking variety of structural features and interesting electronic and magnetic properties. The 14-1-11 family $R_{14}(TM)Pn_{11}$ (R = Ca, Sr, Ba, Eu, Yb; TM = Mn, Zn, Cd; Pn = P, As, Sb, Bi) is such an example that offers a wide range of interesting properties. $Eu_{14}MnSb_{11}$ is an intermetallic collosal magnetoresistive material, presenting a metal-insulator transition associated with a ferromagnetic phase transition at 92 K.[2] $Eu_{14}MnBi_{11}$ orders antiferromagnetically and shows a large negative magnetoresistance possibly associated with strong ferromagnetic fluctuations.[3] $Yb_{14}MnSb_{11}$ exhibits a ferromagnetic transition at 52 K with well-separated Mn^{3+} ions acting as local moments.[4] $Yb_{14}AlSb_{11}$ is a nonmagnetic nonmetallic Zintl compound; when substituting trivalent aluminum ions with divalent Zn, the isostructural compound $Yb_{14}ZnSb_{11}$ is formed with Yb ions in intermediate valence to balance the charge.[5] The 14-1-11 family is not the only example that is reluctant to deviate from balanced charge. $Yb_9Zn_4Bi_9$ crystallizes in the orthorhombic $Ca_9Zn_4Bi_9$ structure type, and magnetic susceptibility measurements indicated intermediate oxidation state of Yb^{2+}/Yb^{3+}.[6] So this compound was rationalized as $(Yb^{3+})(Yb^{2+})_8(Zn^{2-}$

$)_4(Bi^{2-})_2(Bi^{1-})_7$. This discovery raised questions as to the nature of the parent compound $Ca_9Zn_4Bi_9$, which contains the same $[Zn_4Bi_9]^{19-}$ ribbons.[7] However, there are only nine divalent cations (Ca^{2+}) in this compound and obviously the electron count falls one electron short. Later Kauzlarich and co-workers reported Zintl compounds $Yb_9Zn_{4+x}Sb_9$ and $Ca_9Zn_{4.5}Sb_9$, the structure of which can be regarded as an interstitially stabilized variant of the $Ca_9Zn_4Bi_9$ structure type.[8] The charges of these two compounds can be balanced by accommodating additional Zn atoms, with both ytterbium and calcium ions in +2 oxidation state, which is supported by magnetic measurements. This discovery opened up the opportunity to reexamine the nature of previously reported fully stoichiometric compounds $AE_9TM_4Pn_9$ (AE = Ca, Sr; TM = Zn, Cd, Mn; Pn = Sb, Bi). It might be interesting to study this system by substituting divalent Zn with trivalent Al atoms in an attempt to tune the electronic properties.

Herein we describe the synthesis, structural characterization and physical properties of new Zintl phase $Yb_9Al_3Sb_9$ grown from Al flux. It also crystallizes in the $Ca_9Zn_4Bi_9$ structure type; the Zintl concept in this compound still holds with one of the Al sites half occupied. During an attempt to explore the quaternary system Yb/Al/Sb/Si in liquid Al, another new phase Yb_3AlSb_3 was formed. It crystallizes in the Ca_3AlSb_3 structure type and is the first rare earth analogue of the family AE_3MPn_3 (AE = Ca, Sr, Ba; M = Al, Ga; Pn = Sb, Bi). Notably, Yb_3AlSb_3 has the same stoichiometry as $Yb_9Al_3Sb_9$, while they present different structure types and properties. In this chapter, synthesis, crystal structure, physical properties and electronic structure calculations of Yb_3AlSb_3 and $Yb_9Al_3Sb_9$ will be described.

7-2. Experimental Section

Reagents:

The following reagents were used as obtained: Yb (Cerac, 99.9%), Sb (Cerac, chips, 99.999%), Al (Cerac, 99.5%, -20 mesh).

Synthesis:

All manipulations were performed in a nitrogen-filled dry box. Yb, Sb and Al metals were loaded in alumina crucibles, which were then put into the silica tubes (13mm in diameter). These silica ampoules were sealed under vacuum (~10^{-4} Torr).

Initially $Yb_9Al_3Sb_9$ was obtained by combining 1 mmol Yb metal (0.173 g) and 1 mmol Sb (0.122 g) with a large excess amount of Al (0.810 g). The sample was heated to 1000 °C in 15 h, maintained at this temperature for 36 h, then slowly cooled to 250 °C in 3 d. Finally the temperature was brought down to 50 °C in 5 h. The excess aluminum was removed by soaking the crucible in aqueous 5M NaOH solution overnight. The solid product remaining after the isolation procedure was rinsed with water and acetone. The yield of $Yb_9Al_3Sb_9$ was about 60% with the side products mainly $Yb_{14}AlSb_{11}$[1c] and AlSb[9].

After the structure of $Yb_9Al_3Sb_9$ was determined by single crystal X-ray diffraction, we tried to produce a pure phase of $Yb_9Al_3Sb_9$ by stoichiometric reactions. The mixtures of the elements in ratio of 3:1:3 for Yb:Al:Sb were heated to 750 °C in 2 d, stayed at this temperature for 24 h and then slowly cooled to room temperature. $Yb_9Al_3Sb_9$ was obtained as the major phase (80% yield) with trace amount of impurity phases $Yb_{11}Sb_{10}$[10] and $Yb_{14}AlSb_{11}$[5].

Yb_3AlSb_3 was found during an attempt to explore the system Yb/Al/Sb/Si using Al as a flux. 1 mmol Yb metal (0.173 g), 3 mmol Si (0.084 g), 1 mmol Sb (0.122 g) and 20 mmol Al (0.270 g) were combined in an alumina crucible. The sample was heated to 1000 °C in 48 h, maintained at this temperature for 36 h, then cooled to 500 °C in 36 h. Yb_3AlSb_3 can also be formed by direct combination reactions. The mixture with molar ratio 1.5:0.5:1.5 for Yb:Al:Sb was heated to 1000 °C in 15 h, maintained at this temperature for 4 h, then cooled to 850 °C in 2 h. It was annealed at 850 °C for 8 d, followed by slowly cooling down to 50 °C at a rate of 8 °C/h. Yb_3AlSb_3 was found as the major phase with traces of Yb_5Sb_3 as the side product.[11]

Differential Thermal Analysis:

Differential thermal analysis (DTA) was performed on Yb_3AlSb_3 and $Yb_9Al_3Sb_9$ with a Shimadzu DTA-50 thermal analyzer. The ground samples (~20 mg) were sealed in carbon-coated silica ampoule under vacuum. A silica ampoule containing equal amount of alumina was sealed and placed on the reference side of the detector. The samples were heated to 1000 °C at 10 °C/min and held for 5 min, followed by cooling at −10 °C/min to 50 °C. The residue of the DTA experiment was examined with powder X-ray diffraction.

X-ray Crystallography:

Single crystal X-ray diffraction data were collected for $Yb_9Al_3Sb_9$ and Yb_3AlSb_3 at room temperature on a Bruker AXS SMART CCD X-ray diffractometer. Single crystals grown from Al flux were selected and mounted on glass fibers. The data

collections (Mo Kα radiation, λ = 0.71073 Å) were acquired covering a full sphere of reciprocal space. The data acquisition and cell reduction were done with the SMART[12] software package and data processing was performed with the SAINTPLUS software package.[13] An empirical absorption correction was applied to the data using the SADABS program.[14] The structures were solved using direct methods and refined with the SHELXTL package program.[15]

Inspection of systematic absence conditions of $Yb_9Al_3Sb_9$ revealed two possible space groups: centrosymmetric space group *Pbam* (#55) and non-centrosymmetric *Pba*2 (#32). These two candidates presented similar figure of merit. The centrosymmetric space group *Pbam* was chosen and later structure refinement confirmed this choice. Direct methods gave a structure solution with five Yb sites, five Sb sites and two Al sites. Among them there were four atomic sites — Al(2), Yb(4), Yb(5) and Sb(5) showing unreasonable high thermal parameters. Examination of Al(2) site revealed that it was only 50% occupied (Al is the lightest element in this compound). After this cycle of refinement, the R_1 factor dropped to 12.54% and the thermal parameters of Al(2) changed back to normal. All the other three atomic sites Yb(4), Yb(5) and Sb(5) were found fully occupied; and an analytical absorption correction was applied but could not solve the problem of high thermal parameters. The bond distances between Al(2) and Yb(4) or Yb(5) atom are 2.879(11) Å, 3.044(11) Å and 3.106(17) Å, respectively, which are shorter than the other Yb-Al bond distances (3.262(2) Å ~ 3.503(17) Å); while the bond distance from Al(2) to Sb(5) is 3.027(17) Å, much longer than the other Al-Sb bond distances (2.728(9) Å ~ 2.768(9) Å). We believe that it is the disordered Al(2) site that

raises the thermal shifts of Yb(4), Yb(5) and Sb(5) atoms resulting in high thermal parameters, position uncertainty and high standard deviations of bond distances.

The structure of Yb_3AlSb_3 was solved in a straightforward fashion. Inspection of the systematic absence conditions brought two possible space groups: $Pna2_1$ (#33) and *Pnma* (#62). *Pnma* is a centrosymmetric space group; plus its figure of merit is much lower (2.59), so *Pnma* was chosen and later structure refinement proved that this was the right one. Moreover, review of the literature revealed that Ca_3AlSb_3 has similar cell parameters and same space group: *Pnma*, a = 12.835(5) Å, b = 4.489(2) Å, c = 14.282(5) Å.[16] This implies that Yb_3AlSb_3 is an isostructural compound of Ca_3AlSb_3. All the seven atomic sites were proved to be fully occupied and refined anisotropically. The R_1 factor finally dropped to 2.44% with highest residual peak 1.98 $e^-/Å^{-3}$, almost the same as the deepest hole –1.87 $e^-/Å^{-3}$.

Data collection parameters and refinement details for $Yb_9Al_3Sb_9$ and Yb_3AlSb_3 can be found in Table 7-1. Atomic positions, displacement parameters and anisotropic displacement parameters for $Yb_9Al_3Sb_9$ and Yb_3AlSb_3 are listed in Tables 7-2, 7-3, 7-4 and 7-5.

X-ray powder diffraction data were collected at room temperature with a CPS 120 INEL X-ray diffractometer (Cu Kα) equipped with a position-sensitive detector. Experimental powder patterns were compared to the patterns calculated from the single crystal structure solution (by the CrystalDiffract program[17]) to determine the phase identity and purity.

Charge transport measurements:

Electrical conductivity and thermopower measurements were made on $Yb_9Al_3Sb_9$ and Yb_3AlSb_3. The samples were ground and made into pellets. Conductivity measurements were performed in the usual four-probe geometry. Thermopower data were from 300 K to 400 K with a MMR Technologies, Inc. Seebeck measurement system.

Magnetic Susceptibility Measurements:

Magnetic susceptibility measurements were performed with a MPMS Quantum Design SQUID magnetometer. The data were collected in the temperature range 3-300 K at 1000 G, while field dependent magnetic measurements, conducted at 5 K, were carried out in fields up to ± 55000 G. A diamagnetic correction was applied to the data to account for core diamagnetism.

Band Structure Calculations:

To understand the bonding inYb_3AlSb_3, we carried out *ab initio* band structure calculations using the density functional theory (DFT) formalism. The calculations were performed using the self-consistent full-potential linearized augmented plane wave method (LAPW), with the generalized gradient approximation (GGA) for the exchange and correlation potential. Spin-orbit interactions were included in the calculations.

Table 7-1. Selected crystal data and structure refinement details for $Yb_9Al_3Sb_9$ and Yb_3AlSb_3.

Empirical formula	$Yb_9Al_3Sb_9$	Yb_3AlSb_3
Formula weight	2734.05	911.35
Temperature	293(2) K	293(2) K
Crystal system	Orthorhombic	Orthorhombic
Space group	*Pbam* (# 55)	*Pnma* (#62)
Unit cell dimensions	a = 12.433(2) Å	a = 12.838(5) Å
	b = 21.916(4) Å	b = 4.5028(17) Å
	c = 4.5876(9) Å	c = 14.220(5) Å
Volume	1250.1(4) $Å^3$	822.0(5) $Å^3$
Z	2	4
Density (calculated)	7.264 Mg/m^3	7.364 Mg/m^3
Absorption coefficient	42.905 mm^{-1}	43.497 mm^{-1}
F(000)	2256	1504
Crystal size	0.16 × 0.12 × 0.10 mm^3	0.43 × 0.26 × 0.33 mm^3
Theta range for data collection	1.86 to 27.94°	2.14 to 28.21°
Limiting indices	$-15 \le h \le 15$	$-16 \le h \le 16$
	$-28 \le k \le 28$	$-5 \le k \le 5$
	$-6 \le l \le 5$	$-17 \le l \le 18$
Reflections collected	12689	8651
Independent reflections	1612 [R(int) = 0.0765]	1099 [R(int) = 0.0512]
Completeness to theta = 37.00°	95.7 %	97.3 %
Refinement method	Full-matrix least-squares on F^2	
Data / restraints / parameters	1612 / 0 / 73	1099 / 0 / 44
Goodness-of-fit on F^2	1.282	1.092
Final R indices [I>2sigma(I)]	R_1 = 0.0648	R_1 = 0.0244
	wR_2 = 0.1010	wR_2 = 0.0517
R indices (all data)	R_1 = 0.0838	R_1 = 0.0339
	wR_2 = 0.1053	wR_2 = 0.0541
Largest diff. peak and hole	5.987 and – 7.848 $e.Å^{-3}$	1.978 and –1.868 $e.Å^{-3}$

$R1 = \Sigma(|F_o|-|F_c|)/\Sigma|F_o|$; $wR2 = [\Sigma[w(F_o^2 - F_c^2]/ [\Sigma(w|F_o|^2)^2]^{1/2}$

Table 7-2. Atomic coordinates ($Å \times 10^4$) and equivalent isotropic displacement parameters ($Å^2 \times 10^3$) for $Yb_9Al_3Sb_9$.

Atom	Wyk. Symbol	x	y	z	Occu.	$U_{(eq)}$*
Yb(1)	2*b*	0	0	5000	1.0	14(1)
Yb(2)	4*g*	-1347(1)	2366(1)	0	1.0	11(1)
Yb(3)	4*g*	1247(1)	1325(1)	0	1.0	9(1)
Yb(4)	4*g*	-844(1)	4153(1)	0	1.0	33(1)
Yb(5)	4*h*	-2910(1)	958(1)	5000	1.0	25(1)
Sb(1)	4*h*	-451(1)	1498(1)	5000	1.0	10(1)
Sb(2)	4*h*	-2031(1)	3303(1)	-5000	1.0	8(1)
Sb(3)	4*g*	-3932(1)	1920(1)	0	1.0	9(1)
Sb(4)	4*g*	-1886(2)	38(1)	0	1.0	10(1)
Sb(5)	2*d*	0	5000	-5000	1.0	53(2)
Al(1)	4*h*	1097(7)	2380(4)	-5000	1.0	9(2)
Al(2)	4*h*	-2298(13)	4545(8)	-5000	0.5	9(6)

$U_{(eq)}$ is defined as one third of the trace of the orthogonalized U_{ij} tensor.

Table 7-3. Anisotropic displacement parameters ($Å^2 \times 10^3$) for $Yb_9Al_3Sb_9$.

Atom	U^{11}	U^{22}	U^{33}	U^{23}	U^{13}	U^{12}
Yb(1)	12(1)	14(1)	15(1)	0	0	2(1)
Yb(2)	11(1)	6(1)	15(1)	0	0	2(1)
Yb(3)	10(1)	8(1)	10(1)	0	0	2(1)
Yb(4)	11(1)	8(1)	78(3)	0	0	-3(1)
Yb(5)	26(1)	28(1)	21(1)	0	0	16(1)
Sb(1)	8(1)	11(1)	11(1)	0	0	0(1)
Sb(2)	10(1)	3(1)	10(1)	0	0	0(1)
Sb(3)	7(1)	6(1)	14(1)	0	0	-2(1)
Sb(4)	11(1)	5(1)	14(1)	0	0	0(1)
Sb(5)	123(5)	28(2)	9(2)	0	0	41(3)
Al(1)	10(4)	4(4)	12(4)	0	0	1(3)
Al(2)	0(9)	8(10)	19(11)	0	0	-3(6)

The anisotropic displacement factor exponent takes the form:
$-2\pi^2[h^2a^{*2}U^{11}+...+2hka^*b^*U^{12}]$

Table 7-4. Atomic coordinates (Å × 10^4) and equivalent isotropic displacement parameters (Å^2 × 10^3) for Yb_3AlSb_3.

Atom	Wyk. Symbol	x	y	z	$U_{(eq)}$*
Yb(1)	4*c*	9404(1)	2500	6114(1)	13(1)
Yb(2)	4*c*	2272(1)	2500	7212(1)	13(1)
Yb(3)	4*c*	6500(1)	2500	4941(1)	14(1)
Sb(1)	4*c*	7562(1)	-2500	6190(1)	11(1)
Sb(2)	4*c*	8864(1)	2500	3905(1)	11(1)
Sb(3)	4*c*	9599(1)	2500	8507(1)	11(1)
Al	4*c*	9334(3)	2500	2031(2)	13(1)

$U_{(eq)}$ is defined as one third of the trace of the orthogonalized U_{ij} tensor.

Table 7-5. Anisotropic displacement parameters (Å^2 × 10^3) for Yb_3AlSb_3.

Atom	U^{11}	U^{22}	U^{33}	U^{23}	U^{13}	U^{12}
Yb(1)	10(1)	13(1)	16(1)	0	0(1)	0
Yb(2)	12(1)	11(1)	16(1)	0	-2(1)	0
Yb(3)	14(1)	13(1)	15(1)	0	-1(1)	0
Sb(1)	10(1)	8(1)	15(1)	0	1(1)	0
Sb(2)	11(1)	11(1)	10(1)	0	0(1)	0
Sb(3)	9(1)	9(1)	14(1)	0	1(1)	0
Al	12(1)	12(1)	14(1)	0	1(1)	0

The anisotropic displacement factor exponent takes the form:
$-2\pi^2[h^2a^{*2}U^{11}+...+2hka^*b^*U^{12}]$

7-3. Results and Discussion

Synthesis and Differential Thermal Analysis:

Initially both $Yb_9Al_3Sb_9$ and Yb_3AlSb_3 were prepared in molten Al. The isolated crystals were shiny and black with needle morphology. The stoichiometries of the two compounds are identical, however they adopt different structure types which will be described in detail in the crystal structure section.

Both compounds can be made by stoichiometric reactions, and small amount of impurity phases such as $Yb_{11}Sb_{10}$ and Yb_5Sb_3 were also detected by powder X-ray diffraction analysis. $Yb_9Al_3Sb_9$ was synthesized at 750 °C, but reactions at high temperatures (850 °C) formed Yb_3AlSb_3, which suggests that Yb_3AlSb_3 is probably a more thermodynamically stable phase. This argument is also supported by DTA experiments. Powder X-ray diffraction pattern after DTA showed that $Yb_9Al_3Sb_9$ converted to Yb_3AlSb_3 along with some Yb_5Sb_3. The more thermodynamically stable phase Yb_3AlSb_3 melts at 820 °C and recrystallizes at 801 °C.

Crystal Structure of $Yb_9Al_3Sb_9$:

The crystal structure of $Yb_9Al_3Sb_9$ is shown in Figure 7-1. The main feature of this structure, as described elsewhere,[6,7] is the ribbon-like chains (Figure 7-2A) composed of four $AlSb_4$ tetrahedral units running along the *c*-axis. The four $AlSb_4$ units are connected with each other by sharing Sb corners. Sb(2), Sb(3) and Sb(4) atoms are shared by Al(1)- and Al(2)-centered tetrahedra to form a ribbon, see Figure 7-2A. The Sb(5) atom is bridging two double-chains in a linear fashion with Al(2)-Sb(5)-Al(2) angle of 180°. The five different Yb cations occupy the empty spaces between the chains to

counter-balance the charge. Their coordination environments are shown in Figure 7-2B~F, all featuring a distorted octahedral geometry composed of Sb atoms. The bond distances between Yb and Sb atoms fall in the range of 3.090(2) ~ 3.423(2) Å. For the Yb(3), Yb(4) and Yb(5) atoms, they are also capped by four, two and one Al atom, respectively. The disorder of Al(2) results in unusual close contact of Yb(4)-Al(2) which is 2.879(11) Å, much shorter than the other Yb-Al bond distances (3.044(11) ~ 3.503(17) Å).

An interesting feature of the structure of $Yb_9Al_3Sb_9$ is on the Al(2) site. There are two independent Al sites: Al(1) is fully occupied, while Al(2) site is only 50% occupied. The possibility that this site could be occupied by a lighter element was excluded since EDS analysis did not detect any other element.

According to the Zintl concept, the formal charge of a four-bonded Zn atom can be assigned as Zn^{2-} and those one-bonded Sb and two-bonded Sb atoms can be assigned as Sb^{2-} and Sb^{1-}. So for the $AE_9TM_4Pn_9$ family (AE = Ca, Sr; TM = Zn, Cd; Pn = Sb, Bi), the anion lattice can be described as $[(TM^{2-})_4(1b\text{-}Pn^{2-})_2(2b\text{-}Pn^{1-})_7]^{19-}$, which requires 19 electrons to balance the charge. However the divalent alkaline metal cations can only provide 18 electrons, which challenges the correctness of this structure. The publication of the charge-balanced Zintl phase $Yb_9Zn_4Bi_9$ first raised this concern.[6] In this formula the Yb ions are mixed-valent of Yb^{2+}/Yb^{3+} instead of divalent, and this argument is supported by magnetic susceptibility measurements. So $Yb_9Zn_4Bi_9$ can be rationalized as $[(Yb^{3+})(Yb^{2+})_8][(Zn^{2-})_4(1b\text{-}Bi^{2-})_2(2b\text{-}Bi^{1-})_7]$. Later two other members $Yb_9Zn_{4.5}Sb_9$ and $Ca_9Zn_{4.5}Sb_9$ were discovered.[8] Additional Zn atoms were found in these two structures which connect two $[Zn_4Sb_9]^{19-}$ ribbons to form a $[Zn_{4.5}Sb_9]^{18-}$ anionic sub-lattice.

Therefore the ytterbium or calcium cations in $Yb_9Zn_{4.5}Sb_9$ and $Ca_9Zn_{4.5}Sb_9$ are in divalent oxidation state. The present compound $Yb_9Al_3Sb_9$ demonstrates its Zintl nature by requiring less Al components since divalent Zn ions are substituted by trivalent Al atoms. According to the simple formal oxidation rules, this $Yb_9Al_3Sb_9$ composition gives a complete charge balance: $(Yb^{2+})_9[(Al^{3+})_3(Sb^{3-})_9]$.

Crystal Structure of Yb_3AlSb_3:

As mentioned before, Yb_3AlSb_3 crystallizes in the Ca_3AlSb_3 structure type.[16] Ca_3GaAs_3, Ca_3InP_3 and Sr_3InP_3 are isostructural compounds that belong to this family.[18] As shown in Figure 7-3, this structure is composed of $AlSb_4$ tetrahedra which form an infinite chain along the *b*-axis by sharing Sb corners; these $[AlSb_3]^{6-}$ anionic species are separated by Yb ions, which occupy the empty spaces and provide charge balance. Interestingly, Ba_3AlSb_3 and Ba_3GaSb_3 have the same stoichiometry as Yb_3AlSb_3; however in these two compounds two distorted MSb_4 (M = Al, Ga) tetrahedra are connected by a common Sb-edge to form an isolated dimeric anion $[M_2Sb_6]^{12-}$. Another compound with the same stoichiometry was reported by Cordier — Sr_3GaSb_3, in which distorted $GaSb_4$ tetrahedra are connected by common Sb corners, to give strands with groups of four tetrahedra as the repeating unit.[18] It is not clear at this point whether size determines the structure type; since Yb and Ca are similar in size, although Sr is a larger cation than those two.

Figure 7-4A depicts how the $AlSb_4$ tetrahedra form a polymeric chain by sharing Sb atoms. The MPn_4 (M = Al, Ga; Pn = As, Sb, Bi) tetrahedron is a very common unit and it has been observed in many Zintl phases, such as $A_5M_2Pn_6$,[19] $A_{11}MPn_9$[20] and

$A_{14}MPn_{11}$.[20a, 21] In Yb_3AlSb_3, the Al-centered tetrahedra are built of three crystallographically inequivalent Sb atoms: Sb(1), Sb(2) and Sb(3). The bond distances are quite similar: 2.713(4) Å, 2.732(4) Å and 2.744(2) Å for Al-Sb(1), Al-Sb(2) and Al-Sb(3) respectively. The $AlSb_4$ tetrahedron unit is in a distorted fashion with Sb-Al-Sb angles 112.46(8)° and 108.96(9)°, which are deviated from the ideal tetrahedral angle of 109.5°.

The three independent Yb sites occupy the space between the $AlSb_4$ tetrahedra; and their local coordination environments are shown in Figure 7-4B,C&D. Both Yb(1) and Yb(3) atoms are sitting in distorted octahedral geometries composed of six Sb atoms. The Yb-Sb bond distances are in the range of 3.1173(9) Å ~ 3.4113(15) Å, which are comparable to the sum of the covalent radii of Yb and Sb atoms (3.20 Å). The Yb(2) atoms are also in distorted octahedral geometries; in addition, the Yb(2) atom is also bonded to two capping Al atoms with Yb-Al distance 3.237(3) Å.

According to the Zintl concept, the formal charge of a four-bonded Al atom can be assigned as Al^{1-} and those one-bonded and two-bonded Sb atoms can be assigned as Sb^{2-} and Sb^{1-}. So the formula Yb_3AlSb_3 can be rationalized as $(Yb^{2+})_3[(Al^{1-})(1b\text{-}Sb^{2-})_2(2b\text{-}Sb^{1-})]$. Alternatively one can also describe the formula as $(Yb^{2+})_3[(Al^{3+})(Sb^{3-})_3]$ using formal oxidation numbers.

Charge Transport Measurements:

To assess the thermoelectric properties of these two Zintl phases, we conducted preliminary studies of the electrical conductivity and thermoelectric power on Yb_3AlSb_3 and $Yb_9Al_3Sb_9$. Yb_3AlSb_3 and $Yb_9Al_3Sb_9$ exhibit similar charge transport properties.

The electrical conductivity for Yb_3AlSb_3 and $Yb_9Al_3Sb_9$ at room temperature was 230 S/cm and 272 S/cm, respectively, comparable to the other Zintl phases such as $Ba_4In_8Sb_{16}$[1] (135 S/cm) and $Yb_5In_2Sb_6$ (100 S/cm).[22] The thermoelectric power of polycrystalline pellets of Yb_3AlSb_3 and $Yb_9Al_3Sb_9$ was measured as a function of temperature (Figure 7-5). So far the thermopower of $Yb_9Al_3Sb_9$ could only be measured up to 400 K due to the fact that pressed pellets often lose contact at higher temperatures. In both cases of Yb_3AlSb_3 and $Yb_9Al_3Sb_9$, the positive values of thermopower indicate holes as the charge carrier. The value of the thermopower for Yb_3AlSb_3 was about 10 μV/K at room temperature and rose to ~21 μV/K at 700 K. For $Yb_9Al_3Sb_9$, the thermopower varied from +29 to +45 μV/K between 300 and 400 K, and showed a linear increase with rising temperature.

Magnetic Susceptibility Measurements:

Single crystals of Yb_3AlSb_3 and $Yb_9Al_3Sb_9$ grown from Al flux were picked and ground into powders for the magnetic susceptibility measurements. In both cases, the high temperature (above 60 K) magnetic susceptibility data was nearly temperature independent, as expected for divalent Yb ions ($\mu_{eff} = 0$). This observation is consistent with electron counting and band structure calculations. The low temperature magnetic susceptibility might come from impurities such as Yb_2O_3.

Band Structure Calculations:

In order to compensate for the inability of Density Functional Theory (DFT) to accurately model the highly correlated f-electrons, the calculations were performed on four different compounds Yb_3AlSb_3, Lu_3AlSb_3, La_3AlSb_3 and Ca_3AlSb_3, three of which have different f-level configurations. The Ca system does not have an f-level in the energy range of interest and it is isostructural with the three rare earth systems. The density of states (DOS), as computed for the above mentioned compounds are shown in Figure 7-6. There are several similar features in these diagrams: a narrow band located at -10 eV, corresponding to the s levels of the Sb ions, a smaller band at -6 and -5 eV, due to the Al s level and finally the wide valence and conduction bands which indicates the strong hybridization between the Al s, p and Sb p states.

The sharp, narrow bands corresponding to the f-level of Yb, Lu and La are visible in Figure 7-6A, B and C respectively. In the cases of Yb and Lu, the f-levels are very narrow (0.1 eV) and are energetically split in two groups because of the spin-orbit coupling. The crystal field splitting can also be seen on the f-level of the Lu ion. In contrast the empty f-level of La is much broader (0.5 eV), due to strong hybridization with the conduction band.

The DOS at the Fermi level of Lu_3AlSb_3 and La_3AlSb_3 is nonzero, indicating metallic character of these compounds. In the case of the Yb system, the bands near the Fermi level are composed of f states of Yb, p and s orbitals of Al and p states of Sb. The nonzero DOS at the Fermi level suggests that this is also a metallic system. However, the number of electrons occupying the conduction band may be very small. Further a small downward shift in the position of the f-level will make Yb_3AlSb_3 a semiconductor. In

this case the Yb ions are in a 2+ oxidation state, consistent with our charge balanced formulism and the diamagnetic nature of the compound. The DOS plot in Figure 7-6D shows a semiconducting gap of about 0.4 eV for Ca_3AlSb_3. Since DFT tends to underestimate the band gap value, the actual semiconducting gap may be larger than 0.4 eV.

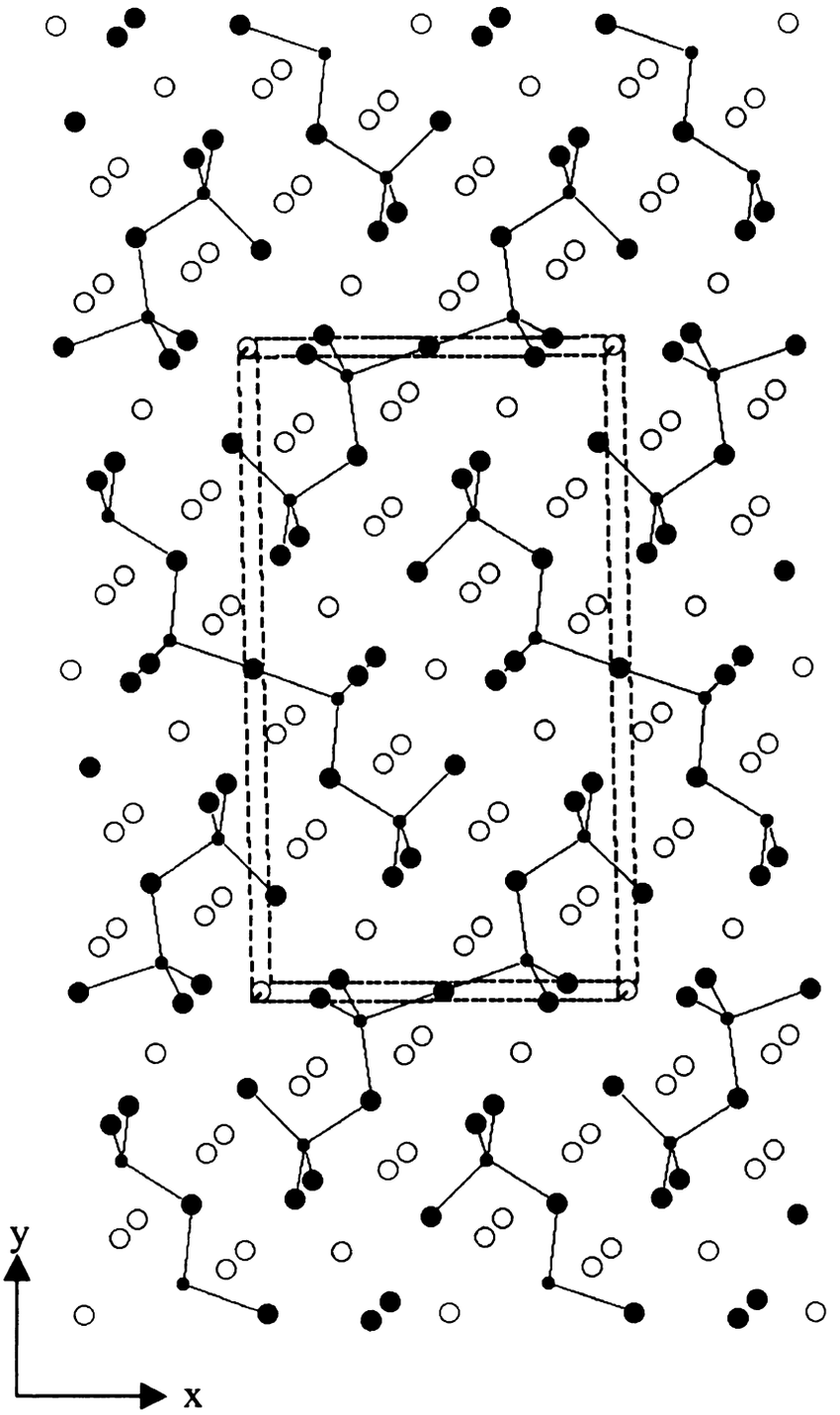

Figure 7-1. Crystal structure of $Yb_9Al_3Sb_9$ viewed down the *c*-axis. Large empty circles: Yb; black small circles: Al; gray medium circles: Sb.

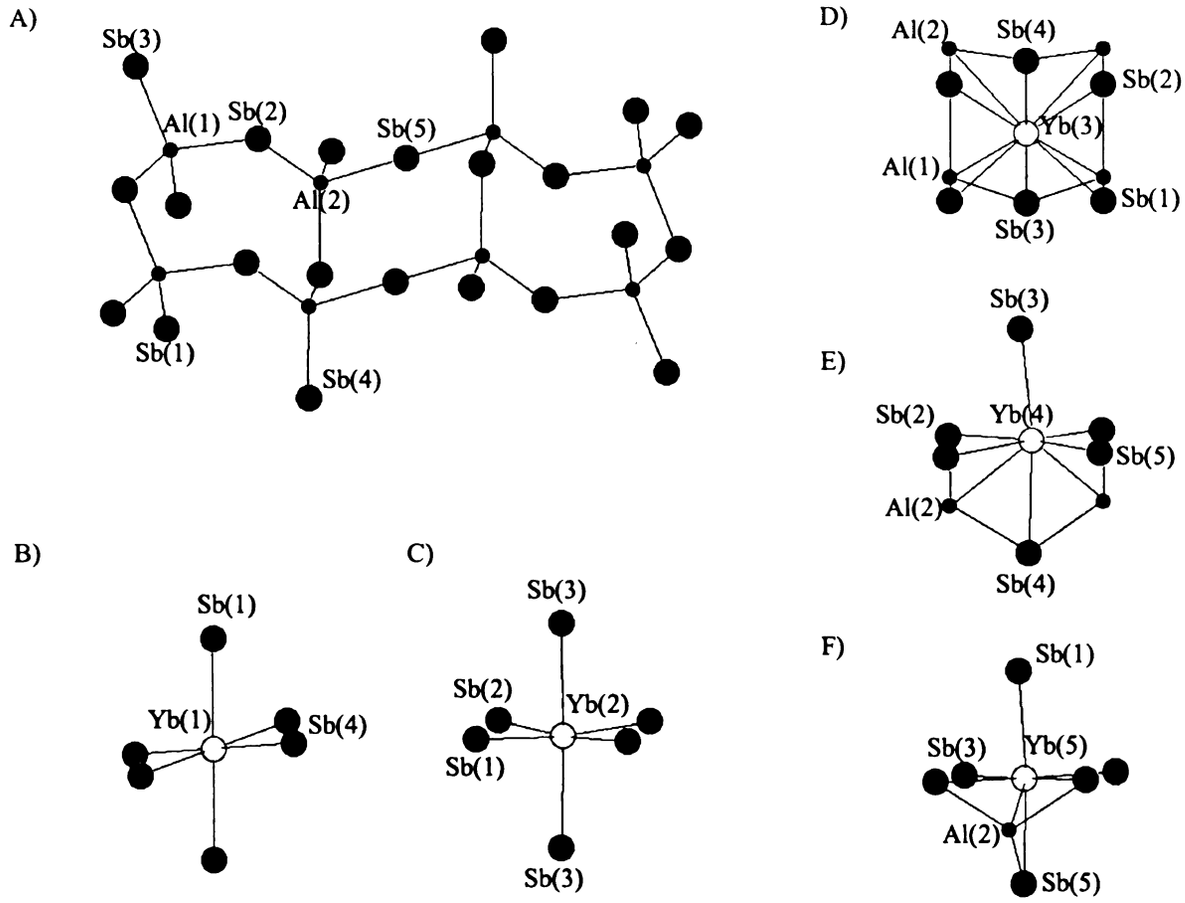

Figure 7-2. Structure of $Yb_9Al_3Sb_9$. A) The fragment of $[Al_3Sb_9]^{18-}$ ribbon. B) ~ F) Coordination environments of Yb atoms.

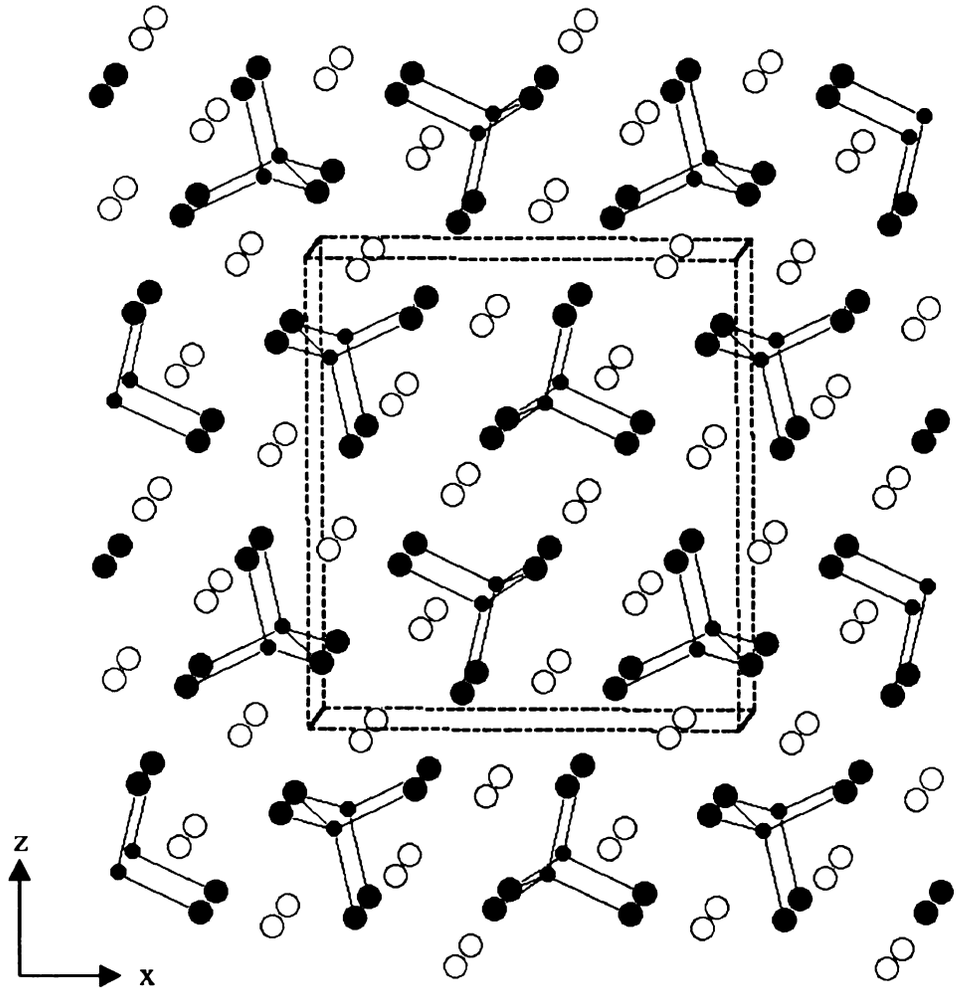

Figure 7-3. Crystal structure of Yb_3AlSb_3 viewed along the *b*-axis. Large empty circles: Yb; black small circles: Al; gray medium circles: Sb.

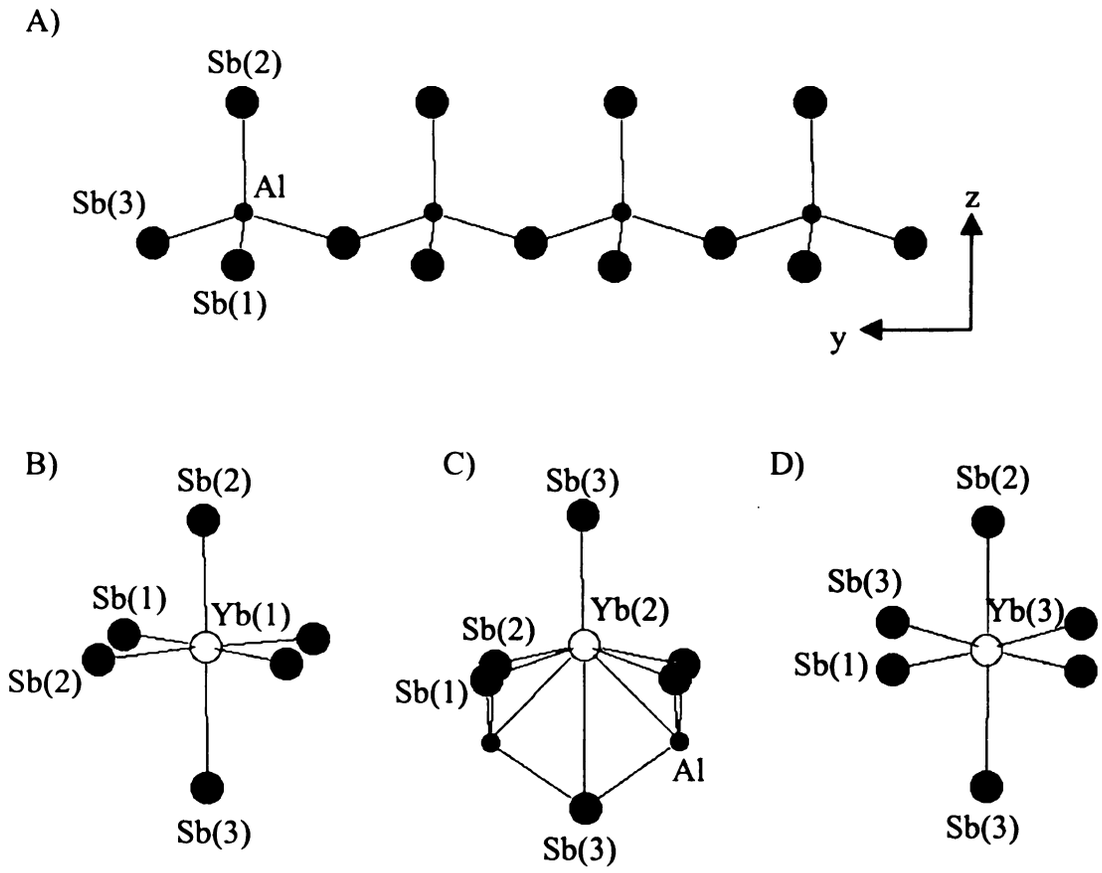

Figure 7-4. Structure of Yb_3AlSb_3. A) Polymeric chain $[AlSb_3]^{6-}$ viewed down the *a*-axis. B) C) D) Immediate coordination environment of Yb atoms.

Table 7-6. Selected bond lengths (Å) for $Yb_9Al_3Sb_9$.

Bond	Distance	Bond	Distance
Yb(1)-Yb(3) ×4	4.0117(11)	Yb(4)-Al(2)	3.044(11)
Yb(1)-Sb(1) ×2	3.330(2)	Yb(4)-Sb(2)	3.3029(17)
Yb(1)-Sb(4) ×4	3.2813(14)	Yb(4)-Sb(3)	3.345(2)
Yb(2)-Yb(3)	3.9506(19)	Yb(4)-Sb(4)	3.423(2)
Yb(2)-Yb(3)	4.1452(19)	Yb(4)-Sb(5)	3.1318(10)
Yb(2)-Yb(4) ×2	3.967(2)	Yb(4)-Yb(4)	4.265(3)
Yb(2)-Yb(5) ×2	4.3084(19)	Yb(4)-Yb(5) ×2	4.317(2)
Yb(2)-Sb(1) ×2	3.1818(17)	Yb(5)-Al(2)	3.106(17)
Yb(2)-Sb(2) ×2	3.1937(16)	Yb(5)-Sb(1)	3.278(3)
Yb(2)-Sb(3)	3.359(2)	Yb(5)-Sb(3) ×2	3.3653(18)
Yb(2)-Sb(3)	3.386(2)	Yb(5)-Sb(4) ×2	3.3086(18)
Yb(3)-Yb(4) ×2	3.765(2)	Yb(5)-Sb(5)	3.3404(18)
Yb(3)-Al(1) ×2	3.262(6)	Sb(1)-Al(1)	2.728(9)
Yb(3)-Al(2) ×2	3.489(12)	Sb(2)-Al(1)	2.767(9)
Yb(3)-Sb(1) ×2	3.1404(16)	Sb(2)-Al(2)	2.743(17)
Yb(3)-Sb(2) ×2	3.2427(17)	Sb(3)-Al(1) ×2	2.760 (5)
Yb(3)-Sb(4)	3.090(2)	Sb(4)-Al(2) ×2	2.730(9)
Yb(4)-Al(2)	2.879(11)	Sb(5)-Al(2)	3.026(16)

Table 7-7. Selected bond lengths (Å) for Yb_3AlSb_3.

Bond	Distance	Bond	Distance
Yb(1)-Yb(1) ×2	4.1772(13)	Yb(2)-Sb(3)	3.1582(14)
Yb(1)-Yb(3)	4.0839(15)	Yb(3)-Sb(1) ×2	3.1747(10)
Yb(1)-Sb(1) ×2	3.2670(11)	Yb(3)-Sb(2)	3.3733(14)
Yb(1)-Sb(2) ×2	3.1645(11)	Yb(3)-Sb(3) ×2	3.3500(10)
Yb(1)-Sb(3)	3.4113(15)	Yb(3)-Sb(3)	3.2910(12)
Yb(2)-Al(1) ×2	3.237(3)	Sb(1)-Al(1)	2.713(4)
Yb(2)-Sb(1) ×2	3.2205(10)	Sb(2)-Al(1)	2.732(4)
Yb(2)-Sb(2) ×2	3.1173(9)	Sb(3)-Al(1) ×2	2.744(2)

A)

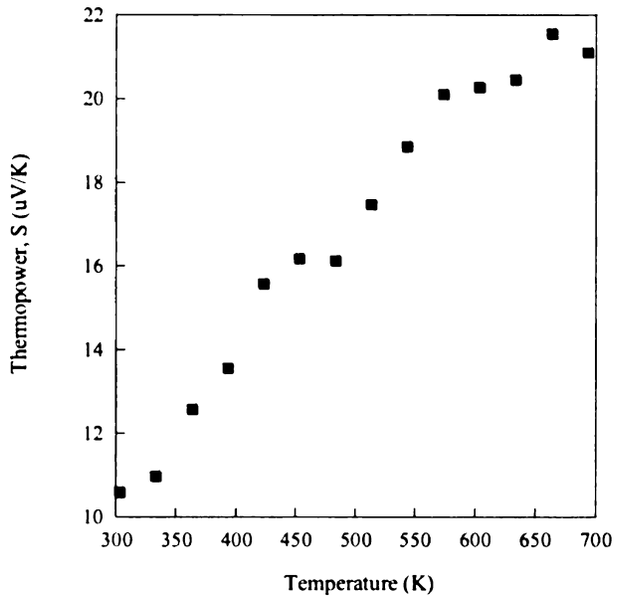

B)

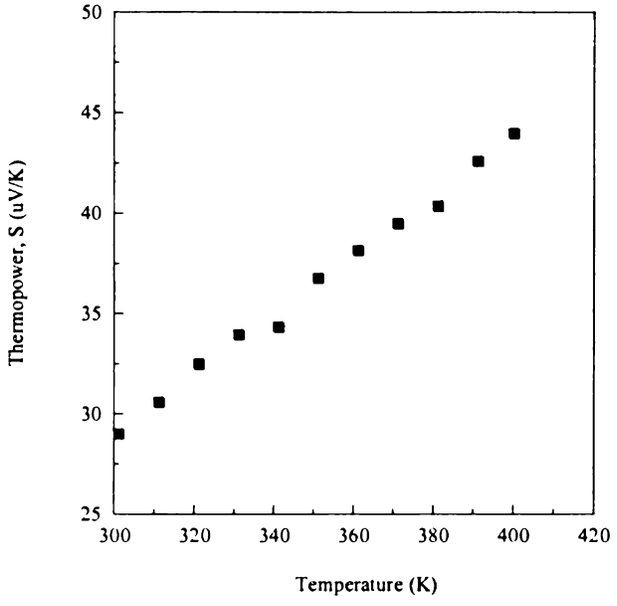

Figure 7-5. A) Temperature dependence of the thermopower for a pressed pellet of Yb_3AlSb_3 from 300 to 700 K. B) Temperature dependence of the thermopower for a pressed pellet of $Yb_9Al_3Sb_9$ from 300 to 400 K.

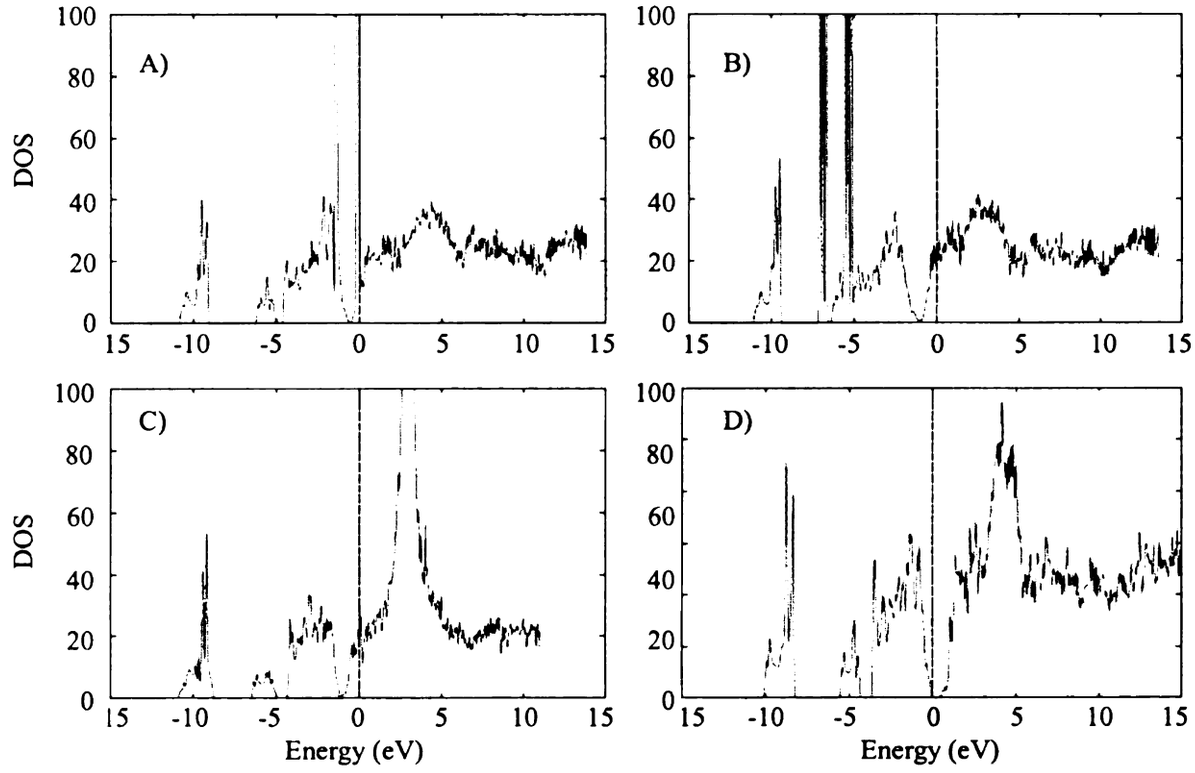

Figure 7-6. (A) The total DOS of Yb_3AlSb_3. The upper spin-split f-band ($f_{7/2}$) is located near the Fermi level. (B) The total DOS of Lu_3AlSb_3. The filled f band is located below -5 eV. (C) The total DOS of La_3AlSb_3 with the empty f-level located in the conduction band. (D) The total DOS of Ca_3AlSb_3. A band gap of about 0.4 eV shows the semiconducting character of the Ca compound.

7-4. Conclusions:

We have synthesized and structurally characterized the new ternary zintl phases Yb_3AlSb_3 and $Yb_9Al_3Sb_9$. Both phases can be obtained by the Al flux method and direct combination reactions. The fact that Yb_3AlSb_3 was obtained at higher temperature implies that Yb_3AlSb_3 is a more thermodynamically stable phase, and DTA experiments confirmed this conclusion. Although these two phases present the same stoichiometry, they exhibit different structure types. Yb_3AlSb_3 is composed of $AlSb_4$ tetrahedra forming infinite chains along the *b*-axis; while the main feature of $Yb_9Al_3Sb_9$ is a ribbon-like chain composed of four $AlSb_4$ tetrahedra which connect with each other by sharing Sb corners. The discovery of $Yb_9Al_3Sb_9$ demonstrated the zintl nature of the 9-4-9 family: this structure managed to maintain charge-balance by reducing ¼ of the Al atoms. Thus the charge of the anionic chain is –18; and the Yb cations are in divalent oxidation state which is supported by magnetic susceptibility measurements.

References:

[1] a) Corbett, J. D. *Angew. Chem. Int. Ed.* **2000**, *39*, 670. b) Chan, J. Y.; Olmstead, M. M.; Kauzlarich, S. M.; Webb, D. J. *Chem. Mater.* **1998**, *10*, 3583. c) Fisher, I. R.; Budko, S. L.; Song, C.; Canfield, P. C.; Ozawa, T. C.; Kauzlarich, S. M. *Phys. Rev. Lett.* **2000**, *85*, 1120. d) Kim, S. J.; Hu, S. Q.; Uher, C.; Kanatzidis, M. G. *Chem. Mater.* **1999**, *11*, 3154. e) Holm, A. P.; Park, S. M.; Condron, C. L.; Olmstead, M. M.; Kim, H.; Klavins, P.; Grandjean, F.; Hermann, R. P.; Long, G. J.; Kanatzidis, M. G.; Kauzlarich, S. M.; Kim, S. J. *Inorg. Chem.* **2003**, *42*, 4660. f) Park, S. M.; Kim, S. J.; Kanatzidis, M. G. *Inorg. Chem.* **2005**, *44*, 4979.

[2] Chan, J. Y.; Kauzlarich, S. M.; Klavins, P.; Shelton, R. N.; Webb, D. J. *Chem. Mater.* **1997**, *9*, 3132.

[3] Chan, J. Y.; Kauzlarich, S. M.; Klavins, P.; Shelton, R. N.; Webb, D. J. *Phys. Rev. B* **1998**, *57*, 8103.

[4] Fisher, I. R.; Wiener, T. A.; Budko, S. L.; Canfield, P. C.; Chan, J. Y. Kauzlarich, S. M. *Phys. Rev. B* **1999**, *59*, 13829.

[5] Fisher, I. R.; Budko, S. L.; Song, C.; Canfield, P. C.; Ozawa, T. C.; Kauzlarich, S. M. *Phys. Rev. Lett.* **2000**, *85*, 1120.

[6] Kim, S. J.; Salvador, J.; Bilc. D.; Mahanti, S. D.; Kanatzidis, M. G. *J. Am. Chem. Soc.* **2001**, *123*, 12704.

[7] Brechtel, E.; Cordier, G.; Schäfer, H. *Z. Naturforsch. B* **1979**, *34*, 1229.

[8] Bobev, S.; Thompson, J. D.; Sarrao, J. L.; Olmstead, M. M.; Hope, H.; Kauzlarich, S. M. *Inorg. Chem.* **2004**, *43*, 5044.

[9] Owen, E. A.; Preston, G. D. *P. Phys. Soc. London* **1924**, *36*, 341.

[10] Clark, H. L.;Simpson, H. D.;Steinfink, H. *Inorg. Chem.* **1970**, *9*, 1962.

[11] Brunton, G. D.; Steinfink, H. *Inorg. Chem.* **1971**, *10*, 2301.

[12] *SMART*, version 5; Siemens Analytical X-ray Systems, Inc.: Madison, WI, 1998.

[13] Saint, Version 4; Simens Analytical X-ray Instruments Inc., Madison, WI.

[14] SADABS, Sheldrick, G. M.; University of Göttingen, Göttingen, Germany.

[15] G.M. Sheldrick, 1995, SHELXTL. Structure Determination Programs, Version 5.0. Siemens Analytical X-ray Instruments, Inc. Madison, WI.

[16] Cordier, D.;Schäefer, H.;Stelter, M. *Z. Naturforsch. B* **1984**, *39*, 727.

[17] CrystalDiffract is © 1995-1996, Dr. David C. Palmer.

[18] a) Cordier, G.; Schäfer, H.; Stelter, M. *Z. Naturforsch. B* **1987**, *42*, 1268. b) Cordier, G.; Schäfer, H.; Stelter, M. *Z. Naturforsch. B* **1985**, *40*, 1100.

[19] a) Cordier, G.; Schäfer, H.; Stelter, M. *Z. Naturforsch. B* **1984**, *39*, 727. b) Cordier, G.; Schäfer, H.; Stelter, M. *Z. Naturforsch. B* **1985**, *40*, 975. c) Cordier, G.; Schäfer, H.; Stelter, M. *Z. Naturforsch. B* **1985**, *40*, 1100. d) Kim, S.; Ireland, J. R.; Kannewurf, C. R.; Kanatzidis, M. G. *J. Solid State Chem.* **2000**, *155*, 55.

[20] a) Cordier, G.; Schäfer, H.; Stelter, M. *Z. Naturforsch. B* **1985**, *40*, 868. b) Bobev, S.; Fritsch, V.; Thompson, J. D.; Sarro, J. L.; Eck, B.; Dronskowski, R.; Kauzlarich, S. M. *J. Solid State Chem.* **2005**, *178*, 1071.

[21] a) Cordier, G.; Schäfer, H. *Z. Anorg. Allg. Chem.* **1984**, *519*, 183. b) Brock, S. L.; Weston, L. J.; Olmsted, M. M.; Kauzlarich, S. M. *J. Solid State Chem.* **1993**, *107*, 513.

[22] Kim, S. J.; Ireland, J. R.; Kannewurf, C. R.; Kanatzidis, M. G. *J. Solid State Chem.* **2000**, *155*, 55.

CHAPTER EIGHT

Conclusions and Future work

It has been demonstrated that the Al flux method is an effective approach to synthesize single crystals of new intermetallic phases. To better understand the reaction pattern of Al with a transition metal and silicon or germanium, we systematically investigated the system RE/Au/Al/Ge in liquid Al. In this system, Al is serving as a reactive solvent and it tends to form quaternary compounds with Ge. In addition, parallel chemistry was found between the first row and the third row transition metals, especially between Au and Ni. The hexagonal phase $RETMAl_4Ge_2$ can be formed both with Au and Ni; $REAuAl_4(Au_xGe_{1-x})_2$ and $RENiAl_4(Si_{2-x}Ni_x)$[1] are isostructural phases which have a transition metal and tetrelide on the mixed-occupied site.

Our results in the system RE/Au/Al/Ge also gave a clear comparison between Si and Ge chemistry. Au reacts with RE and Si in liquid Al to form a number of new phases such as the $Th_2(Au_xSi_{1-x})[AuAl_2]_nSi_2$ homologous series,[2] $REAu_4Al_8Si$,[3] $RE_2AuAl_6Si_4$[4] and $REAu_3Al_7$.[5] The common feature of these compounds is the hexagonal antifluorite-type slabs regarded as fragments of the bulk $AuAl_2$ structure, which is absent from our Ge-containing compounds $REAuAl_4Ge_2$ and $REAuAl_4(Au_xGe_{1-x})_2$ (x = 0.4). To further understand both the similarities and differences between Si and Ge systems, reactions with the second row transition metals especially Ru, Rh and Ag should be looked at in the future.

Our investigations of the ternary systems V/Al/Ge and Co/Al/Si led to the discovery of three new phases: $V_2Al_5Ge_5$, $Co_{19}Al_{45}Si_{10-x}$ (x = 0.13) and $Co_5Al_{14}Si_2$. $V_2Al_5Ge_5$ was the first known ternary member in the V/Al/Ge system. Its structure

features unusual pentagonal columnar building blocks with a one dimensional V-V chain running along the central axis of the pentagonal columns. Magnetic susceptibility measurements indicate Pauli paramagnetism for this compound, which is consistent with the metallic behavior predicted by electronic structure calculations. $Co_{19}Al_{45}Si_{10-x}$ (x = 0.13) and $Co_5Al_{14}Si_2$ are two new silicides exhibiting highly complicated structures and large unit cells. $Co_5Al_{14}Si_2$ shows remarkable oxidation resistance with only less than 3% weight gain up to 900 °C. These ternary systems can be extended to the quaternary ones $TM_1/TM_2/Al/Si(Ge)$. Although some alloys formed in these systems have been used as advanced materials, there is a significant lack of structural information about these phases. Considering the fact that the metal flux method is very powerful to grow single crystals of intermetallics, explorations on the systems $TM_1/TM_2/Al/Si(Ge)$ might be helpful in understanding the composition, structure and properties of these alloys. Given the fact that there are more than twenty transition metals available, a rich chemistry is expected from the systems $TM_1/TM_2/Al/Si(Ge)$. The systems TM/Al/Si(Ge) and $TM_1/TM_2/Al/Si(Ge)$ are of particular interest not only from a viewpoint of discovering new materials but also desirable properties, especially oxidation resistance properties.

Of all the rare earth-containing intermetallic compounds, Yb-based ones are particularly interesting because they often exhibit unique properties associated with mixed valency of Yb^{2+}/Yb^{3+}. $Yb_3Ni_5Al_{19}$ and $YbNi_3Al_9$ have been characterized and both show intermediate valence behaviors. Other rare earth analogues of $Yb_3Ni_5Al_{19}$ have also been synthesized, among which the $Sm_3Ni_5Al_{19}$ analogue shows interesting magnetic properties. It has two different magnetic ordering events occurring at 5 K

(antiferro-) and 150 K (ferro-) with the applied magnetic field perpendicular to the *a*-axis. When the field is parallel to the *a*-axis, these transitions are far less significant and it could be due to the fact that the spins are confined to the *bc*-plane.

The discovery of YbGaGe, which showed zero thermal expansion (ZTE) between 10 K and 300 K, prompted us to carry out more investigations on the Yb-containing compounds.[6] Since YbGaGe and $Yb_3Ni_5Al_{19}$ show similar intermediate valence behavior, $Yb_3Ni_5Al_{19}$ could be a good candidate to study the unusual zero thermal expansion property. We successfully substituted Ni in $Yb_3Ni_5Al_{19}$ with Fe and other transition metals and observed larger cell volume of the substituted compounds. Substitution of Ni by Fe or Mn did not significantly change the thermal expansion property of $Yb_3Ni_{5-x}TM_xAl_{19}$ from 100 K to 298 K; while the thermal expansion coefficient of $Yb_3Ni_{5-x}Cu_xAl_{19}$ was much lower than that of the parent compound $Yb_3Ni_5Al_{19}$, however, no clear trend was observed when the x values increased. On the other hand we found that substitutions of Ni with other transition metals, especially Cu, can modify the magnetic properties of the parent compound $Yb_3Ni_5Al_{19}$. The substitution of Ni by Cu causes cell volume expansion so this system is driven by negative chemical pressure towards the Yb^{2+} regime while still in the Yb^{2+}/Yb^{3+} intermediate state. With more Cu added into the structure, the effective magnetic moment μ_{eff} for $Yb_3Ni_{5-x}Cu_xAl_{19}$ (x = 1) appears to be very close to that of the free Yb^{3+} ion (theoretical value μ_{eff} = 7.86 μ_B per formula), which could be due to an increment of the number of conduction electrons, and hence a rise of the Fermi level. Therefore the hybridization between the 4f electrons and the conduction band is decreased, causing a quenching of the Kondo effect. In order to explain the changes in the hybridization between 4f electrons and the

conduction band, both volume and Fermi level modification have to be taken into account.

The use of chemical pressure to tune Yb hybridization can be also applied to the other Yb-containing compounds, such as the charge-balanced Zintl phase $Yb_9Al_3Sb_9$ in which the Yb ions are in a divalent oxidation state. The partial substitution of Al ions by larger Zn ions might cause changes of the 4f-conduction electron hybridization, which can be tracked by magnetic susceptibility measurements.

When we tried to substitute Ni with Fe in $Yb_3Ni_5Al_{19}$, new quaternary intermetallics $RENi_{2-x}Fe_xAl_8$ (RE = Eu and Yb) were isolated from liquid aluminum. The $RENi_{2-x}Fe_xAl_8$ species are the first quaternary analogues with the $CaCo_2Al_8$ structure type.[7] Both magnetic properties and Mössbauer spectra of $YbNi_{2-x}Fe_xAl_8$ show that the Fe atoms do not carry magnetic moments. Temperature dependent magnetic susceptibility measurements indicate that the Yb atoms are in an intermediate oxidation state with effective magnetic moment $\mu_{eff} = 2.19\ \mu_B$. The magnetization behavior studies indicate that the *ab* plane is the easy plane on which the magnetic moments are confined. The discovery of these new phases might give us a direction to explore the systems $RE/TM_1/TM_2/Al$ using Al as a flux. It has been discovered that in the presence of a divalent rare earth metal or alkaline earth metal, Au reacts with an early transition metal to form cubic phases $M_3Au_{6+x}Al_{26}T$ (M = Ca, Sr, Eu, Yb; T = early transition metals from groups 4-7).[8] The crystal structure is a stuffed variant of the $BaHg_{11}$ type and the transition metal site can be a host for a variety of early transition metals. Therefore it would be interesting to examine the systems containing a rare earth metal, an early transition metal, a late first row transition metal in liquid aluminum. We would be

especially interested in Ce- and Yb-containing intermetallic phases with an eye on the behaviors associated with 4f-conduction electron interactions.

References:

[1] Sieve, B. Ph. D. Dissertation, Michigan State University, 2002.

[2] Latturner, S. E.; Bilc, D.; Mahanti, S. D.; Kanatzidis, M. G. *Chem. Mater.* **2002**, *14*, 1695.

[3] Latturner, S. E.; Kanatzidis, M. G. *Chem. Commun.* **2003**, *18*, 2340.

[4] Latturner, S. E.; Kanatzidis, M. G. *Inorg. Chem.* **2003**, *42*, 7959.

[5] Latturner, S. E.; Bilc, D.; Ireland, J. R.; Kannewurf, C. R.; Mahanti, S. D. ; Kanatzidis, M. G. *J. Solid State Chem.* **2003**, *170*, 48.

[6] Salvador, J. R.; Guo, F.; Hogan, T.; Kanatzidis, M. G. *Nature* **2003**, *425*, 702.

[7] Czech, E.; Cordier, G.; Schaefer, H. *J. Less-Common Met.* **1983**, *95*, 205.

[8] Latturner, S. E.; Kanatzidis, M. G. *Inorg. Chem.* **2004**, *43*, 2.